EÖTVÖS LORÁND TUDOMÁNYEGYETEM
TERMÉSZETTUDOMÁNYI KAR

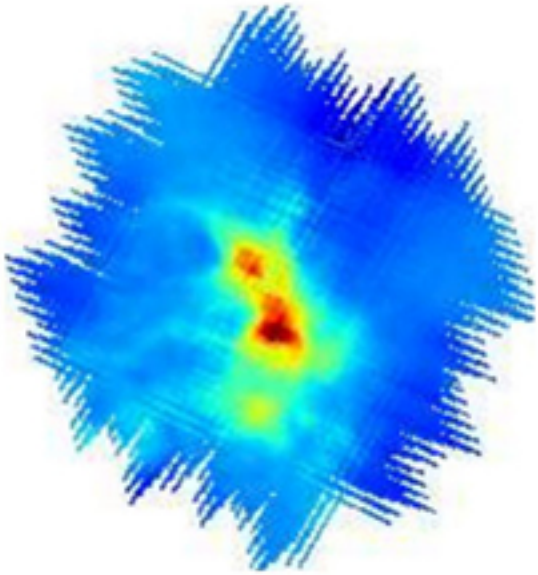

INFRARED ASTRONOMY

L. VIKTOR TÓTH
SAROLTA ZAHORECZ
CSABA KISS

Infrared Astronomy

edited by L. Viktor Tóth

L. Viktor Tóth

Sarolta Zahorecz

Csaba Kiss

Infrared Astronomy: *edited by L. Viktor Tóth*

L. Viktor Tóth
Sarolta Zahorecz
Csaba Kiss
lector: Attila Moór Póczos Valéria

Made in the project entitled "E-learning scientific content development in ELTE TTK" with number TÁMOP-4.1.2.A/1-11/1-2011-0073. Consortium leader: Eötvös Loránd University, Consortium Members: ELTE Faculties of Science Student Foundation, ITStudy Hungary Ltd.

Table of Contents

Preface - The Fox's Secret:

In the book of Antoine de Saint-Exupéry the *Le Petit Prince* the fox tells the little prince: *Voici mon secret. Il est très simple: On ne voit bien qu'avec le cœur. L'essentiel est invisible pour les yeux*. In English: 'And now here is my secret, a very simple secret: It is only with the heart that one can see rightly; what is essential is invisible to the eye' (translation by Katherine Woods 1943).

Figure 0.1: A fox as seen at night by an infrared camera with an infra-red flash at North Buckhead Atlanta, GA USA (Hinson 2009, http://www.nbca.org/Wildlife/New_Pictures.htm)

Humans at normal body temperature, radiate most strongly in the infrared, which is definitely not seen by human eyes. The scientific discovery that the heat we all feel coming from the Sun is largely a radiation beyond the visible red colour of the solar spectrum was made by William Herschel in 1800. He named the invisible radiation measured by his thermometers (see later the Herschel experiment) as *infrared*. Infra- (Latin) is a prefix meaning “below”. In other words the experiment in which infrared radiation was discovered was in fact an astronomical measurement. Astronomers were active in the infrared detector developments in the early years as well as they are today.

Infrared astronomy was introduced in Hungary by Lajos G. Balázs in the 1980s when he started to analyze and interpret IRAS data at the Konkoly Observatory Budapest. By the 2010s Hungarian astronomers (including the authors) contributed to the work of the Herschel PACS Consortium and various research projects.

The goals of the authors were to help the reader understanding the basics of infrared radiation and observing techniques, to give a broad view of astronomical objects and processes that are observable in the infrared, and to provide some help in the use of publicly available archives of infrared observatories.

We are thankful for our lectors Péter Ábrahám, Csaba Kiss and Attila Moór for their corrections and suggestions. Special thanks to Sarolta Zahorecz and Csaba Kiss for their contribution. We also ask all our readers to suggest how to further develop this e-book, and to send their contributions (text, figures, and animations) to be included.

Budapest, October 2013.

L.V. Tóth

Figure 0.2: The structure of cirrus as seen in far-infrared by the Herschel Space Telescope in the Vulpecula (Little Fox) constellation. Three colors composite image from blue=70µm, green=160µm, red=250µm. (ESA/PACS & SPIRE Consortium, Sergio Molinari, Hi-GAL Project, http://oshi.esa.int/#detail=image.html?id=27)

Chapter 1. Introduction – the discovery and use of infrared

In this chapter we give the basic definitions and laws of radiometry and spectroscopy, and mention the milestones of the early history of experimental and observational infrared astronomy. The use of infrared techniques at various non-astronomical applications is also addressed.

1.1 Herschel and his discovery of infrared

> *"The life of Herschel had the rare advantage of forming an epoch in an extensive branch of astronomy."* (Arago)

Sir Frederick William Herschel (*Friedrich Wilhelm Herschel*, 1738-1822) was born in Hanover, Germany, but immigrated to England in 1757 and became a respected musician in the town of Bath also as composer and director of the orchestra. He was the best telescope-maker of his time. With his sister Caroline they surveyed the sky that resulted in several catalogs and a model of our Galaxy or as he called it he mapped "*The Construction of the Heavens*". Herschel is perhaps most famous for his discovery of the planet Uranus in 1781, the first new planet found since antiquity.

In the year 1800, Herschel made an important experiment. He was curious to know the colour of light carrying the heat of the Sun. To his great surprise, his carefully positioned thermometers detected heat also where light separated into colours by the prism was lost in darkness beyond the red end of the visible spectrum. Initially he wanted to measure how much heat passed through the different colored filters he used observing the Sun. He noticed that filters of different colors pass different levels of heat. Herschel thought that the colors themselves might contain different levels of heat, so he devised an experiment to investigate his hypothesis.

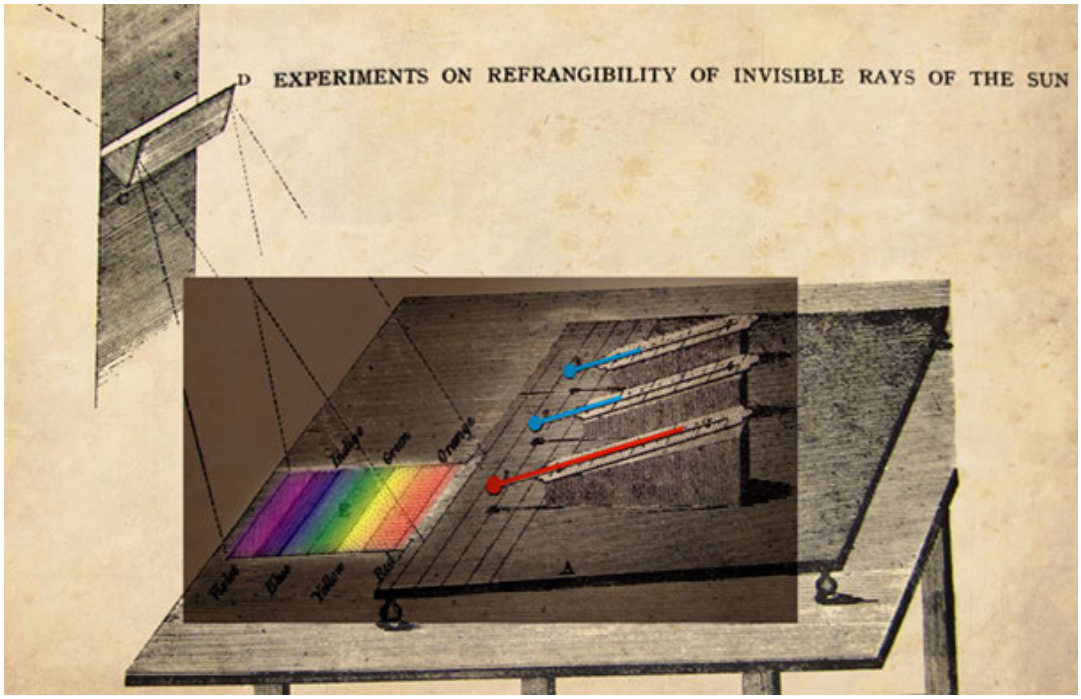

Figure 1.1 *The Herschel experiment. (Illustration by Vilmos Thernesz based on the original figure in Herschel, W., 1800: "Experiments on the refrangibility of the invisible rays of the Sun" Phil. Trans. Roy. Soc. London 90, 284–292)*

Herschel directed sunlight through a glass prism to create a spectrum - the "rainbow" created when light is divided into its colors - and measured the temperature of each color. He used three thermometers with blackened bulbs (to

better absorb the heat) and placed one bulb in each color while the other two were placed beyond the spectrum as control samples. As he measured the temperatures of the violet, blue, green, yellow, orange and red light, he noticed that all of the colors had temperatures higher than the controls and that the temperature of the colors increased from the violet to the red part of the spectrum. Herschel placed a thermometer also beyond the red end of the visible spectrum meant to be a control to measure the ambient air temperature in the room. Surprisingly it showed a higher temperature than the ones at the visible spectrum. Herschel's concluded that there must be an invisible form of light beyond the visible spectrum that he called as "calorific rays" (the Latin word *calor* means heat). The results were reported to the Royal Society: *In this case, radiant heat will at least partly, if not chiefly, consist, if I may be permitted the expression, of invisible light; that is to say, of rays coming from the sun, that have such a momentum as to be unfit for vision* (Herschel 1800).

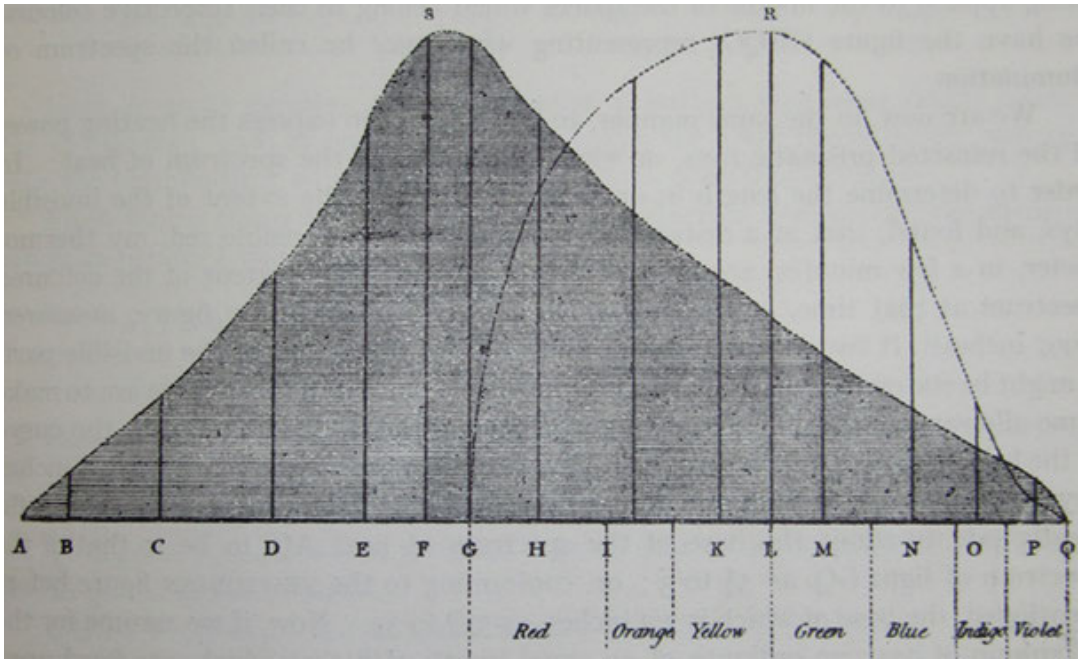

Figure 1.2Spectral energy distribution for the Sun as observed by Herschel. *We note that the peak is shifted to the IR because of the prism used (Herschel W., 1800: Experiments on the solar and on the terrestrial rays that occasion heat ... (2d part). Philosophical Transactions of the Royal Society, 90, 437-538.)*

A comparison of the radiant heat and light through the spectrum was also made by Herschel (1800b), and as shown in Figure 1.2 the calorific rays showed a maximum outside the visible range (G to Q). Herschel also tried to measure the total power received from the Sun. The solar constant (the total power received from the Sun per unit surface perpendicular to its direction at a distance of 1 A.U.) constant was first successfully measured by Claude Pouillet by his ‘pyrrhéliomètre’ instrument (Pouillet 1838).

1.2 Black body radiation – the first experiments of infrared radiometry

Historically the radiation properties of a heated body were known from experiments well before a comprehensive theory was made. Researchers of the late nineteenth century, like Wilhelm Wien (Nobel Prize laureate 1911) punched a small hole in the side of an otherwise completely closed oven, and began to measure the radiation coming out. The temperature of the oven, a platinum cylinder sheet within a ceramic tube, could be varied between -188 C and 1600C. That was their experimental black body.

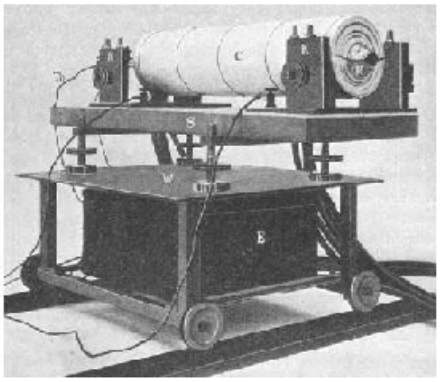

Figure 1.3: Otto Lummer and Ferdinand Kurlbaum's black-body experiment from 1898: platinum cylinder sheet within a ceramic tube (Hoffmann, 2000, Physikalische Blätter Volume 56, Issue 12, p 43).

In the beginning the emitted infrared radiation was measured by bolometers. The bolometer used was developed based on a similar device by the American astronomer Samuel Pierpont Langley, consisted of two platinum strips covered with lampblack. One strip was shielded from radiation and one exposed to it. The strips formed two branches of a Wheatstone bridge which was fitted with a sensitive galvanometer and connected to a battery as seen in Langley's drawing of the circuit diagram in Figure 1.4. Electromagnetic radiation falling on the exposed strip (at "A") would heat it and change its resistance. The bolometer was enclosed into a cylindrical holder made of non-conducting material. It had the capability to detect radiation from a cow standing 400 meters away, and was sensitive to differences in temperature of 0.001K (Langley 1881). A basic bolometer circuit diagram and explanation can be found also e.g. at http://electriciantraining.tpub.com/14193/css/14193_106.htm

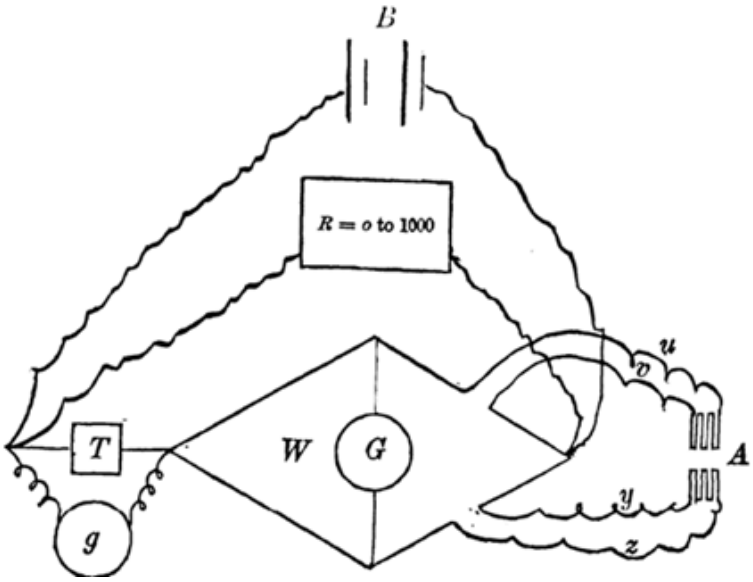

Figure 1.4: Circuit diagram of Langley's bolometer. The bolometer "A" was connected to the Wheatstone bridge by the insulated copper wires "u, v, y, z". (Figure 3 in Langley, S.P., 1881, Proceedings of the American Academy of Arts and Sciences, Vol. 16, p. 342 http://www.jstor.org/stable/25138616).

The name bolo-meter is formed from the Greek word "βολή" [bolo] that means shot. This instrument enabled Langley to discover new atomic and molecular absorption lines in the invisible infrared portion of the electromagnetic spectrum. But he also interpreted his measurements as a demonstration that "heat" and "light" from the Sun is just different names of the same physical phenomena.

The Wien's Displacement Law was observed as the v frequency at which the emitted radiation was most intense was directly proportional to the T absolute temperature of the radiating body. The wavelength of the electromagnetic radiation is related to the frequency with the following equation:

$$\nu = c / \lambda \tag{1.1}$$

where c is the speed of the electromagnetic radiation in m/s, ν is the frequency in hertz (Hz) and λ is the wavelength in meter. That means:

$$\lambda_{max} = b / T \tag{1.2}$$

where λ_{max} is the wavelength of the peak of the emission of a black body and the b constant of proportionality is called as Wien's displacement constant, b = 2.8977685(51)×10^{-3} mK. Stefan's Law or Stefan-Boltzmann law (1879) was also recorded from experiments i.e. that the total power P radiated from one square meter of black surface at temperature T goes as the fourth power of the absolute temperature:

$$P = \sigma_S T^4 \tag{1.3}$$

The Stefan's constant is $\sigma_S = 2\pi^5 k_B{}^4 c^{-2} h^{-3} = 5.6704 \times 10^{-8}$ $Js^{-1}m^{-2}K^{-4}$ where k_B is the Boltzmann constant (1.38×10^{-23} J/K), h is the Planck constant (6.626×10^{-34} Js), and c is the speed of light (299,792,458 m/s). The observational evidences provided at the University of Berlin, by Wien and Lummer at the last years of the 19th century lead to the theories of the spectral energy distribution functions, one of which was the Planck law of black body radiation.

Black-body radiation (also called as "cavity radiation") is the type of electromagnetic radiation within or surrounding a body in thermodynamic equilibrium with its environment, or emitted by a black body (an opaque and non-reflective body) held at constant, uniform temperature. The radiation has a specific spectrum and intensity that depends only on the temperature of the body. A blackbody is a theoretical perfect absorber and emitter. It absorbs radiation of all wavelengths falling on it and radiates electromagnetic energy at all frequencies. The power emitted by a blackbody from a unit area to a unit solid angle in a spectral interval, i.e. the specific intensity (see also chapter 5) of the blackbody radiation is given by the Planck's law that can be written in 2 forms:

$$B_\nu(T) = \frac{2h\nu^3}{c^2} \frac{1}{e^{\frac{h\nu}{k_B T}} - 1} \tag{1.4}$$

$[Wm^{-2}Hz^{-1}sterad^{-1}]$

$$B_\lambda(T) = \frac{2hc^2}{\lambda^5} \frac{1}{e^{\frac{hc}{\lambda k_B T}} - 1} \tag{1.5}$$

$[Wm^{-2}\mu m^{-1}sterad^{-1}]$

where T is the temperature of the object, Figure 3.3 shows Planck's law for different temperatures. Planck used the (1.5) form in his paper (Planck 1900).

$$E_\lambda \, d\lambda = \frac{c_1 \lambda^{-5}}{e^{\frac{c_2}{\lambda \vartheta}} - 1} \cdot d\lambda$$

Figure 1.5 a: *The Planck law by Planck, M., 1900, Zur Theorie der Gesetzes der Energieverteilung im Normal-Spektrum, Verhandlungen der Deutschen Physikalisches Gesellschaft Nr. 17, p. 237).*

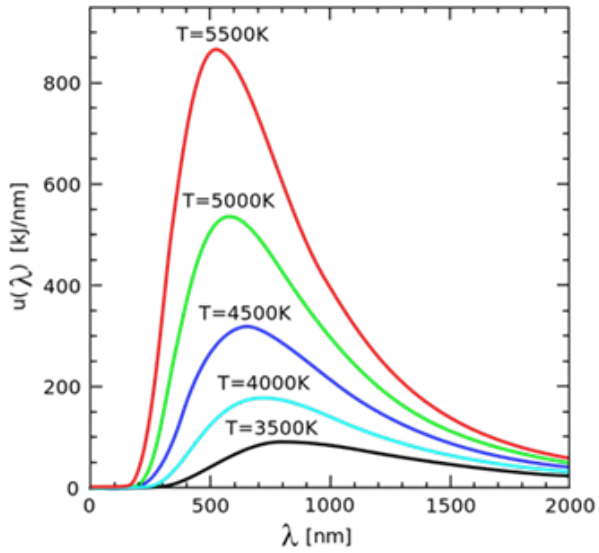

Figure 1.5: Planck's law for different temperatures: *The peak of the spectra shifts to shorter wavelengths for higher temperatures, and the area under the curve grows rapidly with increasing temperature.*

(http://upload.wikimedia.org/wikipedia/commons/thumb/a/a2/Wiens_law.svg/300px-Wiens_law.svg.png)

Human eye sees the blackbody colors at temperatures around 5000-7000 K as nearly white. An interactive animation was made by the PhET Development Team at University of Colorado helping us to understand the properties of the Planck function. Try to decrease the temperature below 3000K then further down to 300K while zooming in by the (+) button at the intensity axis, and zooming out using the (-) button below the wavelength axis! The animation is available at: http://phet.colorado.edu/sims/blackbody-spectrum/blackbody-spectrum_en.html

1.3 The photosphere of the Sun as a black body and the Herschel experiment

The photosphere of the Sun is not a precise blackbody, but its radiation may be approximated with that of a T_{eff}=5780 K (T_{eff} is the effective surface temperature outside sunspots). In Figure we show a standard called "CIE D65" (see eg. http://cvision.ucsd.edu/cie.htm ,`daylight' normalized to the solar flux at 560 nm) together with the solar spectrum. As it is well seen the spectral energy distribution outside the terrestrial atmosphere peaks are at around 400-500nm, and that we consider blue. Due to atmospheric scatter we see the energy peak of the solar spectrum at around 600nm, but that is definitely not in the infrared. So why did Herschel observe the highest reading in the infrared?

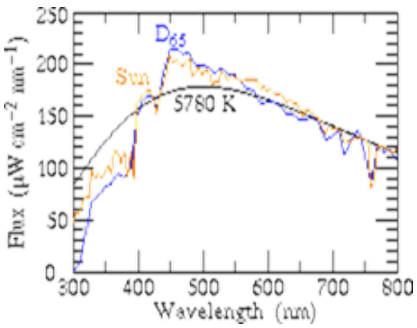

Figure 1.6: The spectrum of the Sun as seen from above the Earth's atmosphere*, together with the spectrum of a blackbody at 5780 K with the same total flux as the Sun, and the spectrum of CIE D65 `daylight' normalized to the solar flux at 560 nm. The Sun's spectrum was taken from R. L. Kurucz, I. Furenlid, J. Brault & L. Testerman (1984) Solar Flux Atlas from 296 to 1300 nm. (*http://casa.colorado.edu/~ajsh/colour/Tspectrum.html*)*

In Herschel's experiment, sunlight was refracted by a glass prism that is now on display at the National Museum of Science and Industry in London, England. (http://www.sciencemuseum.org.uk/on-line/treasure/objects/1876-565.asp). The index of refraction (or refractive index) *n* of the glass varies non-linearly with wavelength (dispersion, see Figure) and the sunlight is dispersed into its various colors. In fact the dispersed wavelengths were not uniformly spaced along Herschel's measuring table, there was a concentration toward the infrared, and that made the observed "temperature" increasing toward longer wavelengths. See also Chester, 1999.

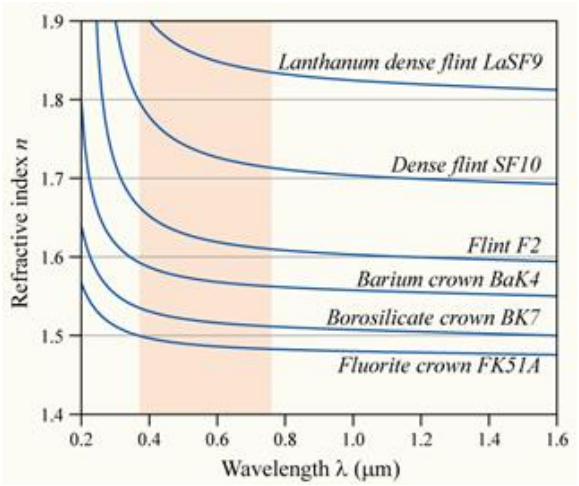

Figure 1.7: Plot of refractive index vs. wavelength of various glasses - dispersion. *The wavelengths in the red-shaded portion correspond to the visible spectrum. (By Bob Mellish* http://en.wikipedia.org/wiki/File:Dispersion-curve.png*)*

1.4 The infrared radiation of the human body

Using late 19 century laboratory physics, and recent biophysics we may find out why the human body radiates most at a wavelength of about 10μm. The specific intensity of the human skin can be approximated with that of a modified black body.

$$I_\lambda = \varepsilon(\lambda) \mathrm{B}_\lambda(\mathrm{T}) \tag{1.6}$$

The ε(λ) emissivity of human skin in the wavelength range of 1μm< λ <14μm is nearly unity, ε(λ)=0.98±0.01 (Hobbie and Roth 2007). We may actually say it radiates like a black body. The Wien's displacement law may be used to find out in which wavelength range it radiates most. Assuming a skin temperature of 300 K < T < 310 K we arrive to 9.3μm < λ_{max} (T) < 9.7μm. The total surface area of the human body can be approximated by the depth-weight formula as

$$\mathrm{Area} = 71.85 \mathrm{w}^{0.425} \mathrm{H}^{0.725} \tag{1.7}$$

where w is the weight in kg and H is the depth in cm (Du Bois and Du Bois 1916). The total surface area for a typical adult male is Area ~ 1.73m^2 . The total radiated power at a skin temperature of T = 306 K may be calculated from Stefan's law as:

$$\mathrm{L} = \mathrm{Area}\ \sigma_s \mathrm{T}^4 = 860W \tag{1.8}$$

Although only a 5/7 fraction of the total skin surface is considered as effective radiator, the uncovered skin is a bright infrared source. We shine bright in the infrared while the human eye detects only 1% of the light at 0.69 μm, and 0.01% at 0.75 μm, and so we effectively cannot see wavelengths longer than about 0.75 μm.

It is not only the radiation of the human body that we can not see by our eyes. In space, there are many regions which are hidden from optical telescopes because they are embedded in dense regions of gas and dust. However, infrared radiation, having wavelengths which are much longer than visible light, can pass through dusty regions of space without being scattered. This means that we can study objects hidden by gas and dust in the infrared, which we cannot see in visible light, such as the center of our galaxy and regions of newly forming stars.

1.5 The use of infrared

Astronomical measurements require high angular resolution and sensitivity, and a very low noise level. That put constraints on optics, detector techniques and electronics, and triggers continuous advances in the technology. We may see then benefits in a wide range of non-astronomical applications. The first advanced application of IR technology in the civil section may have been a device to detect the presence of icebergs from steamships using a mirror and thermopile, patented in 1913, just after the catastrophe of the Titanic. Today, infrared technology has many exciting and useful applications. While in the field of infrared astronomy, new and fascinating discoveries are being made about the Universe, satellites with infrared imaging capabilities are also used to monitor the Earth's weather, to study vegetation patterns, and geology and "measure" ocean temperatures. Since the 1960s infrared radiometers are used in meteorology measuring at wavelengths up to 35µm to derive surface and cloud temperatures (see eg. : Combs et al. 1965).

1.2.1 Aerial or space infrared photography

Besides mapping cloud covers and other meteorological applications (see Figure 1.8), aerial or space infrared photography is used in yield predictions in farming as well as detecting diseases, insect infestation and other problems in plants. Plants reflect near-infrared light, however when they are under stress less infrared radiation is reflected, a stressed plant will be much darker in the near-infrared than one that is functioning normally and healthily (see Fig. 1.9). The same technique may reveal algae at shores, and contamination of waters by chemical or biological waste.

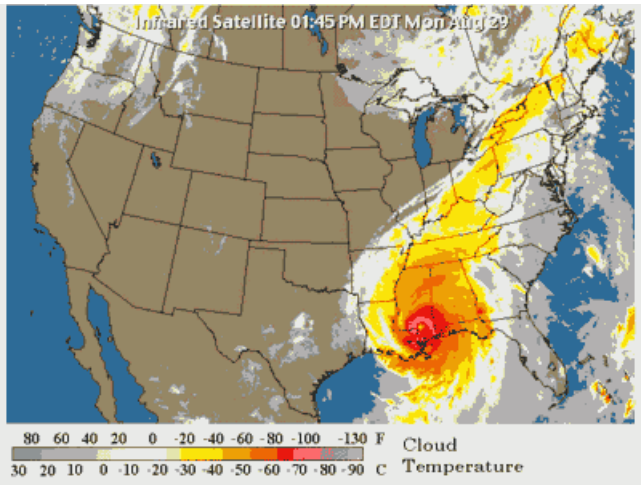

Figure 1.8: *Temperatures of Hurricane Katrina in 28 August 2005 from GOES infrared satellite data (*http://911review.org/Hurricane_Katrina/HURRICANEKATRINA.html*)*

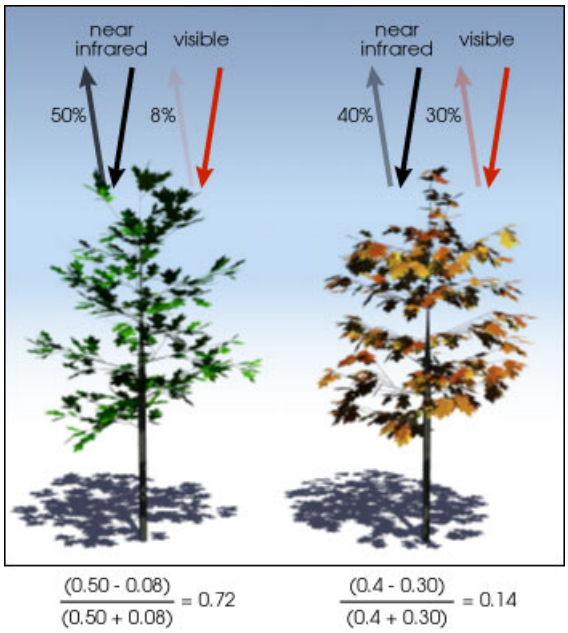

Figure 1.9:*Healthy vegetation (left) absorbs most of the visible light, and reflects about the half of the near-infrared light. Unhealthy vegetation (right) reflects relatively more visible light and less NIR light. Normalized Difference Vegetation Index (NDVI) is calculated from the visible and near-infrared light reflected by vegetation.* $NDVI = (NIR - VIS)/(NIR + VIS)$ *Real measured values are given as an example below the picture. (Robert Simmon, http://earthobservatory.nasa.gov/Features/MeasuringVegetation/measuring_vegetation_2.php)*

Differences in infrared colors may help to identify wild animals hidden in the vegetation, but as well as military installations camouflaged with dead foliage covers. One of the military's primary uses of infrared is for target acquisition that works both in daylight and in complete darkness, to track jet engines as well as persons in smog or fog, an advantage that helps also rescue activities in fire fighting. Infrared cameras are also installed on cars to an early detection of objects, animals, and people on the road in front of the vehicle (see Figure 1.10).

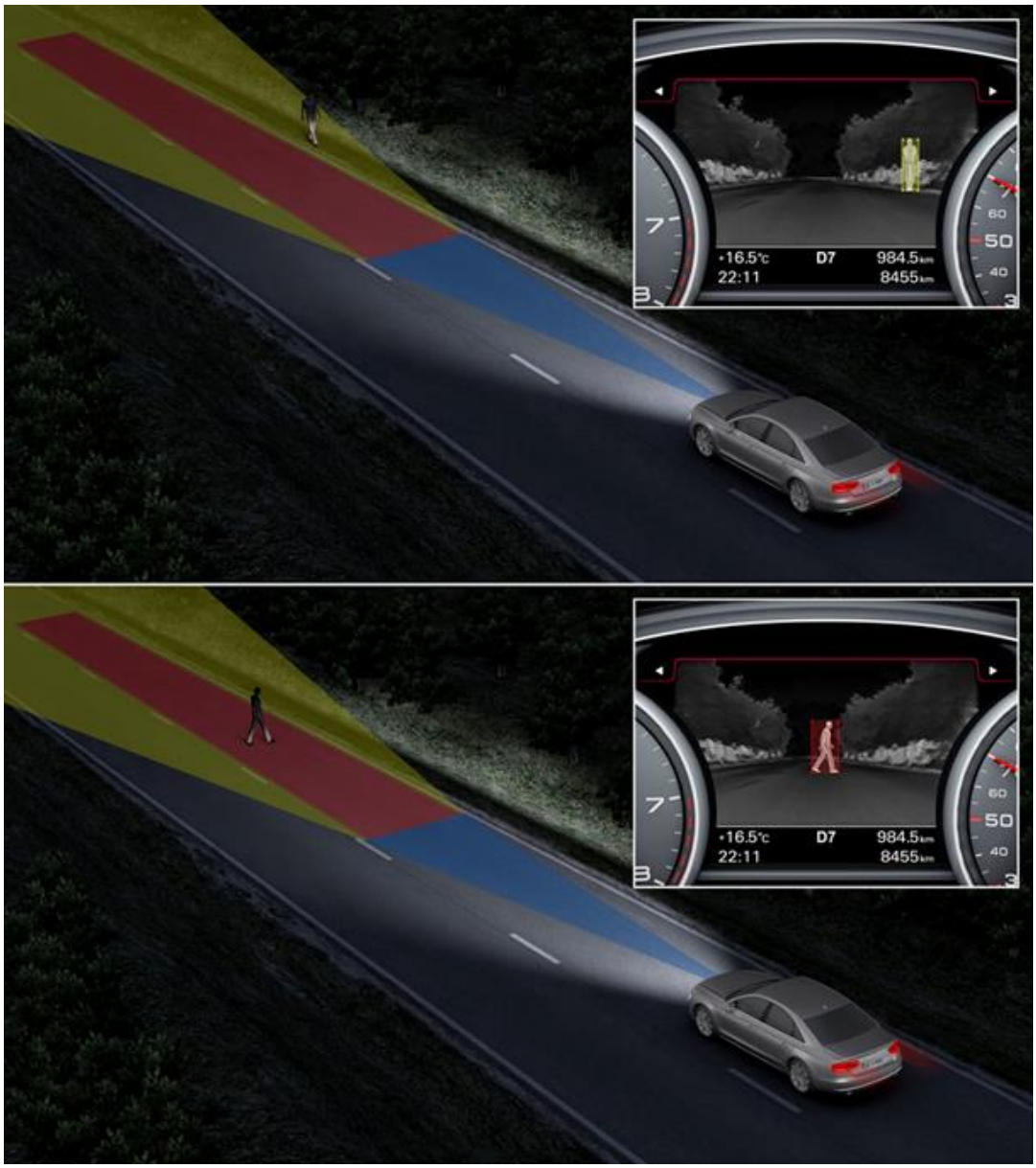

***Figure 1.10**: On board infrared camera detects a person on the road and an image processing and evaluation system warns the car driver on a night vision screen, see also a video:*
http://m.audi-technology-portal.com/var/site/storage/original/video/d4e5036f1624c6c3f5195fd7bd6b0547.mp4

1.2.2 Thermograms of small and large objects

Infrared imaging is used in testing electronic systems. Infrared thermography allows an evaluation of the level of warming of printed circuit boards as well as high voltage systems. This enables the early identification of defective components (such as loose connections, overloaded or imbalanced circuits, damaged switches, faulty fuses) helping to avoid costly downtimes and eliminates safety hazards (see Figure 1.11).

Figure 1.11: *Thermogram of an industrial electrical fuse block with a fault (bright yellow area)* http://en.wikipedia.org/wiki/File:Electrical_fault.jpg

Infrared video and still cameras are used to map surface heat variations allowing energy auditors to check the effectiveness of insulation in a building's construction. Thermograms help auditors determine whether a building needs insulation and where in the building it should go. Because wet insulation conducts heat faster than dry insulation, thermographic scans of roofs can often detect roof leaks. Three kinds of devices may be used: a spot radiometer to measure radiation from one spot at a time, a thermal line scanner shows radiant temperature viewed along a line, or a thermal imaging camera, which produces a 2-dimensional thermal picture. In all cases the inspector notes the differences in temperature to detect heat loss, from which the 2D thermal imaging is the easiest to interpret also by non-experts.

Figure 1.12*: Thermography – or infrared scanning – in use to detect thermal defects and air leakage in building envelopes.* http://energy.gov/energysaver/articles/thermographic-inspections

Infrared cameras are used in crime prevention and security purposes, these allow a homeowner or police officer to record a crime in progress without the perpetrator ever knowing that the camera existed. Modern CCTV cameras now have a ring of infrared LEDs built in to help illuminate the scene at night, a very useful installation for surveillance purposes. Article 8 of the European Convention on Human Rights provides that "everyone has the right to respect for his private and family life, his home and his correspondence". There is a debate if the police may freely use that technology to look also inside homes without being intrusive. Forensics investigators use infrared photography to see hidden details in a crime scene, and can pick up traces of soil, drops of water or biological waste such as urine, blood and sperm which may be otherwise invisible to the naked eye. Infrared photography can register the difference in temperature between an object and its environment.

1.2.3 Medical infrared thermography (MIT) or thermology

Thermology also called as medical infrared imaging or tele-thermology utilizes high resolution thermographic pictures of the skin surface. It is a non-contact way of examination and there is no energy imparted into the body. As we discussed in the first chapter, the human body is a strong infrared emitter. MIT provides a visual map of the skin temperature distribution but cannot quantify absolute temperature values. It is used in orthopedics, derma-

tology, breast cancer research, surgery, and other areas. One of the beneficial application of MIT is the screening of sportsmen for overuse injuries (see eg. Hildebrandt et al., 2012).

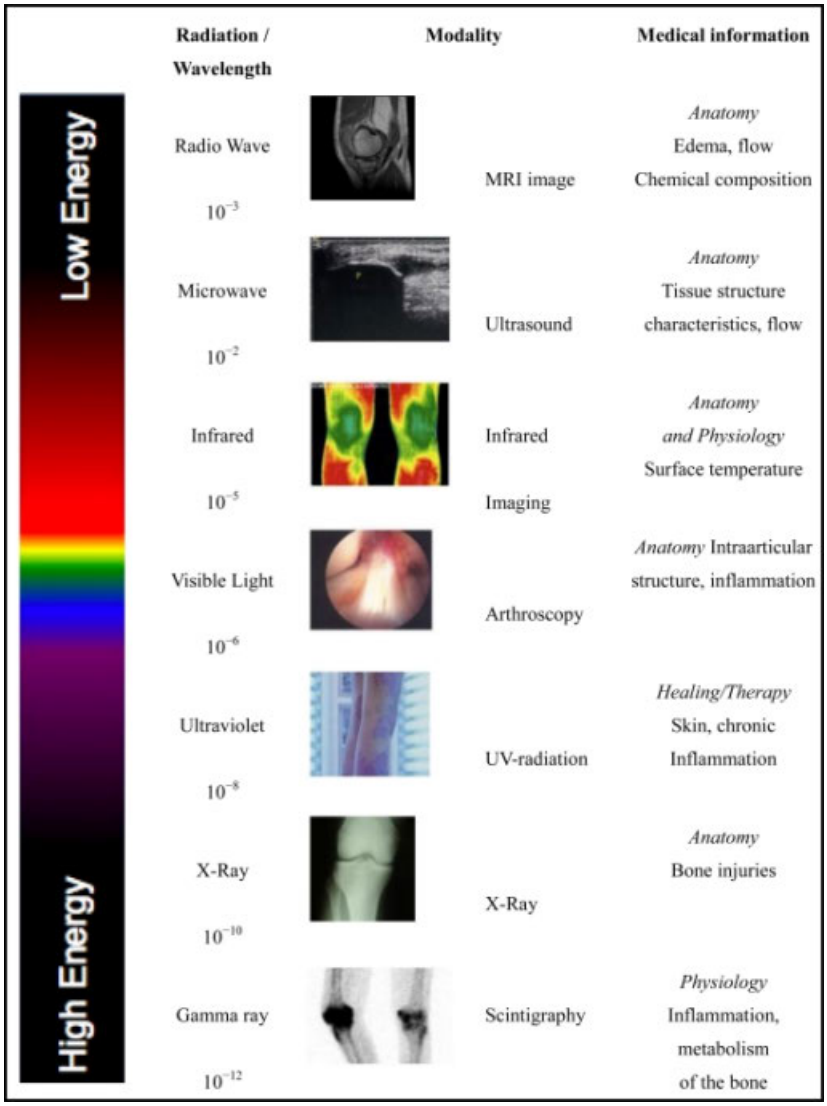

***Figure 1.13**: Electromagnetic radiation is used at various areas of human medicine on of which is measuring the skin surface temperature*

The medical use of infrared also includes healing by so called medical heat lamps, where a part of the body is heated up using infrared radiation. (Hildebrandt et al. 2012)

1.2.4 Arts and infrared

Famous paintings were often modified before the final version was painted. Under drawings or outlines drawn by the artist may be traced. Art historians and conservators can use infrared photography to see beneath a painting's surface and view detail that would otherwise remain forever unseen. This non-invasive examination is also helpful validating that works of art are authentic. It also revealed details of the making of a painting of French impressionist artist Pierre-Auguste Renoir. *Luncheon of the Boating Party* was several times modified before the final version was painted, and that can be traced by seeing "all brush strokes" by infrared imaging (http://en.wikipedia.org/wiki/Luncheon_of_the_Boating_Party). Paints which are reflective in the visible spectrum are in many cases transparent beyond 1µm (near-infrared, see later). A commercial InGaAs (Indium Gallium Arsenide) near infrared camera can "see" through the paint, and images the "underdrawing" (see Figure 1.10 and reports on the examination: Greenwood (1998)).

Figure 1.14: *Underdrawing image taken with Goodrich ISR-P's SU320M-1.7RT camera.* (http://www.sensorsinc.com/img/overview/renoir_camera.jpg)

Infrared films capture light in the part of the spectrum which we can't see with the naked eye, these renditions apply when infrared absorption and reflection are involved, photography can capture this invisible light. The first known infrared photographs were produced by Robert Williams Wood using sensitized photographic plates and very long exposures (published in the Royal Photographic Society's October 1910 Photographic Journal).

Kodak developed emulsions that were sensitive to infrared light, and infrared films became commercially available in the 1930s, also including a 35 mm false-color infrared film from 1960s. Infrared sensitive photographic plates (see Figure 1.15) were also used in astronomy for several decades, but since the demand decreased Kodak discontinued the production. When using black and white infrared film the first and most important thing to remember is to use a suitable filter, because the film is highly responsive to light so you need to filter out everything except the red and infrared spectrum (see eg. http://www.coolmint.co.uk/infrared/guide/).

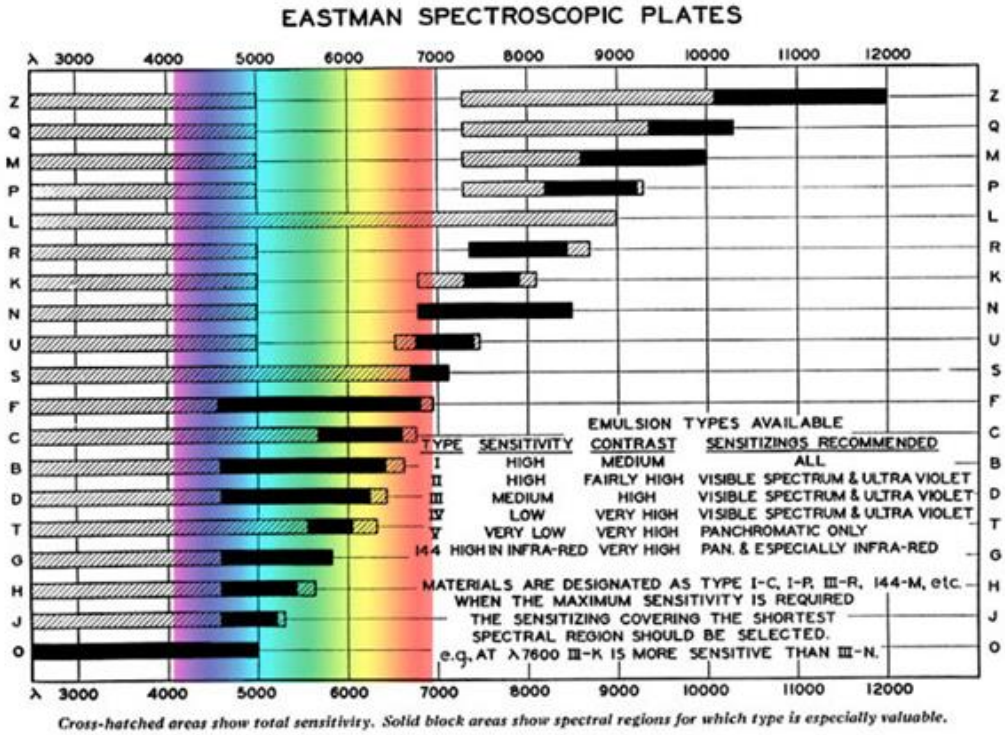

Figure 1.15: *The range of sensitisings available in 1937 at Eastman (O to Z on the vertical axis) and their optimal spectral range as the black bars running horizontally. The wavelenth (horizontal axis) is expressed in Angstroms. The visible part of the spectrum is marked. All the emulsions retain their UV-blue sensitivity, even the ones for the infrared. (Malin 2011).*

References and further reading to the chapter:

Brandes, T., 2004: *"Quantum Mechanics I" (P303 / M326)* ,UMIST, http://wwwitp.physik.tu-berlin.de/brandes/public_html/qm/umist_qm/node3.html

Combs, A. C. et al., 1965: "*Application of Infrared Radiometers to Meteorology",* J. Appl. Meteor., 4, 253

Chester, T., 1999: "*Reconciling the Herschel Experiment*", http://tchester.org/znet/calculations/herschel/index.html

Du Bois D., & Du Bois E. F. 1916: "*A formula to estimate the approximate surface area if depth and weight be known"*, Arch. Intern. Medicine, 17, 863-71.

Greenwood, K. F., 1998: *"Partnership With Industry - Princeton and photonics firms join forces to create new technologies"*, Daily Princetonian, Volume 120, Number 60

Herschel, W., 1800: "*Experiments on the refrangibility of the invisible rays of the Sun*", Phil. Trans. Roy. Soc. London 90, 284–292

Herschel W., 1800b: *"Experiments on the solar and on the terrestrial rays that occasion heat ... (2d part)"*, Philosophical Transactions of the Royal Society, 90, 437-538.

Hildebrandt, C. et al. 2012: *The Application of Medical Infrared Thermography in Sports Medicine* in the book: "An International Perspective on Topics in Sports Medicine and Sports Injury", page 14, DOI: 10.5772/28383) http://www.intechopen.com/books/an-international-perspective-on-topics-in-sports-medicine-and-sports-injury/the-application-of-medical-infrared-thermography-in-sports-medicine

Hinson, L., 2009: "*Recent North Buckhead Wildlife Photos*", http://www.nbca.org/Wildlife/New_Pictures.htm

Hobbie, R. K. , Rot, B.J.: 2007, *Intermediate Physics for Medicine and Biology*, Springer

Hoffmann, D.: 2000, Physikalische Blätter, Vol 56 Issue 12, *100 Jahre Quantenphysik: Schwarze Körper im Labor: Experimentelle Vorleistungen für Plancks Quantenhypothese* http://onlinelibrary.wiley.com/doi/10.1002/phbl.20000561215/abstract

Langley, S.P.,: 1881, *"The Bolometer and Radiant Energy"*, Proceedings of the American Academy of Arts and Sciences, Vol. 16, p. 342

Malin, D. 2011: "About Astronomical Photography", Australian Astronomical Observatory, http://www.aao.gov.au/images/general/photography.html

Planck, M.: 1900, *Zur Theorie der Gesetzes der Energieverteilung im Normal-Spektrum,* Verhandlungen der Deutschen Physikalisches Gesellschaft Nr. 17, p. 237

Pouillet, C., 1838: *Mémoire sur la chaleur solaire, sur les pouvoirs rayonnants et absorbants de l'air atmosphérique, et sur la température de l'espace*. Comptes Rendus de l'Académie des Sciences, 7, 24-65.

Stefan, J.: 1879, *Über die Beziehung zwischen der Wärmestrahlung und der Temperatur*, in: Sitzungsberichte der mathematisch-naturwissenschaftlichen Classe der kaiserlichen Akademie der Wissenschaften, Bd. 79, S. 391-428.

An astronomical IR picture album: http://www.ipac.caltech.edu/Outreach/Gallery/gallery.html

Herschel: http://en.wikisource.org/wiki/William_Herschel_and_his_work

Wien: http://www.nobelprize.org/nobel_prizes/physics/laureates/1911/

Planck: http://www.nobelprize.org/nobel_prizes/physics/laureates/1918/planck-facts.html

Thermograms of electric circuits: http://www.arl.army.mil/arlreports/2005/ARL-TR-3690.pdf or http://www.datacentir.com/ppm.html

Thermograms of buildings: http://energy.gov/energysaver/articles/thermographic-inspections

http://electriciantraining.tpub.com/14193/css/14193_106.htm

http://en.wikipedia.org/wiki/Luncheon_of_the_Boating_Party

http://phet.colorado.edu/sims/blackbody-spectrum/blackbody-spectrum_en.html

http://www.coolmint.co.uk/infrared/guide/

http://www.princeton.edu/paw/archive_old/PAW97-98/12-0325/0325feat.html

http://www.sciencemuseum.org.uk/on-line/treasure/objects/1876-565.asphttp://cvision.ucsd.edu/cie.htm

Chapter 2. History of infrared astronomy

As early as in 1842 Luigi Magrini (Magrini, 1843) measured the infrared radiation from the solar corona during an eclipse. The Sun, Moon and bright stars became targets of infrared observations, the “heat of the stars" Sirius, Pollux, and Regulus was detected by William Huggins (Huggins, 1869). Late nineteenth century the solar infrared spectrum was investigated. William de Wiveleslie Abney published his map of the solar infrared lines (see Abney, 1881, 1886). He obtained the spectrum by a grating spectrograph and photographic recording using a special silver salt as he describes the emulsion. The lines were listed in the wavelength range of 715 nm < λ < 1000 nm. Those years even the strongest atmospheric infrared lines were not yet well identified. His report on measurements at sea level (London) and at high altitudes (Zermatt) could be used to discuss the effect of water vapor on the spectrum and the assumed presence of oxygen lines. A few of the detected solar spectral (non-atmospheric) lines were called metallic, but few of them were named as “X” (4 lines) or “Y” (at λ_2= 898.65nm and λ_1= 899.04nm) without a clue of the radiating particles. The setup of Abney’s spectrograph is shown in Figure , where the sunlight enters the tube in the slit “S” and via the right-angle prism “p” it is reflected to mirror M’ then to the grating “G” another spherical mirror M” then reflects the spectrum to the photographic plate “P”.

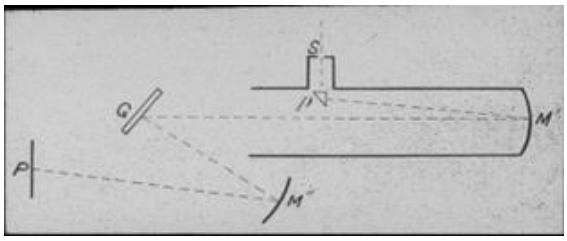

Figure 2.1: Abney’s apparatus measuring the solar near-infrared spectrum. *(*Abney, 1886, Philosophical Transactions of the Royal Society London, Vol. 177, page 460*)*

Early attempts in the late 1930s at finding infrared stars were hindered by the fact that the work relied on narrow-field optical telescopes and photographic detection; the relatively short wavelengths to which photographic emulsions were sensitive (below one micron) further limited the work. Photon detectors and image converters were developed in the first half of the 20th century. Infrared spectroscopy emerged and became the key analytical techniques available to chemists. The image converter, developed on the eve of World War II, enabled man to see in the dark and was immediately applied by the military. The post WWII developments of the lead salt family semiconductors started actually in the 1930s when Edgar W. Kutzscher (University of Berlin) discovered that lead-sulphide was photoconductive and had response to about 3 μm. The technique was already used in air-borne IR systems from 1943. Photoelectric detectors capable of sensing the infrared were developed during World War II also by R. Cashman of Northwestern University. Although astronomers acquired a few PbS (lead sulfide) cells and later photomultipliers in the 1940s and 1950s, much of the technology remained classified.

2.1 The Two-Micron-Sky Survey (also IRC or Caltech 2.2 micron survey)

The infrared telescope built by Neugebauer and his associates at Caltech utilized PbS photomultipliers which by the 1960s were generally available. The instrument was designed to gather infrared radiation at 2.2 microns, in the K photometric band, a region of the spectrum which is relatively free from absorption by water vapor in the Earth’s atmosphere. Detection at this wavelength was achieved by using an array of four liquid nitrogen cooled lead sulfide detectors. Radiation was focused onto the detectors by a 64-inch focal length 62-inch diameter parabolic reflector. The entire telescope as well as the protective shed were constructed by Caltech personnel, graduate and undergraduate students. The Santa Barbara Research Corp built the lead sulfide detectors.

The mirror was of ”spin-cast” design. An aluminum dish was rotated rapidly on a mill as epoxy resin was poured onto its surface. Under rotation, the fluid resin assumed a parabolic shape. The dish was spun until the resin hardened and was then aluminized to provide the reflecting surface. The electromechanical system used to diminish interference from background radiation involved first conversion of the signal from celestial sources to an alternating current by rocking the primary mirror slightly at 20 Hz back and forth relative to the detectors. Since the background signal (sky plus instrument noise) remained in the focal plane, it remained as direct current and it could be filtered out electronically (Neugebauer 1969). After the Caltech team demonstrated the successful operation of the telescope in an alley outside the Ryerson Laboratory on the Caltech campus the telescope was disassembled, moved to Mt. Wilson and reassembled.

The Caltech infrared telescope was first put into operation in 1963 on Mt. Wilson and then moved to White Mountain, also in California. Operated by several generations of graduate students from Caltech it was used as a survey instrument through the late 1960s. The telescope was programmed to mechanically sweep a 15 degree wide arc in a raster pattern. About 75% of the sky could be surveyed over one year. Data were collected on a strip chart recorder.

Infrared sources were then located by inspection of the charts and keyed manually onto paper tape for subsequent computer processing. The two complete northern sky surveys, one at 0.84µm and one at 2.2µm were completed by 1968. These surveys revealed a surprisingly large number of infrared sources.

The IRC catalogue contains 5562 stars brighter than K=3.0, with positions accurate to ≈ 1 arcminute. Only roughly 30% of these corresponded to visible objects. One of the strong infrared sources that were faint in the visible was the Becklin-Neugebauer object in the Orion nebula (Becklin & Neugebauer, 1967). The Solar System size object hides a luminous, massive young star ($8M_\odot<M<15M_\odot$), and although the star may have an effective temperature of 30000 K, the “infrared star” i.e. the dusty envelope shows a color temperature of only about 700K.

Another famous IR discovery was IRC+10216, a luminous carbon star with a thick circumstellar disk which obscures its visible light. When the survey was completed, the telescope was used through the mid-1970s to explore many of the infrared sources it had discovered, such as variable infrared stars like IRC+10216, the brightest star in 5 micron (Becklin et al., 1969), and dense clouds that are the sites of star birth. The telescope provided much useful data on the structure of our galaxy because near-infrared radiation from the center of the Milky Way is attenuated by only a factor of 10 by the interstellar medium, whereas visible light is attenuated by a factor of 10 billion.

Data from the telescope revealed features of the Milky Way, such as the distribution of infrared stars along the galactic plane; the telescope also provided data on the location of red giant stars and detected a strong infrared source at the center of the galaxy. This inexpensive and ingenious instrument produced data that led to over 78 scientific publications. It helped to found a new branch of astronomy.

See also references on the IRC or Caltech 2.2 micron survey at the end of the chapter.

2.2 Other important early discoveries with ground based telescopes

One can distinguish inside of OMC-1 two intense infrared sources: the punctual object of Becklin-Neugebauer (BN, see in Chapter 2.1) and, 10” to the south, the Kleinmann-Low Nebula that was found to be an ”extended source of very low temperature” (i.e. 70K) as mapped at 22µm with a 30” beam. ”The discovery of the infrared nebula in Orion means that early stages of star and star-cluster formation can be observed in the far infrared” (Kleinmann & Low 1967)

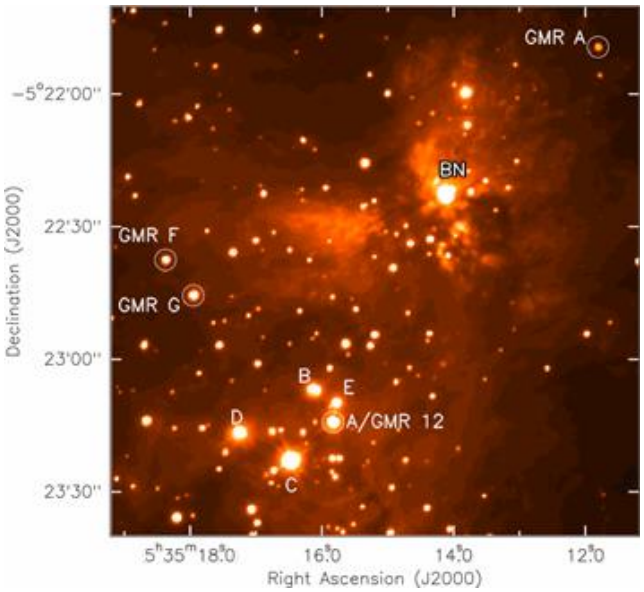

Figure 2.2: Infrared K-band image of the Orion Nebula Cloud and the BN/KL region *(courtesy M. McCaughrean, University of Exeter). The Trapezium stars (A, B, C, D and E) and the BN object are labeled. The image was taken with the ESO Very Large Telescope. (Menten K.M. et al. 2007 A&A 474, 515,* http://www.aanda.org/articles/aa/full/2007/41/aa8247-07/aa8247-07.html, http://dx.doi.org/10.1051/0004-6361:20078247*)*

The infrared point sources (IRS) in the W3 region as many as 9 were found, with low 2 μm and bright 20 μm emission indicating highly obscured bright sources. 4 of them are identified as compact radio HII condensations of 0.1pc diameter, one of which is towards the W3(OH) source. Four others are without radio continuum counterpart but associated with water maser sources. One of these W3IRS5 was thought to be a massive protostar (forming O star).

2.3 Balloon-borne infrared observatories

Balloon-borne observatories were designed to observe the cold radiation of the Universe from a stratospheric balloon-borne platform. At this altitude the atmosphere is almost transparent to the sub-millimeter radiation. However the environment is quite hostile, very close to space conditions: no thermal convection, energetic particles, hard Sun radiation, and extreme temperature excursions.

2.3.1 Far-Infared Spectrometer (FIS):

This instrument, also known as the Woody-Richards experiment (see Fig. 2.3), was one of the first designed to test the theory of the Big Bang by analyzing that radiation. The Fourier transform far infrared spectrometer worked on the principle of an interferometer. To achieve maximum sensitivity the assembly was immersed in a cryostat cooled with superfluid helium. Helium 3, used in last flight cooled the bolometer to below one degree above absolute zero, the first time such a low temperature had been used for astronomical observations. The whole package was borne to high altitudes far above most of the earth's atmosphere by a large helium filled balloon. The spectrometer was used for three flights in the mid-1970s. The results showed a blackbody radiation with a temperature of 2.96K (Woody & Richards 1979) provided the most widely accepted support for the Big Bang theory until the announcement of data from the Far Infrared Absolute Spectrometer (FIRAS) flown on the Cosmic Background Explorer (COBE) satellite. The Woody-Richards experiment combined novel technologies that were later used on FIRAS/COBE. It was donated to NASM in 1997 by Professor Paul Richards of the Department of Physics at the University of California, Berkley. (see also: http://www.lbl.gov/Science-Articles/Research-Review/Magazine/1997-fall/notes/index.html)

Figure 2.3: *Paul Richards stands with elements of the Woody-Richards cosmic microwave background instrument package (*http://www.lbl.gov/Science-Articles/Research-Review/Magazine/1997-fall/notes/index.html*)*

2.3.1 PRONAOS

The balloon-borne experiment (”PROjet NAtional d’Observation Submilletrique”) was a French (state-of-art) successor of the early probes. It consisted of a gondola hosting a 2m segmented sub-millimeter telescope. The first flight of the instrument was performed in September 1994 and gave only limited scientific results (see Ristorcelli et al. 1998) due to pointing problems.

During the second flight from Fort-Sumner (NM, USA) on September 22, 1996 data could be obtained under good conditions for more than 20 hours. The fine pointing of the payload is ensured by a star tracker allowing night and day detection of stars to a relative accuracy of about 5” rms. Details of the gondola stabilisation and pointing are given in Berrivin et al. (1997).

The focal plane instrument, SPM (”Spectro Photometre Submillimetrique”), is a sub-millimeter photometer observing simultaneously in four channels. They measure the sub-millimeter flux in the spectral ranges 180-240, 240-340, 340-540, and 540-1200 µm, band 1-4, with sensitivity to low brightness gradients of about 1 $MJysr^{-1}$ in band 4. The effective wavelengths are 200, 260, 360 and 580 µm for an emissivity grey body spectrum at 30 K) in wide bands (60, 100, 200 and 660 µm respectively). A detailed description of the SPM photometer and the PRONAOS gondola and telescope is given in Lamarre et al. (1994). The beam of the instrument is modulated on the sky with an amplitude of 6.0’ at a frequency of 20 Hz using an internal wobbling mirror. Detection is achieved using four bolometers cooled to 0.3 K by two compact, closed cycle fridges. The FWHM beam size, as measured on a map of Saturn during the flight, is 2, 2, 2.5 and 3.5 arcmin respectively. The in-flight response of the SPM instrument is measured using an Internal Calibration System (ICS) which is composed of two blackbodies at 310 and 370 K. The differential signal of the ICS is injected at the entrance of the instrument between each observation using a movable mirror.

Sensitive measurements toward the high latitude cirrus cloud in the Polaris Flare allowed for the first time to study in details the sub-millimeter dust emission of cirrus at the arc minute scale. The extended cirrus as well as a compact condensation already identified as an NH_3 core were well detected in the four photometric channels of the instrument.

Bernard et al. (1999) proposed that the optical properties of dust in regions such as the Polaris cirrus, which exhibit large excess over their emission, are modified compared to those prevailing in the general diffuse interstellar medium in the Galaxy. This change in the optical properties of large grains is likely connected to the coagulation of smaller dust particles on large size grains.

The central region of the Orion A cloud complex has been observed in the sub-millimeter range, using the PRONAOS-SPM during its first flight, in 1994 September. An area covering 50' x 10' and including the M42 Nebula has been mapped in four sub-millimeter photometric bands: lambda 180-240, 240-340, 340-540, and 540-1200μm, with high sensitivity (≤ 2MJysr^{-1}) and an angular resolution from 2' to 3.'5, see Figure 2.4. Four brightness enhancements are visible and have been identified with the following sources: (1) the brightest peak corresponding to the central core of the nebula, in the BN/KL source direction; (2) an extended emission region around 5' x 8', to the southeast of BN/KL, correlated with 100 μm IRAS and ^{13}CO emission (this has been identified as a gas-density enhancement associated with a shock region); (3) the edge of an ionized part of the cloud, correlated with the 100 μm emission; and (4) a very cold and extended condensation, discovered at 16' northwest of BN/KL. The emission spectra obtained for these sources show a variation of the dust emissivity spectral index within a large range, from 1±0.1 to 2.2±0.2. The dust opacity has a frequency dependence $\kappa_\nu = \kappa_0(\nu/\nu_0)^\beta$, where β is the emissivity spectral index of dust emission. The cold condensation discovered (T = 12.5±3 K) has a very low brightness emission, undetected on the 100 μm IRAS map. It extends over approximately 0.7 pc (FWHM), with a total mass of 11 $M_\odot$ and a total luminosity of 2.4 $L_\odot$ (Ristorcelli et al., 1998).

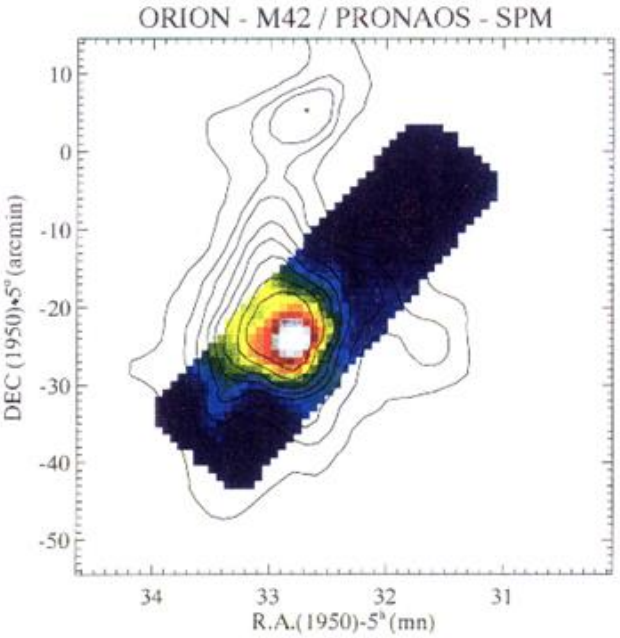

Figure 2.4: PRONAOS-SPM (210 μm) deconvolved signal of the M42*. The contours are 100 μm IRAS image (Figure 4 from Ristorcelli et al. 1998)*

2.4 Rocket flights

The Aerobee rockets were liquid-propellant sounding rockets procured by the US Air Force's Geophysics Laboratory for its infrared astronomy, or Hi Star program. The Hi Star program of the late 1960's to mid-1970's used infrared telescopes carried by Aerobee and other rockets to refine its target sighting instrumentation in the development of anti-satellite weapons systems. The weapons were required to detect infrared targets at the greatest possible range and the sightings had to permit discrimination of the target from the background of the celestial sky as well as celestial and other radiations.

Altogether, the Air Force acquired four Aerobee 350's but this one was not flown because the simpler and less expensive Aires solid-fuel sounding rocket replaced the Aerobees. This Aerobee, the largest and most sophisticated member of the Aerobee sounding rocket family which lasted from 1947 to 1985, is flyable and though lacks its solid-fuel booster. The Aerobee 350 was an expendable vehicle and the usual scientific payload it carried had a parachute attached for data recovery purposes. Typical payloads were large telescopes and mass spectrometers, and smaller instruments for measuring micrometeorites, airglow spectra, electromagnetic waves, radiation, ion composition, stellar spectra and aurora phenomena (http://www.astronautix.com/lvs/aeree350.htm).

The first IR astronomical flight detected sky noise only at the bands 1-to 3 μm and 3-to 7μm (Harwitt et al. 1966).

AFCRL and AFGL infrared sky surveys were carried out by the US Air Force Cambridge Research Laboratory. The 16.5cm aperture rocket-borne telescopes surveyed the sky in the 3-to 5µm 8-14µm and 16-24µm bands. It discovered objects like the pre-planetary nebulae RAFGL 2688 ”the EGG nebula” (Ney et al. 1975), and RAFGL 618 (Westbrook et al. 1975) (see also Lo & Bechis, 1976). The surveys also discovered ”possible pre-main-sequence objects” in the densest central portions of large interstellar clouds (Werner, Becklin & Neugebauer 1977), and ”nebulous objects” like CRL2789 or V645 Cygni which was turned out to be a young stellar object associated with a bipolar molecular outflow with a modest degree of collimation. (Cohen, 1977.).

The following catalogs were created:

Walker, R. G.: 1975, ”AFCRL infrared sky survey. Volume 1: Catalog of observations at 4, 11, and 20 microns”

Price, S. D.; Walker, R. G.: 1976, ”The AFGL four color infrared sky survey: Catalog of observations at 4.2, 11.0, 19.8 and 27.4 micrometers”

The latest developments in observational technique allow infrared measurements using large telescopes and interferometry. The collecting area allows us to study faint objects and the resolution increases

http://learn.hamamatsu.com/tutorials/java/airymag/

2.5 COBE

The Cosmic Background Explorer (COBE), launched by NASA in November 1989, to study both infrared and microwave characteristics of the cosmic background radiation (the remains of the extreme heat that was created by the Big Bang). Over a ten month period, COBE mapped the brightness of the entire sky at several infrared wavelengths. COBE carried three instruments, a Far Infrared Absolute Spectrophotometer (FIRAS) to compare the spectrum of the cosmic microwave background radiation with a precise blackbody, a Differential Microwave Radiometer (DMR) to map the cosmic radiation sensitively, and a Diffuse Infrared Background Experiment (DIRBE) to search for the cosmic infrared background radiation. Each COBE instrument yielded a major cosmological discovery. The Nobel Prize in Physics 2006 was awarded jointly to John C. Mather and George F. Smoot for their discovery with COBE of the blackbody form and anisotropy of the cosmic microwave background radiation.

2.5.1 FIRAS

The cosmic microwave background (CMB) spectrum is that of a nearly perfect blackbody with a temperature of 2.725 ± 0.002 K, see Figure 2.5. This observation matches the predictions of the hot Big Bang theory extraordinarily well, and indicates that nearly all of the radiant energy of the Universe was released within the first year after the Big Bang.

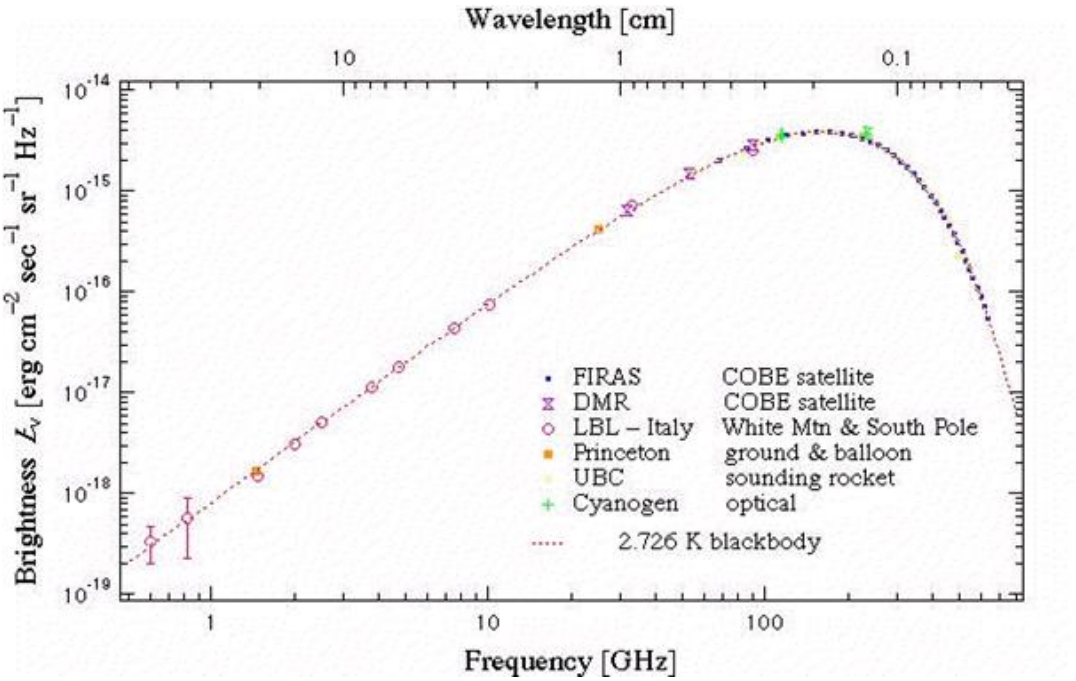

Figure 2.5: *CMB intensity plot. Blue points represent the FIRAS measurements. The fitted line is a single temperature blackbody with T=2.726 K. (http://aether.lbl.gov/www/projects/cobe/CMB_intensity.gif)*

2.5.2 DMR

The CMB was found to have intrinsic ”anisotropy” for the first time, at a level of a part in 100,000. Figure 2.6 shows the reduced DMR map (i.e., both the dipole and Galactic emission subtracted). This map has been smoothed with a 7 degree beam, giving an effective angular resolution of 10 degrees. An all-sky image in Galactic coordinates is plotted using the equal-area Mollweide projection. The plane of the Milky Way Galaxy is horizontal across the middle of the picture. These tiny variations in the intensity of the CMB over the sky show how matter and energy was distributed when the Universe was still very young. Later, through a process still poorly understood, the early structures seen by DMR developed into galaxies, galaxy clusters, and the large scale structure that we see in the Universe today.

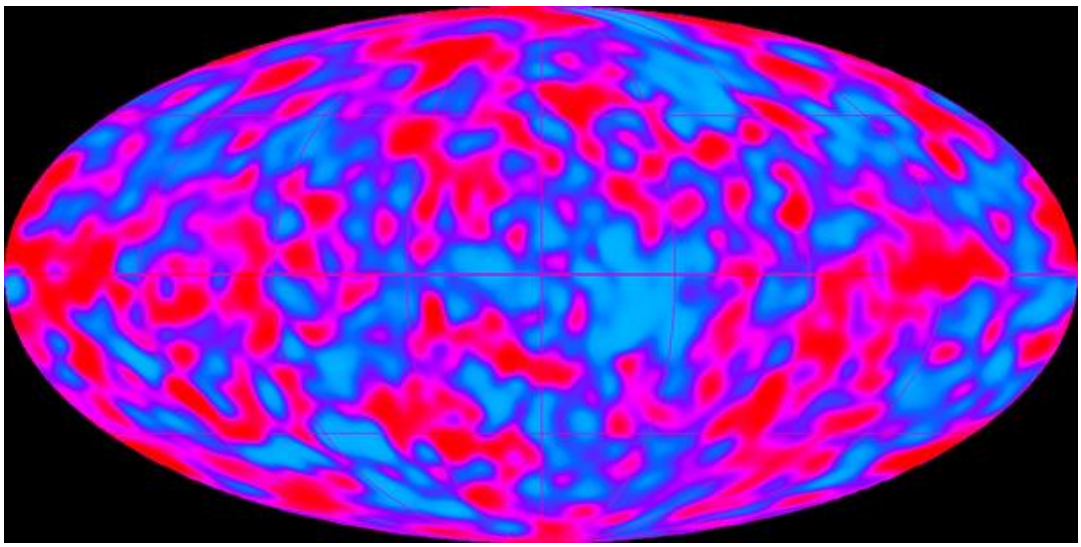

Figure 2.6: *Reduced map based on two years of DMR observation (http://aether.lbl.gov/www/projects/cobe/COBE_Home/cmb_fluctuations_big.gif)*

2.5.3 DIRBE

Infrared absolute sky brightness maps in the wavelength range 1.25 μm to 240 μm were obtained in 10 bands to carry out a search for the cosmic infrared background (CIB). Figure 2.7 and 2.8 show the galactic plane emission in bands 1-5 and 6-10. These data contain the signal from the CIB and the foreground emissions from extragalactic sources, our Galaxy, and dust and other sources in our solar system.

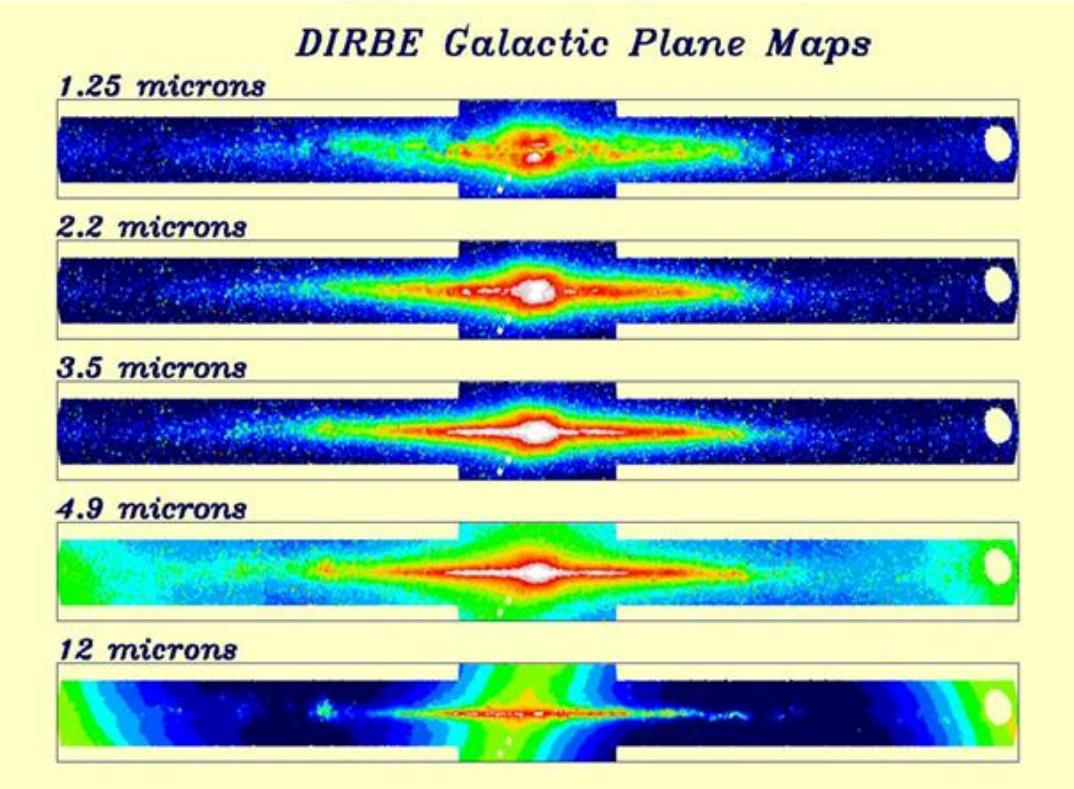

Figure 2.7: *Galactic plane emission in bands 1-5 (http://aether.lbl.gov/www/projects/cobe/gal_plane_b1_b5_big.jpg)*

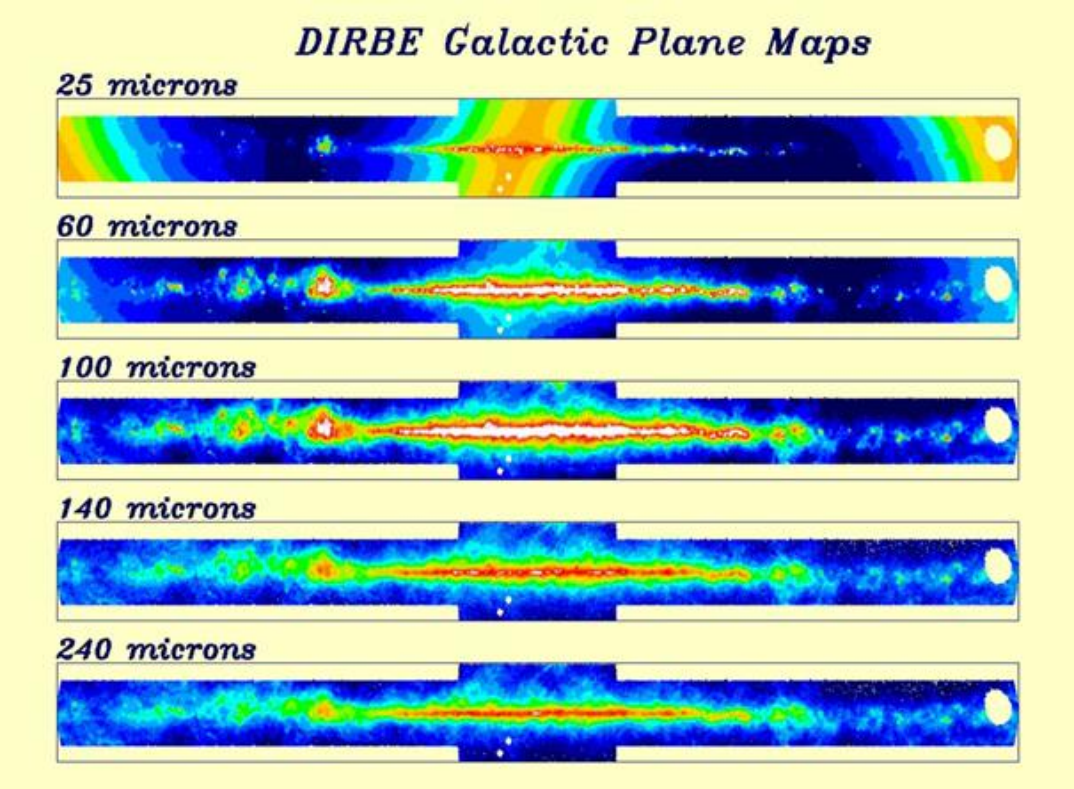

Figure 2.8: *Galactic plane emission in bands 6-10 (http://aether.lbl.gov/www/projects/cobe/gal_plane_b6_b10_big.jpg)*

The CIB was originally detected in the two longest DIRBE wavelength bands, 140 and 240 μm, and in the short wavelength end of the FIRAS spectrum. Subsequent analyses have yielded detections of the CIB in the near-infrared DIRBE sky maps. The CIB represents a ”core sample” of the Universe; it contains the cumulative emissions of stars and galaxies dating back to the epoch when these objects first began to form. The COBE CIB measurements constrain models of the cosmological history of star formation and the buildup over time of dust and elements heavier than hydrogen, including those of which living organisms are composed. Dust has played an important role in star formation throughout much of cosmic history.

We can access DIRBE Data Online at: http://lambda.gsfc.nasa.gov/product/cobe/. See http://astron.berkeley.edu/davis/dust/index.html (Schlegel et al. 1998) for “Maps of Dust IR Emission for Use in Estimation of Reddening and CMBR Foregrounds”.

2.6 Development of IR instrumentation

The development of instrumentation resulted in an increase of sensitivity and angular resolution as an example we show FIR images of the M51 galaxy from the 1980s and at 2009 on Figure 2.9. Science with IRAS, ISO, Spitzer and Herschel Space Telescopes will be discussed in Chapter 6.1, 7.1, 7.2 and 7.3

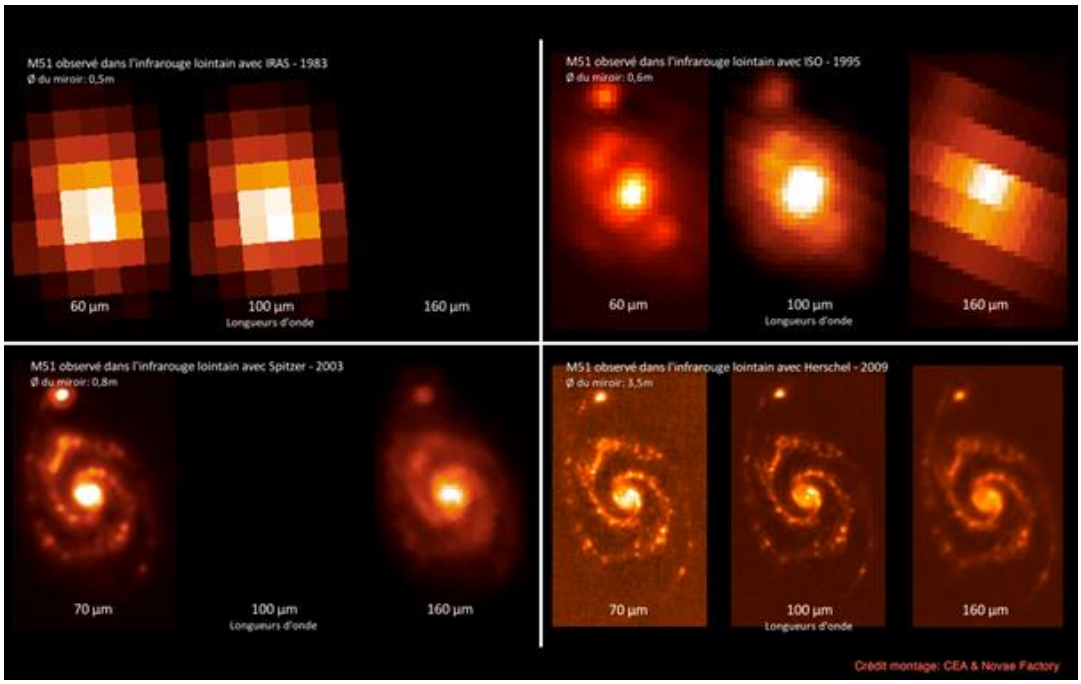

Figure 2.9: *FIR images of M51 observed with IRAS at 60 and 100 µm, ISO at 60, 100 and 160 µm, Spitzer Space Telescope at 70 and 160µm and Herschel Space Observatory at 70, 100 and 160 µm (http://a136.idata.over-blog.com/3/69/76/43/Au-nom-de-la-loi/M51---resolution---diffraction---Herschel.jpg)*

References and further reading to the chapter:

Abney, WdW, 1881: *"Capt. Abney's map of the infra-red end of the solar spectrum"*, MNRAS, 41Q, 231

Abney, WdW, 1886: *"The Solar Spectrum, from λ 7150 to λ 10,000"*, Philosophical Transactions of the Royal Society London, Vol. 177, page 457

Becklin, E. E. & Neugebauer, G. 1967: *„Observations of an Infrared Star in the Orion Nebula"*, ApJ. 147. 799

Becklin, E.E. et al. 1969: *"The Unusual Infrared Object IRC+10216",* ApJ, 158, L133

Bernard, J. P. et al. 1999: *"PRONAOS observations of MCLD 123.5 + 24.9: cold dust in the Polaris cirrus cloud"*, A&A 347, 640

Berrivin, S. et al. 1997: *"The PRONAOS Pointing and Stabilisation System"*, ESASP, 381, 597

Cohen, M., 1977: *"The nature of V645 Cygni = CRL 2789"*,ApJ, 215, 533.

Johnson, H., 1966: "*Infrared Stars*," Sky and Telescope, 73-77

Harwitt, M. et al., 1966:"Results of the first infrared astronomical rocket flight",AJ, 71, 1026

Huggins, W., 1869: "*Note on the Heat of the Stars*", Proceedings of the Royal Society of London, Vol. 17, p. 309

Kleinmann, D. E. & Low, F. J. 1967: *„Discovery of an Infrared Nebula in Orion"*, ApJ, 149, L1.

Lamarre, J. M. et al., 1994: *„SPM, a submillimeter photometer for PR0NAOS",* InPhT, 35, 277

Lequeux, J., 2009*: "Early Infrared Astronomy"*, Journal of Astronomical History and Heritage, 12(2), 125. http://www.narit.or.th/en/files/2009JAHHvol12/JAHHvol12no2Complete.pdf

Lo, K. Y., Bechis, K. P., 1976: *"CRL 2688 and CRL 618 - Proto-planetary nebulae"*, ApJ, 205, L21.

Magrini, L., 1843*: L'ecclisse solare totale dell'8 Luglio 1842. Relazione*

Neugebauer, G., 1969: *Infrared Observations in Space Astronomy*, Optical Telescope Technology, NASA SP-233, NTIS, Springfield, VA, 25-32.

Neugebauer, G., Becklin, E. E. 1971: *"Infrared Sources of Radiation"*, ARA&A, 9, 67

Neugebauer, G., Becklin, E. E., 1973: "*The Brightest Infrared Sources*," Scientific American 228:28-40.

Neugebauer, G., Leighton, R, 1968: "*The Infrared Sky*," Scientific American 218:50-61.

Neugebauer, G., Leighton, R., 1969: *Two-Micron Sky Survey - A Preliminary Catalog*. NASA SP-3047, NTIS, Springfield, VA, 25-32.

Neugebauer, G., Martz, D., Leighton, R. 1965: "*Observations of Extremely Cool Stars*," ApJ, 142, 399

Ney, E. P. et al., 1975: *"Studies of the infrared source CRL 2688"*, ApJ, 198, L129

Price, S. D. , 1988: "*The Infrared Sky: A Survey of Surveys*," Publications of the Astronomical Society of the Pacific, pp. 171-186.

Rieke, G. H., 2009**:** *History of infrated telescopes and astronomy*, Exp Astron, 25, 125 DOI 10.1007/s10686-009-9148-7

Ristorcelli, I. et al. 1998: *"Discovery of a Cold Extended Condensation in the Orion A Complex"*, ApJ, 496, 267.

Schlegel, D. J., Finkbeiner, D. P. & Davis, M., 1998, *"Maps of Dust IR Emission for Use in Estimation of Reddening and CMBR Foregrounds"*, ApJ, 500, 525

Werner, M. W., Becklin, E. E., Neugebauer, G., 1977: *" Infrared studies of star formation"*, Science, vol. 197, p. 723-732.

Westbrook, W. E. et al., 1975: *"Observations of an isolated compact infrared source in Perseus"*, ApJ, 202, 407

Woody, D. P.; Richards, P. L. 1979: "*Spectrum of the cosmic background radiation*", 1979PhRvL..42..925W

Report of the Astronomy Survey Committee, Astronomy and Astrophysics for the 1970s, Vol. 1. National Academy of Sciences, Washington, DC 1972, 83-85.

http://www.astronautix.com/lvs/aeree350.htm

http://learn.hamamatsu.com/tutorials/java/airymag/

http://www.nasm.edu/nasm/dsh/artifacts/SS-caltech2.htm

http://www.nasm.edu/nasm/dsh/artifacts/RM-Aerobee350.htm

http://www.nasm.edu/nasm/dsh/artifacts/SS-Far-Infrared.htm

Chapter 3. Definition of infrared and the origin of the infrared radiation

In this chapter we describe the technological and observational justification of the infrared band. Atomic and molecular transitions are investigated as the origin of the infrared radiation.

Electromagnetic radiation is classified by wavelength into gamma rays, X-rays, ultraviolet, visible, infrared, microwave and radio, see on Figure 3.1. Infrared radiation lies between the visible and microwave part of the electromagnetic radiation.

3.1 The definition of the infrared band

The quantum efficiency is a measure of a device's electrical sensitivity to light. It is the incident photon to converted electron ratio, i.e. the percentage of photons hitting the device's photoreactive surface that produce charge carriers. It is measured in electrons per photon or amps per watt. As we see in Figure 3.1 the quantum efficiency of the human eye is around 1% to 10%, over most conditions (see eg. http://psych.nyu.edu/pelli/pubs/pelli1990efficiency.pdf). It gets slightly better for red colour at low light levels (photopic vision), but our eyes lose all sensitivity beyond the red end of the visible spectrum ($\lambda > 0.75$ μm).

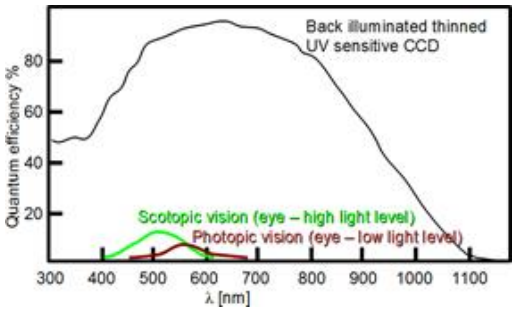

Figure 3.1: *Quantum efficiency of human eye and CCD*

The infrared quantum efficiency of typical photoemulsions is similar to the human eye, however infrared sensitive astrographic photo plates (Kodak IVN) were sensitive up to $\lambda \approx 1$ μm. We can not use any more most of the visible band technologies such as photography, CCDs and photocathodes for $\lambda > 1.1$ μm, and that wavelength limit can be considered as a technical border of infrared at the short wavelength side. Referring to Figure 3.1 we note that the CCD surface has channels used for charge transfer that are shielded by polysilicon gate electrodes which absorb light (mostly blue). Such losses are eliminated in the back-illuminated CCD, where the light falls onto the back of the CCD in a region that has been thinned so it is transparent. The wavelength dependent specific detectivity D^* is defined as reciprocal of noise-equivalent power (NEP), normalized per unit area:

$$D^* = \frac{\sqrt{\text{Area}}}{\text{NEP}}, \tag{3.1}$$

where Area is the photosensitive region of the detector. The unit of D^* is: $cmHz^{½}W^{-1}$.

Figure 3.1 shows the specific detectivity D of the most common compounds used as detectors which include:

Gallium Arsenide – GaAs, Lead Sulfide – PbS, Indium Antimonide – InSb, Germanium doped with Copper - Ge:Cu, Germanium doped with Zinc - Ge:Zn, Germanium doped with Gold - Ge:Au, Germanium doped with Gallium - Ge:Ga, Lead Telluride – PbTe, phosphorus-doped silicon – Si:P.

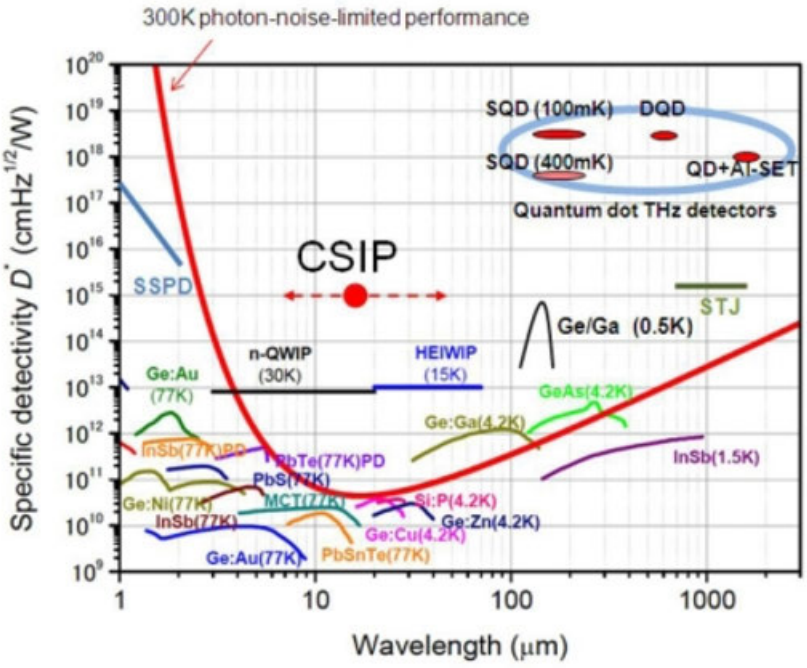

Figure 3.2: Spectral response characteristics of various infrared detectors. (Ueda T, Komiyama S, 2010, http://openi.nlm.nih.gov/detailedresult.php?img=3231243_sensors-10-08411f7&req=4)

The highest available frequency band of terrestrial sub-mm observatories is at 810GHz (0.37mm). The ”end” of the infrared region is again technologically defined: it is the wavelength (≈ 350μm) where radio techniques such as superheterodyne receivers tend to be used in preference to the ”optical style” infrared approach and the incoming radiation tends to be thought of as waves rather than individual photons. The region from 0.35mm to 1mm is referred to as the sub-millimeter region. It may be regarded as a subdivision of radio astronomy.

Astronomical justification for the definition is that already at 2.2μm the sky has a significantly different appearance from the visible one. The cooler end of the stellar population becomes predominant and some objects turn out to have infrared fluxes much higher than predicted from their visible spectra.

These infrared excesses can be due to cool dust shells surrounding them or to circumstellar free-free emission for example. The most important sources of the infrared photons are Solar system objects, stars and extended galactic objects, extragalaxies. The cosmic microwave background (CMB) is the relic of the Big Bang. It is characterized by a blackbody spectrum of temperature 2.73K. The rise of its spectrum marks the end of the infrared.

The vibrational transitions of molecules results infrared photons, whereas we observe their rotational transitions spectra in the sub-mm and radio region.

Infrared is divided into three parts: near, mid and far-infrared. Near-infrared refers to the part of the infrared spectrum that is closest to visible light and far-infrared refers to the part that is closer to the microwave region. Mid-infrared is the region between these two. The boundaries between these regions are not exact and can vary. (Table 3.1. shows the general properties of the infrared ranges.)

Infrared radiation	**Wavelength range [μm]**	**Astronomical objects**
Near	1-5	Red giants Cooler red stars
Mid	5-30	Planets, comets and asteroids Protoplanetary disks
Far	30-400	Central regions of galaxies

Infrared radiation	Wavelength range [µm]	Astronomical objects
		Emission from cold dust

Table 3.1: *Properties of the infrared ranges*

A justification based on the observational conditions can be made as well. Beyond 2.3µm blackbody radiation from the telescope and the atmosphere itself begins to dominate other sources of background. Measurements of faint astronomical objects have to be made by alternatively observing the field containing the source and a nearby ”empty” one. This process is known as chopping. The signals are subtracted to eliminate the strong background. Alternatively the measurement is taken outside the atmosphere with a cooled observing system.

In the NIR, MIR and FIR the main sources of the background are terrestrial, Zodiacal light and galactic ISM radiation. From about 300µm CMB starts to dominate the background. Except bands in the NIR, the infrared sky is to be observed by air-borne or space-borne instruments.

The sub-millimeter region however can be accessed again in selected atmospheric windows by terrestrial telescopes located at high altitude, low precipitable water vapor (pwv) sites like Mauna Kea or South Pole. Precipitable water is the measure of the depth of liquid water at the surface that would result after precipitating all of the water vapor in a vertical column over a given location, usually extending from the surface to 300 mb (http://forecast.weather.gov/glossary.php?word=precipitable%20water).

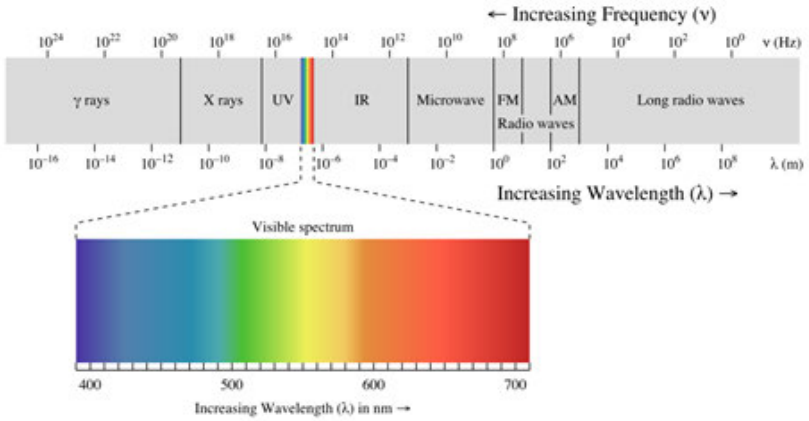

Figure 3.3: Electromagnetic spectrum (http://en.wikipedia.org/wiki/File:EM_spectrum.svg) from 10^{-16} to 10^{8} m. The visible spectrum located in the middle, it covers only a small part of the spectrum.

Observations at different wavelengths reveal various pictures from astronomical objects. Figure 3.4 shows the M51 Spiral Galaxy at different wavelengths: from visible to far infrared. Observations of visible light show the stars that make up the galaxy. Infrared observations reveal the mixture of gas and dust from which new stars can be born.

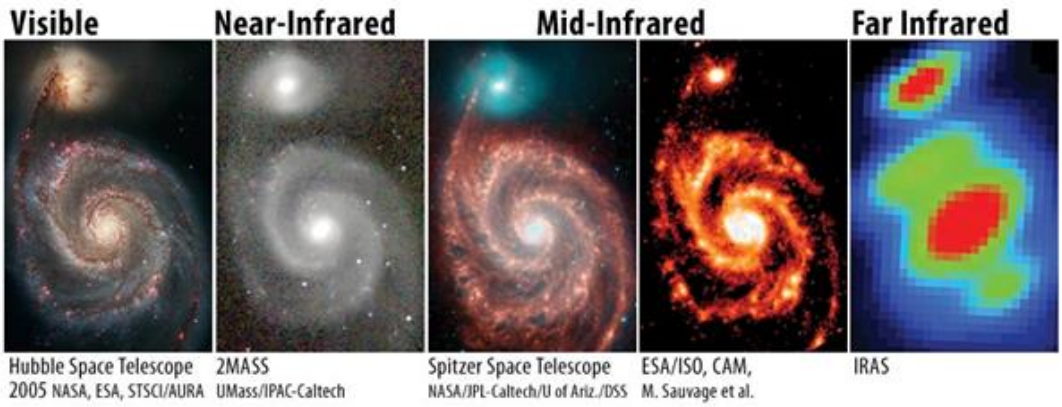

Figure 3.4: Hubble, 2MASS, Spitzer Space Telescope, ISO and IRAS observations of M51 Spiral Galaxy. Shorter wavelengths show the star content of it, on longer wavelengths the radiation of gas and dust dominate. (http://astromic.blogspot.de/2011/02/infrared-astronomy.html)

Near-infrared observations have been made from ground based observatories since the 1960's. This part of the infrared radiation can be observed with similar technique as visible light, but it requires special infrared detectors. Mid and far-infrared observations, where the wavelength is longer than 20 μm, can only be made by observatories which can get above our atmosphere. These observations require the use of special cooled detectors.

3.2 The origin of infrared radiation

The primary source of infrared light is the thermal radiation. This is produced by the motion of atoms and molecules in an object. Every object which has a temperature greater than absolute zero (-273°C), radiates in the infrared. All atomic and molecular motion ceases at absolute zero temperature. The wavelength at which an object radiates most intensely depends on its temperature. In general, as the temperature of an object cools, it shows up more prominently at farther infrared wavelengths. When an object is not quite hot enough to radiate visible light, it will emit most of its energy in the infrared.

There are 2 approximations of Planck's law: at long wavelengths the Rayleigh–Jeans law and at short wavelengths the Wien's law.

Rayleigh-Jeans law: at the low frequency end ($h\nu << k_B T$), the Planck function is a power-law ($B_\nu \sim \nu^2$)

$$B_\nu(T) = \frac{2\nu^2 k_B T}{c^2} \tag{3.2}$$

$$B_\lambda(T) = \frac{2ck_B T}{\lambda^4} \tag{3.3}$$

Wien's law: at the high frequency end ($h\nu >> k_B T$), it has an exponential cut-off

$$I(\nu,T) = \frac{2h\nu^3}{c^2} e^{-\frac{h\nu}{k_B T}} \tag{3.4}$$

$$I(\lambda,T) = \frac{2hc^2}{\lambda^5} e^{-\frac{hc}{\lambda k_B T}} \tag{3.5}$$

Wien's displacement law states that the Planck function at any temperature has the same shape as the distribution at any other temperature. There is an inverse relationship between the peak wavelength and temperature of the emission of a black body, where λ_{max} is the peak wavelength, T is the temperature and b is the Wien's displacement constant (2.898×10^{-3} mK).

$$\lambda_{max} T = b \tag{3.6}$$

In terms of frequency ν (in Hz), Wien's displacement law is the following:

$$\nu_{max} / T = a \tag{3.7}$$

where $a = 5.879 \times 10^{10}$ Hz/K

Observing directly the radiation of a blackbody, we will see a continuum spectrum, because a blackbody emits at every wavelength (see on Figure 3.5a). If there is an absorbing material (see on Figure 3.5b, cloud of cooler gas is the absorber) between us and the blackbody, then we will see an absorption spectrum. Observing only the cooler gas cloud (see on Figure 3.5c) we will see an emission line spectrum, where the emission lines are exactly in the same position of the spectrum as the absorption lines in the second case.

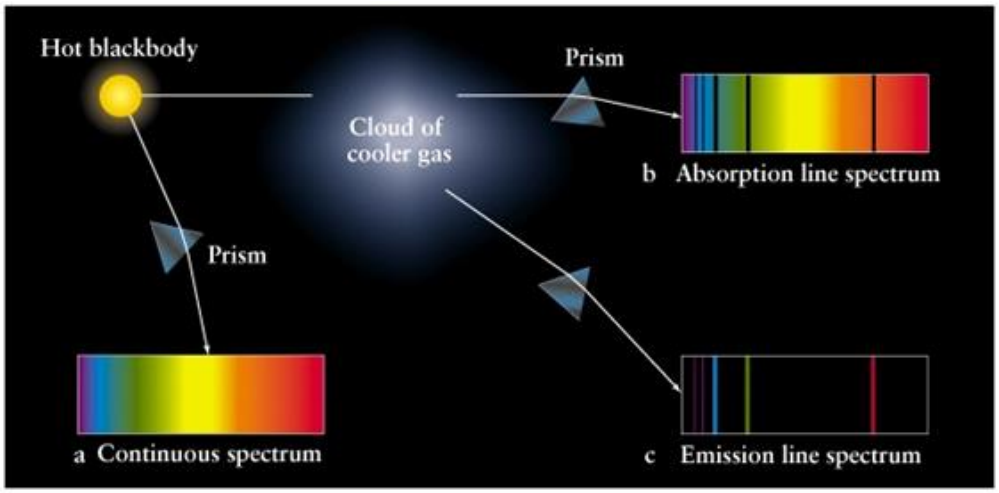

Figure 3.5: Figure 5-14 from Universe by Freedman and Kaufmann, (https://www.cfa.harvard.edu/~jbattat/a35/cont_abs_em.html)

Observing directly the radiation of a hot blackbody, we will see a continuum spectrum. If there is some colder gas as absorber between us and the blackbody, then we will see an absorption spectrum. Observing only the cooler gas cloud, an emission line spectrum is visible.

3.2.1 Atomic transitions

Investigation of emission and absorption spectra of the astronomical objects allows us to determine their chemical compositions and physical properties, surface temperatures. Based on their main spectral lines in their spectra, stars are classified into different spectral types.

Infrared spectroscopy in astronomy involves detection of both absorption and emission lines due to atomic transitions, e.g. the hydrogen Paschen, Brackett, Pfund, and Humphreys series are all observable mainly in the near infrared range (see hydrogen's energy levels on Figure 3.6.). The energy differences between the levels are given by the Rydberg formula, see Equation 3.8., where n is the initial energy level, n' is the final energy level and R is the Rydberg constant, $R = 1.097373 \times 10^{7}\, m^{-1}$.

$$\frac{1}{\lambda} = R\left(\frac{1}{(n')^2} - \frac{1}{n^2}\right) \tag{3.8}$$

Table 3.2 contains the n' values and wavelength ranges for the hydrogen series.

n'	Name	Wavelength range
1	Lyman series	UV
2	Balmer series	Visible
3	Paschen series	IR
4	Brackett series	IR
5	Pfund series	Far IR
6	Humphreys series	Far IR

Table 3.2: *Basic properties of hydrogen series*

Lines and bands of different molecules are found in the entire infrared range. One of the most important type of molecules is PAHs (polycyclic aromatic hydrocarbons) whose transitions are most prominent in the mid-infrared.

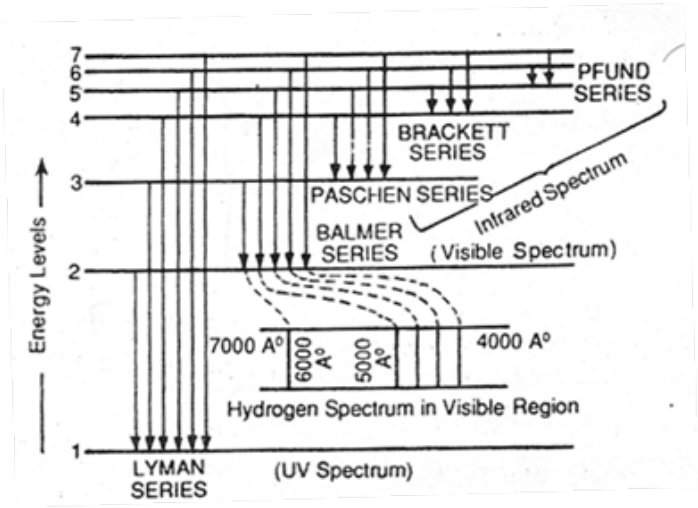

Figure 3.6: Energy levels of hydrogen. (http://chemistry-desk.blogspot.de/2011/05/hydrogen-spectrum.html). Lyman series are in the UV range, Balmer lines are in the visible region and Paschen, Brackett and Pfund series are observable in the infrared wavelength range.

3.2.2 Molecular transitions

The energy levels of a molecule in the order of decreasing energy are: electronic, vibrational and rotational. The Born-Oppenheimer Approximation is the assumption that the electronic motion and the nuclear motion in molecules can be separated. It is based on the assumptions that the nuclear motion is much slower than electron motion and the nuclear motion (e.g., rotation, vibration) occurs in a smooth potential from the speedy electrons. The $\Psi_{molecule}$ wavefunction is approximated by separated wavefunctions for the motions of the nuclei and the electrons:

$$\Psi_{molecule}(\bar{r}_j, \bar{R}_j) = \Psi_{electrons}(\bar{r}_j, \bar{R}_j)\Psi_{nuclei}(\bar{R}_j) \tag{3.9}$$

, where r_j and R_j are the positions of electrons and nuclei respectively. The quantized energy stored in a molecule thus can be thought of as the sum of energy stored in distinct modes of rotation, vibration, and electronic. Electronic transition occurs so rapidly that the internuclear distance can't change much in the process. Vibrational transitions occur between different vibrational levels of the same electronic state. Rotational transitions occur mostly between rotational levels of the same vibrational state, although there are many examples of combination vibration-rotation transitions for light molecules. Molecular transitions result in emission or absorption of photons: the electronic transitions in UV or optical, vibrational transitions in infrared, rotational transitions in microwave range.

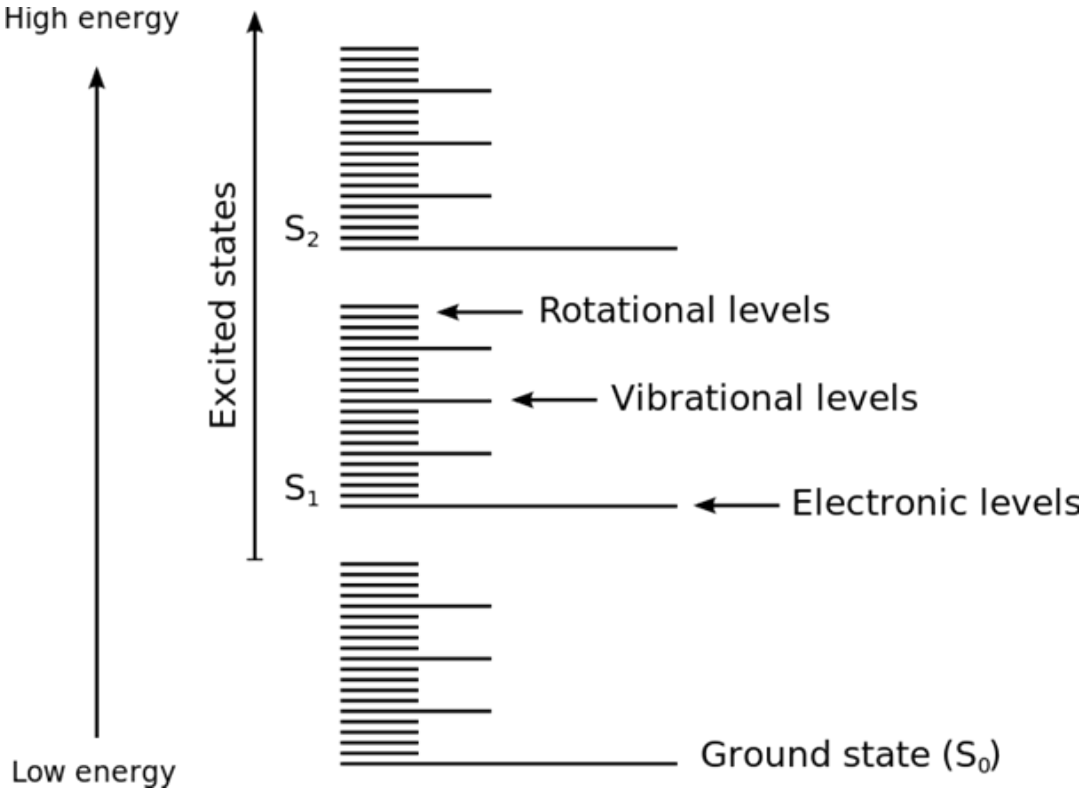

Figure 3.7: Energy-levels in a molecule: electronic, vibrational and rotational levels (Levien van Zon, based on figure 1a in Lichtman & Cochello, 1995 DOI: 10.1038/nmeth817, http://commons.wikimedia.org/wiki/File:Molecular_energy_levels_en.svg).

A molecular vibration occurs when atoms in a molecule are in periodic motion while the molecule as a whole has constant translational and rotational motion. A molecular vibration is excited when the molecule absorbs a quantum of energy, E, corresponding to the vibration's frequency, ν, according to the relation (3.7). Vibrational energy levels of the diatomic HCl molecule is presented in Figure 3.8. as an anharmonic oscillator, the electronic states can be represented as a function of internuclear distance.

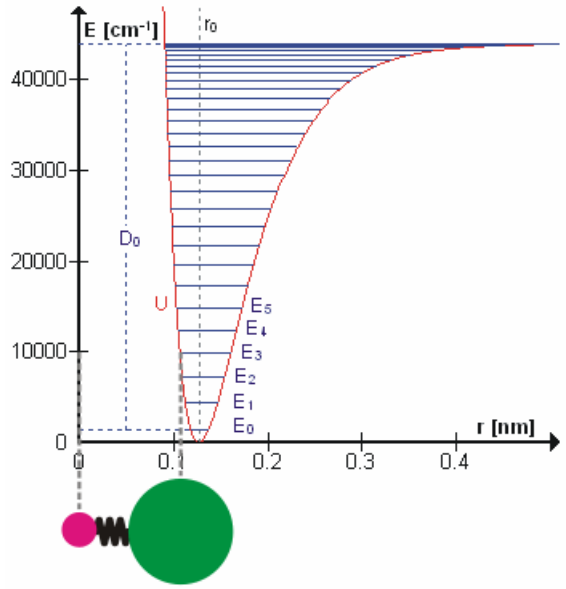

Figure 3.8: The HCl molecule as an anharmonic oscillator vibrating at energy level E_3. D_0 is dissociation energy here, r_0 bond length, U potential energy (Morse potential). Energy is expressed in wavenumbers. The hydrogen

chloride molecule is attached to the coordinate system to show bond length changes on the curve. (https://upload.wikimedia.org/wikipedia/commons/b/bb/Anharmonic_oscillator.gif)

Since the vibrational transitions of molecules result in infrared photons, these will be further discussed later. Simple diatomic molecules with only 2 nuclei perform a vibration that resembles to a harmonic oscillator. There are several ways the relative positions of atoms may change in a more complicated molecule, these are:

- Stretching: a change in the length of a bond
- Bending: a change in the angle between two bonds
- Rocking: a change in angle between a group of atoms
- Wagging: a change in angle between the plane of a group of atoms
- Twisting: a change in the angle between the planes of two groups of atoms
- Out-of-plane: a change in the angle between any one of the bonds and the plane defined by the remaining atoms of the molecule

Vibrational modes (2 stretching and 1 bending) are shown for the lineal molecule CO_2 with wavelengths in Figure 3.8. See also a few animated examples of vibration modes at https://en.wikipedia.org/wiki/Molecular_vibration.

Although there are also large molecules know in astronomical objects (see eg. polycyclic aromatic hydrocarbons), the most common molecules are simple. One reason is that polyatomic molecules usually can not survive temperatures above 4000K and that UV photons destroy them even far from stars. In astronomical applications typically the lowest vibrational levels are populated. The excitation is usually made either by collision or by radiation.

3.3 Radiation of molecules

3.3.1 Molecular hydrogen

The most abundant molecule in the ISM is molecular hydrogen (H_2) an important coolant and actor of molecular chemistry. It is rather difficult to observe H_2 directly, because it is a simple, homonuclear molecule. It consists of two identical atoms, the center of mass and the center of charge coincide, resulting in no permanent dipole moment. Thus only quadrupole rotational transitions, the $\Delta J=0$ and $\Delta J=\pm 2$ occur, while the $\Delta J=\pm 1$ (dipole) rotational transitions are strictly forbidden. This means that H_2 emits no microwave rotational lines.

The small mass and small size gives a low moment of inertia for the H_2 molecule. The first pure rotational transition, J=2-0, occurs at 28μm, that is unobservable from the ground due to water-vapor absorption in the atmosphere. The $h\nu/k = 514$K excitation energy is very large for this transition, as compared to typical average temperatures (T~20K) of giant molecular clouds. The next pure rotational transition J=4-2 at λ=12μm with $h\nu/k$ =1200 K. Excitation by thermal motions and collisions in such cold environment is unlikely. The high energies of the first excited states of H_2 means that we may expect H_2 emission at unusually warm ($500K<T<1000K$) H_2 gas in proximity to hot stars or in regions of active star formation. In general, H_2 is only directly observable as

1. Absorption at Far-UV wavelengths in the diffuse ISM along sight lines toward nearby stars.
2. Emission by Infrared rotational-vibrational transitions in the electronic ground state of H_2 at wavelengths between 1 and 28μm in relatively warm regions. The molecular gas must be warm (500-2000K), excited either by shocks, outflows, or UV fluorescence from nearby stars, then we may see the 2.12 μm [(1–0) S(1)] vibrational line or the S(0), S(1), S(2) pure rotational lines at 28 μm, 17 μm, and 12 μm, respectively.

3.3.2 Ices and other molecules

Carbon monoxide and H_2 are formed at similar densities in the ISM, CO is formed also in the atmosphere of late type giants both oxygen (M type) and carbon rich (C type). CO has several near-infrared vibration bands at λ=4.7μm

(ν=1-0), at λ =2.3μm (ν =2-0 and ν =3-1), λ =1.65μm (ν =3-0 and ν=4-1) to be detected at red supergiants and post-AGB stars. Water vapor was detected in the infrared spectra of both M dwarfs and around YSOs as well as in the ISM. SiO near- and mid-infrared lines are seen at G to M giants.

Molecules with low boiling and condensation temperatures are also called as volatiles (T_{cond} < 1100K), or very volatile substances (T_{cond} < 700K). Volatiles with melting points over 100K are called as ices, referring to the status of such material in the Solar System, i.e. such volatiles will be easily iced. Ices are solidified compounds that are gases at standard (room) temperature (300K) and pressure (1 bar). While oxygen is called as gas, CO_2, and H_2O are considered as ices. We may all recall the polar ice on Mars with the northern cap bearing mostly H_2O ice and the southern one more rich in dry ice. Water ice is found even near the Sun, near-infrared reflectance anomalies were found in permanently shadowed craters at the polar regions of Mercury by the MESSENGER (MErcury Surface, Space ENvironment GEochemistry, and Ranging, http://www.nasa.gov/mission_pages/messenger/media/PressConf20121129.html) mission. The bright spots were interpreted as regions covered with H_2O ice (Neumann et al. 2013) in accordance to the results of previous radar measurements using the Arecibo radio telescope (Slade et al., 1992). Water was found in shadowed craters of the Moon as the Moon Mineralogy Mapper on board of Chandrayaan-1 has recently detected absorption features resembling to water bearing materials near 2.8 to 3.0 μm (Pieters et al. 2009). The same feature is also seen in the near-infrared spectra of star forming regions eg. by ISO SWS at the famous W33A (Gibb et al. 2000), along with absorbing bands of other ices like CO_2, NH_3, CO, which are also the most common ices in the Solar System with infrared detections (see Figure 3.9). Surfaces of several Jovian and Saturnian satellites are rich in water ice, but ices appear on Plutoids as well. Volatiles freeze out to interplanetary dust as well as onto the surfaces of dust grains in the ISM or in circumstellar disks forming a mantle. Icy mantles may help the coagulation of particles and a grain growth up to large fluffy objects of a =1μm.

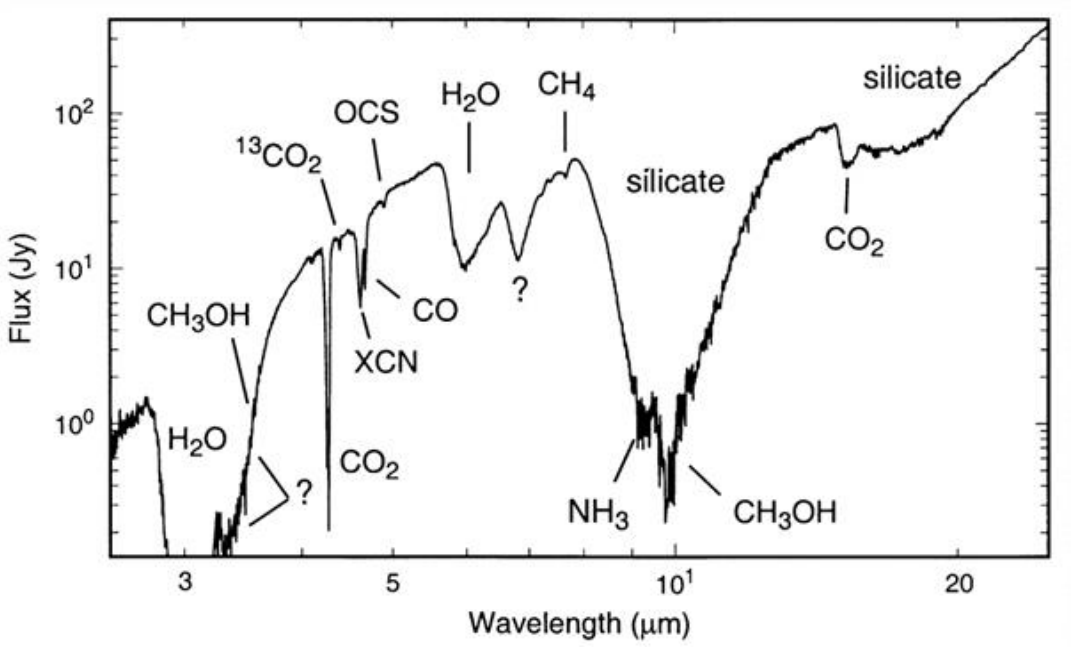

Figure 3.9: Complete 2.4-25 μm SWS flux spectrum of W33A. The principal identified and unidentified spectral features are labelled (Figure 1 from Gibb et al (2000)).

3.4 Radiation of dust

The interstellar dust appears at the astronomical measurements in various ways: wavelength-dependent extinction, polarization of starlight, scattering starlight (including also infrared) as cloud-shine and core-shine, mid- and far-infrared emission, scattering of X-rays, microwave emission.

Extinction by dust decreases the intensity of starlight:

$$\frac{dI}{I} = -C_{ext} n_d ds \tag{3.10}$$

, where C_{ext} is the extinction cross section, n_d is the number density of dust grains and ds is the path length. The extinction is partly due to scattering, partly due to absorption.

$$Q_{ext} = \frac{C_{ext}}{\pi a^2} = Q_{sca} + Q_{abs} \tag{3.11}$$

, where the extinction andabsorption coefficiences are $Q_{ext}(\nu)$ and $Q_{abs}(\nu)$ respectively. Scattering strongly depend on the particle size. For small particles ($a << \lambda$) Rayleigh scattering dominates:

$$Q_{ext} \approx Q_{sca} \propto \lambda^{-4} \tag{3.12}$$

For large grains ($a >> \lambda$) the $Q_{sca}(\nu)$ coefficient is constant.

The infrared mission from dust grains reveals 3 dust populations by 3 radiation processes:

1. Thermal continuum emission at mid- to far-IR wavelengths from dust grains in radiative equilibrium with the local radiation field.
2. Thermal continuum emission from non-equilibrium heating of very small grains emitted at near- to mid-IR wavelengths (1 < μm λ < 25μm).
3. Infrared emission bands (some are unidentified).

3.4.1 Heating and cooling of dust

A spherical dust grain with radius a located a distance d away from a star with luminosity $L_\nu(*)$ in radiation equilibrium has a balance of the absorbed and emitted power:

$$\pi a^2 \int_0^\infty \frac{L_\nu}{4\pi d^2} Q_{abs}(\nu) d\nu = 4\pi a^2 \int_0^\infty Q_{em}(\nu) \pi B_\nu(T_{gr}) d\nu \tag{3.13}$$

, where $Q_{em}(\nu)$ is the emission efficiency, T_{gr} is the grain temperature.

$$Q_{abs}(\nu) \propto \nu^\alpha \tag{3.14}$$

where 1<α<2, thus the grain absorbs most in UV and visible wavelengths, but it radiates in the infrared. The following estimation can be made for the thermal balance:

$$\frac{L(*)}{4\pi d^2} \langle Q_{UV} \rangle \approx 4 \langle Q_{IR} \rangle \sigma T_{gr}^4 \tag{3.15}$$

where $\langle Q_{UV} \rangle, \langle Q_{IR} \rangle$ are the averaged UV absorption and IR emission coefficients.

The observed spectrum of optically thin dust will be a modified blackbody spectrum, where N_{gr} is the total number of dust grains, and a is a typical size (assuming spherical grains):

$$L_\nu = N_{gr} 4\pi a^2 Q_\nu(a) \pi B_\nu(T_{gr}) \tag{3.16}$$

where the usual dust emissivity law is:

$$Q_\nu(a) = \left(\frac{2\pi a \nu}{c}\right)^\beta \tag{3.17}$$

The power-law index, β, has values between 1 and 2. We note here that at high temperatures (T_{gr} > 1500K) the dust will start to evaporate, so there will be a dust free zone near to luminous UV emitting sources.

3.4.2 Refractory dust

The mass loss from late type giant stars and supernova explosions ejects a considerable amount of metals and molecules into the circumstellar and interstellar space. The so called refractory elements (T_{cond} > 1300K) will be condensed in the universe except the vicinity of heating sources. Intermediate-mass stars (0.8 M_O < M <8.0 M_O) eventually evolve on the Hertzsprung-Russell diagram, up to the asymptotic giant branch (AGB). The refractory grains which are formed in the outer atmosphere of AGBs are mostly ejected by a super-wind (v=1000 kms^{-1}) in the post-AGB phase and are well seen in the infrared spectra of these proto-planetary nebulae. PPNs can have either oxygen (O)- or carbon (C)-rich chemistries depending on the chemistry of the AGB star. Stellar winds contain oxides of Al, silicates, and crystalline or amorphous carbon.

3.4.3 Silicates

Silicates are the most common form of minerals, they consist of silica tetrahedras (SiO_4 , i.e. 4 oxygen atoms around a silicon atom) which are combined with metal cations, such as Mg_2^+ or Fe_2^+ in a lattice structure. **Crystalline silicates** have ordered lattice structures, the tetrahedras can share their oxygen atoms with other tetrahedras. Crystalline silicates are: olivines: $(Mg, Fe,..)_2SiO_4$, pyroxenes: $(Mg, Fe,..)SiO_3$ or quartz: SiO_2.

Amorphous silicates have unordered structures, the number of shared oxygen-atoms may vary for each silica-anion (see on Figure 3.11).

Silicates, both amorphous and crystalline alike, show resonances in the mid-infrared, and so we see silicate spectral features at λ=9.7 μm (Si-O stretching) and at λ=18 μm (O-Si-O bending). Sharp peaked resonances may be seen when the tetrahedras are aligned, and broad features (blended bands) when they aren't. Crystalline silicates can also be distinguished from amorphous silicates due to the presence of lattice modes at 25 μm.

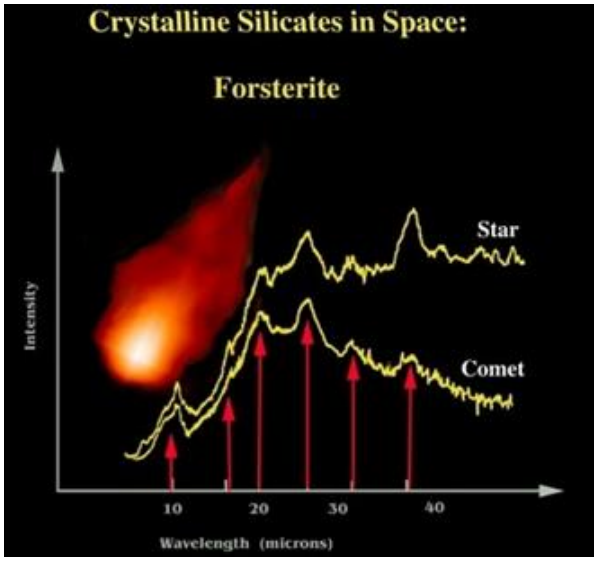

Figure 3.10: *Forsterite seen in the mid-infrared spectra of the young star HD100546 and comet Hale-Bopp observed by the ISO SWS (ESA, 2000).*

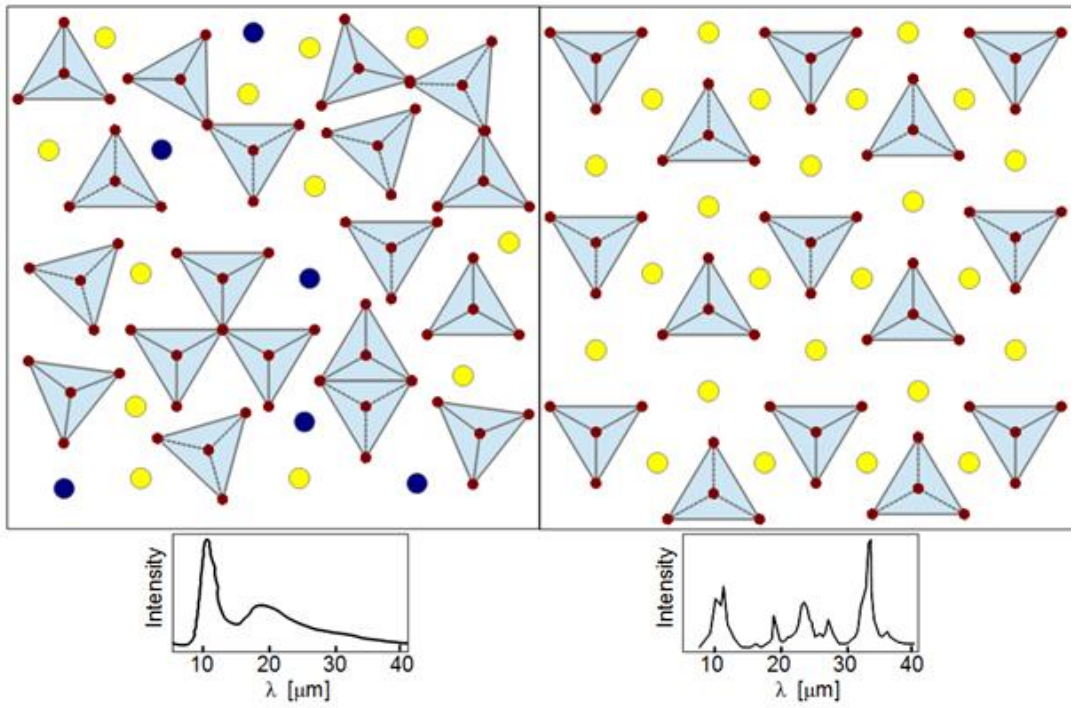

Figure 3.11: *Amorphous (left) and crystalline (right) silicates and their schematic infrared spectra. The structure in the right picture corresponds to olivine* $(Mg, Fe)_2SiO_4$ *when the color circles correspond to oxygen and silicon atoms (red), and magnesium and iron atoms (yellow). The typical infrared spectra of amorphous and crystalline silicates are shown.*

Figure 3.12: *Olivine (*http://en.wikipedia.org/wiki/File:Peridot2.jpg*).*

3.4.4 Large dust grains

Normal-sized (a > 0.01μm) dust grains are in thermal equilibrium with the ambient radiation field and due to their low temperature (10K < T_d < 40K) they emit far-infrared and sub-mm radiation (mostly at λ > 60 μm). The radiation can be approximated by a modified blackbody spectrum. The cool ones are most abundant in the dense ISM producing the so called “cirrus” emission (grains in equilibrium with the general Galactic ISRF) while warmer dust grains appear at star forming regions near YSOs.

Ices may help the dust grains to coagulate and form fluffy large particles with sizes a=1 μm and even larger.

3.4.5 Polycyclic Aromatic Hydrocarbons

Polycyclic Aromatic Hydrocarbons (PAHs) are dominant constituents of the so called very small grain population. Exposed to UV radiation PAHs can experience transient heating (Draine & Anderson 1985, Duley & Poole 1998) to high temperatures and will show a strong radiation at their various infrared bands/features.

The strongest PAH bands are at 3.3, 6.2, 7.7, 8.6, 11.2, and 12.6 μm. These bands correspond to the vibration modes: C-C stretch, C-H stretch, C-H in-plane rotation, and C-H out of plane rotation as illustrated in Figure 3.13 (see a mid-infrared spectrum of NGC7027 by Draine, 2003 on Figure 3.12).

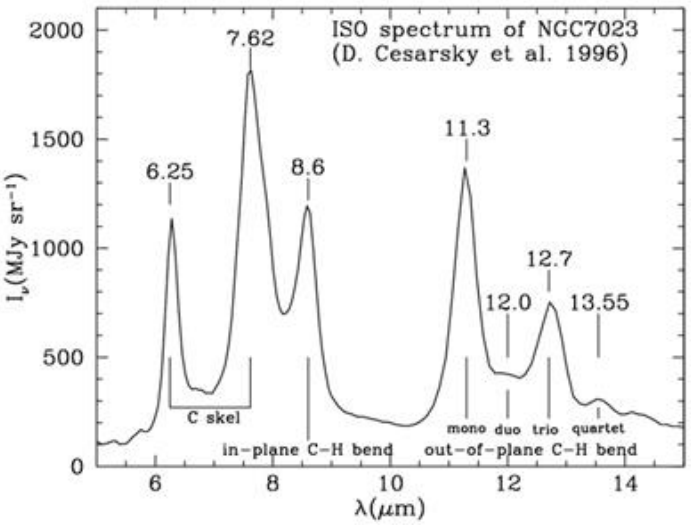

Figure 3.13: *PAH emission fetaures in the 5-15 μm emission spectrum of NGC7027 (http://ned.ipac.caltech.edu/level5/March04/Draine/Figures/figure3a.jpg)*

PAHs dominate the mid-infrared spectrum of most star-forming galaxies since they are excited near young massive stars. Thus PAHs are used to identify galaxies with intense star formation up to redshifts of z = 3.

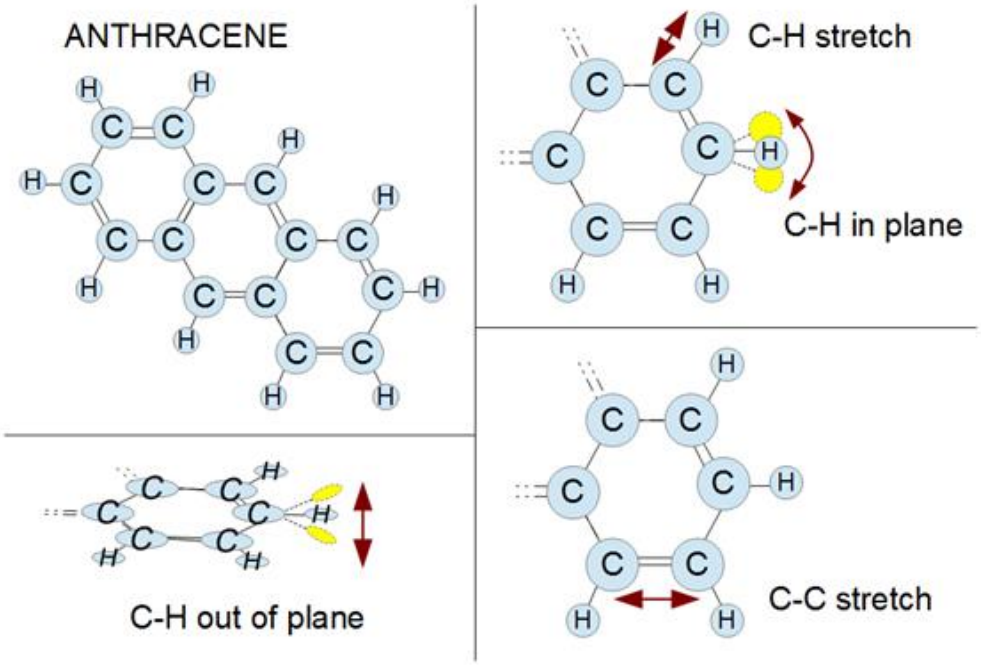

Figure 3.14: *A PAH molecule, anthracene (top left) and its vibration modes (zoomed in).*

PAHs have fundamental role in photoelectric heating of the gas, reinforcing the coupling of the gas and dust components (Draine et al., 2013)

References and further reading to the chapter:

Draine, B. T., 2003: *"Interstellar Dust"*, http://ned.ipac.caltech.edu/level5/March04/Draine/paper.pdf

Draine, B. T. & Anderson, N. 1985: *"Temperature fluctuations and infrared emission from interstellar grains"*, ApJ, 292, 494

Draine, B. T. et al, 2013: *"Andromeda's Dust"*, http://arxiv.org/pdf/1306.2304v1.pdf

Duley W.W. & Poole, G. 1998: *"Very Cold Grains in the Interstellar medium"*, ApJ, 504, 113

Gibb, E. L. et al. 2000: *"An Inventory of Interstellar Ices toward the Embedded Protostar W33A"*, ApJ, 536, 347

Glass, I.S., 1999: "*Handbook of infrared astronomy"*, Cambridge Observing Handbooks for Research Astronomers (No. 1), Cambridge University Press, ISBN: 9780521633857

Neumann G.A. et al., 2013: *"Bright and Dark Polar Deposits on Mercury: Evidence for Surface Volatiles"*, Science, 339, 296

Pieters, C.M. et al. 2009: *"Character and Spatial Distribution of OH/H_2O on the Surface of the Moon Seen by M^3 on Chandrayaan-1"*, Science, 326, 568

Slade, M, A. et al., 1992: *"Mercury radar imaging - Evidence for polar ice"*, Science, 258, 635

http://astronomy.nmsu.edu/geas/lectures/lecture19/slide02.html

https://en.wikipedia.org/wiki/Molecular_vibration

http://www.astronomy.ohio-state.edu/~ryden/ast822/week1.pdf

http://www.astronomy.ohio-state.edu/~ryden/ast822/week2.pdf

http://coolcosmos.ipac.caltech.edu/cosmic_classroom/ir_tutorial/what_is_ir.html

http://www.ipac.caltech.edu/outreach/Edu/Regions/irregions.html

http://www.nasa.gov/mission_pages/messenger/media/PressConf20121129.html

http://psych.nyu.edu/pelli/pubs/pelli1990efficiency.pdf

Chapter 4. Transmission, background noise

In this chapter we present the atmospheric transmission windows. We characterize the components of the infrared background radiation. The method of subtracting background and foreground emissions is also addressed.

4.1 Atmospheric transmission

Astronomical objects emit electromagnetic radiation at all wavelengths, but their entire electromagnetic spectra are not observable from the ground level of Earth. Most of the electromagnetic spectrum gets absorbed or blocked by the atmosphere. Figure 4.1. shows which parts of the EM spectrum are observable from the Earth.

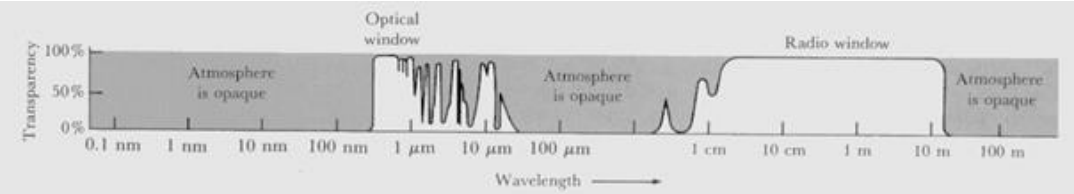

Figure 4.1: Atmospheric windows. Two main atmospheric windows are seen: the optical and radio window. There is a partial transmission between 1 and 30 μm. (http://violet.pha.jhu.edu/~wpb/spectroscopy/figures/trans.gif)

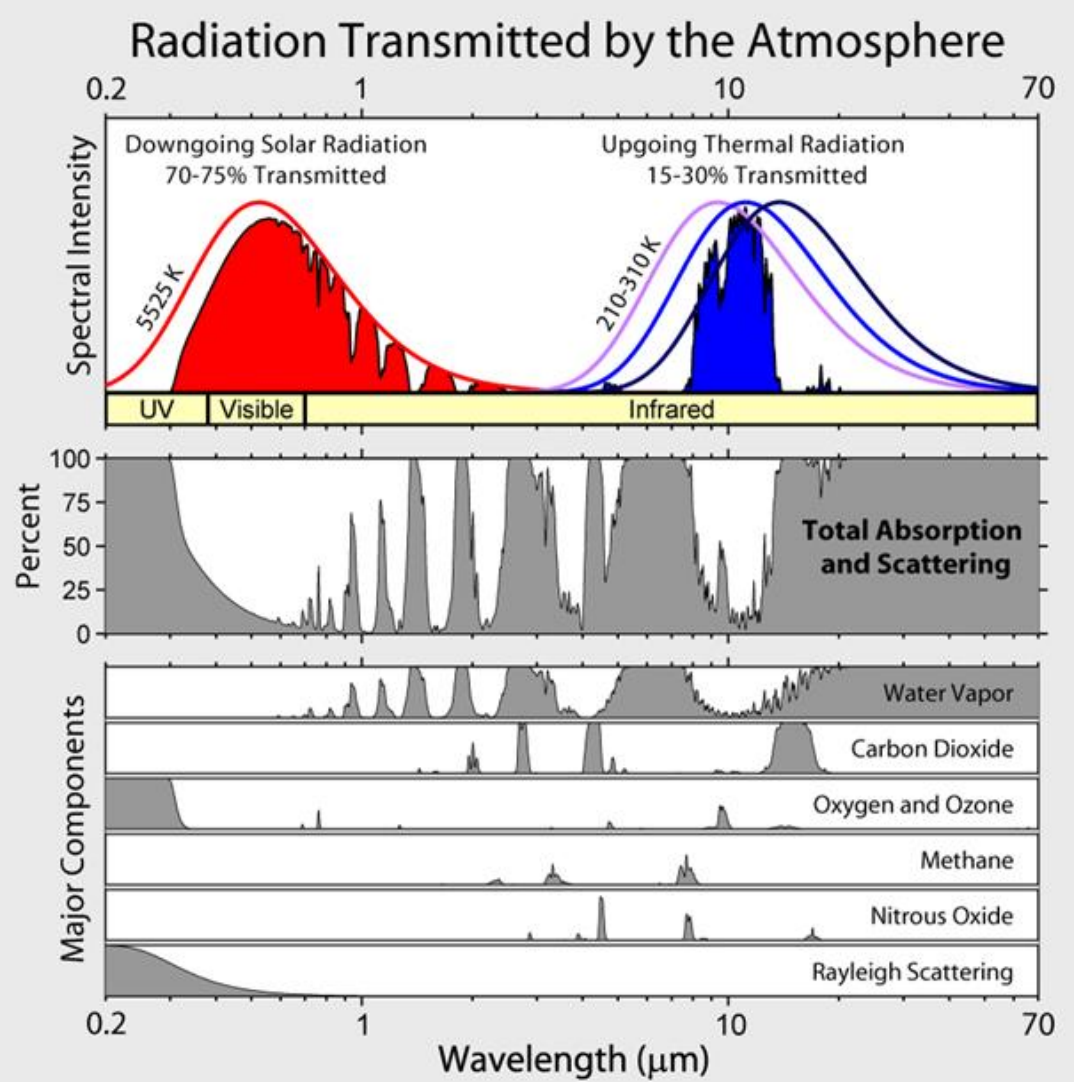

Figure 4.2: Atmospheric transmission with the major absorbing components of the terrestrial atmosphere and Rayleigh scattering. Low absorption+scattering levels mark the bands in which terrestrial observations are possible. Water vapour and CO_2 dominate the IR absorption. Seasonal variations (Figure 4.3) are due to variation of H_2O content. (Rohde, R.A http://www.globalwarmingart.com/wiki/File:Atmospheric_Transmission_png)

Most of the infrared light is absorbed by water vapour and carbon dioxide in the Earth's atmosphere. The absorption by these molecules occurs in certain wavelength bands, between which the atmosphere is transparent. Only in these few narrow wavelength ranges, in the atmospheric windows, the small portion of the infrared light can partially get through the atmosphere. Table 4.1 contains the infrared windows, in which ground based telescopes can observe the infrared universe. The best infrared windows for ground based telescopes are the bands with the highest transparency and smallest infrared radiation. They are located below 4 microns. Infrared filters can match with these windows or narrower passbands can also be defined within each window. Different filter sets are not identical, therefore the determination of the effective wavelengths and passbands is important.

Band	**Wavelength range [μm]**	**Sky transparency**	**Sky brightness**
J	1.1 – 1.4	high	low
H	1.5 – 1.8	high	very low
K	2.0 – 2.4	high	very low
L	3.0 – 4.0	fair	low
M	4.6 – 5.0	low	high

Band	Wavelength range [μm]	Sky transparency	Sky brightness
N	7.5 – 14.5	low	very high
Q	17 – 25	very low	very high
Z	28 – 40	very low	very high

Table 4.1: *Properties of infrared windows*

The precipitable water vapour content of the atmosphere varies strongly with temperature. Since temperature drops quickly with altitude in the Troposphere (se eg. http://www.srh.noaa.gov/jetstream/atmos/atmprofile.htm), the scale depth of water H_w is much smaller than that of the air pressure for example. The number density of water molecules at altitude z is $n_w(z)$:

$$n_w(z) = n(z_0)\exp((z - z_0)/H_w) \tag{4.1}$$

where $n(z_0)$ is the water density at the surface. The water vapour content is thus sensitive to the altitude of the observatory, and this is why most infrared ground based observatories are located at high, dry sites. The atmosphere blocks out the infrared radiation above 20 μm, as well as very low energy radio waves.

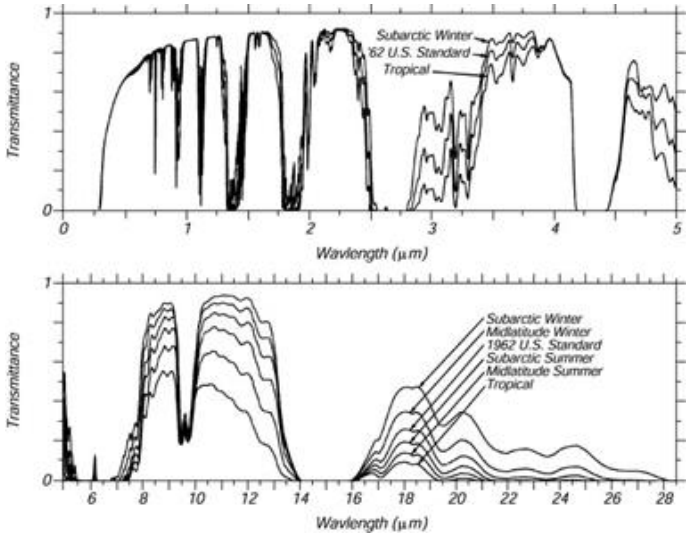

Figure 4.3: Atmospheric transmittance for six model atmospheres from subarctic to tropical atmospheres between 0.2 – 28 μm. Difference is observable above 3 μm. (Selby & McClatchey, 1975)

The atmospheric transmission is different for the different observing places. Figure 4.3. shows the atmospheric transmittance for a vertical path to space from sea level for six model atmospheres with very clear, 23km, visibility, including the influence of molecular and aerosol scattering. Notice how water vapor modulates the transparency of the 10-14 μm atmospheric window, hence it modulates the net longwave radiative flux (QLW), which is a maximum at these wavelengths. From Selby and McClatchey (1975). Ideal sites for infrared observations are those where water vapour, CO_2 and O_2 levels are low, these are the cold dry summits of high mountains as well as the Antarctica.

4.2 Background radiation

Figure 4.4 shows the sky background for the wavelength range between 0.1 μm and 10,000 μm (Figure 1. from Leinert et al., 1998). It has the following components: airglow from the upper atmosphere, zodiacal light, integrated starlight of the stars not individually accounted for, diffuse galactic light (cirrus), extragalactic background light. A common way to present the spectral energy distribution is λI_λ or νI_ν as in Figure 4.4 being plotted against wavelength. Please note the logarithmic scales on both axes.

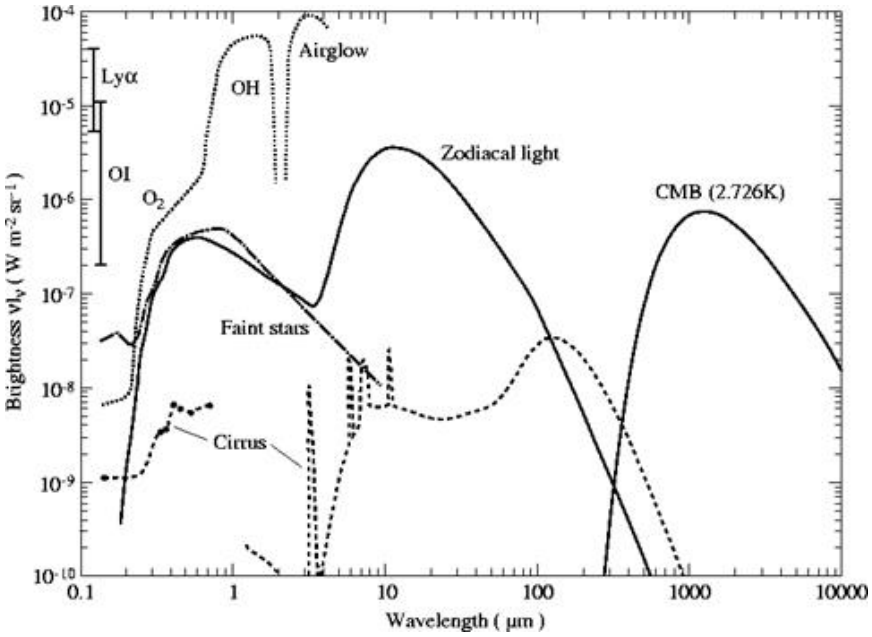

Figure 4.4: Overview on the brightness of the sky outside the lower terrestrial atmosphere at high ecliptic and galactic latitude (Figure 1 from Leinert et al. 1998, http://aas.aanda.org/articles/aas/full/1998/01/ds1449/img36.gif). The main components of the sky background radiation in the optical range are the radiation of faint stars, O_2 and OH. The zodiacal light, the galactic cirrus emission and the airglow are dominating the infrared range. At longer wavelengths, the CMB is appearing.

The infrared sky background consists of the following components (see also Figure 4.4):

1. Emission by atmospheric particles: specific ions, molecules and airglow (near-infrared).
2. Faint stars in the Milky Way appear at near-infrared and mid-infrared.
3. Zodiacal Light and minor bodies in the solar system shine at mid-infrared.
4. Galactic cirrus emission, a quasi-thermal emission by large dust particles dominates the emission at far-infrared wavelengths $\lambda>70\mu m$.
5. Unresolved light of distant galaxies, especially active star forming galaxies also at cosmological distances.
6. The far-infrared part of the cosmic microwave background.

4.2.1 Terrestrial background radiation

The Earth's atmosphere strongly radiates in the infrared. Below 2 μm it is mainly Rayleigh scattered starlight and moonlight and thermal radiation of the atmosphere at somewhat longer wavelengths (all dominated by sunlight and scattered sunlight during daytime). The blackbody radiation from T≈300K terrestrial sources has its maximum at $\lambda_{max}\approx9\mu m$. At mid-IR wavelengths, broad-band array detectors must be read out several tens of times per second to avoid saturation with background photons. With an appropriate measurement technics we derive a differential signal (see chapter 4.3), in fact the observed source is usually visible only on the differential image. The telescope itself also contributes to the background radiation. That can be reduced applying cold baffles masking out warm zones at the exit pupil of the telescope. There are also attempts (using special coatings) to keep the emissivity of the surfaces at a very low level. The contrast between an emission line and the background can be high, so high spectral resolution spectroscopic observations are often done without chopping.

4.2.2 Airglow

Airglow (also called as nightglow) is the dominant source of background for broadband observations in the J, H and K bands (see Figure 4.5). This highly variable infrared radiation peaks at around 3 μm.

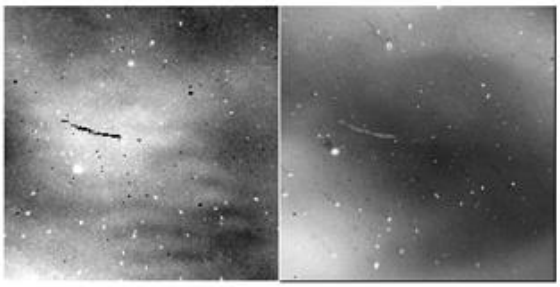

Figure 4.5 a: Airglow in H band 9x9 flatfielded images of the same portion of sky with a time difference between the two images of 7 minutes. (Adams & Skrutskie 1996).

Figure 4.5 b:*Green and red airglow across the constellation Orion (three Belt stars at center right) photographed by space shuttle astronaut Don Pettit from orbit. Credit: NASA - See more at:* http://astrobob.areavoices.com/2009/02/25/is-there-true-darkness/#sthash.ebUfDH51.dpuf

The airglow is emitted by atoms and molecules in the upper atmosphere which are excited by solar UV radiation during the day. There are various sources of the infrared airglow: photodissociation, chemical reactions and atomic and molecular collisions. Mainly it may arise from rotational transitions (e.g. around 17 μm from water vapour) or from electronic transitions (e.g. around 1.2-1.5 μm from O_2) and vibrational-rotational transitions within the ground electronic state. It includes emission from OH, CO_2, O_3, NO and H_2O. The earthshine can excite only the lower vibrational levels of the infrared active molecules, while the sunshine has an important role in exciting higher vibrational levels.

Airglow is mainly radiated by excited hydroxyl radical OH^-, and appears in the spectrum as the so called Meinel bands, between 1 and 1.65 μm. The chemical reaction behind the excitation is:

$$H + O_3 \rightarrow OH^- + O_2 \tag{4.2}$$

The other prominent airglow source is the layer of molecular oxygen emitting at a peak altitude at about 95 km. Further contributors to the airglow are the layers of sodium, iron, potassium and calcium. The altitude of the airglow emission is about 85-100km, it effects all terrestrial sites. The lines and bands are numerous and their strength is highly spatially and temporally variable with quasi periods of few 10km and ~10 minutes. The airglow lines and bands can be used for wavelength calibration of observed NIR spectra.

4.2.3 Zodiacal light

The name zodiacal light refers to the faint, diffuse white glow seen in the vicinity of the Sun just after sunset and before sunrise, see on Figure 4.6. It is present in the ultraviolet, visual and near-infrared regions and is due to the sunlight scattered by dust particles in the inner Solar System.

Figure 4.6: Zodiacal light (a triangular, faint, diffuse white glow visible near to the horizon) and light pollution photographed at ESO's La Silla Observatory in Chile in September 2009. (http://www.eso.org/public/images/zodiacal_beletsky_potw/)

The zodiacal emission is dominated by the thermal emission ~270K of the solid particles, which are originated from comets, collisions of asteroids and from interstellar dust. The cloud formed by these particles is the Interplanetary Dust Cloud. The distribution of the interplanetary dust is not uniform, denser regions are present due to comets, asteroids. The total mass of this dust cloud is only ~10^{16}-10^{17} kg (it is ~30-500 times the mass of the Halley's comet), but it dominates the infrared sky brightness between 3 μm and 70 μm. Dust particles are spiralling slowly into the Sun, so a continuous supply is needed to maintain the interplanetary dust cloud. There is a seasonal variation in the brightness of the zodiacal light because of the motion of the observer in heliocentric distance and with respect to the symmetry plane of interplanetary dust cloud. From this seasonal variation we could make con-

clusions for its large scale structure. The most precise model is based on the observations of the DIRBE (Diffuse InfraRed Background Explorer) instrument on board of COBE (Cosmic Background Explorer) and its temperature distribution was measured by ISOPHOT.

We can estimate the size and chemical composition of the interplanetary dust from the zodiacal light's spectrum between 2 μm and 15 μm. Based on ISO observations, the cloud consists of relatively large dust grains, ~100 μm < a < 1 mm.

4.2.4 Galactic cirrus emission

The galactic cirrus emission was discovered by the IRAS satellite in 1984 and was named due to the similarity to cirrus clouds in the Earth's atmosphere. The structure of the cirrus emission is similar to that of a fractal, which was first investigated by Gautier in 1992 based on IRAS 100 μm images. The emission is not connected to the plane of the Milk Way, this is the dominant source of the background radiation of the whole sky at wavelengths > 60 μm. It comes from dust in low-density galactic HI clouds with a typical temperature of ~18 K.

We can separate the cirrus clouds into three classes at high galactic latitude, based on their radial velocity and distance: low-velocity clouds (distances approx. 100pc, velocity < 20 km/s), intermediate-velocity clouds (distances < 1kpc, velocities between 20 km/s and 100 km/s) and high-velocity clouds (distances > 1000pc, velocity > 100 km/s).

4.3 Subtracting background and foreground emission

For near- and mid-infrared ground-based observations the atmosphere and telescope are bright sources of radiation. In addition the sky brightness is highly variable with high time and spatial frequencies. These effects are accounted for with the "chopping and nodding" technique. The "chopping" is done by moving the secondary mirror between the target position and a nearby position on the sky. The pairs of images are subtracted during the data reduction. The amount and distribution of infrared radiation from the telescope itself will be slightly different at the two secondary mirror positions, thus after the subtraction a residual radiative offset will appear. We can get rid of this offset moving the entire telescope, which is called "nodding". The nodding offset (amplitude and direction) is set to be the same as the chop, that way the target switches chop positions between the two nod positions. A pair of subtracted chop/nod observations produces a positive image of the target in the centre which corresponds to half of the exposure time, and two displaced negative images of the target, each of which corresponds to 1/4 of the exposure time. If the chop and nod are large enough the negative images are off of the array and are not seen. Figures 4.7 and 4.8 show 2 implementations of the chopping-nodding technique, both of these two yield the same signal-to-noise ratio in the background noise-limited case.

The differential image is calculated as:

$$I_{diff} = \left(I(nodA, chop.1) - I(nodA, chop.2)\right) - \left(I(nodB, chop.1) - I(nodB, chop.2)\right) \tag{4.3}$$

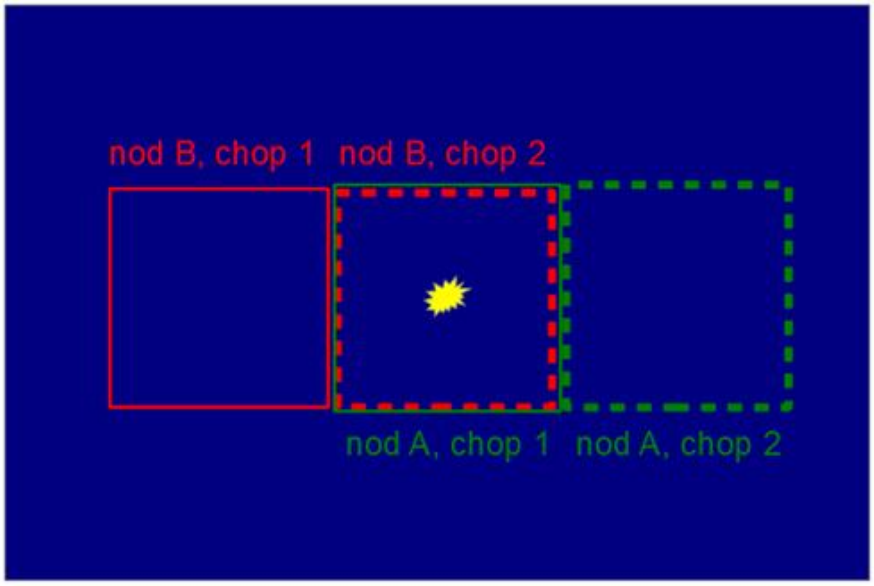

Figure 4.7: Chop-nodding observation – completely off-chip

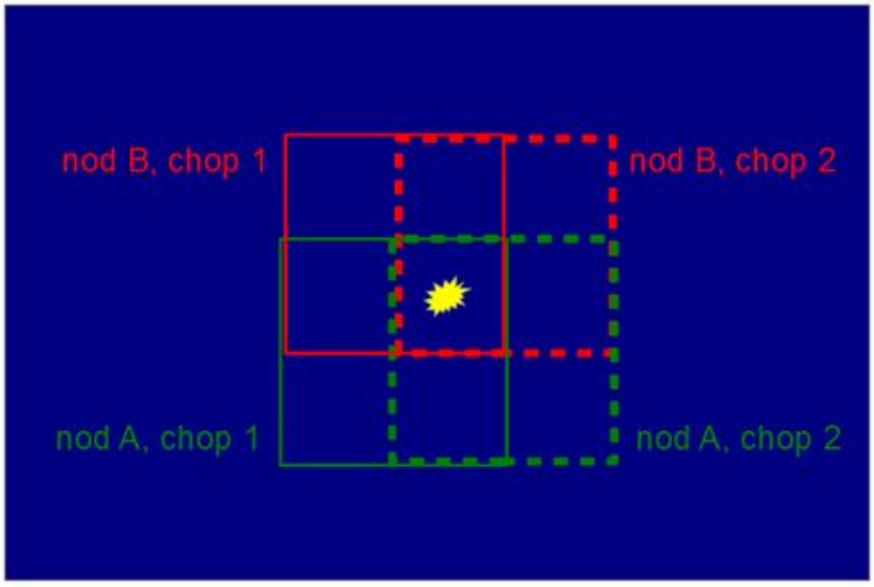

Figure 4.8: Chop-nodding observation – on-chip

References and further reading to the chapter:

Adams, J. & Skrutskie, M. 1996: *„Wide-field Airglow Experiment"* , University of Massachusetts, Amherst, http://www.astro.virginia.edu/~mfs4n/2mass/airglow/airglow.html

Gautier, T.N. et al. 1992: *"A calculation of confusion noise due to infrared cirrus"*, AJ, 103, 1313

Glass, I.S., 1999: "*Handbook of infrared astronomy"*, Cambridge Observing Handbooks for Research Astronomers (No. 1), Cambridge University Press, ISBN: 9780521633857

Leinert, Ch. et al. 1998: *"The 1997 reference of diffuse night sky brightness"*, A&ASS, 127, 1

Selly, J.E.A. & McClatchey, R.A. 1975: *"Atmospheric transmittance from 0.25 to 28.5 microns: Computer code LOWTRAN 3"*, Environmental Research Papers Air Force Cambridge Research Labs., Hanscom AFB, MA

http://www.srh.noaa.gov/jetstream/atmos/atmprofile.htm

Chapter 5. Infrared photometry

In this chapter we give the photometry's basic definitions, the relationship between magnitude and flux in the different wavelength ranges and colour correction.

The most spectacular results of an astronomical observation using ground based large telescopes or space observatories are the marvellous pictures. They are needed as a first step in classifying objects based on their morphology, but for the next step, we need quantitative information from the objects.

Originally, the term photometry was used by opticians, and referred to measurement of the various energy quantities associated with visual sensations. It was thus closely linked to the spectral properties of a rather specific detector, the human eye.

Radiometry, in the classical sense, deals more generally with the energy transported by electromagnetic radiation, at whatever wavelength.

The term photometry, as it is used in astronomy, covers the general meaning of radiometry. We note that most of the quantities to be defined refer to some specified wavelength or frequency, and that, strictly speaking, the correct term would be spectrophotometry, which is indeed often used. Photometry is very closely linked to the general ideas of spectroscopy. In photometry, objects are measured relative to standard stars, and the absolute level is a quantity which must be set in some way.

Assume some radiation (I_v) passing through a surface and consider an element of the surface of area dA. Some of the radiations will leave the surface element within a beam of solid angle $d\omega$ at an angle of θ to the surface. Solid angle is dimensionless and it is usually measured in steradians (sr). The whole sky corresponds to 4π steradians. The definition of I_v, dA, $d\omega$ and θ are given on Figure 5.1.

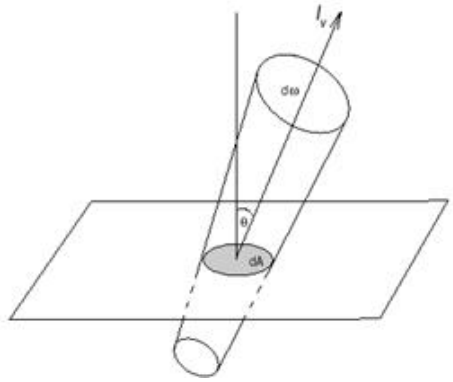

Figure 5.1: Definition of physical properties in case of some radiation passing through a surface (http://www.starlink.rl.ac.uk/docs/sc6.htx/node8.html)

Equation 5.1 define the amount of energy entering the solid angle within a frequency range [ν, ν+dν] in a time dt, where I_ν is the specific intensity of radiation at ν frequency in the direction of the solid angle. I_ν 's dimensions is $Wm^{-2}Hz^{-1}sr^{-1}$.

$$dE_\nu = I_\nu \cos\Theta dA d\nu d\omega dt \tag{5.1}$$

The total intensity (I) includes the intensity at all possible wavelengths is:

$$I = \int_0^\infty I_\nu d\nu \tag{5.2}$$

Flux and flux density (F, Fν) gives the power of the radiation per unit area and hence has dimensions of Wm^{-2} or $Wm^{-2}Hz^{-1}$. For practical purposes it is often convenient to scale the flux density values and use Janskys instead of $Wm^{-2}Hz^{-1}$, where 1 Jy=10^{-26} $Wm^{-2}Hz^{-1}$.

The Stefan-Boltzmann law gives us the flux of energy radiated from the surface of a blackbody object. $\sigma = 5.67\times10^{-8}Wm^{-2}K^{-4}$ is the Stefan-Boltzmann constant.

$$F = \sigma T^4 \tag{5.3}$$

If the investigated source radiates isotropically, the total emitted flux (L, luminosity) is given by Equation 5.4.

$$L = 4\pi r^2 F \tag{5.4}$$

We can define the bolometric luminosity as the luminosity of the object measured over all wavelengths.

To specify the relative brightness of stars, Hipparchus created the magnitude system more than 2000 years ago. He divided the stars into 6 classes. The brightest stars were in the first class. The response of the human eye to the brightness is not linear, rather logarithmic. As it is seen in Figure 5.2 the just noticeable difference of luminance is related to the signal. This relation however changes, there are 3 fuctions up to the threshold of perception. The horizontal axis of Figure 5.2 is the light stimulus, the vertical is perception. The Weber-Fechner law (linear part of the curve) holds for a range of roughly 4 orders of magnitudes.

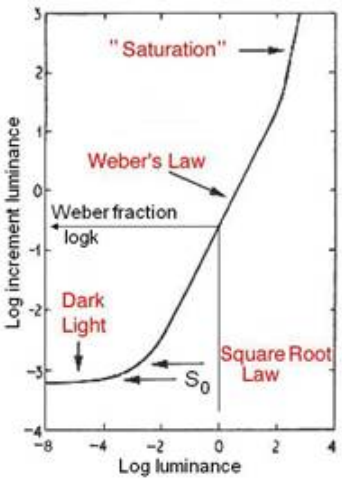

Figure 5.2*: The Weber-Fechner law for a just noticeable difference of luminance for the rod vision.(Schellart 2005,* http://onderwijs1.amc.nl/medfysica/doc/Weber-Fechner%20law.htm*)*

An increase in magnitude by 2.5 means an object is a factor of 10 dimmer.

In 1857 Pogson defined the modern magnitude scale. The apparent magnitude (m) of a star with an observed flux density F is

$$m = -2.5\log\frac{F}{F_0} \tag{5.5}$$

where F_0 is a standard flux density, or the zero-magnitude flux. che zero-magnitude fluxes and main properties of the common used infrared bands.

Band	**λ[μm]**	**Wavelength range [μm]**	**Zero-magnitude flux [Jy]**
2MASS J	1.235	1.105-1.349	1594±27.8
2MASS H	1.662	1.504-1.709	1024±20.0

Band	λ[μm]	Wavelength range [μm]	Zero-magnitude flux [Jy]
2MASS K_S	2.159	1.989-2.316	666.7±12.6
Spitzer IRAC 3.6μm	3.6	3.179-3.955	280.9±4.1
Spitzer IRAC 4.5μm	4.5	3.955-5.015	179.7±2.6
Spitzer IRAC 5.8μm	5.8	5.015-6.442	115.0±1.7
Spitzer IRAC 8μm	8	6.442-9.343	64.13±0.94
Spitzer MIPS 24μm	23.675	20.335-29.462	7.17±0.11
Spitzer MIPS 70μm	71.42	60.927-80.581	0.778±0.0119
Spitzer MIPS 160μm	155.9	139.804-188.160	0.16±0.00245
WISE W1	3.4	2.5-4	309.540±4.582
WISE W2	4.6	3.8-5.5	171.787±2.516
WISE W3	12	7-18	31.674±0.450
WISE W4	22	19-28.55	8.363±0.293
IRAS 12μm	12	8.5-15	28.3
IRAS 25μm	25	19-30	6.73
IRAS 60μm	60	40-80	1.19
IRAS 100μm	100	83-120	0.43
AKARI IRC S9W	9	6.7-11.6	56.26±0.8214
AKARI IRC L18W	18	13.9-25.6	12.00±0.1751

Table 5.1: *Properties of the common used infrared bands*

If 2 stars have observed flux densities: F_1 and F_2, their apparent magnitudes are related by

$$m_1 - m_2 = -2.5 \log \frac{F_1}{F_2} \tag{5.6}$$

We distinguish between apparent (m_v), absolute (M_v) and absolute bolometric (M_b) magnitudes.

The absolute magnitude is defined as the apparent magnitude of a star located at 10 pc distance. The relationship between stars' apparent and absolute magnitudes is the following:

$$m - M = 5 \log r - 5 + A \tag{5.7}$$

where r is the distance of the star and A is the interstellar extinction.

Figure 5.2 shows a simple linear graph with various astronomical objects plotted on the apparent magnitude scale.

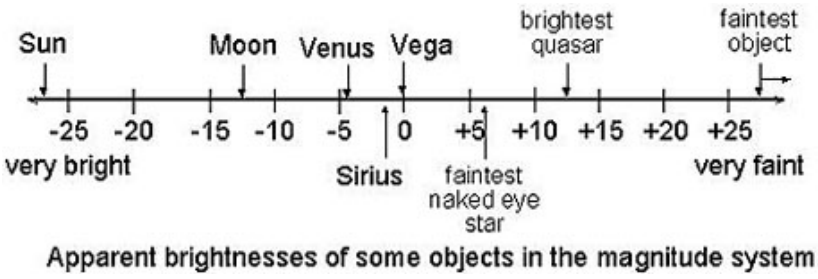

Figure 5.3*: Apparent brightnesses of some astronomical objects (from Nick Strobel's Astronomy Notes, https://www.fas.org/irp/imint/docs/rst/Sect20/A5.html)*

The absolute bolometric magnitude describes the brightness of the star at all wavelengths. It cannot be measured directly. This value is relative to the Sun.

$$M_b = -2.5 \log \frac{L}{L_{Sun}} + 4.72 \tag{5.8}$$

where L_{Sun} is 3.9×10^{33} erg s^{-1}, the luminosity of the Sun. 4.72 is the Sun's absolute bolometric magnitude.

The first observations of the stars and estimates of their magnitudes were based on naked eye observations or later they were made by direct observation through an optical telescope. Magnitudes estimated in this way are visual magnitudes. 0.55 μm is the peak sensitivity of the human eye. The observed flux density of astronomical objects strongly depends on the wavelength. Different filters are used to investigate the astronomical object's radiation in different wavelength ranges. The sensitivity to incident radiation is defined by the detectors and filters used. Table 5.1 contains the basic data of the common used infrared filters and Figure 5.4 shows the transmission of light as a function of wavelength for the WISE filters. The relative system response curves are from Wright et al. 2010. The width of the response functions for W1 and W2 is ~1.5 μm, while for the W3 and W4, it is ~10 μm.

Photometric systems are divided into different classes according to the widths of their passbands: narrow band (less than 10 nm wide), intermediate band (between 10 and 30 nm wide) and wide band (wider than 30 nm) systems.

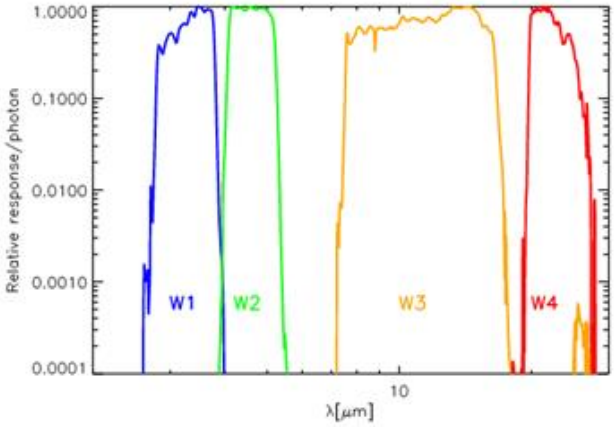

Figure 5.4: Normalized WISE spectral response functions on logarithmic scales. They cover the wavelengths range 2 – 30 μm.

To get comparable, reproducible results, we have to convert the instrumental response to standard magnitudes. The definition of the magnitude scale of optical, near- and mid-infrared systems is based on the observations of standard stars.

Instruments working in the thermal IR wavelength range were first calibrated against planets, but with the development of more sensitive instruments, these objects were too bright. In the far-IR the emission from stellar photosphere is too faint. A set of secondary calibrators were chosen from dust-rich sources: ultra-compact HII regions (UCHII), protostars, protoplanetary nebulae, AGB stars with dust envelopes. But they are often embedded in dust clouds, which provide variable, strong background. Asteroids are potential sources in the far-IR and submm range for calibration, together with the brightest standard stars and the planets Uranus and Neptune.

A set of 10 asteroids was used for calibration during the ISO mission. They show only small lightcurve variations over typical observational integrational times of less than 30 minutes. Their excellent visibility during the mission and the absence of strong emission or absorption features supported this decision. The calibration programme included Ceres, see the calibrated, background subtracted image on Figure 5.5.

The brightness level of the point-like asteroids and the high accuracy of the model predictions allow their usage in calibrations for space observatories, where high S/N is needed.

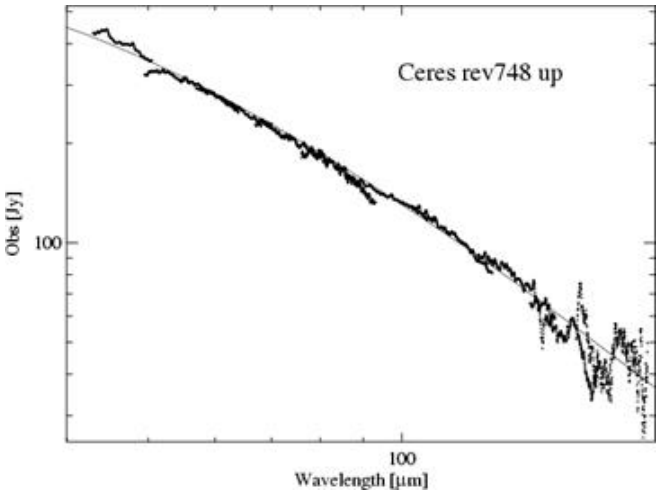

Figure 5.5: *Calibrated and background subtracted ISO spectrum of Ceres.*

For ground based observations, we have to correct for the atmospheric extinction when calibrating instrumental magnitudes. The longer the path length the light traverses through the atmosphere, the more it is dimmed. The observed brightness of a given star will change during the night, as it its zenith distance varies.

The air mass, X(z) is the path length through the atmosphere, where z is the zenith distance. X(z) is normalized, its value is 1 at the zenith. The relation between the magnitude of the observed objects outside the atmosphere ($m_0(\lambda)$) and at the Earth's surface ($m(\lambda)$) at λ wavelength is the following:

$$m(\lambda) = m_0(\lambda) + \kappa(\lambda)X(z) \tag{5.9}$$

$\kappa(\lambda)$ is the extinction coefficient at wavelength λ.

For photometry bands with broad wavelength coverage, we have to apply colour correction for a detailed analysis. The response of the system changes considerably with wavelength. Considering that also the spectral energy distributions (SEDs) of the measured objects vary widely, the quoted flux will be appropriate to some isophotal wavelength, unique to each object. These may not be close to the nominal or effective wavelength of each band.

The calculated flux densities are usually based on a constant energy spectrum.

If the input spectral distribution is not constant, then the colour correction (K) must be applied. We can calculate the correction factor with the following equation:

$$K = \frac{\int F(\nu)R(\nu)d\nu}{F(\nu_c)} \Big/ \frac{\int F_{flat}(\nu)R(\nu)d\nu}{F_{flat}(\nu_c)} \tag{5.10}$$

The correction depends on the shape of the intrinsic energy distribution and on the details of the wavelength response of the system. Deriving true flux densities requires a knowledge of the intrinsic energy distribution of the astronomical sources.

In practice we can make the colour correction with the following steps:

1. use the correction factors given by the instrument's handbook. Assumed shape of the SED and temperature are needed, or

2. calculate the correction factor based on available photometric data

   a. constrain the SED and fit the profile: depending on the source radiation we can fit the SEDs only with modified blackbody functions, or precomputed stellar SEDs

b. with the use of the instrument's filter function and Equation 5.10, we can calculate the correction from the derived SED shape in 2b.) step

c. correct the fluxes and if needed, refit the SED

References and further reading to the chapter:

Glass, I.S., 1999: "*Handbook of infrared astronomy"*, Cambridge Observing Handbooks for Research Astronomers (No. 1), Cambridge University Press, ISBN: 9780521633857

Ishihara, D., Onaka, T., Kataza, H. et al., 2010:*"The AKARI/IRC mid-infrared all-sky survey"*, A&A, 514, A1

Koornneef, J., 1983: *"Near-infrared photometry. II - Intrinsic colours and the absolute calibration from one to five micron"*, A&A, 128, 84

Müller, T. G. & Lagerros, J. S. V., 2002: *"Asteroids as calibration standards in the thermal infrared for space observatories"*, A&A, 381, 324

Schellart, N.A.M. 2005: "*Principles of Medical Physics and Medical Technology*", Academic Medical Center University of Amsterdam

Wright, E. L. et al., 2010, *"The Wide-field Infrared Survey Explorer (WISE): Mission Description and Initial On-orbit Performance"*, AJ, 140, 1868

Yamamura, I., Makiuti, S., Ikeda, N. et al., 2010: *"AKARI/FIS All-Sky Survey Bright Source Catalogue Version 1.0 Release Note"*

http://antonirogalski.com/wp-content/uploads/2012/12/History-of-infrared-detectors.pdf

http://casa.colorado.edu/~ginsbura/filtersets.htm

http://irsa.ipac.caltech.edu/IRASdocs/exp.sup/ch6/C2a.html

http://lambda.gsfc.nasa.gov/product/iras/colorcorr.cfm

http://www.coe.montana.edu/ee/jshaw/classes/EOSystems/F09/ClassResources/EE482_F09_RadiometryOverview_2pp.pdf

http://www.gemini.edu/?q=node/10138

http://www.starlink.rl.ac.uk/docs/sc6.htx/node7.html

http://www.starlink.rl.ac.uk/docs/sc6.htx/node10.html

Chapter 6. All-sky surveys

6.1 IRAS

The Infrared Astronomical Satellite (IRAS) was initiated in 1975, designed and constructed by NASA (USA), NIVR (the Netherlands), and SERC (UK), and launched by NASA (launcher: Delta 3910) on January 25, 1983. It was the first space-borne infrared observatory to scan the entire sky. During its ten months of operation, IRAS scanned more than 96 percent of the sky four times at four infrared bands centered at 12, 25, 60 and 100 microns. Its main task was to discover and measure IR point sources. The IRAS mission has had a major impact on almost every area of astronomy.

6.1.1 The most important results of IRAS:

- Detected about 350,000 infrared sources (see Figure 6.1), increasing the number of cataloged astronomical sources by about 70%.

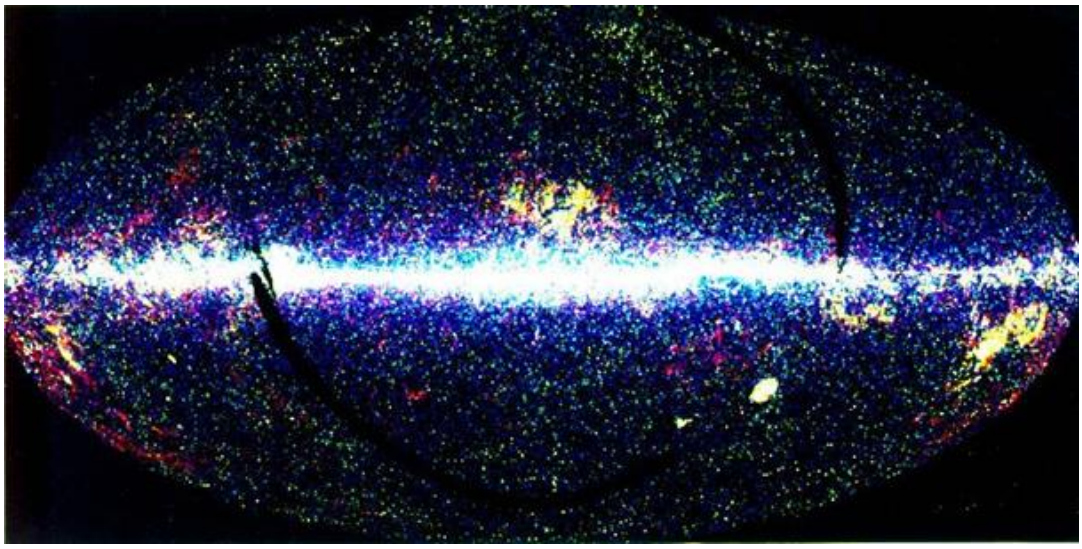

Figure 6.1: *All sky map of IRAS sources (*http://www.iras.ucalgary.ca/~nkoning/irasDb/iras.html*)*

- Discovered 6 new comets
- Found that comets are dustier than previously thought and that dust from comets fills the Solar System
- Detected useful infrared data for 2004 asteroids
- Detected the zodiacal dust bands - bands of infrared emission that girdle our solar system which are likely to be debris from asteroid collisions
- Found evidence of zodiacal dust bands around other stars
- Discovered a disk of dust grains around the star Vega, see Figure 6.2. The significant excess above the photospheric model indicates the presence of cold material around a star.

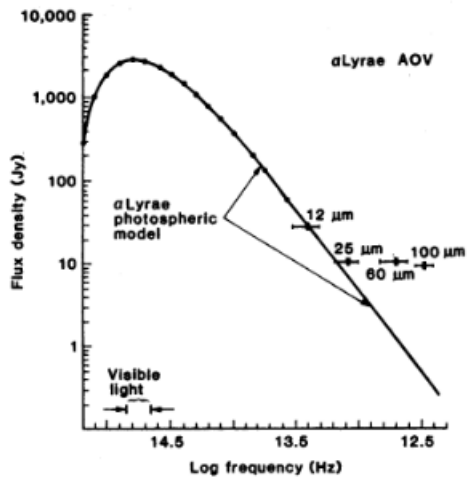

Figure 6.2: *Observed spectral enery distribution of Vega and photosperic stellar model (Neugebauer et al.).*

- Detected disks of material around several other stars.
- Detected several probable protostars embedded in clouds of gas and dust
- Found that some Bok globules contain protostars. e.g. Beichman (1984) showd that the Bok globule, Barnard 5 contains at least four protostars.
- Cataloged thousands of hot, dense cores within clouds of gas and dust which could be newly forming stars
- Cataloged over 12,000 variable stars, the largest collection known to date
- Revealed for the first time the core of our galaxy
- Found infrared cirrus (wisps of warm dust) in almost every direction of space
- Data from IRAS was used to show that our galaxy is a barred spiral galaxy - a galaxy which has an elongated central bar-like bulge from which its spiral arms unwind.
- Detected 75,000 starburst galaxies - galaxies which are extremely bright in the infrared due to intense star formation. It was found that many of these starburst galaxies have ”superwinds” emerging from their centers due to the large number of supernova explosions which occur in these galaxies.
- Detected strong infrared emission from interacting galaxies
- First identified IRAS F10214+4724 - at the time, the most luminous object known in the Universe by a factor of 2. This object may be the best candidate for a forming spiral galaxy yet discovered.

6.1.2 Instruments and observing strategy of IRAS

IRAS telescope system comprised the upper part of the satellite and was composed of a two mirror, Ritchey-Chretien telescope mounted within a toroidal superfluid helium tank, which in turn was mounted within the evacuated main shell. The optical system was protected from contamination before launch and during the first week of the mission by an aperture cover cooled with supercritical helium. After the cover was ejected, the sunshade limited heat flow to the aperture by blocking direct solar radiation and reflecting away terrestrial infrared radiation. The telescope orientation was constrained to prevent sunlight from striking the inner surface of the sunshade and radiation from the Earth from illuminating the radiators around the telescope aperture. The telescope was cooled by contact with the superfluid helium tank to temperatures ranging from 2 to 5 K. The surfaces of the sunshade which could be viewed by the telescope aperture were cooled by a three-stage radiator to about 95 K.

The focal plane assembly contained the infrared and visible detectors, cold electronics, and associated masks, filters and field optics. It consisted of 62 infrared channels and eight visible channels. The infrared channels were divided into eight modules, two for each color band with each module containing either seven or eight detectors. The detector masks were rectangular in aspect and infrared sources scanned across the focal plane parallel to the narrow dimension of the detectors in all observational modes.

6.2 MSX

Midcourse Space Experiment (MSX), a Ballistic Missile Defense Organization satellite, was launched in April 1996 into a 900 km altitude semi-sun synchronous orbit. It carried the 33-c óm SPIRIT III infrared telescope. The first ten months of the mission were devoted to mid-infrared observations with a solid hydrogen cooled telescope. This instrument had five line scanned focal plane arrays that spanned the spectral region from 4.2 µm to 26 µm. The point response ”footprint” was 35 times smaller than the IRAS 12 micron detectors and the sensitivity in the MSX 8.3µm band about four times more sensitive.

Over 200 Gigabytes of astronomy data were obtained on 230 measurements during the 10 month cryogenic phase of the MSX mission. The MSX astronomy experiments included mapping the entire Galactic Plane and surveying the IRAS gaps. Due to its orbit, the IRAS satellite did not observe 4 per cent of the sky, these are the so-called IRAS gaps, which have never been surveyed before in the mid-IR. Raster scan mapping provided deep surveys of selected regions in the Galactic Plane, primarily in the inner Galaxy, large molecular clouds, H II regions and other areas of star formation as well as asteroids and comets. Source catalogs from the Galactic Plane and IRAS gaps surveys and, separately, the Large Magellanic Cloud are available as well as an explanatory supplement. The Air Force Research Laboratory also created full resolution images and large scale panoramas of the Galactic Plane. (http://irsa.ipac.caltech.edu/Missions/msx.html).

Figure 6.3 shows the combined 2MASS-MSX view of the Galactic Center.

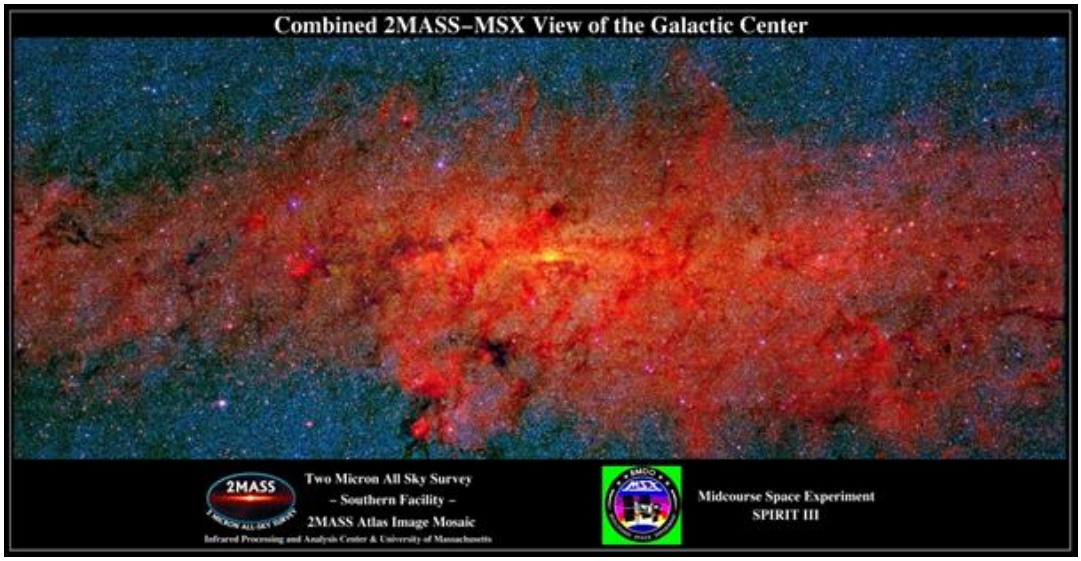

Figure 6.3: *Combined 2MASS-MSX image of the Galactic Center,* combination by E. Kopan (IPAC) *(*http://www.ipac.caltech.edu/2mass/gallery/2mass_msx_gcatlas.jpg*)*.

6.2.1 Infrared dark clouds

One of the major discoveries of MSX are the infrared dark clouds (IRDSs) which appear as dark spots in mid-IR bright regions (see e.g. Simon et al. 2006). Their typical size is: 1-10 pc, masses range from few hundreds to few thousands solar masses. Very high ISM column densities make these clouds infrared opaque (2×10^{23} $cm^{-2}<N(H_2)<10^{24}$ cm^{-2} and A_V up to 100 magnitudes).

Considering also their low temperature (10K <T_{kin}< 20 K) these may be the high mass analogues of globules, but IRDCs have broader and more intense spectral lines than in low mass clouds. IRDCs are quite turbulent and we may see presence of in-fall and outflow motions as signatures of beginning star formation activity in some. IRDCs are located in spiral arms and are related to massive star formation.

As an example see the Long Filamentary Infrared Dark Cloud (G53.2) of Kim et al. (2012), see Figure 6.4.

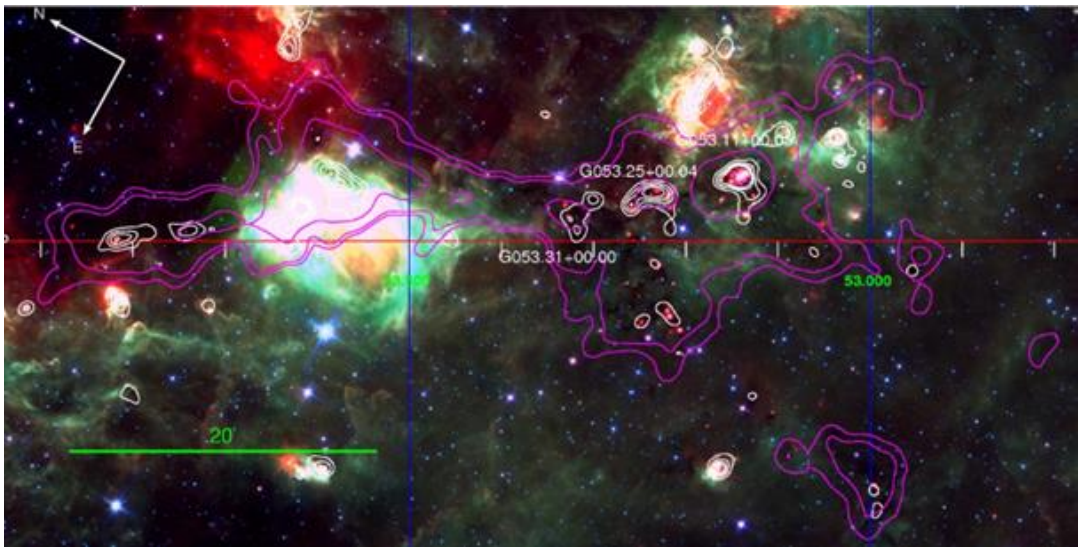

Figure 6.4: *Figure 1 from Kim et al. 2013, IRDC G53.2 from Spitzer IRAC 5.8(blue) + 8.0(green) + MIPS 24(red) μm. Magenta contours are GRS ^{13}CO J=1-0 integrated at v=15-30 km/s showing the boundary of the IRDC. The outermost contour is T_b= 0.42 K. Bolocam GPS 1.2 mm contours are overlaid in white. previously identified 3 IRDCs in MSXDC catalog are marked.*

6.3 AKARI

The AKARI Japanese satellite for infrared astronomical purposes operated with a telescope of 68.5 cm in diameter (Murakami et al. 2007). AKARI's orbit was similar to that of the IRAS satellite, it was a circular Sun-synchronous polar orbit at an altitude of approximately 700 km and an inclination of 98.2°. It flies along the day–night border with an orbital period of approximately 100 min. This is the most suitable orbit for scanning the sky while keeping the telescope direction away from the Sun and the Earth, whose strong emission would be ruinous to the cooled telescope. The telescope and focal plane instruments were cooled to a temperature lower than 6 K in a liquid-helium cryostat (Nakagawa et al. 2007) to avoid the thermal emission of the instruments. One of the main objectives of the AKARI mission was to carry out an all-sky survey. In the pointed observation mode, it also has a capability for imaging and spectroscopy in the wavelength range 2–180 μm. The All-Sky Survey had the highest priority during Phase 1 operations. In Phase 2 the observation plan was highly optimized to fill the scan gaps caused in Phase 1 under constraints of carrying out the maximum number of pointed observations.

The Far Infrared Surveyor (FIS) is one of the two focal plane instruments onboard (Kawada et al. 2007). Four photometric bands were used to scan the infrared sky between 50 and 180μm. Detectors and bands are the following: N60 (65 μm), WIDE-S (90 μm), WIDE-L (140 μm), N160 (160 μm). The AKARI FIS Bright Source Catalog (Yamamura et al. 2010) lists 427071 point sources detected at least at one of the four FIS bands. Figure 6.5-8 show the sky distribution of the detected sources in N60, WIDE-S, WIDE-L and N160 bands. Calibration and characterization of FIS were performed by observing well-established photometric calibration standards, like solar system-objects and stars. These sources were studied well enough (Müller & Lagerros 1998, 2002, Cohen et al. 1999, 2003a, 2003b) and were used as calibration sources in earlier infrared missions (e.g., ISO; Schulz et al. 2002, COBE; Hauser et al. 1998). The quality of the flux densities is given with quality flags: 1 for upper limits, 2 for moderate quality and 3 for good quality (see Yamamura et al. 2010).There are as many as 11543 point sources with 4 good or moderate flux qualities, while 21929 has at least 3, and 73962 has at least 2 good or moderate flux qualities. The typical flux uncertainty is 10 %. The positions of the AKARI FIS BSC point sources are given in J2000 equatorial coordinates with an assumed positional accuracy of 8 arcseconds (Yamamura et al. 2010).

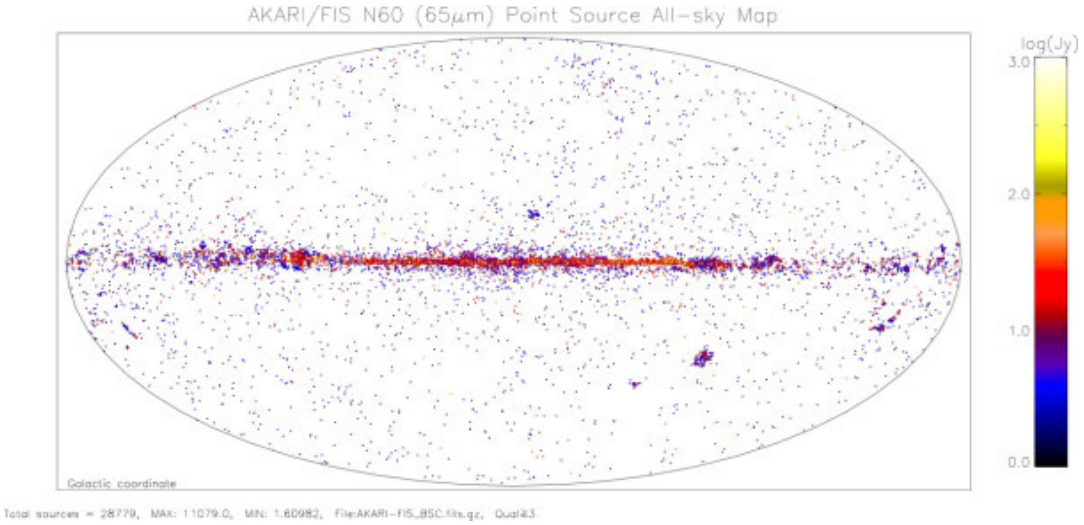

Figure 6.5: Sky distribution of the detected sources in N60 band (Yamamura et al. 2010).

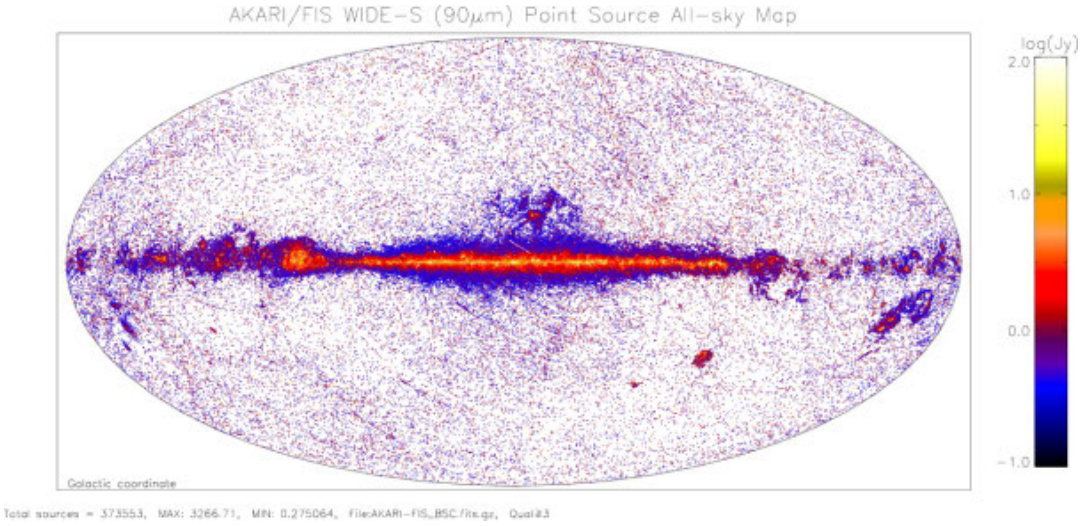

Figure 6.6: Sky distribution of the detected sources in WIDE-S band (Yamamura et al. 2010).

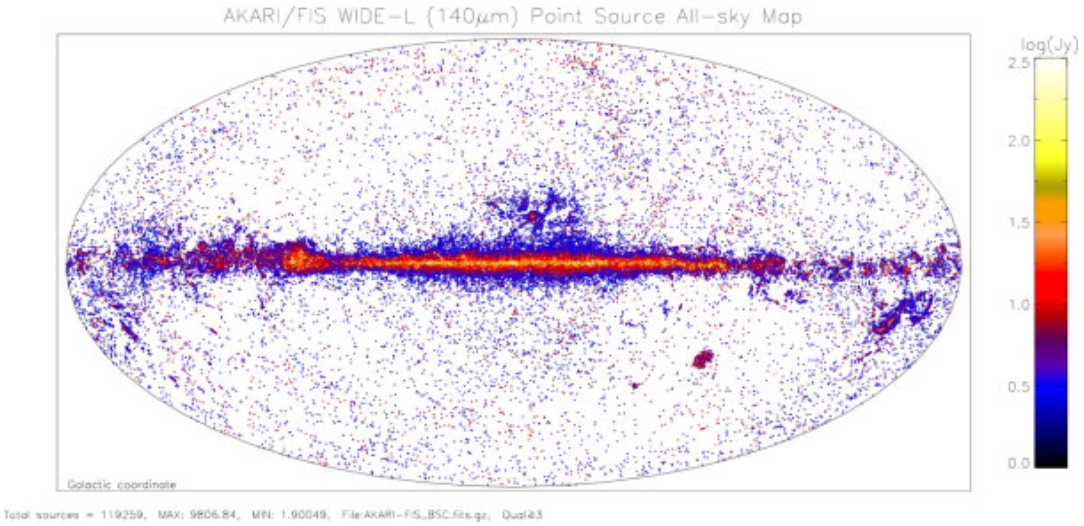

Figure 6.7: Sky distribution of the detected sources in WIDE-L band (Yamamura et al. 2010).

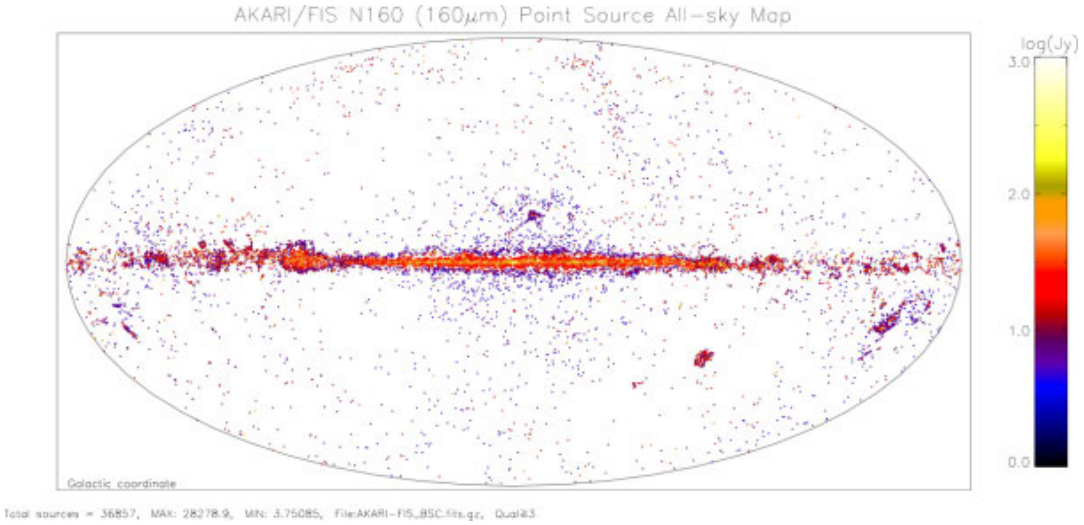

Figure 6.8: Sky distribution of the detected sources in N160 band (Yamamura et al. 2010).

The Infrared Camera (IRC, Kataza et al. 2010**)** is the second focal plane instrument. The all-sky survey has benne done by the MIR-S channel and MIR-L channel. Photometric bands used for the all-sky survey are S9W (6.7 – 11.6 µm; MIR-S) with the effective wavelength at 9 µm and L18W (13.9 – 25.6 µm; MIR-L) with the effective wavelength at 18 µm.

The AKARI/IRC Point Source Catalogue Version 1.0 contains 870,973 sources (844,649 sources in 9 µm band and 194,551 sources in 18 µm band).

6.4 WISE

The Wide-field InfraRed Survey Explorer (WISE, Wright et al. 2010) operates with a 40 cm diameter telescope, including six mirrors before the scan mirror and six mirrors in the camera after the scan mirror. The cryostat uses solid hydrogen to cool the telescope to less than 12.5 K and, and the Si:As detector arrays to less than 7.5 K. WISE was launched on 2009 December 14 and began surveying the sky on 2010 Januar 14. The tanks ran out of hydrogen on 2010 September 29. Until this point WISE was mapping the whole sky since its launch in four bands centered at 3.4, 4.6, 12 and 22 μm. In unconfused regions WISE is achieving 5σ point source sensitivities better than 0.08, 0.11, 1 and 6 mJy with angular resolution 6.1, 6.4, 6.5 and 12.0 arcseconds, respectively. The astrometric precision is better than 0.15 arcseconds for the sources with a high signal-to-noise ratio. The WISE All-Sky Source Catalog (Cutri et al. 2012) lists 563.921.584 sources.

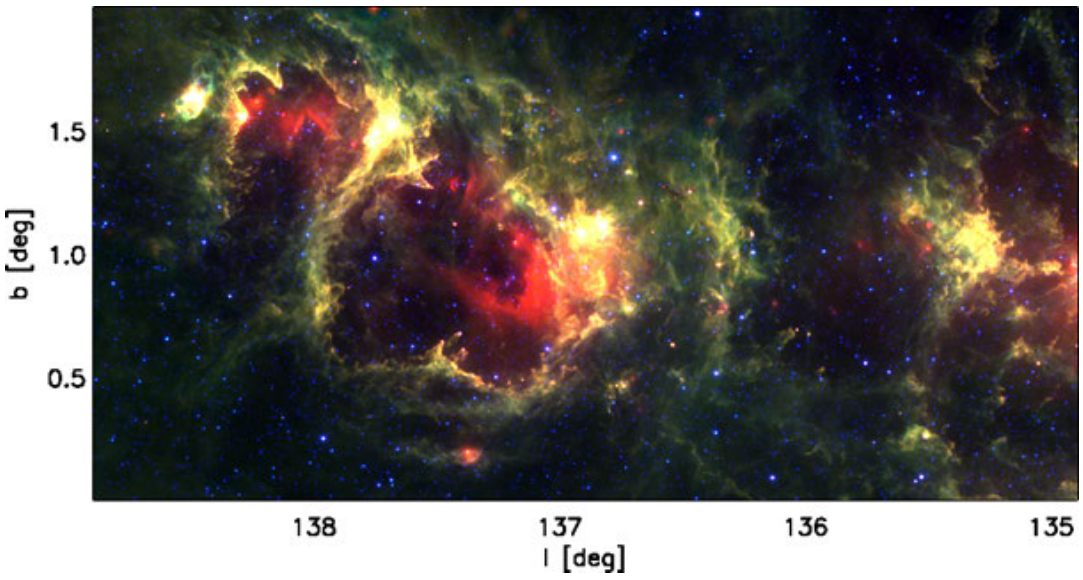

Figure 6.9: *W5 an ionized HII region near the galactic plane. It is an open cluster of young stars surrounded by interstellar dust and gas, located about 2kpc away from the Sun. Stellar winds and UV radiation are responsible for the bubble-like structure and possibly initiated the birth of young stars in the dust shell. The WISE (Wide-field Infrared Surveyor Explorer, Wright et al. 2010) observations at 4.6, 12 and 22 micron were downloaded from the SkyView (http://skyview.gsfc.nasa.gov/) and were used to create the false-color RGB image.*

6.5 Planck

Planck is a European Space Agency (ESA) mission with significant NASA involvement in hardware and science, managed by the Jet Propulsion Laboratory, California Institute of Technology. Planck data products are provided by the Planck Consortium. It was the third generation of space-based cosmic microwave background experiments, after NASA's Cosmic Background Explorer (COBE) and NASA's Wilkinson Microwave Anisotropy Probe (WMAP).

The Planck satellite was launched on 14 May 2009. It was sensitive to a range of frequencies between ~25 and ~1000 GHz and scanned the sky simultaneously and continuously with an angular resolution varying between ~ 30 arcmin at the lowest frequencies and ~ 5 arcmin at the highest. The detectors were arranged into two instruments: the detectors of the Low Frequency Instrument (LFI), covering three bands centred at 30, 44, and 70 GHz; and the detectors of the High Frequency Instrument (HFI), covering six bands centred at 100, 143, 217, 353, 545 and 857 GHz. See the observed all sky maps on Figure 6.10.

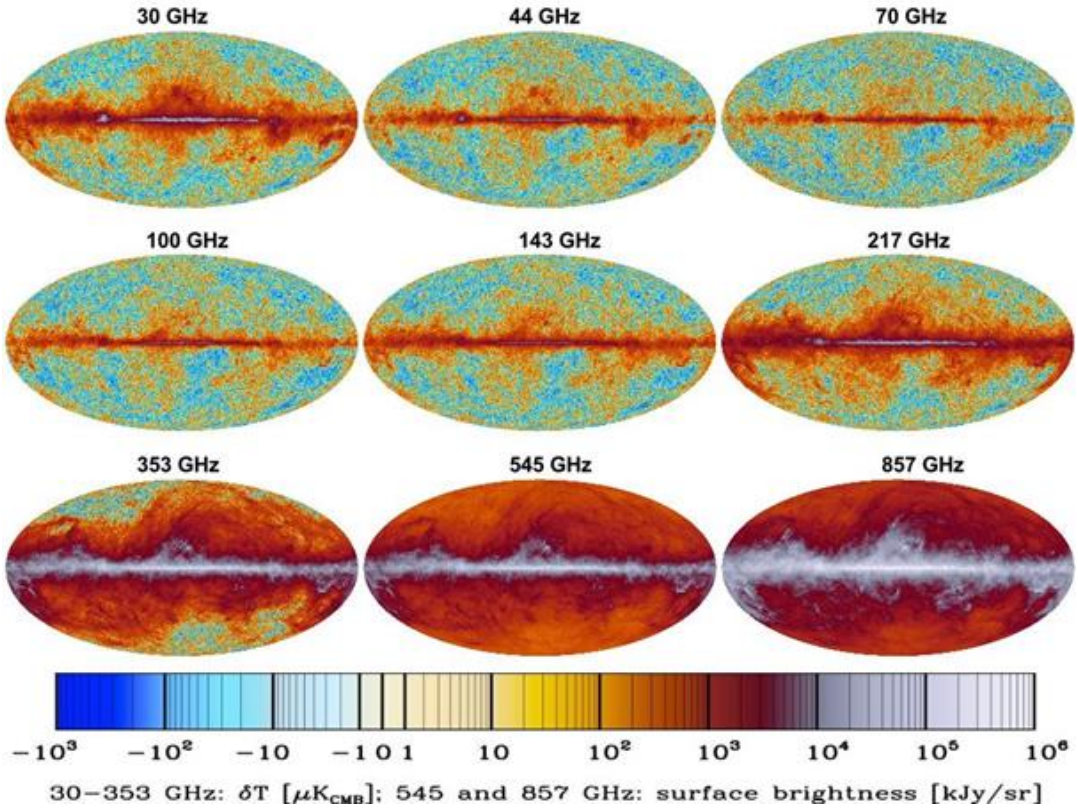

Figure 6.10: *Planck maps at each of the 9 frequencies (http://www.deepspace.ucsb.edu/planck-2013-cosmology-release-march-21/planck3x3)*

The main objective of Planck was to measure the spatial anisotropies of the temperature of the cosmic microwave background (CMB), with an accuracy set by fundamental astrophysical limits. Its level of performance enabled Planck to extract essentially all the information in the CMB temperature anisotropies, see Figure 6.11 and 6.12.

Planck also measured to high accuracy the polarisation of the CMB anisotropies, which encodes not only a wealth of cosmological information, but also provides a unique probe of the thermal history of the Universe during the

time when the first stars and galaxies formed. In addition, the Planck sky surveys produced a wealth of information on the properties of extragalactic sources and on the dust and gas in our own Galaxy.

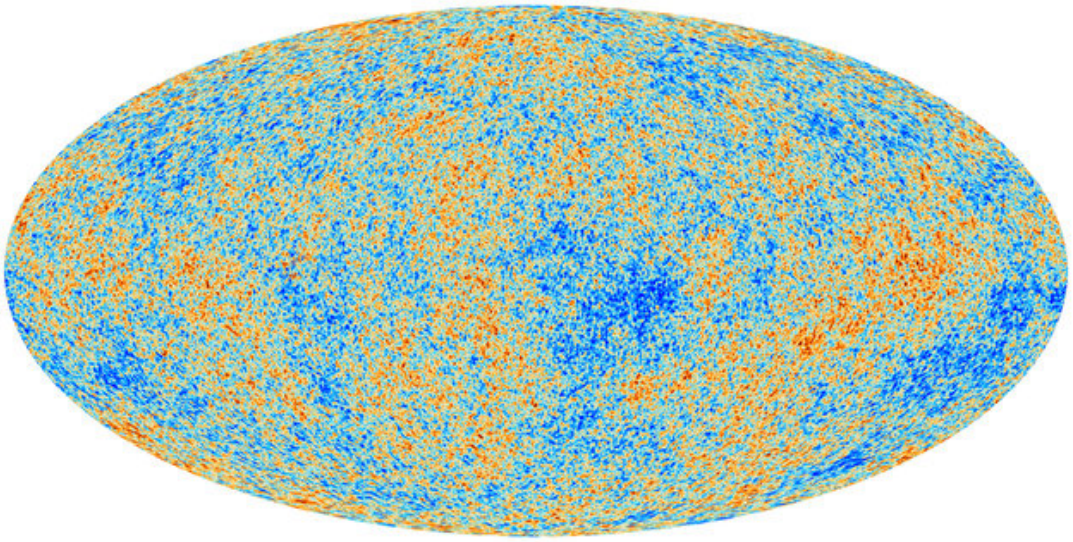

Figure 6.11: *The cosmic microwave background as seen by Planck. (http://www.ctc.cam.ac.uk/news/130322_news-item.php)*

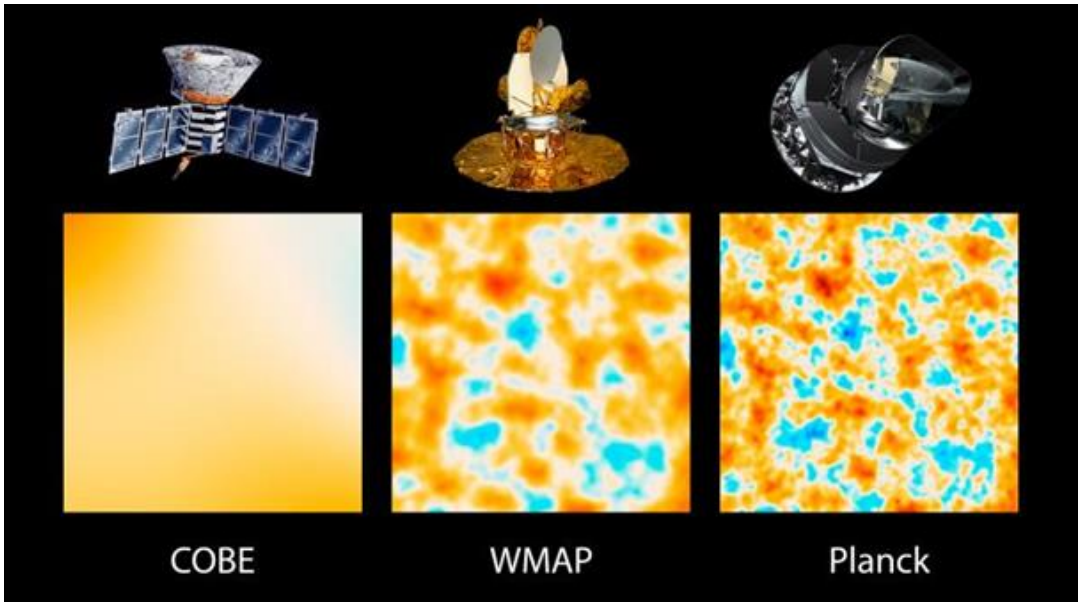

Figure 6.12: *10-square-degree patches of all-sky maps created by COBE, WMAP and Planck (Image Credit: NASA/JPL-Caltech/ESA, http://photojournal.jpl.nasa.gov/jpegMod/PIA16874_modest.jpg).*

The Early Release Compact Source Catalogue (see Figure 6.13) is a catalogue of all high-reliability sources, both Galactic and extragalactic, detected over the entire sky, in the first *Planck* all-sky survey. This includes a sample of clusters detected through the Sunyaev-Zeldovich effect and a catalogue of cold, molecular cloud cores with far-infrared colour temperatures cooler than the ambient $T \sim 18$ K dust in our Galaxy.

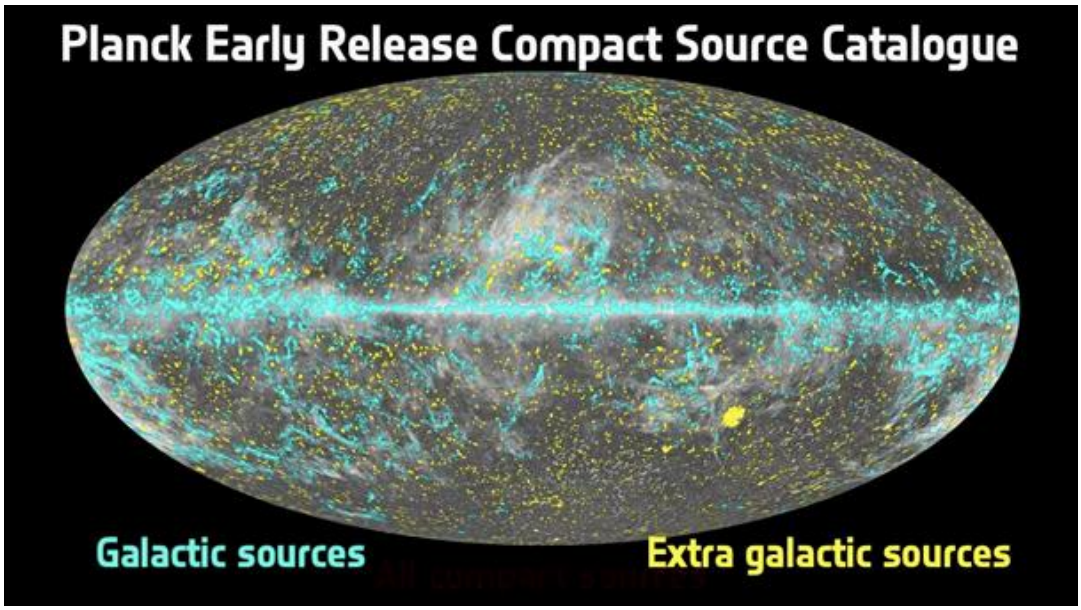

Figure 6.13: *Spatial distribution of galactic and extragalactic sources from the Planck Early Release Compact Source Catalogue (http://irfu.cea.fr/Images/astImg/3030_1.jpg).*

References and further reading to the chapter:

Beichman, C. A. et al. 1984, *"The formation of solar type stars - IRAS observations of the dark cloud Barnard 5"*, ApJ, 278, 45

Cohen, M., Walker, R. G., Carter, B., Hammersley, P., Kidger, M., Noguchi, K., 1999: *"Spectral Irradiance Calibration in the Infrared. X. A Self-Consistent Radiometric All-Sky Network of Absolutely Calibrated Stellar Spectra"*, AJ, 117, 1864

Cohen, M., Megeath, S. T., Hammersley, P. L., Martin-Luis, F. & Stauffer, J., 2003a: *"Spectral Irradiance Calibration in the Infrared. XIII. ``Supertemplates'' and On-Orbit Calibrators for the SIRTF Infrared Array Camera"*, AJ, 125, 2645

Cohen, M., Wheaton, W. A., Megeath, S. T., 2003b: *"Spectral Irradiance Calibration in the Infrared. XIV. The Absolute Calibration of 2MASS"*, AJ, 126, 1090

Cutri R. M. et al., 2012: *"WISE All-Sky Data Release"*, NASA/IPAC Infrared Science Archive , 2012yCat,2311,0C

Hauser, M. G. et al. 1998: *"The COBE Diffuse Infrared Background Experiment Search for the Cosmic Infrared Background. I. Limits and Detections"*, ApJ, 508, 25

Kataza, H. et al., 2010: **"***AKARI/IRC All-Sky Survey Point Source Catalogue Version 1.0- Release Note (Rev.1)"*

Kawada, M., Baba, H., Barthel, P.D., et al., 2007: *"The Far-Infrared Surveyor (FIS) for AKARI"*, PASJ, 59, S389

Kim, H.-J. et al. 2012: *„Star Formation in the Long Filamentary Infrared Dark Cloud at l ~ 53°.2"*, Proceedings of the International Astronomical Union, Symposium 292, Volume 8, pp 46

Kim, H.-J. et al. 2013: *„Star Formation Activity in the Long Filamentary Infrared Dark Cloud IRDC G53.2"*, poster at Protostars and Planets VI, Heidelberg, July 15-20, 2013, http://www.mpia-hd.mpg.de/homes/ppvi/posters/1S015.pdf

Müller, T. G., & Legerros, J. S. V., 1998: *"Asteroids as far-infrared photometric standards for ISOPHOT"*, A&A, 338, 340

Müller, T. G.; Lagerros, J. S. V., 2002: *"Asteroids as calibration standards in the thermal infrared for space observatories"*, A&A, 381, 324

Murakami, H., Baba, H., Barthel, P. et al., 2007: *"The Infrared Astronomical Mission AKARI"*, PASJ, 59, S369

Nakagawa, T. et al. 2007: *"Flight Performance of the AKARI Cryogenic System"* PASJ, 59, 377

Neugebauer, G. et al. "*Early Results from the Infrared Astronomical Satellite"*, (http://www.sciencemag.org/content/224/4644/14.long)

Planck Collaboration, 2011: *"Planck early results. I. The Planck mission"*, A&A, 536, A1

Schlegel, D. J., Finkbeiner, D.P., & Davis, M., 1998: *"Maps of Dust Infrared Emission for Use in Estimation of Reddening and Cosmic Microwave Background Radiation Foregrounds"*, ApJ, 500, 525

Schulz, B., et al. 2002: *"ISOPHOT - Photometric calibration of point sources"*, A&A, 381, 1110

Simon, R., et al., 2006: *"A Catalog of Midcourse Space Experiment Infrared Dark Cloud Candidates"*,ApJ, 639, 227

Wright, E.L., Eisenhardt, P.R.M., Mainzer, A.K. et al., 2010: *"The Wide-field Infrared Survey Explorer (WISE): Mission Description and Initial On-orbit Performance"*, AJ, 140, 1868

Yamamura, I., Makiuti, S., Ikeda, N. et al., 2010, *"AKARI/FIS All-Sky Survey Point Source Catalogues"*, 2010yCat,2298,0Y

http://astron.berkeley.edu/davis/dust/index.html

http://irsa.ipac.caltech.edu/Missions/msx.html

http://lambda.gsfc.nasa.gov/product/cobe/

Chapter 7. Infrared satellite observatories

In this chapter we give an overview of the observing strategy, scientific instruments and main scientific result of Infrared Space Observatory, Spitzer Space Telescope and Herschel Space observatory.

7.1 Infrared Space Observatory (ISO)

ISO observed the infrared sky between February 1996 and April 1998. It was a European Space Agency (ESA) mission, launched in November 1995. The satellite weighed around 2500 kg and was launched with over 2000 litre of liquid helium coolant on board, which lasted for 29 months.

ISO was the first orbiting infrared observatory. It made during its lifetime more than 30 000 individual observations of all kind of astronomical objects: in the solar system and in the most distant galaxies.

The telescope operated between 2.5 and 240 μm. Comparing to IRAS, at 12 μm it was one thousand times more sensitive and had one hundred times better angular resolution.

Figure 7.1 shows ISO's two largely independent modules: the Payload Module and the Service Module. The Payload Module was a large cryostat containing super fluid helium which maintained the telescope and the scientific instruments at temperatures between 2 and 8 K. The Service Module contained the warm electronics of the scientific instruments and all the classical spacecraft subsystems, which are necessary to supply the basic functions. The sun-shield with solar cells always faced the Sun to provide electrical power and to protect the Payload Module from direct irradiation.

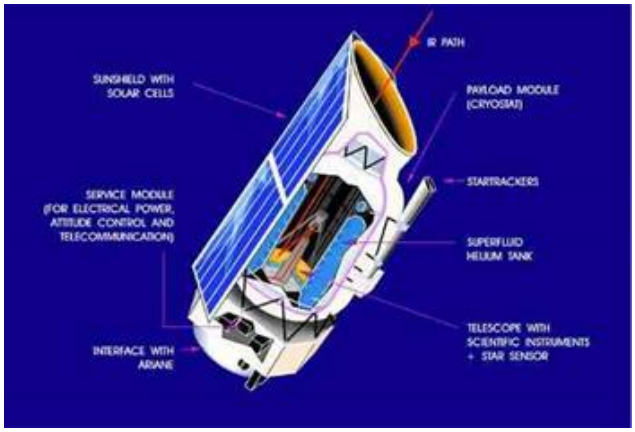

Figure 7.1: Schematic view of the ISO satellite, two largely independent modules are visible: the Payload Module and the Service Module http://vietsciences.free.fr/giaokhoa/vatly/thienvan/gsnguyenquangrieu/images/iso_satellite.jpg

The ISO telescope was a 60 cm diameter Richey-Chrétien system with an overall focal ratio of f/15. This type of telescope is free from coma and spherical aberration, and they have larger field of view than the classical Cassegrain type telscopes. The optical quality of the primary and secondary mirrors provided diffraction limited performance at wavelengths beyond 5 μm, also limited by pointing performance.

ISO had a high Earth orbit with a period of one-to-two days. It was accustomed by previous space observatories.

7.1.1 Scientific instruments and observing strategy

ISO's four scientific instruments are the following: a camera, ISOCAM, an imaging photo-polarimeter, ISOPHOT, and the two spectrometers, a long wavelength LWS and a short wavelength SWS.

The telescope and the scientific instruments operated at ~3K. Some of the infrared detectors were cooled down to 1.8 K. This low temperature enabled observations to made at high sensitivities. Only one instrument was operational in prime mode at a time, but the camera was used in parallel mode to acquire extra astronomical data whenever it was possible. The long-wavelength channel of the photometer was used during satellite slews, this produced a partial sky survey, which covers ~15 % of the sky, at wavelengths around 200 µm. After launch, a parallel/serendipity mode was added for the LWS, in which narrow-band data were obtained at 10 fixed wavelengths in parallel with the main instrument and also during slews.

New generations of space and air-borne integral field spectrometers required large format arrays of low noise equivalent power (NEP) detectors. NEP is the radiant power that produces a signal-to-noise ratio of unity at the output of a given detector at a given data-signaling rate or modulation frequency, operating wavelength, and effective noise bandwidth. In the FIR, photoconductors still offer the higher sensitivity under low background conditions in combination with moderately low operation temperatures (1.7 K to 4 K) when compared to bolometers. In the 40 to 200 µm range, Gallium-doped germanium (Ge:Ga) photoconductors are commonly used because of their high sensitivity. Ge:Ga photoconductors which are mechanically stressed are used to cover the wavelength range from 115 to 210 µm. Unstressed Ge:Ga detectors are used to cover the wavelength range from 40 to 115 µm.

The ISO Camera instrument consisted of two optical channels, used one at a time, each with a 32 x 32 element detector array, operated in the wavelength ranges 2.5-5.5µm and 4-17µm.

The ISOPHOT instrument consisted of three subsystems: ISOPHOT-C, ISOPHOT-P and ISOPHOT-S:

ISOPHOT-C consists of two photometric far-infrared cameras, used one at a time, for the wavelength range 50-240µm. The `C100' camera contained a 3x3 array of Ge:Ga detectors, each with a pixel field of view of 43.5", and 6 filters covering wavelengths up to 105µm. The `C200' camera used a 2x2 array of stressed Ge:Ga detectors with a pixel field of view of 89" and had 5 filters covering wavelengths longwards of 100µm.

ISOPHOT-P was a multi-band, multi-aperture photo-polarimeter for the wavelength range 3-110µm. It contained 13 apertures ranging in size from 5" to 180" and 14 different filters. ISOPHOT-S was a dual grating spectrophotometer which provided a resolving power of ~90 in two wavelength bands simultaneously (2.5-5µm and 6-12µm).

The ISO Long Wavelength Spectrometer covered the wavelength range 43-196.7µm with a spectral resolving power of ~200. Using also the Fabry-Pérot (FP) etalons, the resolution could be increased to around 10,000.

The ISO Short Wavelengths Spectrometer covered the wavelength range 2.38-45.2µm with a spectral resolving power of the order of 1000-2500. Using also the Fabry-Pérot (FP) etalons, the resolution could be increased to more than 25 000 for the wavelength range 11.4-44.5µm.

ISO was operated in a pre-planned manner without any significant routine real-time interaction. ~45% of the observing time was reserved for guaranteed time programmes. But as an observatory, ESO was open to the astronomical community including expert and non-expert users.

Each of the four instruments had a number of possible operating modes. To simplify the definition of an observation and to allow users to specify their observation in terms familiar to them, a set of astronomically-useful operating modes was defined and presented to users as a set of `Astronomical Observation Templates' (AOTs). Each AOT was designed to carry out a specific type of astronomical observation.

~65% of ISO's observing time was distributed to the general community via the traditional method of proposals and peer review. The scientific programme for ISO consisted of more than 1 000 individual proposals.. About 10% of ISO's time was used for Solar System studies, 23% for the Interstellar Medium (ISM), 29% on Stellar/Circumstellar topics, 27% for Extragalactic observations and 11% for Cosmology.

7.1.2 Most important results

ISO has delivered important results in nearly all fields of astronomical research. Nearly 1400 papers have been published in the refereed literature on ISO results. A few example from ISO's most important scientific results:

- the discovery of crystalline silicates outside our own solar system, in the atmospheres of young and old stars and also in comet Hale-Bopp. Figure 7.2 show the ISOCAM image of Hale-Bopp comet at 15 μm. This discovery shows that water is ubiquitous in the cosmos.

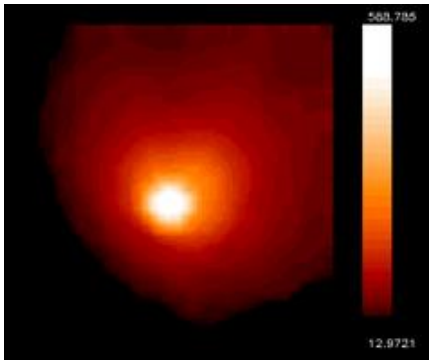

Figure 7.2: ISOCAM image of comet Hale-Bopp at 15 μm (http://iso.esac.esa.int/galleries/sso/halebopp.html, Credit: ESA/ISO, ISOCAM, R. Walsh, B. Altieri, P. Lamy)

- a wealth of water vapour transitions were measured e.g. in Mars, Titan, the giant planets, comets including Hale-Bopp, in shocks, in the cold interstellar medium, in circumstellar envelopes and in the ultra-luminous galaxy Arp220. The spectral resolution of most water observations was limited, but the possibility to observe the full mid- and far-infrared spectrum has opened great possibilities.

- the first detections of the lowest pure rotational lines of H_2 in young massive stars, HH-objects, the diffuse ISM, outer parts of edge-on galaxies. . Temperatures less than a few hundred K could be investigated.

- observing pre-main sequence stars with SWS and LWS spectrographs. These data were used for line detections and to reconstruct the spectral energy distributions. Figure 7.3 shows the spectral energy distribution of 2 Herbig Ae/Be stars. Very different SEDs were observed for Herbig Ar/Be stars, confirming the fact that these objects do not constitute a homogeneous class.

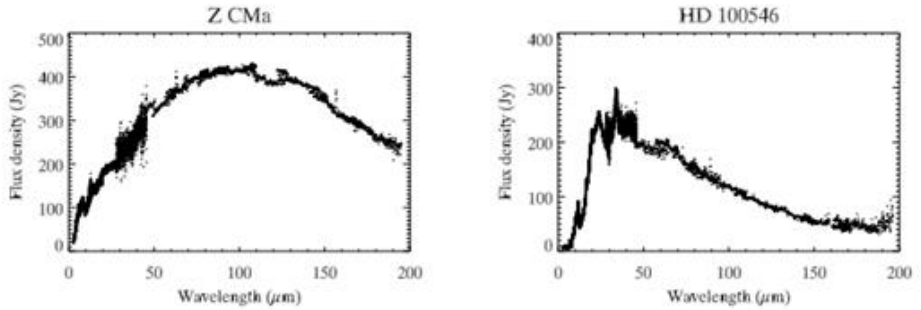

Figure 7.3: *ISO spectra of two Herbig Ae/Be stars (Lorenzetti 2004).*

- detecting planet formation around old, dying stars. E.g. in the vicinity of the Red Rectangle old binary star in the Monoceros constellation, a ring of matter constituting the first stage of planet formation was detected. This discovery contradicted theories that planet formation was only possible around young stars. Figure 7.4 shows two images in red light and the ISO LWS spectrum of the Red Rectangle. The left image was taken by H. van Winckel (Leuven) using the 90 cm Dutch telescope at the European Southern Observatory, La Silla, Chile. The right hand image was taken by G. Weigelt and R. Osterbart (Bonn) using the 2.2m Max Planck telescope, also at E.S.O.. A prominent dark lane is visible across the image, which is due to the disk surrounding the binary system. The tick marks on the spectrum indicate the position of the oxygen-rich olivine bands, suggesting that the disk contains oxygen-rich material. This disk may be the site of on-going planet formation.

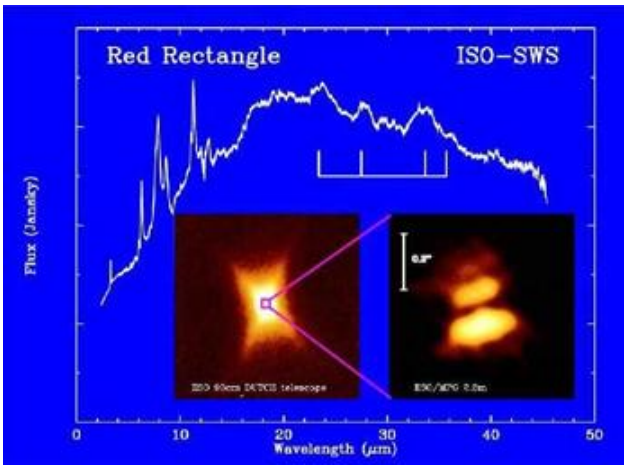

Figure 7.4: *Two images in red light and ISO LWS spectrum of Red Rectangle.(http://coolcosmos.ipac.caltech.edu/image_galleries/ISO/sws/redrec.html)*

- ISO searched for, and found several protoplanetary disks: rings or disks of material around stars which are considered to be the first stage of planet formation.
- the detailed investigations of interstellar solid state features, e.g. CO_2 ices. It gives the possibility to have detailed interplay between observations and laboratory spectroscopy
- obtaining spectral energy distributions of extragalactic objects, which serve as templates for cosmological studies, helped to consolidate the unified scheme or to develop quasar evolutionary scenarios. ISOPHOT SED of NGC6240 are seen on Figure 7.5.

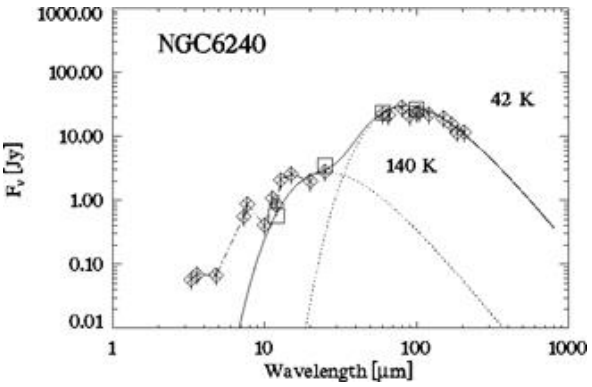

Figure 7.5: ISOPHOT spectral energy distribution of NGC6240. The SED is well fitted with two components: a 140 K and a 42 K blackbody radiation. (http://iso.esac.esa.int/galleries/nor/ngc6240c.htm, Credit: EAS/ISO, ISOPHOT, U. Klaas)

- making deep cosmological surveys at near- and far-infrared wavelengths. It resolved the part of the cosmic infrared background (CIB) into discrete sources and detected fluctuations in the CIB.
- making the European Large Area ISO Survey to explore obscured galaxies and quantify the recent star-formation history of the Universe. This survey discovered 9 hyper luminous galaxies.

7.2 Spitzer Space Telescope

NASA's Spitzer Space Telescope (formerly the Shuttle Infrared Telescope Facility, SIRTF) was launched in August 2003 with a 0.85 m mirror. The first scientific observations were performed in December 2003, it operated at wavelengths from 3.6 to 160 μm. Figure 7.6 shows the schematic view of the Spitzer Space Telescope (SST).

The telescope and science instruments were cooled to their ultimate operating temperatures by liquid helium cryogen, which itself achieves a temperature of about 1.2 K. In case of ISO the telescope was inside the cryostat. Spitzer employs a novel design in which only the science instrument cold assemblies and the super-fluid helium vessel were cold within the vacuum cryostat shell. ~350 litres of helium were loaded into the Spitzer cryogen tank prior to launch, and it run out in May 2009. It was the end of the primary Spitzer mission. July 2009 was the start of warm mission, which is currently approved through the end of September 2014.

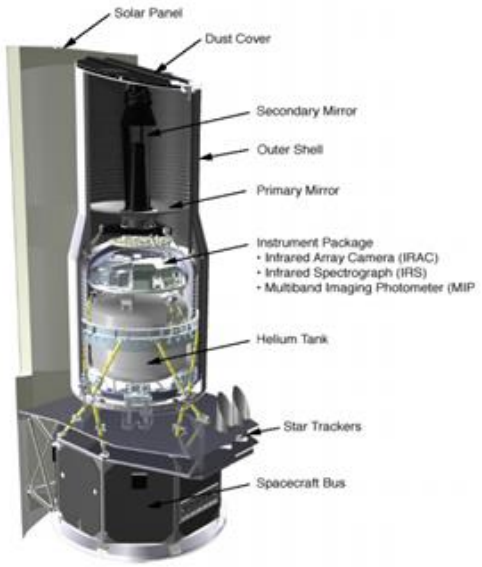

Figure 7.6: Schematic view of Spitzer Space Telescope (http://irsa.ipac.caltech.edu/data/SPITZER/docs/spitzermission/missionoverview/spitzertelescopehandbook/Spitzer_Telescope_Handbook.pdf)

Spitzer uses an Earth-trailing heliocentric orbit with semi-major axis very slightly larger than that of the Earth's orbit. As seen from Earth, Spitzer recedes at about 0.1 AU per year. The following advantages have this orbit: the observatory is getting away from the heat of the Earth; the orbit allows radiative cooling; there are no eclipses, the Earth and Moon are far away, the orbit permits excellent sky viewing and observing efficiency. It has one major disadvantage: with the increasing of the distance, the radio signals become weaker.

Most of the observing time on Spitzer during the cryogenic mission and all the time during the warm mission was awarded to the international astronomical community through the usual peer-review process. Guaranteed Time was awarded to the PIs on behalf of their instrument teams. Legacy Science Program was pioneered by Spitzer.

It was motivated by a desire to enable large observing programs early during Spitzer's prime mission, with the goal of creating a substantial database of archived observations. These programs are large and coherent science projects, which are of general and lasting importance to the broad community. All raw and pipeline-processed data enter the public domain immediately upon Spitzer Science Center verification. The first six Legacy projects were awarded a total of 3160 hours of Spitzer time. These programs were largely completed during the first year of the mission, and additional Legacy programs were selected and carried out annually until the completion of the cryogenic mission. During the Warm Mission ~10,000 hours of observing time were awarded to 10 large programs.

7.2.1 Scientific instruments

SST has three scientific instruments: the InfraRed Array Camera (IRAC), the InfraRed Spectrograph (IRS) and the Multiband Imaging Photometer for Spitzer (MIPS).

IRAC provides images at 3.6, 4.5, 5.8 and 8.0 μm, with two adjacent 5.2' x 5.2' fields of view. One field of view images simultaneously at 3.6 and 5.8 μm and the other at 4.5 and 8.0 μm. All four detector arrays are 256 x 256 pixels with 1.2 arcsecond square pixels.

IRS performs both low and high-resolution spectroscopy. Low-resolution, long slit spectra (= 64–128) can be obtained from 5.2 to 38.0 μm. High-resolution spectra (~600) in Echelle mode can be obtained from 9.9 to 37.2 μm.

MIPS is designed to provide photometry and super resolution imaging, as well as efficient mapping capabilities, in three wavelength bands centered near 24, 70 and 160 μm. MIPS is also capable of low-resolution spectroscopy (~15–25) over the wavelength range 55–95 μm and a Total Power Mode for measuring absolute sky brightness.

7.2.1 Most important scientific results

- identifying molecules in exoplanets' atmosphere. It was a significant step toward being able to detect possible life on rocky exoplanets. Spitzer, obtained spectra for two hot Jupiters: HD 209458b and HD 189733b.
- performing large-area surveys of star-forming regions. It allows us the rapid identification and classification of young stellar objects. The IRAC colours of YSOs can discriminate between objects classified as Class 1, 2 and 3. Figure 7.7 shows the color-color diagram of YSOs in N65 region. Different colors indicate the different evolutionary classes.

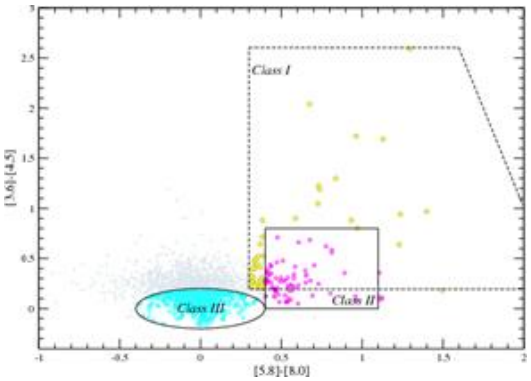

Figure 7.7: Spitzer [3.6]-[4.5] vs. [5.8]-[8.0] colour-colour diagram for classification of young stellar objects in the environment of N65 infrared dust bubble (Petrielle, Paron & Giacani, 2010, A&A, 513, A44). The location of Class I, II and III objects are slightly overlapping.

- Spitzer studies the process of planetary system formation by tracing the dissolution of the circumstellar discs around Class 2 objects. Spitzer observations suggest that the warm dust disappears within a few million years. Some discs, show dramatic evidence for central clearing possibly attributable to planet formation. These proto-planetary disks with AU-scale inner clearings, often referred to as transitional disks, provide a unique sample for understanding disk dissipation mechanisms and possible connections to planet formation.
- Spitzer observations gave evidence for grain and structure evolution in discs around young brown dwarfs similar to that thought to signal the first steps toward planet formation around young stars
- Spitzer's wide wavelength coverage, 3.6–160μm, samples radiation from a range of different constituents of a galaxy, from stellar atmospheres to cold dust in quiescent interstellar clouds. It allows Spitzer to provide striking images and new insights into the distribution of stars, interstellar matter and star formation throughout a nearby galaxy, see e.g. Figure 7.8.

Figure 7.8: Infrared (Spitzer Space Tescope, red) and visible (Hubble Space Tescope, blue-green) combined image of the two merging galaxies: NGC2207 and IC2163. (http://www.jpl.nasa.gov/spaceimages/details.php?id=PIA08097). The infrared data from Spitzer highlight the galaxies' dusty regions, while the visible data from Hubble indicates starlight.

- detection of galaxies at ~z=6. Infrared radiation provides a natural probe of the distant and early universe. With the expansion of the universe, the optical, UV light rom distant galaxies shift into the infrared.
- investigating the atmosphere of brown dwarfs using NASA’s Spitzer and Hubble telescopes, creating the most detailed weather map for these cold, star-like objects
- one of the most precise measurements of the Hubble constant. Spitzer observed 10 cepheids in our own Milky Way galaxy and 80 in the Large Magellanic Cloud. In the infrared bands Spitzer was able to obtain more precise measurements of the stars' apparent brightness, and thus their distances.
- identifying the most distant galaxy cluster, COSMOS-AzTEC3 with NASA's Spitzer, Chandra and Hubble space telescopes, and the ground-based W.M. Keck Observatory and Japan's Subaru Telescope.
- detailed investigation of the spiral structure of our the Milky Way. It has two major spiral arms: the Scutum-Centaurus and Perseus arms. They have the greatest densities of both young, bright stars, and older, so-called red-giant stars. The two minor arms, Sagittarius and Norma, are filled with gas and pockets of young stars. The two major arms seem to connect up nicely with the near and far ends of the galaxy's central bar. Figure 7.9 shows the new view of the Milky Way. The minor arm are located between the major arms. It also includes a new spiral arm, called the "Far-3 kiloparsec arm," discovered via a radio-telescope survey of gas in the Milky Way.

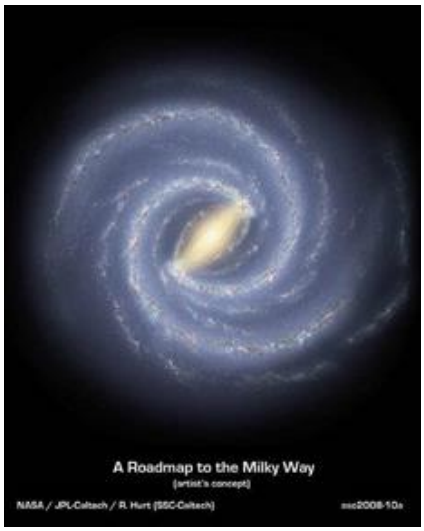

Figure 7.9: *Artist's view of the Milky Way with the 2 major and 2 minor spiral arms.*

7.3 Herschel Space Observatory

ESA's Herschel Space Observatory (formerly FIRST, Far InfraRed Submillimetre Telescope) was launched together with Planck cosmic microwave background mission in May 2009. They separated within 30 minutes after launch and proceeded independently to different orbits about the second Lagrange point of the Sun-Earth system. Herschel ran out of helium in April 2013.

It was the largest space telescope ever launched with a 3.5 m Cassegrain telescope. It has high sensitivity and a spatial resolution a factor of 6 better than any previous far-infrared telescope launched into space. Over much of its wavelength range Herschel is limited in sensitivity mainly by the confusion from the background of faint, unresolved sources.

Figure 7.10 shows the schematic view of Herschel Space Observatory. On the left, we can see the warm side with the sun-shield and on the right, the cold side of the telescope.

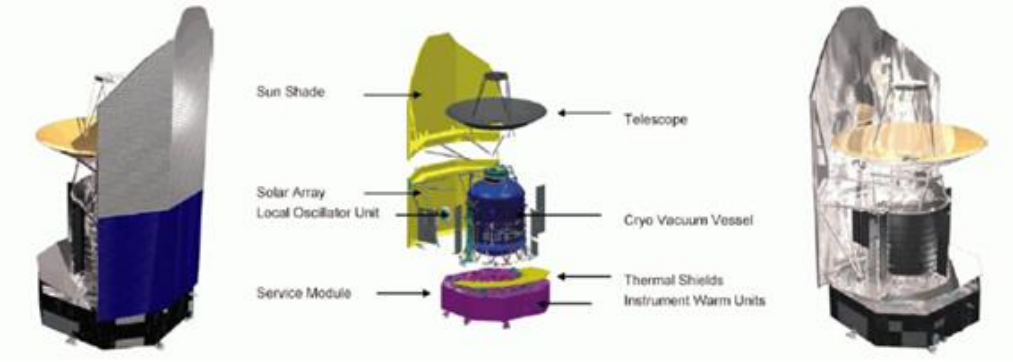

Figure 7.10: Herschel Space Observatory: On the left, facing the "warm" side and on the

right, facing the "cold" side of the spacecraft, the middle image names the major components. (http://herschel.esac.esa.int/Docs/Herschel/html/ch02.html)

7.3.1 Scientific instruments

It covers the wavelength range between 55 and 672 μm, observed the sky with 3 scientific instruments: the Photodetector Array Camera and Spectrometer (PACS), the Spectral and Photometric Imaging Receiver (SPIRE) and

the Heterodyne Instrument for the Far Infrared (HIFI). This wavelength range corresponds to the maximum of emission for black bodies in the range from ~5-50K.

The full wavelength range of Herschel is covered by six broadband filters. In SPIRE, all three filters (250, 350 and 500 μm) are imaged simultaneously on three spiderweb bolometer arrays. PACS users are able to image with a "red" (130-210 μm) and a "blue" (either 60-85 or 85-130 μm) filter simultaneously on two bolometer arrays.

The PACS instrument covered the wavelength range ~60−210μm. It features both, a photometric multi-colour imaging mode, and an imaging spectrometer. Both instrument sections were designed with the goal of maximising the science return of the mission.

The mapping efficiency had high priority, because a large fraction of the Herschel observing time was spent on deep and/or large scale photometric surveys. The PACS photometer was therefore designed around the largest detector arrays available without compromising sensitivity. Simultaneous observation of several bands immediately multiplies observing efficiency. PACS can observe a field in two bands at a time by implementing two camera arrays.

SPIRE consists of a three-band imaging photometer and an imaging Fourier-transform spectrometer. The photometer carries out broad-band photometry ($\lambda/\Delta\lambda \sim 3$) in three spectral bands centred on approximately 250, 350 and 500 μm, and the FTS uses two overlapping bands to cover 194–671 μm.

HIFI is a very high resolution heterodyne spectrometer. It allowed us to produce extremely detailed spectra of atoms and molecules. It observed the complete range of frequencies from 480-1250 GHz, and 1410-1910 GHz. It was optimized for the following projects: observations of the water lines ending in the ground states that are essential for absorption studies of cold water, falling in bands 1 (557 GHz), 4 (1.11 THz), and 6 (1.67 THz); a survey of the molecular complexity of the Universe; and observations of ionized Carbon [CII] at 1.9 THz (band 7).

7.3.2 Most important scientific results

- discovering long, filamentary structures, with dense star-forming knots of material. Figure 7.11 shows the combined Herschel image of the Cygnus X complex. Young stars are observable in the network of filaments, bubbles and pillars.

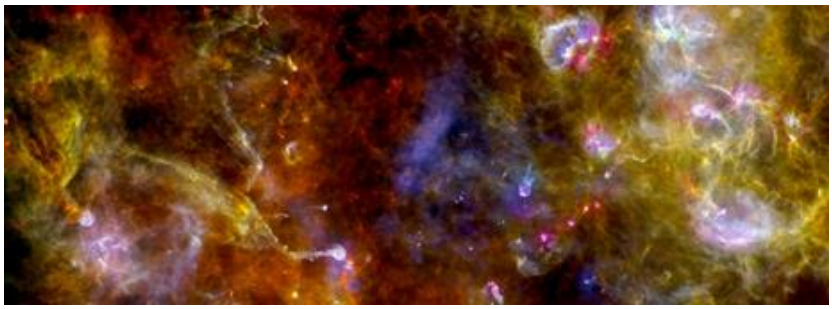

Figure 7.11: Hershel PACS 70 μm (blue), PACS 160 μm (green) and SPIRE 250 μm (red) combined image of the Cygnus X complex. (http://sci.esa.int/science-e/www/object/index.cfm?fobjectid=50336). Rich network of filaments, bubbles, pillars are seen on the combined Herschel image.

- Detecting firstly oxygen molecules in space, and also some other never-before-seen molecules. Figure 7.12 shows the observed oxygen molecular line in the Orion star forming region.

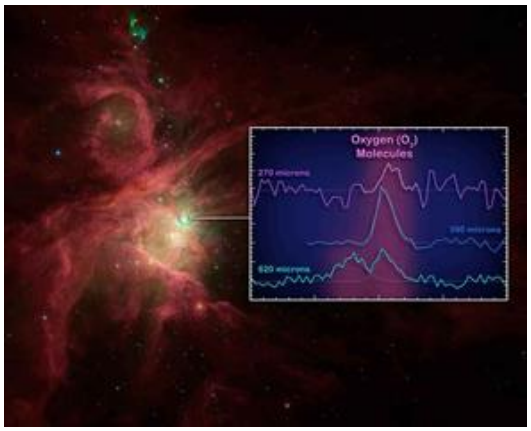

Figure 7.12: Oxygen molecular lines discovered first time with Herscehl in the Orion star-forming complex (http://www.herschel.caltech.edu/index.php?SiteSection=News&NewsItem=nhsc2011-014)

- discovering high-speed outflows around central black holes in active galaxies
- following the trail of water molecules from distant galaxies to the clouds of gas between stars to planet-forming solar systems.
- Examining a comet in our own solar system and finding evidence comets could have brought a substantial fraction of water to Earth.
- discovering a large asteroid belt around Vega
- discovering gravitational lenses with remarkable efficiency based on the Herschel-ATLAS survey
- discovering of some of the youngest stars ever seen in the nearby Orion, (see on Figure 9.1) and a peculiar planet-forming disk around TW Hydra, indicating planet formation may happen over longer periods of time than expected.
- investigating one of the most massive stars in our galaxy, in Spitzer Dark Cloud 335, seen on Figure 7.13. The cloud of gas and dust was discovered by Spitzer satellite. Herschel images show that the region contained a few very cold, dense clumps and the high resolution ALMA images revealed the enormous mass of the protostellar clumps.

Figure 7.13: *NASA's Spitzer satellite (yellow), Herschel (blue), and ALMA (magenta) view of Spitzer Dark Cloud 335. (Image credit: NASA/Spitzer/JPL-Caltech; ESA/Herschel/Hi-GAL; ESO/NOAO/NOAJ/ALMA)*

- discovering a dusty disc around an aging subgiant star, Kappa Coronae Boeralis. Figure 7.14 shows the PACS 100 μm image of the debris disc orbiting the subgiant Kappa CrB. Kappa CrB is a rare example of an intermediate mass star, where a detailed study of the structure of the planetary system can be made.

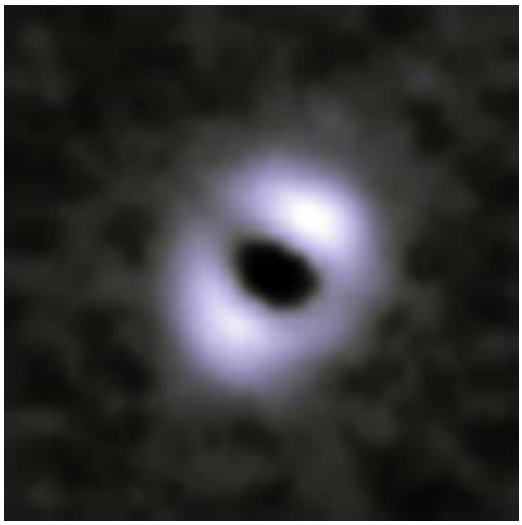

Figure 7.14: *: The debris disc around Kappa CrB, after the extraction of the PSF of the central point source in the Herschel PACS 100 μm image. Credit: ESA/Bonsor et al. (2013)*

Figure 7.15 shows the comparison of images of M51 at 160 μm for ISO, Spitzer and the Herschel telescopes and at 100 μm for IRAS. The improvement of resolution and sensitivity are well observable.

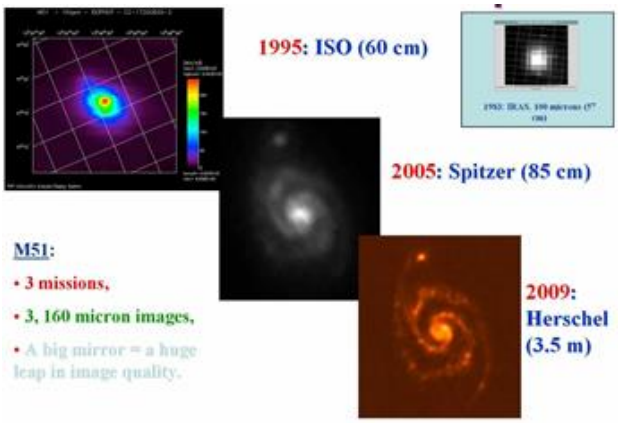

Figure 7.15: ISO, Spitzer, Herschel images at 160

μm and IRAS image at 100 μm of M51 (http://herschel.esac.esa.int/Docs/Herschel/html/ch01.html). A significant improvement of resolution and sensitivity is observable. Spitzer revealed the spiral structure of M51, Herschel were able to observe also the details of the spiral arms.

Figure 7.16: Rho Oph, an optically dark cloud complex in FIR. The complex is composed of cold dust with embedded cluster of young stars. Raw data of 20"/s scan-speed were processed with Scanamorphos (Roussel 2013). Maps were projected with pixel size of 2, 3 and 4 " for the 70, 100 and 160 micron observations, respectively.

Due to the thermal emission the Rho Oph cloud is very bright in the far-infrared regime (see on Figure 7.16). It is the closest star forming region to the Sun with an estimated distance of 131+/-3 pc. Because of the relatively small distance, this cloud is an ideal site for studying the very low-mass star formation, including brown dwarfs with their emission peaking in the far-IR due to their low temperature. RGB colours of the image correspond to the Herschel 70, 100 and 160 micron observations. For the 70 and 100 micron cases the observations of the OT1_pabraham_3 "A deep 70 micrometer study of cold circumstellar disks in rho Oph: down below the brown dwarf limit" (PI.: Péter Ábrahám) were used. 100 micron observations are from the KPGT_pandre_1 "Probing the origin of the stellar initial mass function: A wide-field Herschel photometric survey of nearby star-forming cloud complexes" (PI.: Philippe André).

References and further reading to the chapter:

Lorenzetti, D., 2005: *"Pre-Main Sequence Stars seen by ISO"*, Space Science Reviews, ISO Special Issue, Volume 119, Issue 1-4, pp. 181-199

Gehrz, R. D., Roellig, T. L., Werner, M. W. et al., 2007: *"The NASA Spitzer Space Telescope"*, Review of Scientific Instruments, 78, 011302

Roussel, H., 2013: *"Scanamorphos: A Map-making Software for Herschel and Similar Scanning Bolometer Arrays"*, PASP, 125, 1126

Werner, M. 2006: *"Spitzer: the first 30 months",* Astronomy & Geophysics, 47, 6.11

Herschel Observer's Manual:

http://herschel.esac.esa.int/Docs/Herschel/pdf/observatory.pdf

Herschel PACS Observer's Manual:

http://herschel.esac.esa.int/Docs/PACS/pdf/pacs_om.pdf

Herschel SPIRE Observer's Manual:

http://herschel.esac.esa.int/Docs/SPIRE/pdf/spire_om.pdf

http://herschel.cf.ac.uk/results

ISO Handbook: http://iso.esac.esa.int/manuals/HANDBOOK/gen_hb/

http://home.strw.leidenuniv.nl/~brandl/Spitzer_observatory.pdf

http://iso.esac.esa.int/Mission_overview.html

http://iso.esac.esa.int/science/SSR/

Spitzer Space Telescope Handbook:
http://irsa.ipac.caltech.edu/data/SPITZER/docs/spitzermission/missionoverview/spitzertelescopehandbook/Spitzer_Telescope_Handbook.pdf

http://www.ancient-code.com/herschel-completes-its-cool-journey-in-space/#

Chapter 8. The interstellar medium in infrared

Infrared spectral lines and features are among the most important coolants for the interstellar medium. We may find atomic fine structure lines, molecular emission and dust spectral emission features in nearby galactic clouds as well as in the integrated spectra of distant galaxies.

8.1 The interstellar medium

The interstellar medium (ISM), is divided into regions characterized by the state of the hydrogen. Ionized atomic hydrogen is the main constituent of HII regions and in coronal gas, neutral atomic hydrogen in HI clouds and H_2 in molecular clouds, the filling factor of transient regions is small.

Coronal gas (resembling to the solar corona) has very high kinetic temperatures of 10^6 K < T_{kin} <10^7 K and very low densities n ≤ 10^{-3} cm^{-3}. This gas is heated by collisions in shock waves induced by supernova explosions and also called as hot ionized medium (HIM). The nearest example is the interior of the so called Local Bubble. The majority of nearby HIM is located in supernova remnants in the Galactic disk and at the Disk-Halo boundary, and mostly detected by its diffuse X-ray emission and by highly ionized metal lines in the spectra of Halo stars. We note that similar hot gas can be found in intra-cluster space in galaxy clusters.

Diffuse and compact HII regions are found around early-type stars, with temperature and density of T_{kin}=10^4 K and 0.1 cm^{-3}< n <10^4 cm^{-3} respectively. This is the radiatively heated ISM, and also called as warm ionized medium (WIM). WIM appears as compact or extended spots in UV and optical images with a red color in the latter due to excitations by recombination and a strong Hα line emission as a result of that.

Neutral atomic hydrogen dominated clouds may also be partly ionized and warm with kinetic temperature and density of T_{kin}=6000 K and 0.05 cm^{-3}< n <0.2 cm^{-3}. This is the so called warm neutral medium WNM. The nearest examples of WNM are the few pc size cloudlets in the local interstellar medium (LISM) including the Local Interstellar Cloud (LIC) into which the Solar System is embedded. WNM is traced by its absorption lines.

Cold neutral atomic hydrogen clouds usually referred to as HI clouds with temperature and density of T_{kin}=80 K and n = 1 cm^{-3}. Their size varies from sub-parsec to more than 100pc.

Diffuse molecular clouds are somewhat cooler than HI clouds with 17 K < T_{kin} <80 K and their densities n ≥ 100 cm^{-3} allow higher fraction of hydrogen to be present in molecular than in atomic or ionized form. The largest ones (d~40pc) are quite massive (M > $10^5 M_O$) and called as Giant Molecular Clouds (GMCs), the smallest are of about parsec size. Usually we do not consider the tiny (d<<0.1pc) temporary density enhancements as molecular clouds, although those may also turn to molecular for about 100 years inside an HI cloud.

Dense molecular cloud cores are the sites of star formation. They are either very cold T_{kin} ≤ 10 K, or warm T_{kin} ≥ 100K, the latter type is internally heated by an embedded young massive star and also called as “hot molecular core”. The densities are high 10^3 cm^{-3}< n <10^7 cm^{-3}.

Molecular clouds and cores are dusty and dim the background light when they are nearby, mostly via scattering, but also absorbing. Such nearby dusty clouds are called as dark clouds referring to their optical appearance. Figure 8.1 shows the prototypical dark cloud Barnard 68, where the background stars shine through the otherwise opaque cloud in NIR.

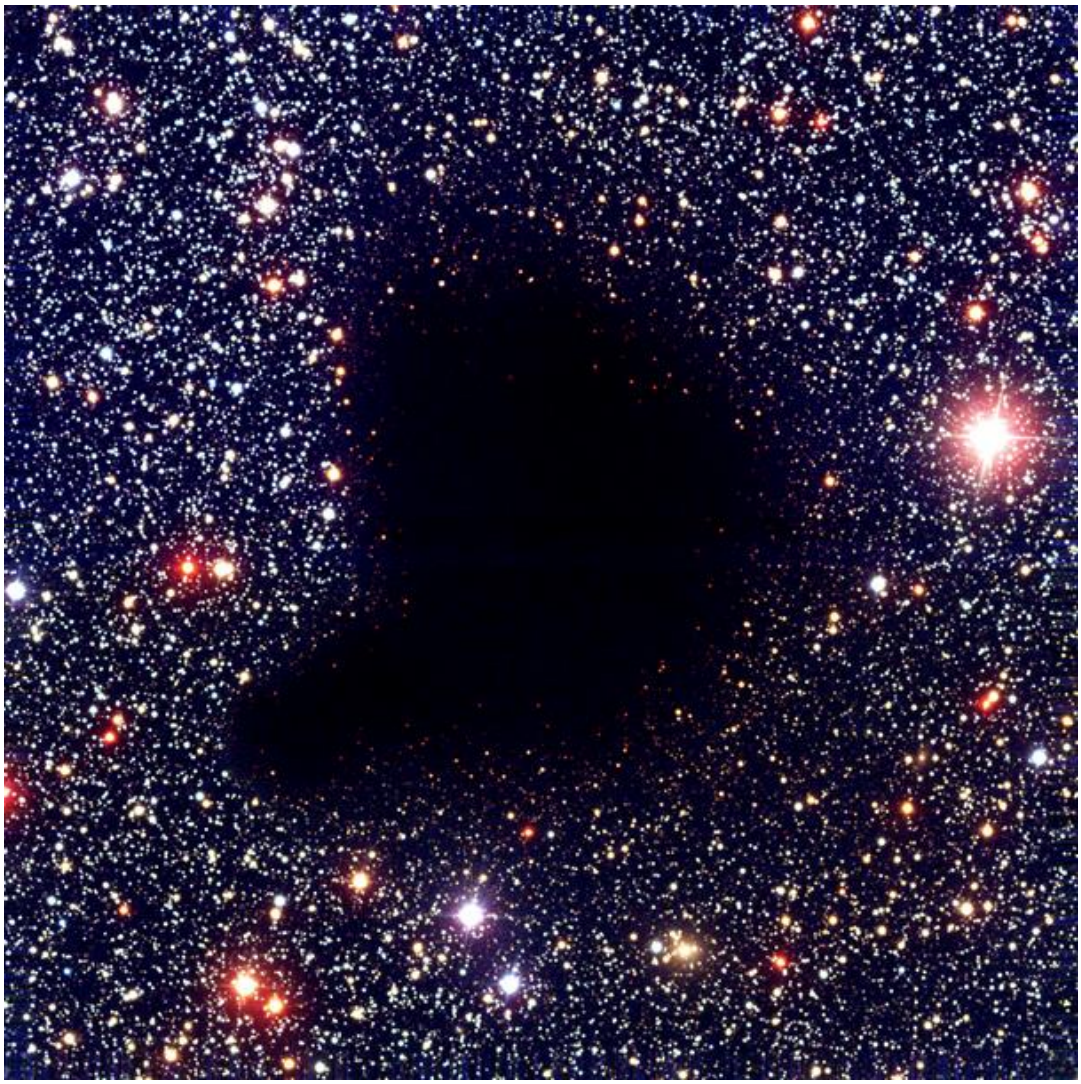

Figure 8.1: *Colour composite of visible and near-infrared images of the dark cloud Barnard 68. This image was obtained with the 8.2-m VLT ANTU telescope and the multimode FORS1 instrument in March 1999. At these wavelengths, the small cloud is completely opaque because of the obscuring effect of dust particles in its interior.*

(http://www.eso.org/public/images/eso0102a/)

8.2 The ISM in infrared

8.1.1 Hot ISM

8.1.2 HII regions

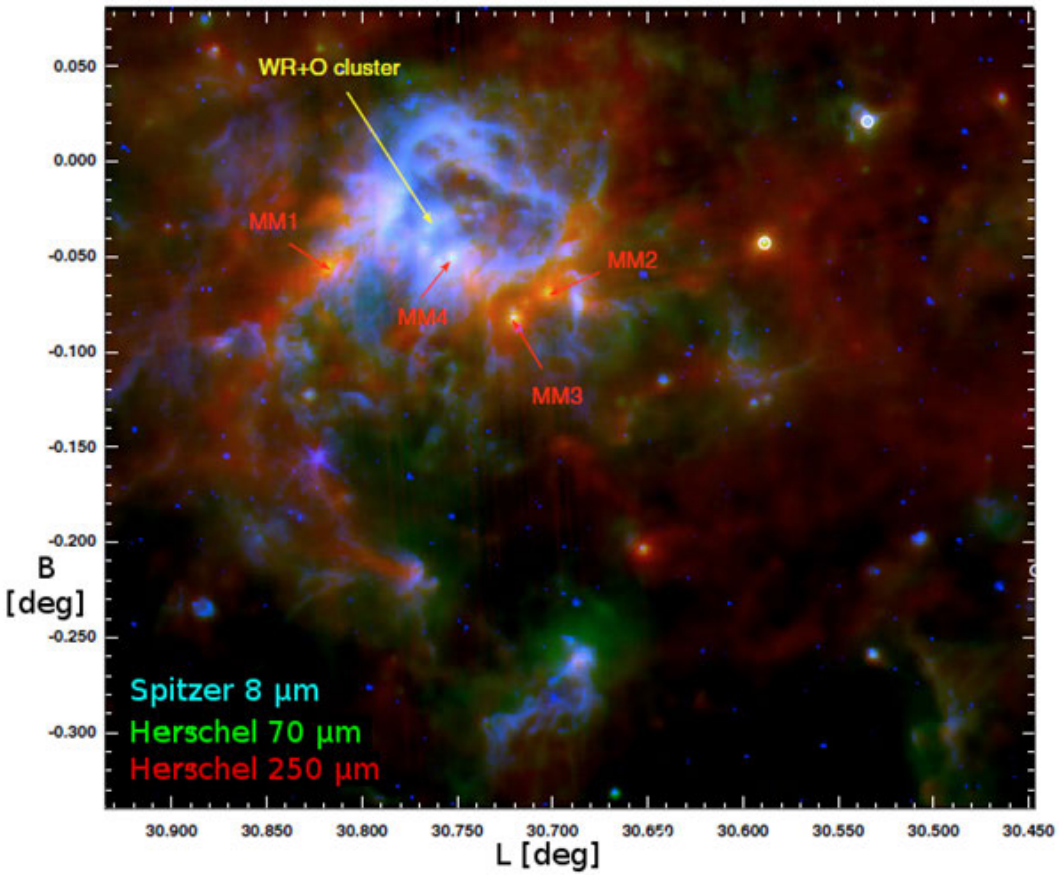

Figure 8.2: *A color composite image of the W43 starburst region (Bally et al. 2010).*

There are a few luminous Galactic star forming complexes, W43 at a distance of 5.5 kpc is one of those. The "mini-starburst" region contains a giant HII region powered by a cluster of OB and Wolf-Rayet stars emitting a Lyman continuum luminosity of about 10^{51} ionizing photons per second (Bally et al. 2010). Most of that UV radiation is absorbed and reemitted by interstellar dust. A color composite image of the W43 starburst region is shown in Figure 8.1. The λ~8μm emission peak regions detected by the Spitzer IRAC (Infrared Array Camera) are seen as blue spots. Emission in the IRAC 8 μm band is partly thermal radiation by warm dust, but it is dominated by polycyclic aromatic hydrocarbons (PAHs, see in Section 3). PAHs are excited by strong ultraviolet radiation from massive hot stars, thus such a mid-infrared bright region is a location of recent high-mass star formation. This is valid for both galactic star bursts such as W33, and for starburst galaxies.

8.1.3 HI clouds

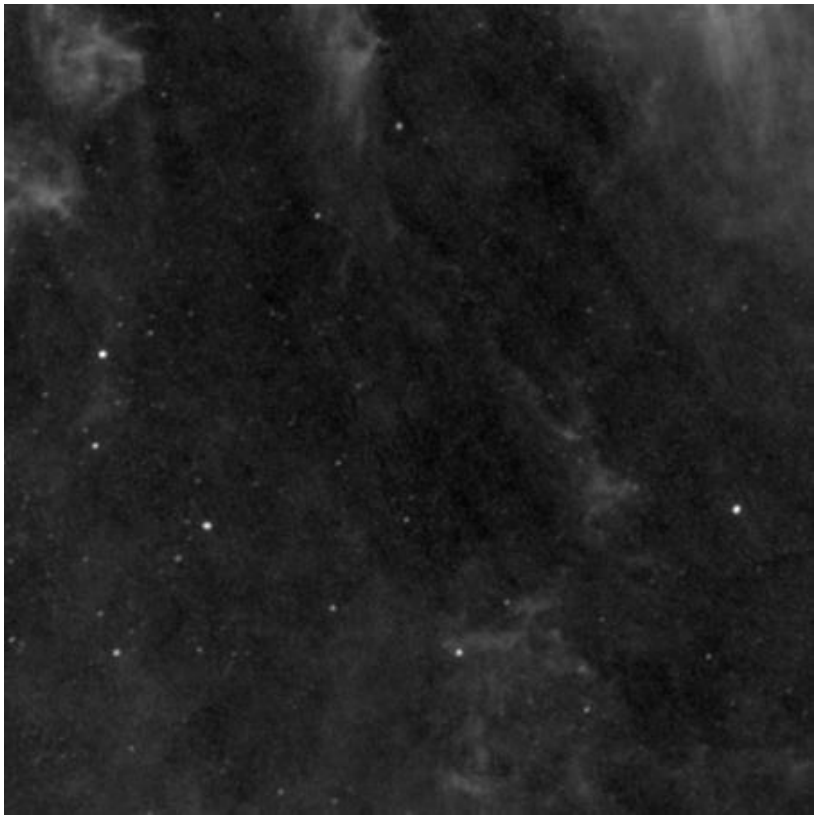

Figure 8.3: *Cirrus emission in the IRAS 100 μm surface brightness image towards the so called Lockmann Hole (Lockman et al. 1986) region. The cloud structure resembles to the terrestrial cirrus clouds. The image shows a 20 by 20 square degrees field centered on RA(J2000)=18^h45^m Dec(J2000)=58°, the darkest and brightest pixels correspond to 0.7MJy/sr and 57.4MJy/sr respectively. Image is processed by the SkyView Virtual Observatory using the IRIS archive (Miville-Deschenes and G. Lagache 2005).*

The low density cirrus clouds can be easily recognized in the *Lockmann Hole* (Lockman et al. 1986) region (see Figure 8.3) which is a line of sight free from dense ISM. "The Hole" is one of the lowest hydrogen column density regions in the sky, and also one of the darkest spots in FIR. It is about 15 square degrees large in the constellation Ursa Major (http://www.google.com/sky/#latitude=58&longitude=-10.75&zoom=4&) where the hydrogen column density drops to as low as $N(H)=5.3\times10^{19}cm^{-2}$. The cirrus emission seen in far-infrared (60μm < λ <200 μm) is typical for cold neutral ISM, its surface brightness correlates well with the hydrogen column density. The colour temperature derived from the cirrus FIR continuum radiation is T_d~18K. The cirrus emission is considered as thermal radiation by large dust grains. Its general galactic presence indicates that large dust grains are mixed well with gas at all densities from the densest cloud cores till the lowest density diffuse HI clouds.

8.1.4 Molecular clouds

Barnard 68 (LDN 57) is a small (d<0.2pc), nearby (distance~150pc), isolated, dense ($n(H)=3.4x10^5$ cm^{-3} in the centre) molecular cloud with a sharp boundary (see eg. Nielbock et al. 2012). Such clouds are also known as Bok globules (Bok & Reilly 1947). Figure 8.4 compares the multiwavelength data of B68.

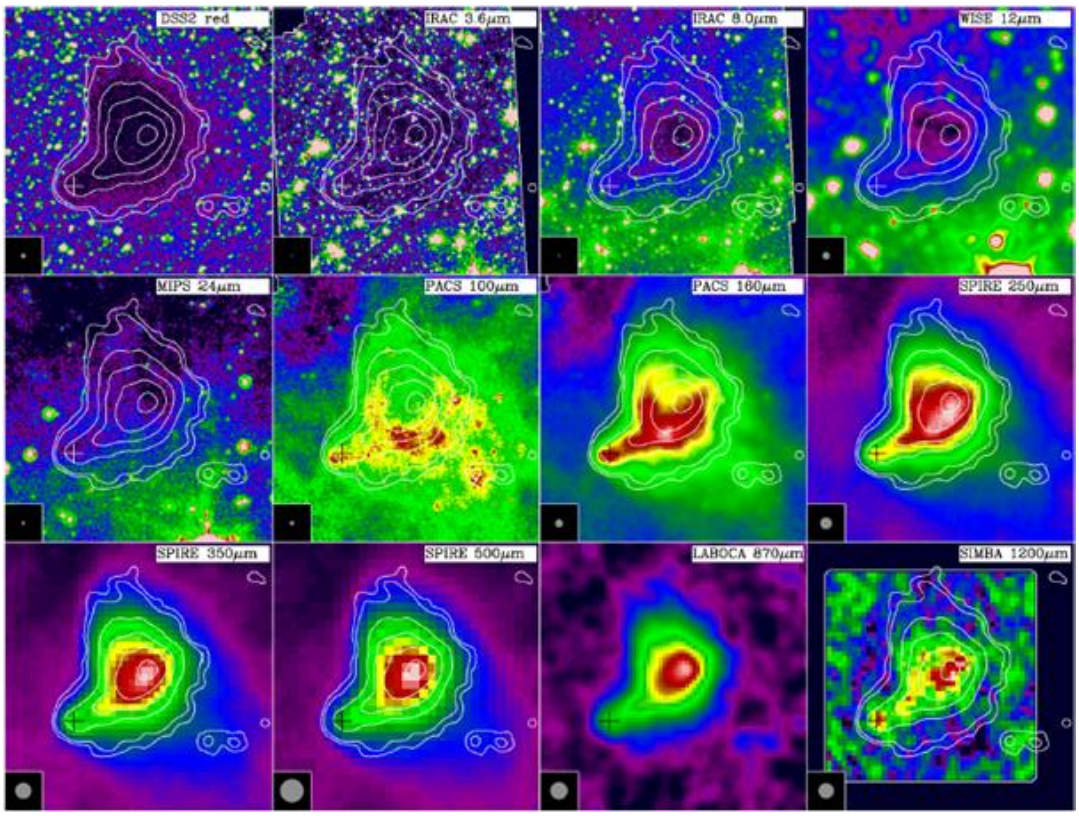

Figure 8.4 *Multi wavelength image gallery of B68. The instruments and wavelengths at which the images were obtained are indicated in the white annotation boxes. Each image has an arbitrary flux density scale. The maps are centered on RA(2000) = 17h22m39s, Dec(2000) = 23d and have a field of view of 7 arcminutes x 7 arcminutes. (see eg. Nielbock 2012)*

Only the densest, the so called infrared dark clouds are opaque in NIR and mid-IR.

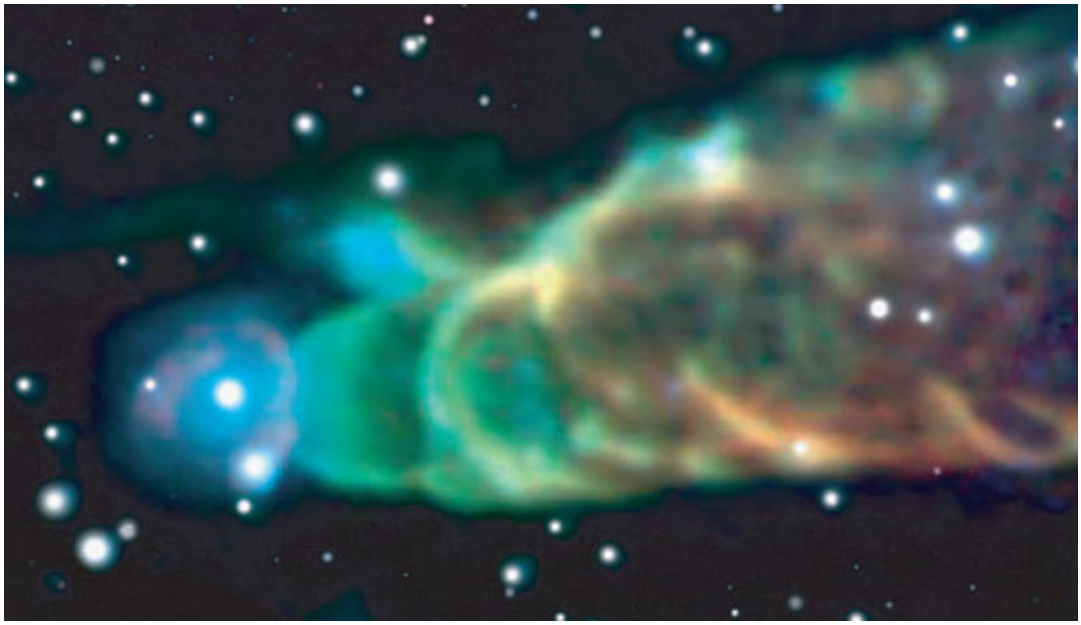

Figure 8.5: *Spitzer IRAC composite image of HH 49/50 in the Chamaeleon I cloud, (3.6 μm; blue, 4.5 μm; green, 6.0 μm; orange, and 8.0 μm; red). The nebula is brightest at 4.5 μm. The cloud core severely decelerates the outflow, the resulting shocks should be bright in H_2 thereby explaining the 4.5 μm emission. (See Bally et al. 2006)*

Figure 8.5 shows aSpitzer IRAC composite image of HH 49/50 in the Chamaeleon I cloud, where the green color represents the 4.5 μm intensity. The nebula is brightest at 4.5 μm, with an apparent pair of intertwined, twisting, helical filaments, a morphology that was named ‘‘tornado.’’ The southern tip of the tornado is associated with the southern end of HH 49/50. The tornado is probably driven from the north, by Cha-MMS1. The cloud core decelerates the outflow, the resulting shocks should be bright in H_2 that explains the 4.5 μm excess emission (See Bally et al. 2006).

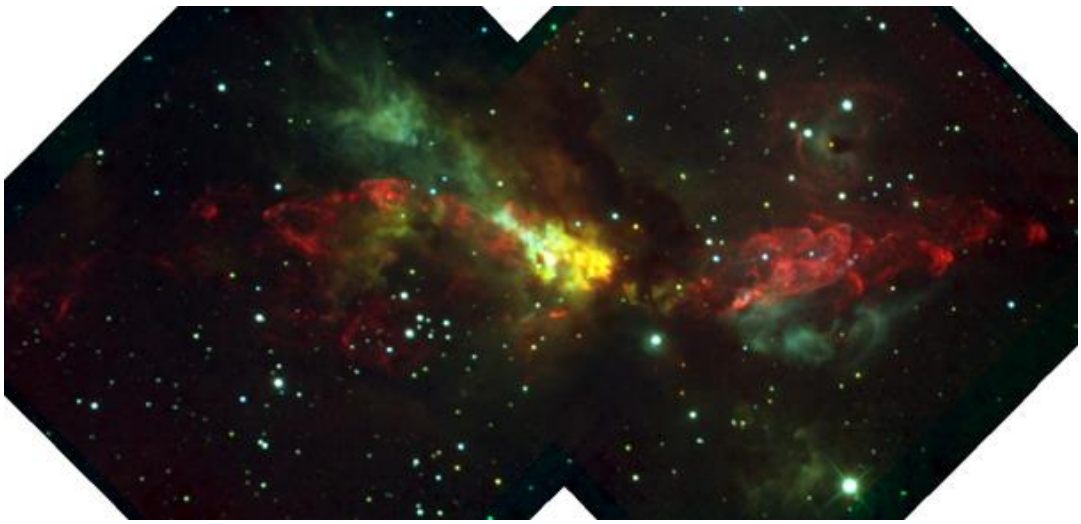

Figure 8.6*: The Cepheus A outflow complex showing shock excited H_2 (red), K_s band 2.2μm (green), and H band 1.6μm emission. Images were obtained with the Apache Point Observatory 3.5 meter telescope using the NICFPS infrared camera. For further details, see Cunningham, Moeckel, and Bally (2009).*

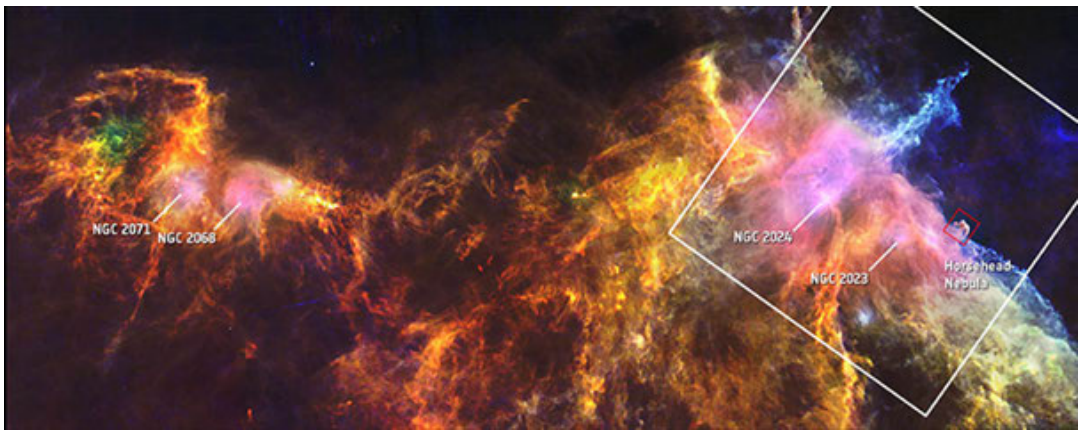

Figure 8.7: *Far-infrared view of the Horsehead Nebula in the constellation Orion by the Herschel Space Observatory. To the left, there are two other prominent massive star forming sites: NGC 2068 and NGC 2071. The image is a composite of the wavelengths of 70 microns (blue), 160 microns (green) and 250 microns (red), and covers 4.5x1.5 degrees. The image is oriented with northeast towards the left of the image and southwest towards the right. (ESA/Herschel/PACS, SPIRE/ N. Schneider, Ph. André, V. Könyves (CEA Saclay, France) for the “Gould Belt survey”)*

The Horsehead Nebula appears as a dark patch shadowing onto the bright background in visible images. It is however bright in FIR due to the reprocessed and reemitted starlight from nearby young stellar objects (see Figure 8.7).

8.1.4.1 Calculating temperature and column density maps from FIR data

Using the Herschel intensity maps we can calculate the colour temperature map. Figure 8.8 shows the intensity map of G10 at 500 μm. This object was observed within the Herschel open time key programme Galactic cold cores (Juvela et al. 2010). We were mapping selected Planck C3PO cold, compact objects with the Herschel PACS and SPIRE instruments (100–500μm). This survey covered ~120 fields between 30'x30' and 80'x80' in size and covered approximately 350 individual Planck detections of cold clumps.

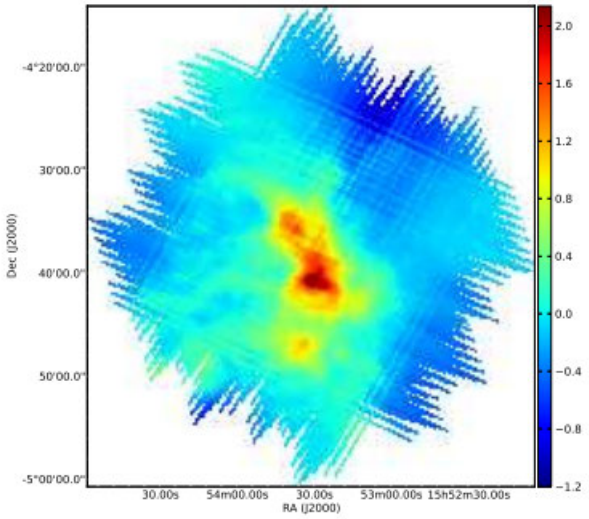

Figure 8.8: *Herschel intensity map at 500 μm in Jy/beam*

First we convolve the maps to a 40 arcsec resolution and then, for each pixel, the SED was fitted with a modified blackbody curve: $B_\nu(T_d)\nu^\beta$, where $B_\nu(T_d)$ is the Planck function for a dust temperature T_d, ν is the frequency and β is the spectral index. As a first approximation, we can keep β at a fixed value of 2.0. But several studies have suggested that the spectral index may increase in cold and dense environments. With the fixed β value, we can underestimate the range of temperature variations and can overestimate the temperature of the coldest regions, leading to an underestimation of the masses of these regions. However, we can identify the major relative temperature variations within the regions.

Figure 8.9 shows the computed temperature map of G10.

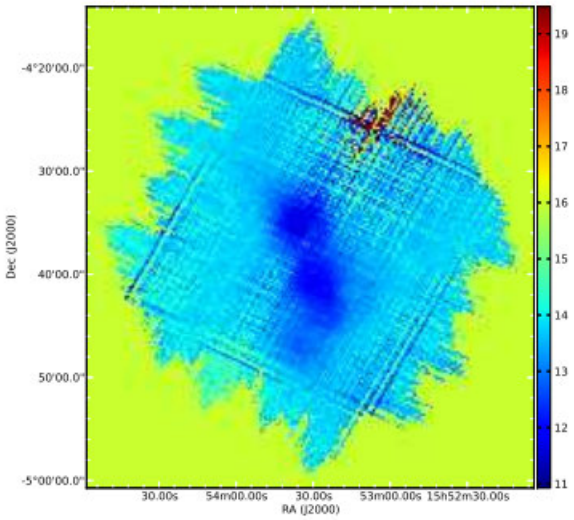

Figure 8.9: *Calculated temperature map in K*

We can calculate the column density with the following equation (Schuller et al, 2009):

$$N(H_2) = \frac{I_\nu R}{B_\nu(T_D)\Omega\kappa_\nu \mu m_H} \tag{8.1}$$

where I_ν is the intensity map in Jy/beam, R is the gas-to-mass ration, $B_\nu(T_d)$ is the Planck function for a dust temperature T_D, T_D is the fitted temperature, Ω is the beam solid angle, κ_ν=5.04 g/cm^2 the dust opacity, μ is the mean molecular weight of the ISM and m_H is the mass of an hydrogen atom.

The column density for G10 averaged over a 40" beam is calculated using the above formula and showed on Figure 8.10. Mass estimates are possible for the sources with available distance estimates.

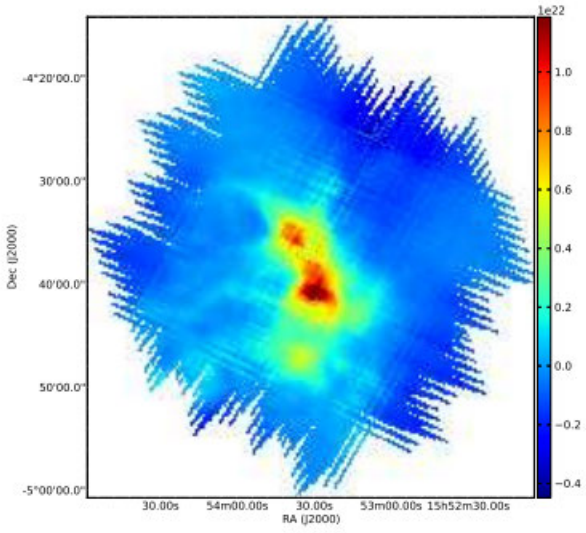

Figure 8.10: *Calculated column density map in 1/cm^2*

8.1.5 The structure of cirrus

8.1.5.1 Topology definitions

Epsilon chain: a finite sequence of points x_0 ... x_N separated by distances of ε or less: |x_i - x_i+1| < epsilon

$$|x_i - x_{i+1}| \leq \varepsilon \tag{8.2}$$

Fractal: (loosely speaking) a self-similar object. It contains "copies" of itself. Zooming in on a fractal always reveals more detail in the structure. A prototypical example is the Cantor set, which is constructed by removing some portion of a line segment (say, the middle third) ad infinitum. The fractal dimension *D* is calculated from the area of the object, *A* and perimeter, *K* as

$$\sqrt{A} = cK^{1/D} \tag{8.3}$$

The *D* fractal dimension can be derived from a series of measurements (see Figure 8.11) of *A* and *K* for substructures as:

$$D = 2\frac{\Delta \log(K)}{\Delta \log(A)} \tag{8.4}$$

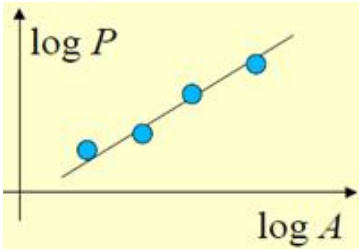

Figure 8.11: *The D fractal dimension is derived from the slope of the logarithms of the perimeter K as a function of area A.*

Tree: a graph with no cycles (loops).

Minimal spanning tree (MST): is the tree of minimum total branch length that spans the data, without closed loops. To construct the MST, one starts with any point and its nearest neighbor, adds the closest point, and repeats until all points are in the tree (Prim's algorithm).

8.1.5.2 Fractal structure of the ISM

The self-similarity of structures seen in various length scales was found in mm wavelength range molecular line measurements as well as from mapping the FIR surface brightness. The 2 dimensional fractal dimension was derived from projected density, column density, or surface brightness distribution:

$$1.2 < D_{2D} < 1.6 \tag{8.5}$$

a value that is surprisingly similar to that of the terrestrial atmospheric clouds. A value of D_{2D}~1.2 was found in nearby interstellar clouds from IRAS 100μm images (Dickman et al. 1990). We note that in a turbulent non-compressible homogenous isotropic medium D_{2D} =4/3, but in spite of the similarity the ISM is in fact compressible.

We note that the derived fractal dimension may be altered by projection effects, our spatial resolution, and the signal to noise ratio (S/N) of our data (see Sánchez et al., 2009). D_{2D} decreases as resolution decreases, since as the pixel size is larger (worse resolution) the perimeter becomes smoother because the irregularities in the cloud contours blend with each other. The D_{3D} three dimensional fractal dimension is:

$$D_{3D} = D_{2D} + 1 \tag{8.6}$$

However Sánchez et al. (2009) found that the observed D_{2D} decreases as D_{3D} increases for fractal clouds having dimensions in the range $2.0 \leq D_{3D} \leq 2.9$.

Very high noise levels artificially increase the structure irregularities and therefore decrease the final value of the fractal dimension. This effect can be minimized by smoothing low-S/N maps before calculating D (Sánchez et al. 2009).

8.1.5.3 Filaments and webs

High spatial resolution Herschel images revealed a rich network of filaments in every interstellar cloud. As an example the column density map of the Snake cloud is shown in Figure 8.12 as derived from Herschel SPIRE images.

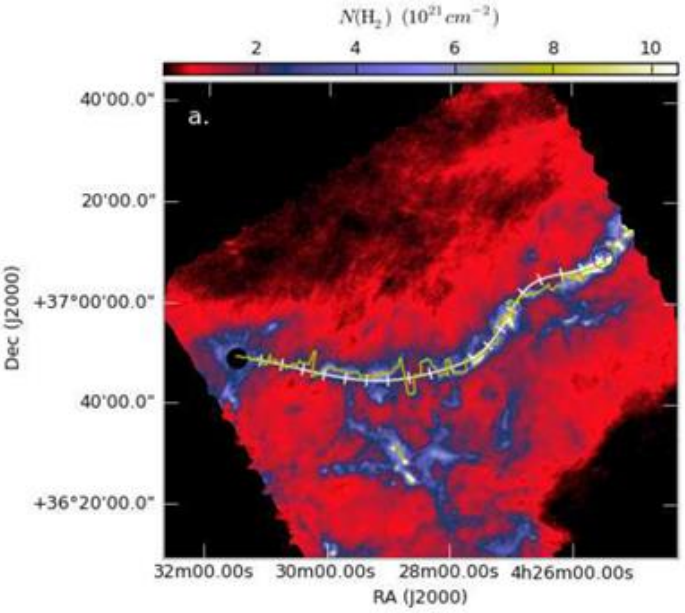

Figure 8.12: *The column density distribution of the Snake cloud G153.82-844, in the California nebula (Juvela at al. 2012).*

The prestellar cores identified with Herschel are preferentially found within the densest filaments with masses per unit length exceeding ~15 M_{sun} /pc and column densities exceeding ~ 7×10^{21} cm^{-2}. Men'shchikov et al. (2010) suggests that dense cores form primarily along filaments. Herschel results favor a scenario in which interstellar filaments and prestellar cores represent two fundamental steps in the star formation process:

(i) large-scale magneto-hydrodynamic turbulence generates a complex web of filaments in the ISM;

(ii) the densest filaments grow and fragment into prestellar cores via gravitational instability.

In this picture, a (proto)stellar cluster forms when a massive filament becomes globally gravitationally unstable and undergoes a large-scale collapse.

8.1.5.4 Galactic Infrared Loops.

Superimposed on the large-scale spiral structure of the Galaxy is a distribution of features known variously as shells, holes, loops, bubbles, arcs, filaments, superbubbles, supershells, etc., which has been referred to as the "Cosmic Bubble Bath" or the "Violent ISM" (McCray & Snow 1979). These structures are characterized by an underdensity or overdensity of interstellar matter – either neutral or ionized – and are thought to be directly connected to the star-formation process (Blaauw 1991), forming loop-like, hole-like and filamentary-like structures. IRAS loops were identified by Könyves et al. (2006) in the framework of an investigation of the large-scale structure of the diffuse ISM, started by Kiss et al. (2004) using the 60 and 100 μm ISSA data (IRAS Sky Survey Atlas, Wheelock et al. 1994). Galactic infrared loops (GIRLs, Könyves et al. 2006) by definition must show an excess far-IR intensity confined to an arc-like feature extending to at least 60% of a complete ellipse shaped ring. The thicknesses of the rings are given in the catalogue for all GIRLs.

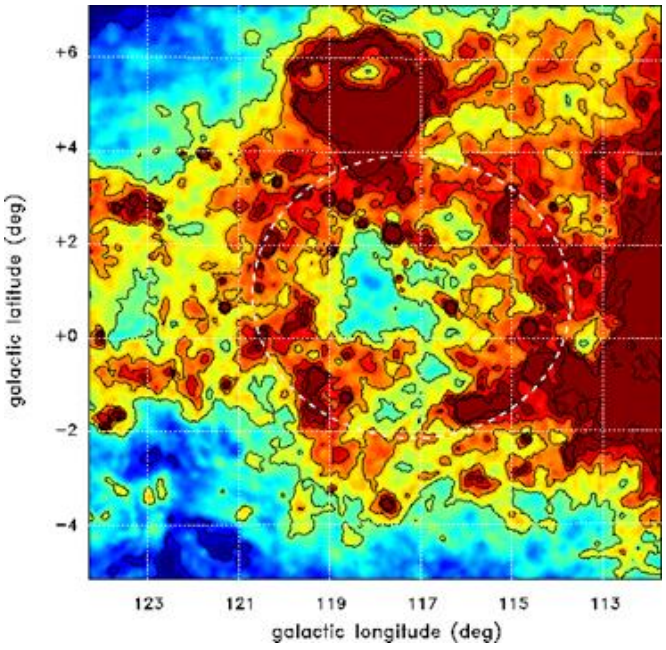

Figure 8.13: *FIR loop GIRL117+0 seen in the mosaicked IRAS 100 μm surface brightness images in the Galactic mid-plane associated with OB associations CasOB14, CasOB4, CasOB5 and HII regions Sh163-171 (Kiss et al. 2004).*

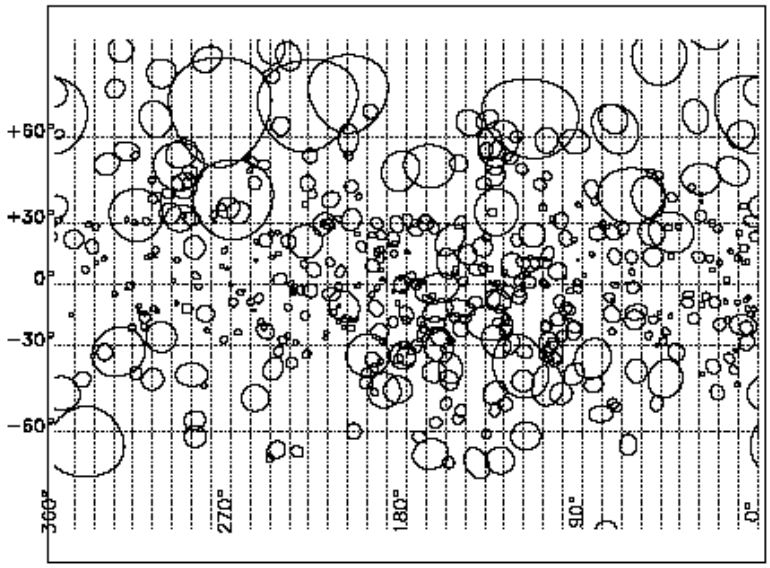

Figure 8.14: *Galactic infrared loops (GIRLs, Könyves et al. 2006)*

For about 20% of them a distance is also provided, that gives an average diameter of 0.09 pc at an average distance of 1.1 kpc. The potential role of the loops in the star-formation process has first been discussed by Kiss et al. (2006) and Tóth & Kiss (2007). The catalogue of IRAS GIRLs (Könyves et al. 2006) contains 462 far-IR loops, 427 objects are not completely within the Galactic plane ($|b| < 5^{\circ}$).

References and further reading to the chapter:

Arzoumanian, D. et al. 2011: "*Characterizing interstellar filaments with Herschel*", A&A 529, L6

Bally, J. et al. 2006: "", ApJ, 132, 1923.

Bally, J. et al. 2010: "*Herschel observations of the W43 ``mini-starburst''*", A&A, 518, L90.

Blaauw, A. 1991: *"OB Associations and the Fossil Record of Star Formation"*, in The Physics of Star Formation and Early Stellar Evolution, ed. C. J. Lada, & N. D. Kylafis, NATO ASIC Proc., 342, 125

Bok, B. J. & Reilly, E. F. 1947: *"Small Dark Nebulae"*, ApJ, 105, 255

Cunningham, N. J., Moeckel, N., and Bally, J. 2009: *"A Pulsed, Precessing Jet in Cepheus A"*, ApJ, 692, 943

Dickman, R., Horvath, M., and Margulis, M., 1990: *"A search for scale-dependent morphology in five molecular cloud complexes"*, ApJ, 365, 586.

Juvela, M et al. 2012, "*Galactic cold cores III. General cloud properties*", A&A, 541, 12

Kiss, C., Moór, A., & Tóth, L. V. 2004: *"Far-infrared loops in the 2nd Galactic Quadrant"*, A&A, 418, 131

Kiss, Cs., Pál, A., Müller, Th., Ábrahám, P., 2006: *"An asteroid model of the mid- and far-infrared sky"*, PADEU, 17, 135

Könyves, V. et al., 2006: *"Catalogue of far-infrared loops in the Galaxy"*, VizieR Online Data Catalog, 346, 31227

Lockman, F.J. et al. 1986: "*The structure of galactic HI in directions of low total column density*". ApJ, 302, 432

McCray, R., & Snow, Jr., T. P. 1979: *"The violent interstellar medium"*, ARA&A, 17, 213

Men'shchikov et al., 2010: *"Filamentary structures and compact objects in the Aquila and Polaris clouds observed by Herschel"*, A&A, 518, L103

Miville-Deschenes, M. and Lagache, G., 2005: "*IRIS: A New Generation of IRAS Maps"*, ApJS, 157, 302.

Nielbock, M. et al. 2012: *"The Earliest Phases of Star formation (EPoS) observed with Herschel: the dust temperature and density distributions of B68"*, A&A, 547, 11

Planck collaboration, 2011: "*Planck early results. XXIII. The first all-sky survey of Galactic cold clumps*", A&A, 536, A23.

Sánchez, N. et al., 2009: *"Determining the Fractal Dimension of the Interstellar Medium"*, RevMexAA (Serie de Conferencias), 35, 76–77.

Simon, R., et al., 2006: *"A Catalog of Midcourse Space Experiment Infrared Dark Cloud Candidates"*, ApJ, 639, 227

Tóth, L. V., & Kiss, Z. T. 2007: *"Footprints of triggering in large area surveys of the nearby ISM and YSOs"*, in IAU Symp. 237, ed. B. G. Elmegreen, & J. Palous, 124

Wheelock, S. L. et al. 1994, *"IRAS sky survey atlas: Explanatory supplement"*, NASA STI/Recon Technical Report N, 95, 22539

Chapter 9. Young stellar objects

We describe the formation and evolution of young stellar objects in this chapter. The protoplanetary disks are also characterized.

One of the most fundamental astrophysical process is star formation. Its feedback effects are influencing the properties of the interstellar medium and the various formation methods are resulting different properties for the host stellar systems. Star formation occurs in molecular clouds, which occupy a small fraction of the volume of the interstellar matter, but include a significant fraction of the mass inside the solar circle. Star formation occurred many times in the past and it is also occurring now. It can be examined in details in the nearby star forming regions.

Nearby, very well known star forming regions are the Taurus and Orion Molecular Cloud, located at 160 and 415 pc (Menten et al. 2007), respectively. Figure 9.1 shows the Herschel and Spitzer view of a bright reflexion nebula, M87 in the Orion. White circles show the reddest and potentially youngest protostars discovered with the use of the Herschel telescope (Stutz et al. 2013).

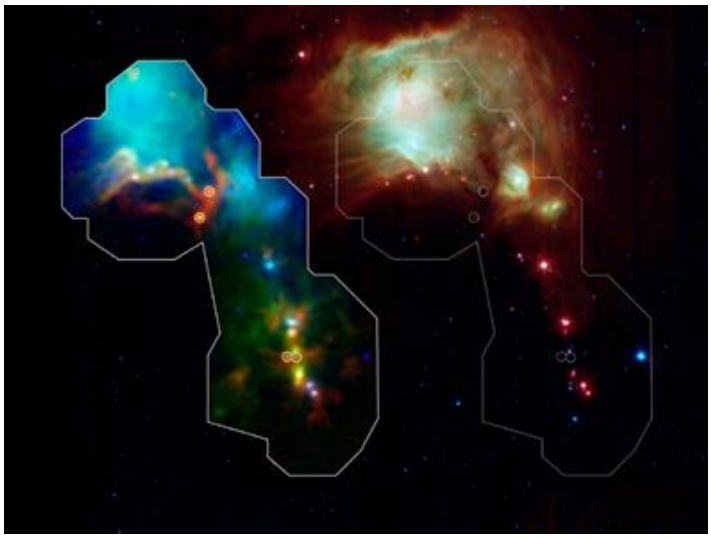

Figure 9.1: Spitzer (right) and Herschel (left) view of M87 in Orion. White circles represent the youngest protostars discovered by Herschel Space Observatory. The main structures are similar on the Spitzer and Herschel images. A few very young objects are appearing only on the Herschel observations. (Source: www.skyandtelescope.com/community/skyblog/newsblog/202173511.html)

9.1 Molecular clouds

Molecular clouds consist mainly of molecular hydrogen and helium, with small amounts of heavier gases. They have temperatures ranging from about 10 to 50 K. With this temperature the gas in the molecular clouds is too cold to radiate at visible wavelengths, but it is observable with radio telescopes. Larger regions can be observed with single dish telescopes and interferometers can be used for detailed studies of smaller, individual regions. Interstellar dust grains are also present in these clouds, which reradiate the absorbed light at infrared wavelengths. A molecular cloud is surrounded by a layer of atomic gas that shields the molecules from the interstellar UV radiation field.

Molecular clouds have a hierarchical structure. They contain filaments, gravitationally bound clumps and also unbound smaller structures. Star-forming clumps are the densest, massive clumps out of which stellar clusters form, and they are generally gravitationally bound. Individual stars and binaries are form in the gravitationally bound cores. The forming stars shine in optical wavelengths, but the surrounding dust absorbs the radiation. The heated dust particles can reradiate the energy in infrared and longer wavelengths, what we can observe.

Using the Virial theorem, we can characterize the minimum mass of a cloud core for the collapse. Equation 9.1 shows the Virial theorem, derived from Newton's 2nd law, where K is the kinetic energy and Ω is the gravitational energy.

$$\frac{1}{2}\frac{d^2 I}{dt^2} = 2K + \Omega \quad (9.1)$$

, where $I = \sum_i m_i r_i^2$, $K = \frac{1}{2}\sum_i m_i v_i^2$

and $\Omega = -\sum \frac{G m_i m_j}{r_{i,j}}$

We can write the above formula as Equation 9.2 for the hydrostatic equilibrium of a gas sphere with a total mass of M.

$$\frac{2kTM}{\mu m_A} = \int_0^M \frac{GM_r}{r} dM_r \quad (9.2)$$

The cloud would collapse if the left side is smaller than the right side. Equation 9.3 gives the minimum mass for the collapse. It is the Jeans mass, M_J. For typical density and temperature values the Jeans mass is around 10^5 $M_\odot$.

$$M > M_J \equiv \left(\frac{3}{4\pi\rho}\right)^{1/2}\left(\frac{5kT}{G\mu m_A}\right)^{3/2} \quad (9.3)$$

We can calculate the collapse timescale as $t_{ff} \approx (G\rho)^{-1/2}$. The collapse depends on the temperature evolution of the cloud. If the cooling timescale (t_{cool}) is much shorter than t_{ff}, the collapse is approximately isothermal. The Jeans mass is proportional to $(\rho)^{-1/2}$, so it will decrease. Inhomogeneities with mass larger than the local M_J will collapse by themselves with their local t_{ff}. This fragmentation process will continue as long as the local t_{cool} is shorter than the local t_{ff}.

Eventually the density of subunits becomes so large, that they become optically thick and their evolution become adiabatic. In this case $M_J \propto \rho^{1/2}$. As the density has to increase, the evolution always will reach a point when $M=M_J$, when we assume that a stellar object is born. From this moment on the cloud would start to evolve in hydrostatic equilibrium.

A giant molecular cloud in this way can form not only a single star, but a group of stars. The fragmentation process determines their mass distribution, which is described by an empirical function: the initial mass function (IMF). This depends on the physical and chemical properties of the cloud. The classic expression for the IMF, determined empirically is the Salpeter's law: $dn/dM = CM^{-x}$, where x=2.35 for $M\backslash M_\odot > 0.5$ and x=1.3 for $0.1 < db/dm < 0.5$ in the solar neighbourhood.

Molecular clouds cannot simply collapse, due to the preservation of angular momentum. During the contraction of the cloud, a protostellar disk will form. Along the axis of rotation, in-falling material has only little angular momentum and the in-fall proceeds relatively unhindered. Therefore, the molecular cloud becomes thinner along the axis of rotation and two cone-shaped voids are formed at the poles by the jets and outflows. It allows stellar light to escape and to illuminate these cones from the inside. Material migrates within the protostellar disk towards the protostar. The spinning-up of protostar and protostellar disk winds up magnetic vortices, leading to strong magnetic fields along the polar axis and the formation of bipolar outflows or jets. These jets may hit the surrounding interstellar medium or the remainders of the collapsing molecular cloud, leading to strong shock fronts, so-called Herbig-Haro objects (HHs). The mechanism of transport of the released gravitational energy switches from convection to radiation. This leads to more efficient cooling of the core. A new star is born when the core becomes hot and dense enough to maintain stable hydrogen fusion. Inside the remaining protoplanetary disk, planets can form. Finally the disk will disappear and a young stellar system will present with the central star and planets. Figure 9.2 gives us an overview of the star and planet formation process, timescales are also presented for the different

evolutionary stages. The initial size of the molecular cloud core is ~10,000 AU, the forming young stellar system is only ~50 AU.

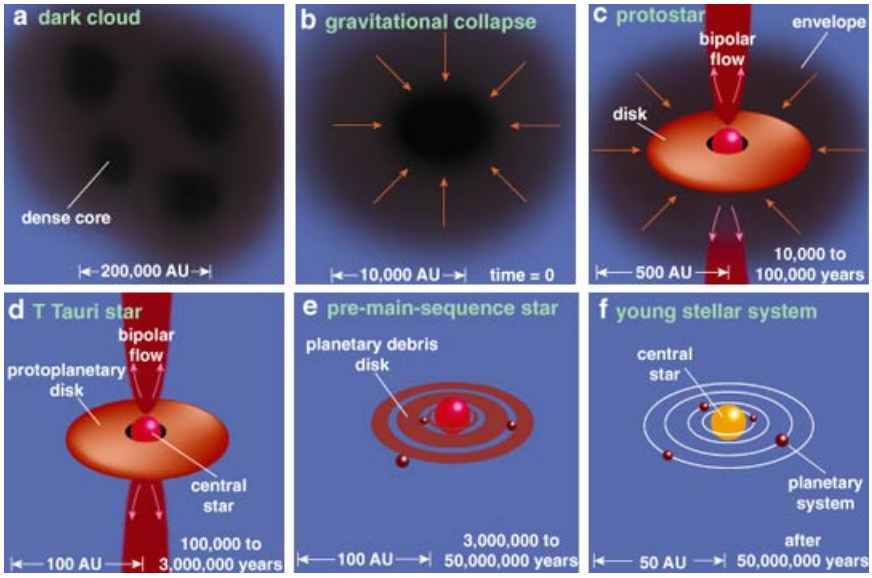

Figure 9.2: Overview of star formation (Greene, 2001): The first phase is the gravitational collapse. The size of the cloud core is ~10,000 AU. The protostar's size is around 1,000 AU, it has disk, bipolar outflows and envelope. In the T Tauri phase, the envelope is disappearing, it's size is ~200 AU. The pre-main-sequence star has only a planetary debris disk and in the young stellar system the central star is surrounded with the planets.

The stages of the process are well defined in stars with masses around one solar mass or less. In high mass stars, the length of the star formation process is much shorter, and the process is not so well defined.

9.1 YSOs on the Hertzsprung-Russel diagram

The radiation from a stellar photosphere is close to the blackbody radiation, so the effective temperature can be defined with Equation 9.4, where R is the radius of the photosphere, L is the luminosity and σ_S is the Stefan-Boltzmann constant .

$$T_{eff} = \left(\frac{L}{4\pi\sigma_s R^2} \right)^{1/4} \tag{9.4}$$

The evolution of the stars is traceable on the Hertzsprung-Russel diagram (HRD), which shows the relationship between the luminosity and surface temperature of the stars, see in Figure 9.3. The exact units on the axes depend on the context: effective temperature (Teff) vs. luminosity (L) or absolute visual magnitude (Mv) vs. B-V (color).

The location of stars in different evolutionary phases is marked on the image. The main sequence is the most prominent, it goes from the hot and bright upper-left to the cold and faint lower-right corner. A main sequence star with a given mass has a unique luminosity and temperature, it is powered by fusion of hydrogen into helium in its core.

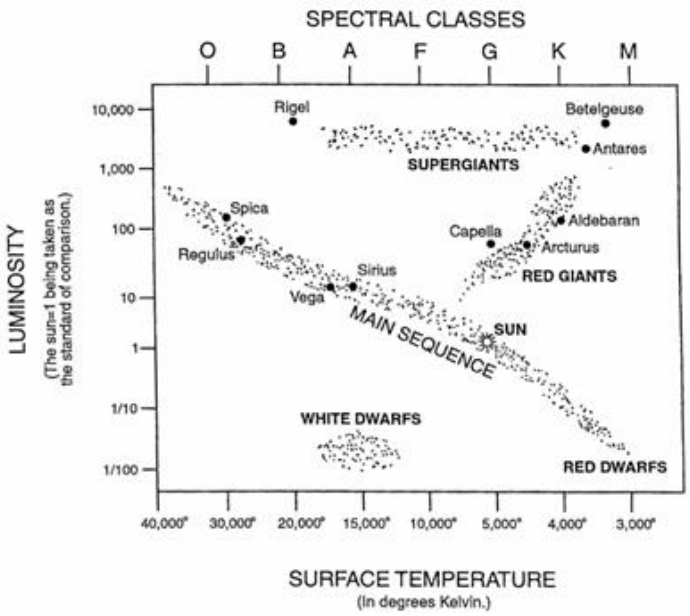

Figure 9.3: Hertzsprung-Russel diagram.

Luminosity vs. surface temperature / spectral class diagram. Stars appear only in certain regions of the diagram. The main sequence is the most prominent. White dwarfs, red dwarfs, red giants and supergiants have also their typical positions on the diagram. http://www.sociostudies.org/journal/files/seh/2005_1/seh_4_1_c_fig_2.JPG

Young stellar objects are in the first phases of their evolution, they have not yet enterred to the main sequence. The star first appears as an optically visible object on the birthline. During the contraction, it begins to descend along a nearly vertical path on the HRD, this is the Hayashi track. The star becomes several times less luminous but it stays at roughly the same temperature. After this phase, the star follows the Henyey track, which is a nearly horizontal track to reach the main sequence. The proper shape and position of these tracks depend on the star's mass and chemical composition.

If accretion of matter to the forming star may be neglected, the object follows a path on the HRD with the effective temperature similar to that given by Equation 9.5.

$$T_{eff} \propto \kappa_0^{-4/51} \mu^{13/51} \left(M/M_{Sun}\right)^{7/51} \left(L/L_{Sun}\right)^{1/102} \tag{9.5}$$

The effect of the chemical composition is reflected by the value of μ and κ_0.

Figure 9.4 shows the evolutionary tracks for pre-main sequence stars with different masses. Blue lines represent the different tracks. Low-mass stars have nearly vertical evolution tracks until they arrive on the main sequence. For more massive stars, the Henyei track follows the Hayashi track. The stellar masses are indicated on the tracks, red curves shows the ages of the stars. The most massive stars have no pre-main-sequence phase, they born onto the main sequence.

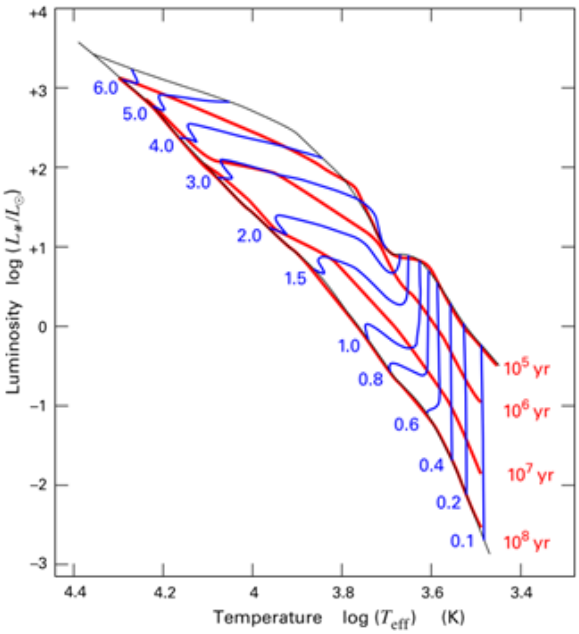

Figure 9.4: Evolutionary tracks on luminosity vs. temperature diagram for pre-main-sequence stars with different masses. Low-mass stars evolve with constant effective temperature until they reach the main sequence, these evolutionary tracks are the Hayashi tracks. For more massive stars, the Henyei tracks are the typical: they evolve with nearly constant luminosity. (http://en.wikipedia.org/wiki/File:PMS_evolution_tracks.svg)

Star formation is traditionally divided into two parts: low-mass and high-mass star formation. The division is at 8 M_O. They form on different timescales and follow different evolutionary tracks. Low-mass protostars have luminosities dominated by accretion, and high-mass stars' accretion is dominated by nuclear burning. The role of the turbulence in the low-mass core is negligible.

9.2 Classification of YSOs

The physical properties of the protostars can be investigated with the use of the spectral energy distribution (SED) of the continuum. Protostellar SEDs are divided into four classes, from Class 0 to Class III according to the spectral index, α or to their bolometric temperature. The bolometric temperature is given as the temperature of a black body with the same mean frequency as the source's SED, see Equation 9.6, where $\langle \nu \rangle$ is the mean frequency, define by Equation 9.7, where S_ν is the flux density measured at ν frequency.

$$T_{bol} = 1.25 \times 10^{-11} \langle \nu \rangle \tag{9.6}$$

$$\langle \nu \rangle = \frac{\int \nu S_\nu d\nu}{\int S_\nu d\nu} \tag{9.7}$$

α is the slope of the SED in logarithmic scale, measured in the range of ~2-25 μm, defined by Equation 9.8, where S_λ is the flux density measured at λ wavelength.

$$\alpha = \frac{d\log(\lambda S_\lambda)}{d\log(\lambda)} \tag{9.8}$$

Figure 9.5 shows the SEDs of the Class 0 – Class III protostars.

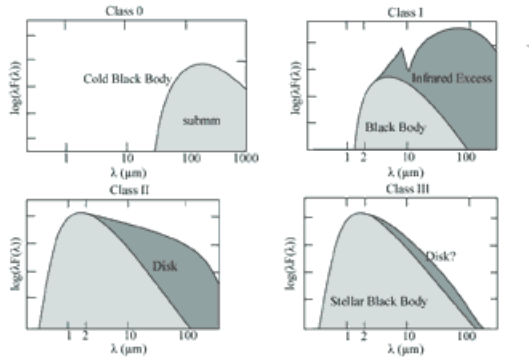

Figure 9.5: Evolution of the spectral energy distribution of young stellar objects. The young stellar objects' evolution has 4 different phases: Class 0, Class I, Class II and Class III. Class 0 is observable only in submm. Class I, II and III sources are characterized with a blackbody radiation and an infrared excess. The amount of infrared excess is decreasing during the evolution. Class II and III objects are also visible in the optical bands. http://www.phys.unsw.edu.au/jacara/pilotscience.php

Class 0 objects are sources with a central protostar that are extremely faint in the optical and near-IR and that have a significant submillimeter luminosity. Class I sources ($\alpha > 0$) are relatively evolved embedded sources with circumstellar disks and envelopes, they are optically invisible stars with SEDs that peak at mid-IR to far-IR wavelengths. Class II, or classical T Tauri stars ($-2 < \alpha < 0$) have significant circumstellar disks, strong emission lines and substantial IR or UV excesses characterized them. Class III, weak emission T Tauri stars ($\alpha < -2$) have weak or no emission lines and negligible excesses, they are no longer accreting significant amounts of matter.

The geometry of the source has an important role in the determination of the SED's shape. Figure 9.6 shows the SEDs for different viewing angle. The Class 0 SED shows that very little stellar radiation is detected from the source except at a pole on view. In this case the bipolar outflows allow us to detect stellar radiation. The density of the circumstellar envelope is smaller for Class I sources. There we can observe much more stellar radiation. The angular size of the bipolar cavity is increasing, so it also allows more radiation to be detected. For Class II sources, the whole envelope is usually dispersed. The Class III sources have only a very thin disk, the SED shape looks very similar from different viewing angles.

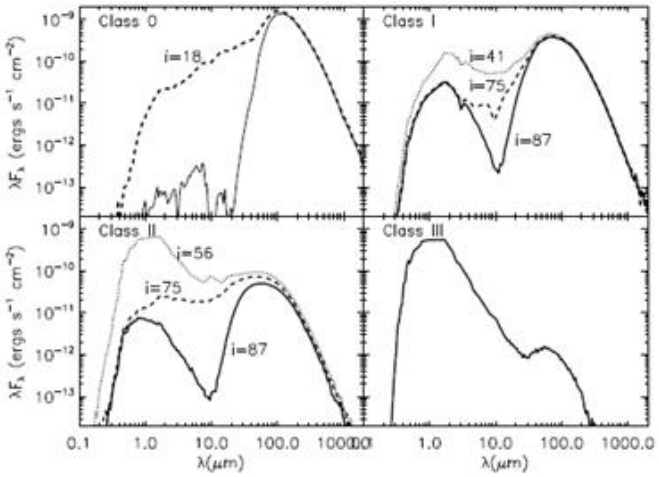

Figure 9.6: SEDs for different viewing angles, based on YSO models from Barbara Whitney and Thomas Robitaille. Inclination has an important effect for the Class I and Class II sources. SED of Class III object looks very similar from different viewing angles.

A new classification scheme is based on the physical properties (e.g. disk mass, envelope accretion rate) of the YSOs. These classes are the Stage 0, I, II and III. Stage 0 and I objects have significant infalling envelopes and possibly disks, Stage II objects have optically thick disks (and possible remains of a tenuous infalling envelope), and Stage III objects have optically thin disks.

9.3 Determining physical properties of YSOs

With more sophisticated modelling of the SEDs we can determine the physical properties of YSOs. Individual radiative transfer modelling is possible, or we can use available pre-computed models. Making two-dimensional radiation transfer models for the selected objects is time consuming, but we can get more precise results.

Robitaille et al. (2006) have calculated 2×10^5 model SEDs, including the effects of outflow cavities. These models can be automatically compared with observed SEDs to infer the properties of the source. This method is fast, but it has limitations. We can use only the pre-computed SEDs with given parameters and select the best fitting models.

Figure 9.7 shows the spectral energy distribution of a Herbig star located in the Cygnus X giant molecular cloud (Krause et al. 2003). Observations were made in the optical with the 0.7 m telescope of Max-Planck Institute for Astronomy and in the infrared with the MAX instrument on the 3.8 m United Kingdom Infrared Telescope. The observed and archive (2MASS, MSX, IRAS) data points marked with different symbols and the fitted model is presented with solid lines. The fitted parameters are written on the model: the strong infrared excess emission is modelled by an optically thick accretion disk.

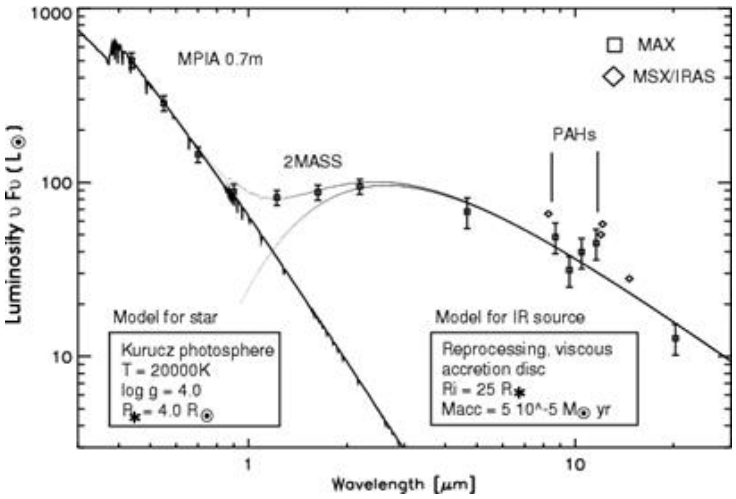

Figure 9.7: Optical and infrared spectral energy distribution of a Herbig star in the Cygnus X giant molecular cloud (Krause et al. 2003). Infrared excess is observable. The spectral energy distribution is well fitted with two components: a Kurucz photosphere with 20,000 K and an accretion disk.

9.4 Protoplanetary disks

Protoplanetary disks are thought to be the birthplaces of planetary systems. Most of our knowledge of the disks is coming from the modelling of spectral energy distributions and spatially resolved spectroscopic observations. We need different observational techniques to investigate the whole structure: from UV to millimetre.

Figure 9.8 shows an illustrative example for a protoplanetary disk. The near-infrared emission traces the warmer inner regions of the disk, the sub-millimeter wavelengths give us information about the outer, cooler regions of the disk. Protoplanetary disks have a rich structure with an inner disk radius around 0.03 AU and an outer disk radius from few tens of astronomical units up to 1000 AU. The temperature in the inner part is ~ 1000 K, while in the outer part is only ~10-30 K.

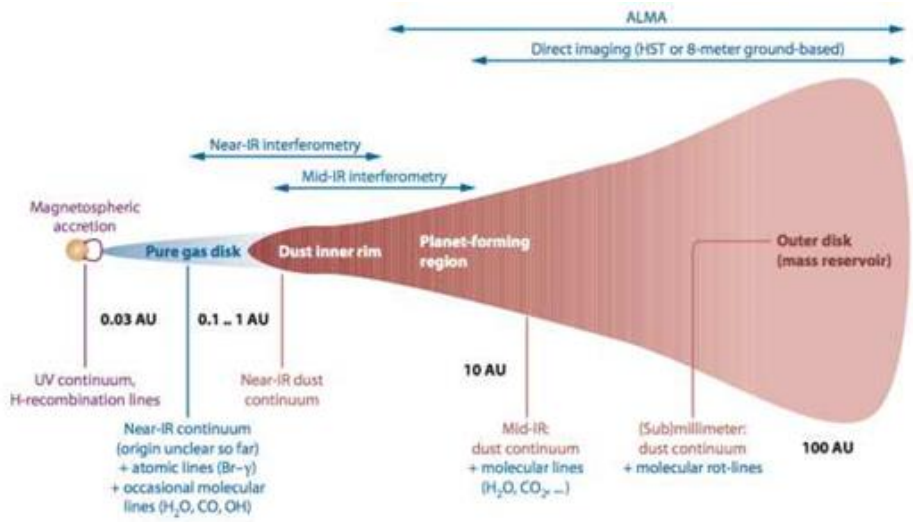

Figure 9.8: Protoplanetary disk around a young star (Dullemond & Monnier, 2010, review)

Figure 9.9 shows the infrared view of young stellar circumstellar disks. These images were taken by NASA/ESA Hubble Space Telescope's Near-Infrared Camera and Multi-Object Spectrometer. The objects are located in the Taurus Molecular Cloud, they are extremely young stars.

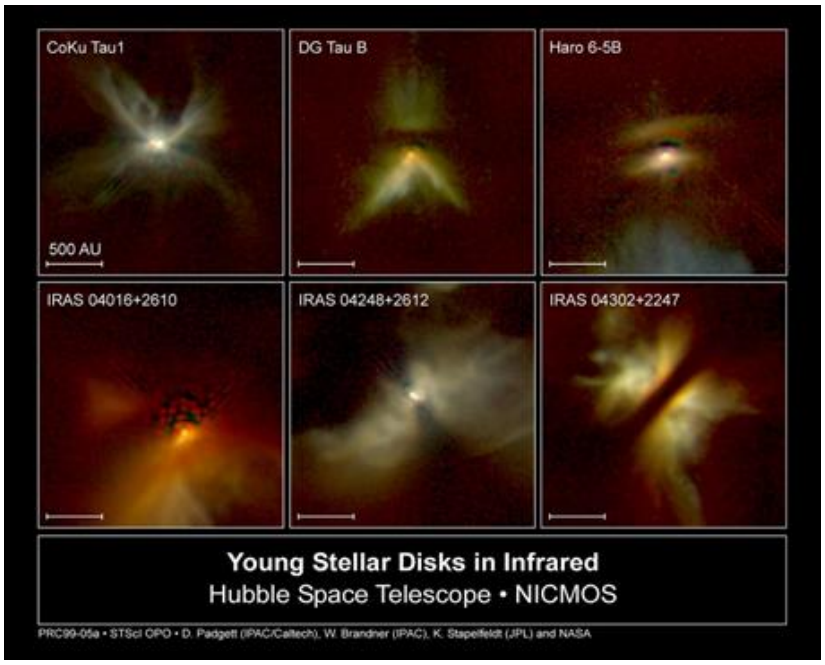

Figure 9.9: Hubble Space Telescope images of 6 young stellar disks. Appearance and size of the infrared view of the disk show great variance. (http://www.spacetelescope.org/images/opo9905b/)

9.4.1 Growth of dust particles

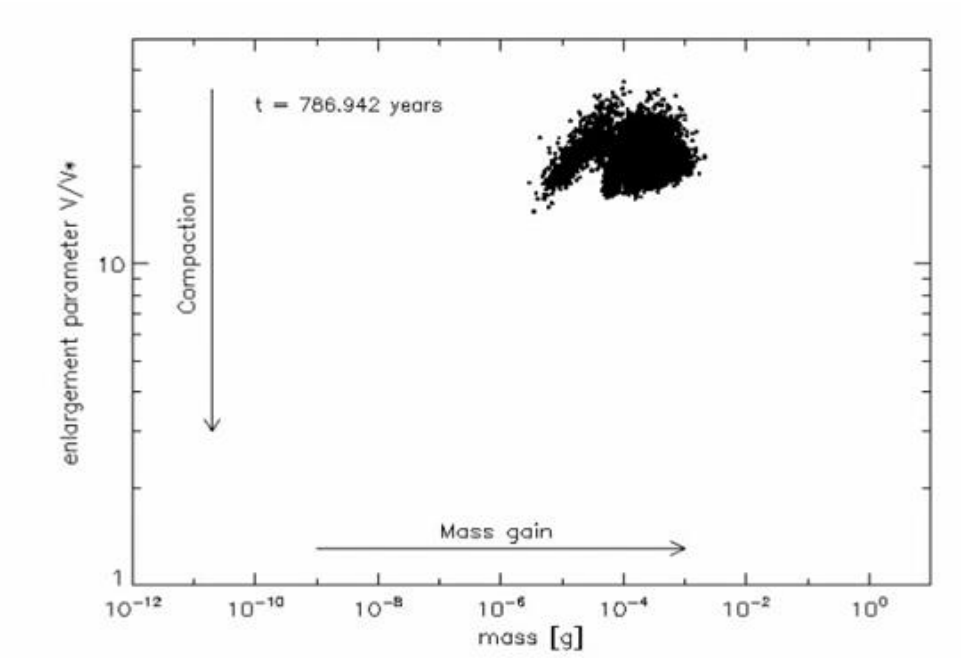

The animation shows how dust particles grow from microns sized silicate spheres (monomers) to mm-cm-sized dust aggregates by coagulation (subsequent collisions between dust particles) in a protoplanetary disk. The simulation is performed in the Minimum Mass Solar Nebula model (Weidenschilling 1977) at 1 AU distance from a Solar-like star in the midplane of the disk. Dust particles collide in the gas disk, if they move relative to each other. Several processes can induce relative dust motions. The ones included in the simulation are Brownian motion (gas particles colliding randomly with the dust and inducing a typically small random relative velocity), and turbulence (turbulent gas eddies induce the relative velocity). When two particles collide, it is necessary to know the outcome of the collision that could be either sticking, bouncing, or fragmentation. The outcome of the collision depends on the aggregate properties (e.g., mass and structure), their relative velocity, and the impact parameter (aggregates tend to collide off-axis). In the case of this simulation, laboratory experiments on silicate dust aggregates are used to model the collisional outcome (Guettler et al 2010). The animation shows the aggregate mass on the x axis and the aggregate porosity (a measure of fluffiness) on the y axis. Every point represents a dust particle in the numerical simulation (see Zsom&Dullemond 2008 for more details). The animation shows that initially dust particles grow by subsequent collisions and they also become fluffier. Once the aggregates start to bounce (at around 3000 yrs), the aggregates do not increase in mass anymore, and the aggregates are compacted in the collisions (see Zsom et al. 2010 for more details). Bouncing prohibits further growth, because it does not result in net aggregate growth. This is called the bouncing barrier, which is one of many barriers in the theory of planet formation. The way around the bouncing barrier and other barriers is an active area of research, but some promising results are described in e.g., Windmark et al. 2012, Drazkowska et al. 2013, Ros & Johansen 2013.

9.5 Detailed analysis of YSOs in practice

Candidate young stellar objects can be selected based on their infrared colours and magnitudes. Different selection criteria were constructed based on IRAS, Spitzer Space Telescope and WISE data. Galaxies, evolved stars could have similar infrared colours as young stars, so we have to remove these objects from our candidate YSO list. As a first step, we can check the astronomical databases (Simbad, VizieR) for available information and data. SIMBAD is the Set of Identifications, Measurements, and Bibliography for Astronomical Data, maintained by the Centre de données astronomiques de Strasbourg (CDS), France. It contains identifications, basic data as e.g. coordinates, optical photometric data, bibliography, and selected observational measurements for several million astronomical objects. The database is available in the following site: http://simbad.u-strasbg.fr/simbad/. Giving the candidate YSO's coordinates, Simbad lists the known objects in a given radius. We discard the source, if an associated non-YSO object (e.g. galaxy, evolved star) is found.

Radiative transfer modelling and pre-computed models are usable for single stars only, so we eliminate the sources, which have close companion and the photometric surveys collected the data from the system and not from the individual sources.

We can check near-infrared images (e.g. 2MASS) to select the single objects. To visualize the images and access data from Simbad and VizieR catalogues, we can use Aladin, which is an interactive software sky atlas.

The software is downloadable from http://aladin.u-strasbg.fr/aladin.gml.

In the *File* > *Load astronomical image* > *Aladin image server* option, we can search and download optical and infrared images. In the *File* > *Load catalog* > *Simbad database* option, associated objects are available.

Figure 9.10 shows the 2MASS K band image of DG Tau. Associated objects are marked with red.

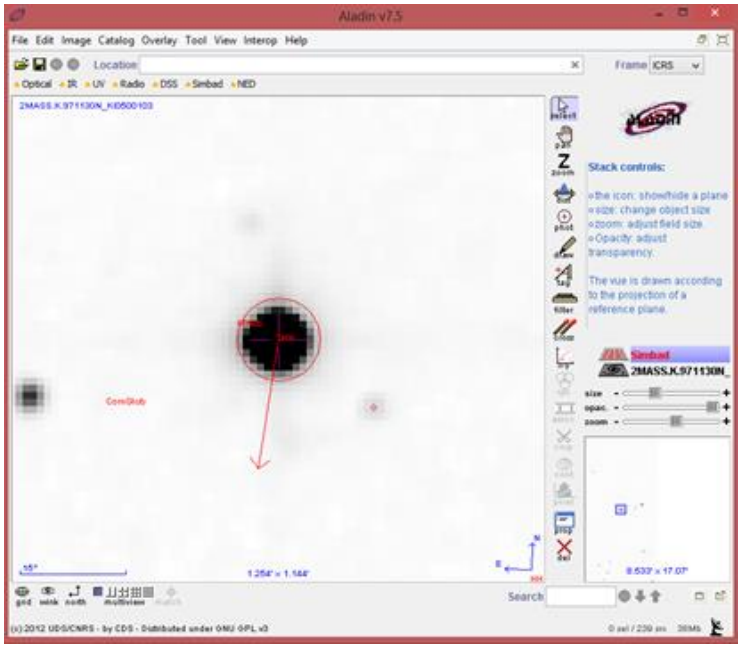

Figure 9.10: Near-infrared image of DG Tau in Aladin. Known objects from the Simbad database are marked with red symbols.

To make a detailed analysis of an YSO, we need photometric data at different wavelengths.

The VizieR Catalogue Service is an astronomical catalog service provided also by CDS (http://vizier.u-strasbg.fr/viz-bin/VizieR). It contains in a homogeneous way thousands of astronomical catalogues. Several query interfaces are currently available for browsing purposes or for use by other data processing systems such as visualisation tools.

We can access the photometric data with the following option in Aladin: *File* > *Load catalog* > *VizieR*.

Robitaille et al. (2006) have calculated 20 071 model YSO SEDs at ten viewing angles. These models can be automatically compared with observed SEDs to infer the properties of the source, with the use of an online SED fitting tool, which is available here: http://caravan.astro.wisc.edu/protostars/. A detailed description about the fitting procedure is in Robitaille et al. (2006).

Figure 9.11 shows the Input form of the SED fitting tool. We can give the different available photometric data: magnitude or flux, distance range and extinction range.

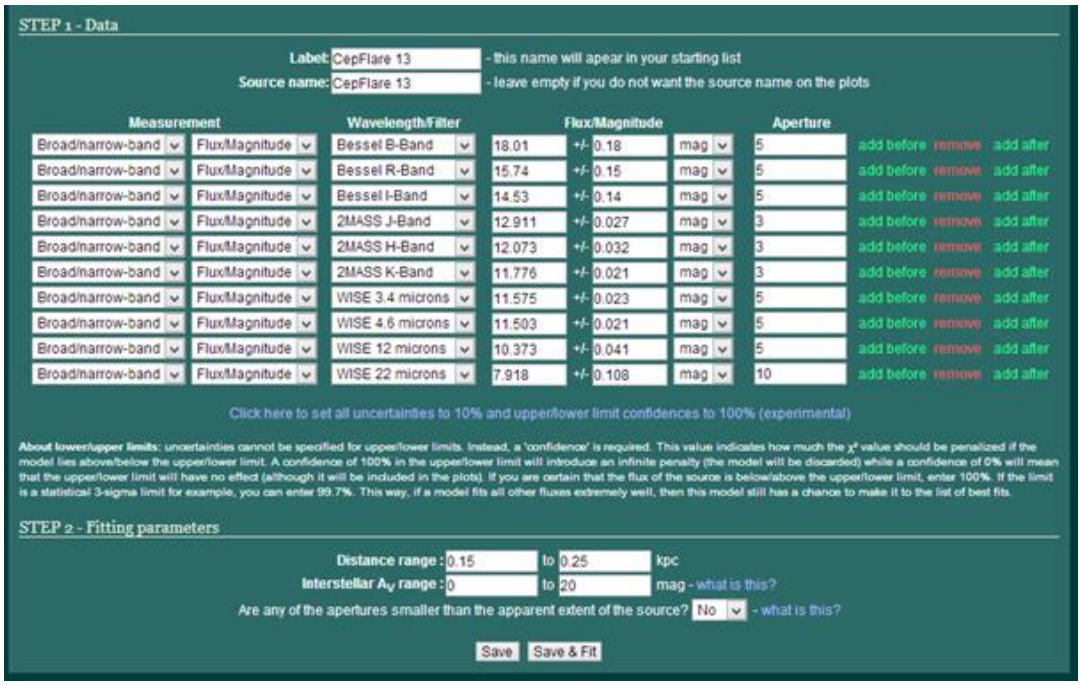

Figure 9.11: Input form for SED fitting (http://caravan.astro.wisc.edu/protostars/)

The SED Fitting Tool gives us the best fitting models: distances, exinction and YSO model parameters. Figure 9.12 shows the best fitting models for a candidate YSO. Black dots represent the photometric data, black solid line shows the best fitting models and gray lines indicate all models that also fit very well, with $\chi^2 - \chi^2_{best} < 3$. The dashed line shows the SED of the stellar photosphere in the best-fitting model.

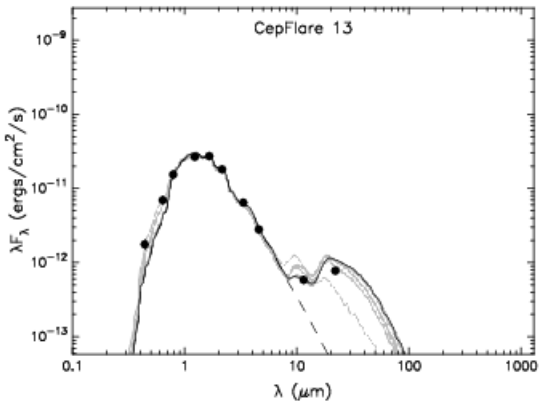

Figure 9.12: *SED of a candidate YSO. See detailed description in Text.*

References and further reading to the chapter:

Dullemond, C. P. & Monnier, J. D. 2010: *The Inner Regions of Protoplanetary Disks*, ARA&A, 48, 205D

Drazkowska, J. et al. 2013: *" Planetesimal formation via sweep-up growth at the inner edge of dead zones"*, A&A, 556, 37

Greene, Th. 2001: *""Stellar embryology" takes a step forward with the first detailed look at the youngest Sun-like stars"*, American Scientist, 4, 316

Güttler, C. et al. 2010: *"The outcome of protoplanetary dust growth: pebbles, boulders, or planetesimals?. I. Mapping the zoo of laboratory collision experiments"*, A&A, 513, 56

Juvela, M., Ristorcelli, I., Montier, L.A. et al. 2010, "*Galactic cold cores: Herschel study of first Planck detections*", A&A, 518, 93

Krause, O., Lemke, D., Tóth, L. V. et al. 2003, A&A, "*A very young star forming region detected by the ISOPHOT Serendipity Survey*", 398, 1007

McKee, Ch. F. & Ostriker, E. C. 2007: "*Theory of Star Formation"*, ARA&A, 45, 565

Menten, K. M. et al. 2007: *"The distance to the Orion Nebula"*, A&A, 474, 515

Robitaille, Th. P., Whitney, B. A., Indebetouw R. & Wood, K. 2007, "*Interpreting Spectral Energy Distributions from Young Stellar Objects. II. Fitting Observed SEDs Using a Large Grid of Precomputed Models*", ApJS, 169, 328

Robitaille, Th. P., Whitney, B. A., Indebetouw R., Wood, K. & Denzmore, P. 2006: "*Interpreting Spectral Energy Distributions from Young Stellar Objects. I. A Grid of 200,000 YSO Model SEDs",* ApJS, 167, 256

Ros, K & Johansen, A. 2013: *"Ice condensation as a planet formation mechanism"*, A&A, 552, 137

Schuller, F., Menten, K. M., Contreras, Y. et al. 2009: "*ATLASGAL - The APEX telescope large area survey of the galaxy at 870 μm*", A&A, 504, 415

Stutz, A. M., Tobin, J. J., Stanke, Th. et. al. 2013: "*A Herschel and APEX Census of the Reddest Sources in Orion: Searching for the Youngest Protostars*", ApJ, 767, 36

Weidenschilling, S. J. 1977: *"The distribution of mass in the planetary system and solar nebula"*, Ap&SS, 51, 153

Windmark, F. et al. 2012: *"Planetesimal formation by sweep-up: how the bouncing barrier can be beneficial to growth",* A&A, 540, 73

Zsom, A. & Dullemond, C. P. 2008: *„A representative particle approach to coagulation and fragmentation of dust aggregates and fluid droplets"* A&A, 489, 931

Zsom, A. et al. 2010: *"The outcome of protoplanetary dust growth: pebbles, boulders, or planetesimals? II. Introducing the bouncing barrier"* A&A, 513, 57

http://aladin.u-strasbg.fr/aladin.gml

http://caravan.astro.wisc.edu/protostars/

http://simbad.u-strasbg.fr/simbad/

http://vizier.u-strasbg.fr/viz-bin/VizieR

http://www.reinervogel.net/index_e.html?/YSO/YSO_e.html

Chapter 10. Extragalactic infrared astronomy

The first infrared data obtained on galaxies was when the central part of ten bright galaxies of various types was measured with 8 colour photometry (U, B, V, R, I , J, K, L bands, see Chapter 3), using a PbS detector by Johnson (1966). The observed NIR colours were represented well by a synthetic galaxy NIR spectrum based on nearby stars, however with a need for significant contribution from cool stars. Most of the first galaxies detected at longer wavelengths (10µm and 20µm) showed violent activities (Seyferts). A review of the first years of extragalactic infrared astronomy is given by Neugebauer et al. (1971)

After surveys by the IRAS, ISO, COBE, Spitzer, AKARI and Herschel space observatories and by SCUBA on JCMT we find that most of the star formation in the Universe is obscured. An example of reprocessed starlight is seen in the infrared spectra of actively star forming galaxies (see Figure: 10.1).

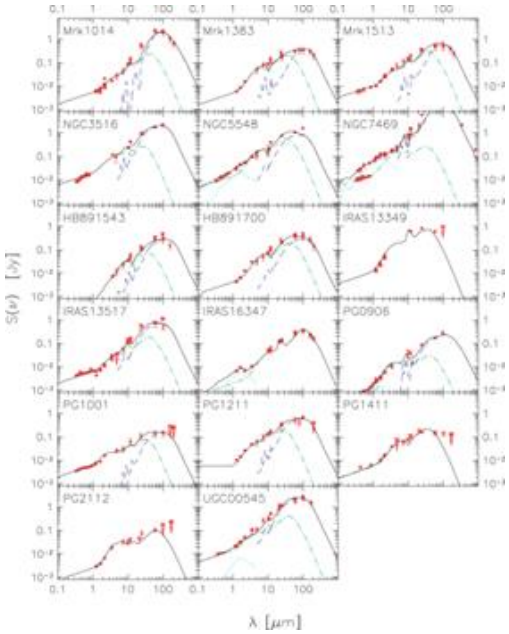

Figure 10.1 Emission of dust seen as FIR excess in the spectra of actively star-forming galaxies (Fritz et al. 2006)

Infrared luminous galaxies at z < 1.5 constitute about 70-80% of the far-infrared background, and may bear most of the star-formation activity at higher redshifts. Surprisingly most of the photons in the universe come from the infrared.

10.1 Nearby galaxies

While the ultraviolet and optical light of galaxies is mostly originated from young and main sequence stars, most of the near-infrared (NIR) radiation is emitted by aged stars. The FIR radiation is dust-reprocessed light from young stars. Roughly 1/2 - 2/3 of all energy emitted by stars gets reprocessed by dust into the IR. Giant molecular clouds of external galaxies which are traced by CO rotational line emission in the mm radio range appear as bright spots in the FIR images as seen in Figure 10.1 for M33 the Triangulum galaxy, the smallest spiral galaxy of the Local Group. The proximity and its nearly face-on view makes M33 a suitable target for the detailed study of the structure of its disk, the location of giant molecular clouds.

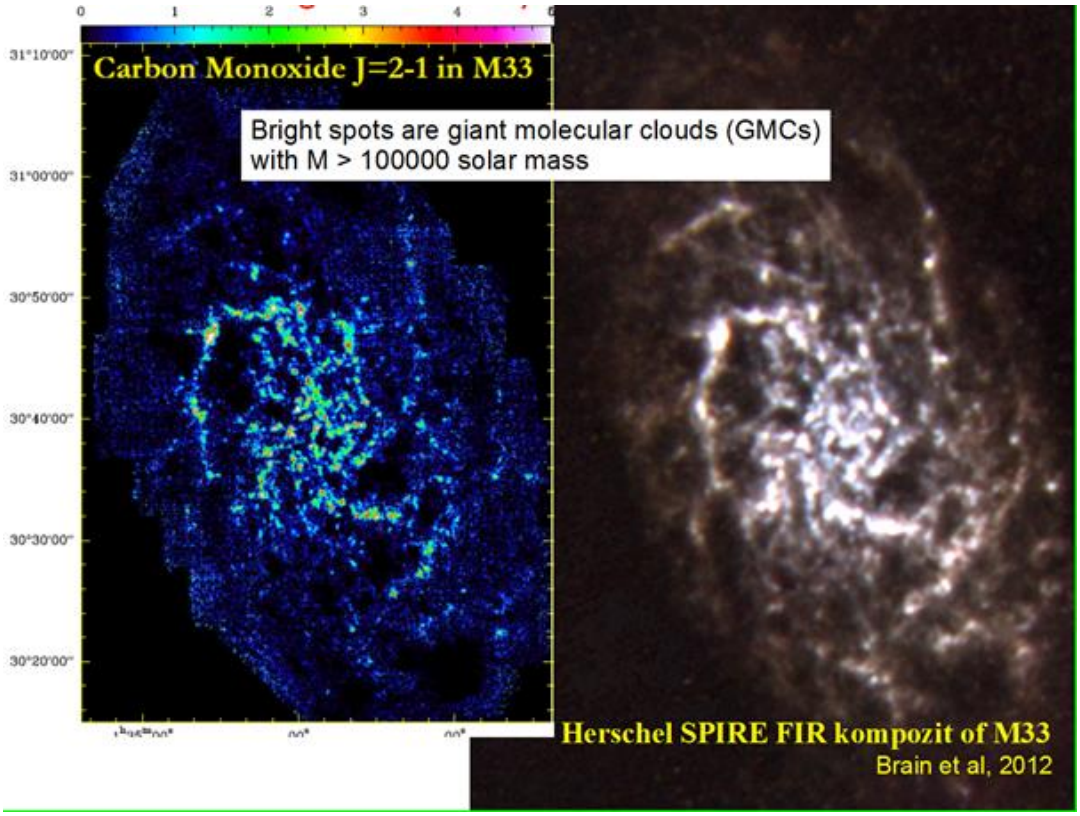

Figure 10.2 *Giant molecular clouds of M33 are seen in CO (2-1) 1.3mm line intensity as well as in the FIR continuum. (Kramer et al. 2010, Braine 2012).*

The multiphase spectral energy distribution is a combination of black body like continuum and narrower features in these wavelength ranges, whereas it is synchrotron radiation in the radio regime. As it is shown in Figure 10.1 the main components are (1) the hot MS stars and HII regions, (2) the non-ionizing stars, (3) the atomic and ionized interstellar gas, (4) the dust in HI, (5) the warm dust in HII regions, (6) cold dust in molecular clouds, (7) molecules in the gas phase of the ISM.

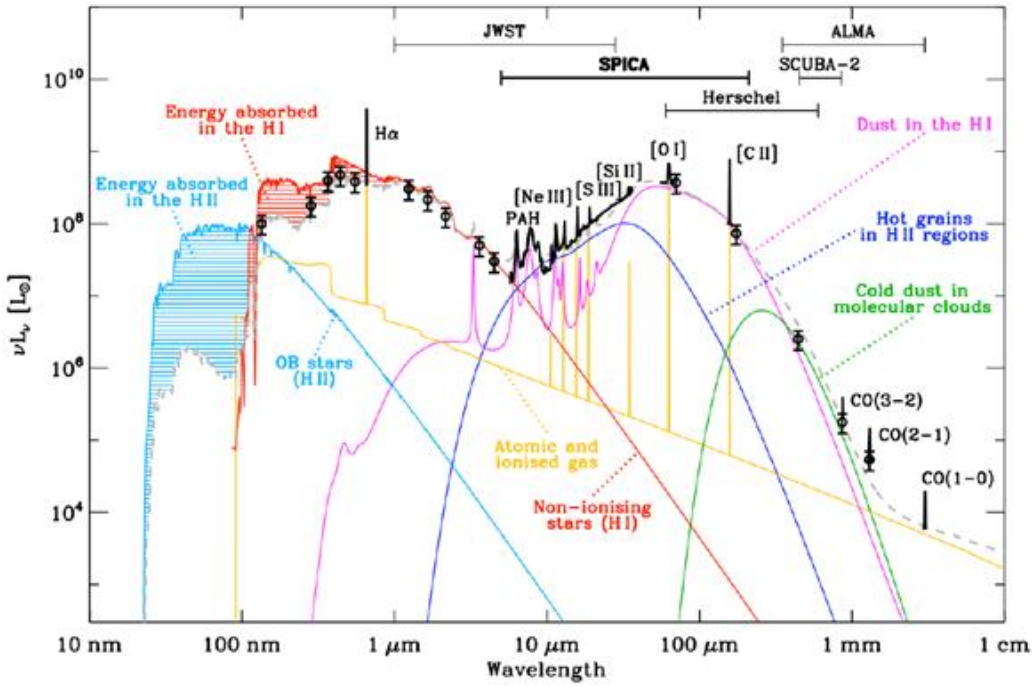

Figure 10.3: The prospective multiphase SED of a galaxy (the model of Galliano et al. 2008), highlighting the combined complexity of the stellar sources, the dust emission and the gas lines. This figure demonstrates the contribution of the various phases of the ISM to the total SED of a galaxy. In the top of the figure the wavelength ranges of the main infrared to millimetre observatories are overlaid. (Galliano et al. 2008**)**

Mid-IR spectra of the interstellar medium is dominated by the so called un-identified infrared (UIR) features. These may be there due to PAH emission. The results of a survey of these features is shown in Figure 10.3. There is no unanimous agreement on PAHs being the carriers of the UIR features. There are also competing models still being discussed, see e.g. Kwok & Zhang.

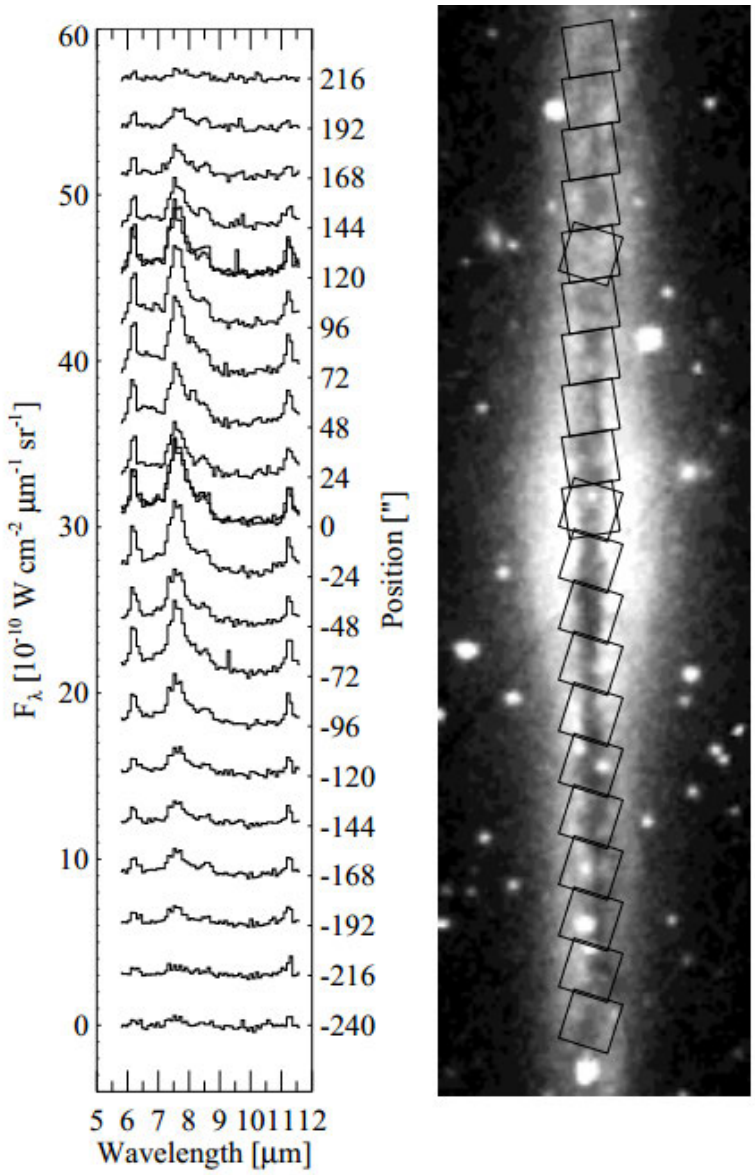

Figure 10.4: *UIR features in the edge on galaxy NGC891. PHT-SL spectra along the major axis of NGC 891. Optical B band image of NGC 891 from the Digital Sky Survey with the observed 24×24 arcsec areas superposed. For the central and the 120 arcsec N positions two spectra and two different aperture orientations corresponding to ISO orbits 656 and 788 are shown. NGC 891 is often regarded as a twin of our own Milky Way Galaxy. (Mattila et al. 1999, Mattila 2006)*

The dust properties of galaxies can be derived observing those in mid-IR and FIR. The "KINGFISH" project used the Herschel observatory to uncover the dust in nearby galaxies. Figure 10.5 displays their observations ordered according to the galaxy types in the so called Hubble tuning fork scheme.

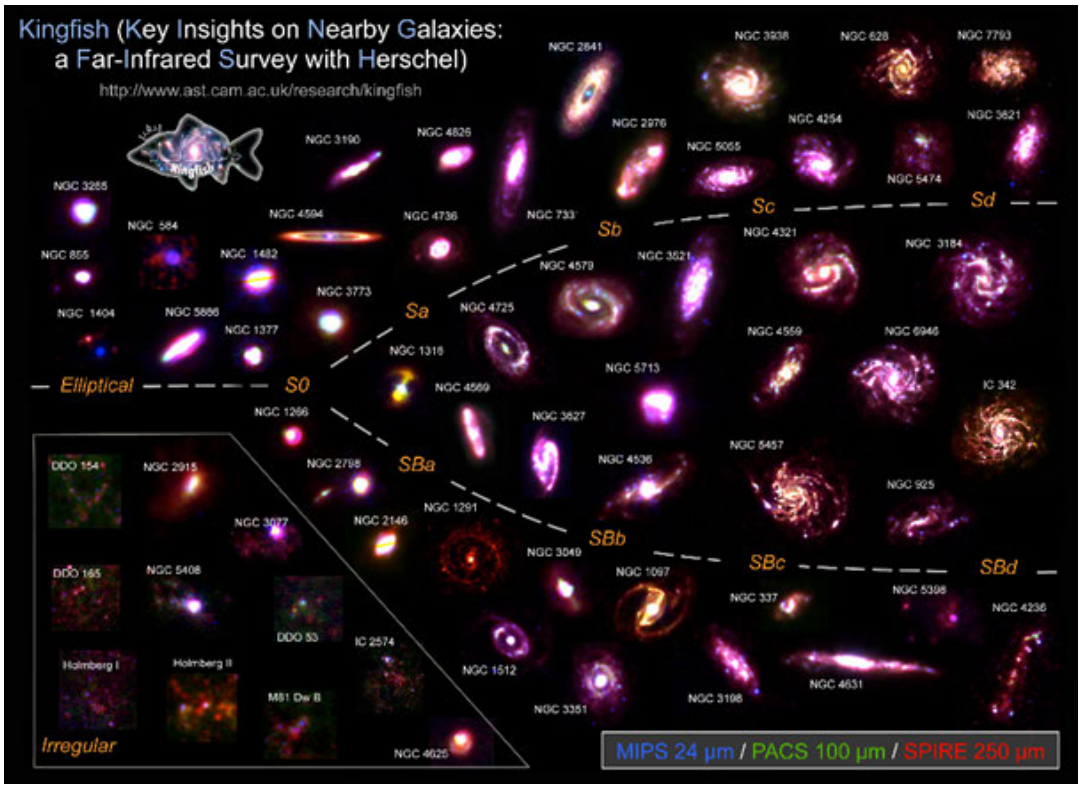

Figure 10.5: **Composite images created from Spitzer (SINGS) and Herschel (KINGFISH) observations.** Each individual image is a three-color composition showing : Blue: Spitzer/MIPS 24um observations tracing the warm dust heated by young stars in the star forming regions. Green: Herschel/PACS 100um observations tracing the cool dust (peak of the dust emission in the infrared). Red: Herschel/SPIRE 250um observations tracing the coldest phases of the dust. Find an interactive version at: http://herschel.cf.ac.uk/kingfish. See more information on KINGFISH at http://www.ast.cam.ac.uk/research/kingfish .

10.2 Luminous and ultraluminous galaxies

The galaxies at the highest infrared luminosities are called as Luminous (10^{11} $L\odot$ < L_{IR} < 10^{12} $L\odot$) and Ultra-Luminous (L_{IR} > 10^{12} $L\odot$) Infrared Galaxies, LIRGs and ULIRGs, respectively (see Wright, Joseph & Meikle 1984; Sanders et al. 1988a). These are in fact the most luminous objects in the local universe. They typically radiate 90% or more of their energy in the far-infrared. Many of these objects were discovered by the *IRAS* survey, and many were previously uncataloged. Multi-wavelength imaging surveys have shown that nearly all ULIRGs are found in systems which have undergone strong tidal perturbations due to the merger of pairs of gas-rich disk galaxies (Murphy et al. 2001a). All of the 10 nearest ultraluminous galaxies (Sanders et al. 1988a) are either merging systems or have tidal tails indicating a recent merger.

The large amounts of gas that are funneled into the centers of these mergers lead to intense star formation, the feeding of a central active galactic nucleus (AGN), extremely compact reservoirs of molecular gas, and infrared luminosities on the order of ten times their optical luminosities.

Ultraluminous ULIRGs have a space density that is a factor of 1.5 − 2 higher than that of optically selected QSOs, the only other known objects with comparable bolometric luminosities (Schmidt & Green 1983).

The dust in the central regions (r < 1 kpc) is in most cases heated predominantly by a starburst (SB) i.e. by recently formed massive stars but also combined with a significant heating by an AGN in the most luminous ULIRGs. The starburst occurs in a circumnuclear disk or ring typically located at radii r < 700 pc from the nucleus of the galaxy, and also contain large quantities of dust (Veilleux et al., 1999).

We may derive a star forming rate (SFR) as a function of infrared luminosity LFIR applying evolutionary stellar models to bursts of age 10-100 Myr, and adopting a standard IMF (Kennicutt, 1998):

$$SFR = 17.2 \times (L_{FIR} / 10^{-11} L_{\odot}) M_{\odot} yr^{-1} \quad (10.1)$$

The 5 main reasons why LIRGs and ULIRGs are so important as summarized by Perez-Torres (2012):

- U/LIRGs account for about 10% of the total radiant energy production and more than 20% of all the high-mass star-formation in the local universe (e.g., Brinchmann et al. 2004).
- The bulk of the energy radiated by ULIRG is infrared emission from warm dust grains heated by a central power source, or sources, whose nature (AGN, starburst, or both) is often unknown, but whose evolution is likely to be related.
- Essentially all LIRGs above ~10^{11} $L_{\odot}$ appear to be interacting galaxies, and all ULIRGs seem to be advanced merger systems. Thus they may represent an important stage in the formation of quasi-stellar objects.
- U/LIRGs are also of cosmological relevance, as they bear many similarities with starforming galaxies at high-z (e.g. local UV-bright starbursts are good analogs to Lyman Break Galaxies (e.g. Meurer et al. 1997).
- U/LIRGs are ideal laboratories to study the complex ecosystems of stars, gas, Black Holes, the interstellar medium (ISM), and test massive star and blackhole/starburst evolution, or probe the Initial Mass Function (IMF) of the high-mass stars.

Figure 10.6 compares ULIRGS, to starburst, disk and elliptical galaxies. We note that the combination of fine structure line ratios, PAH strengths, and continuum fitting (hot dust) provides an accurate assessment of the AGN/SB fraction in ULIRGS.

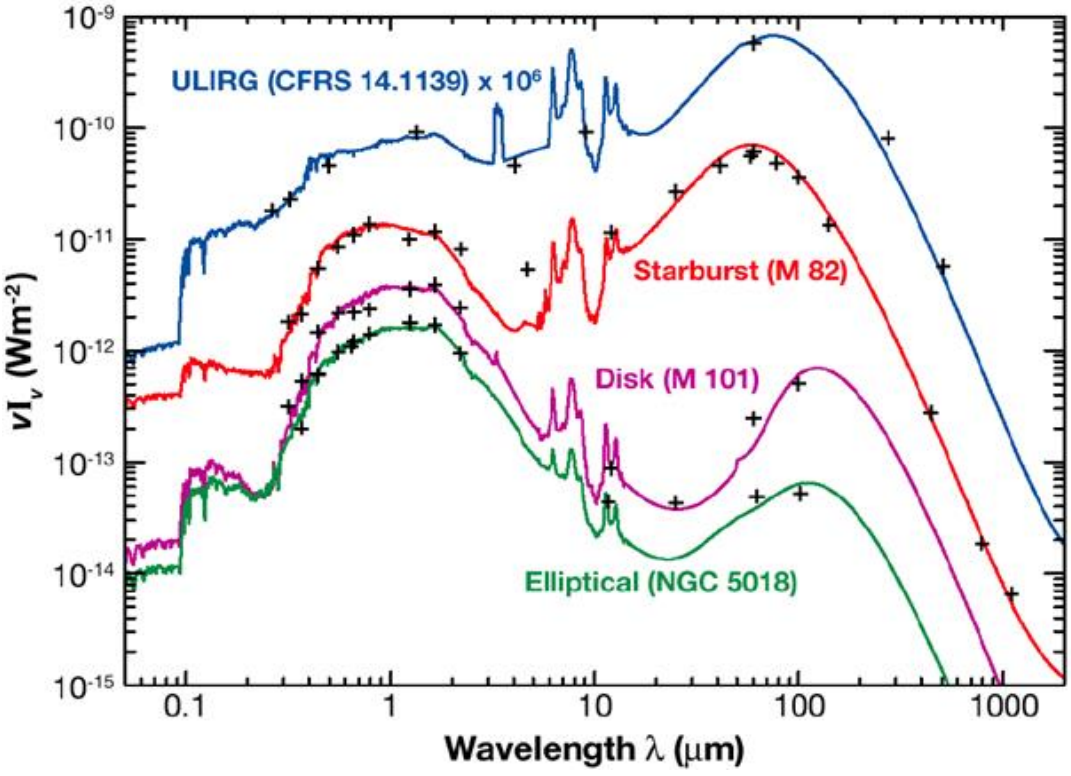

Figure 10.6: *Integrated spectral energy distributions of galaxies. The ULIRG is observed at redshift z=0.66 and is represented in the rest-frame.*

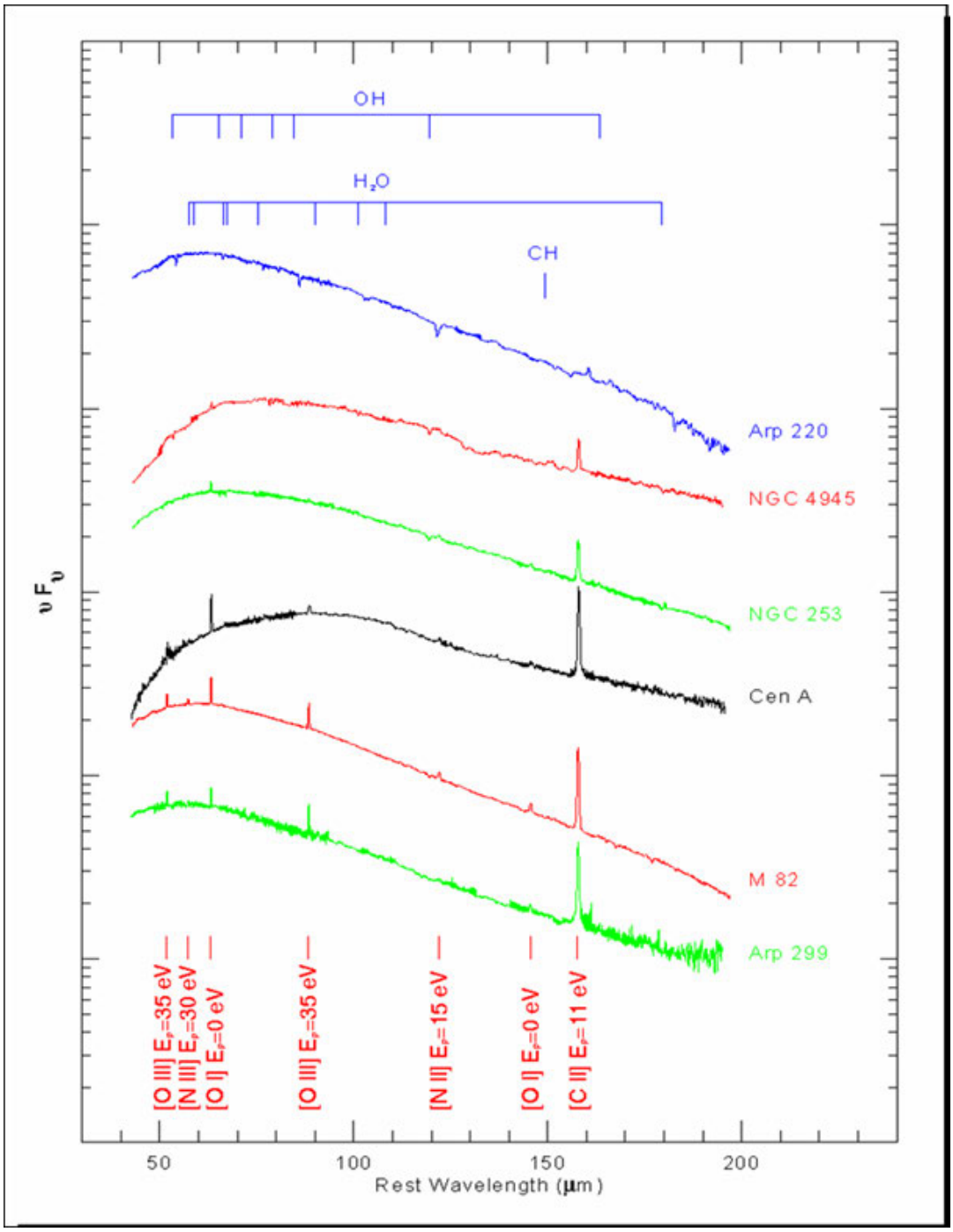

Figure 10.7: *Full ISO LWS spectra of 6 IR-bright galaxies, from Fischer et al. (1999)*
http://www.mpe.mpg.de/380785/Fischer.png

Atomic fine structure lines (OI, OIII, NII, NIII, CII) are important coolants in infrared bright galaxies (see Figure 10.7 for the lines in a few very actively star forming galaxies, where for example M82 is a starburst, Arp 220 is a merger).

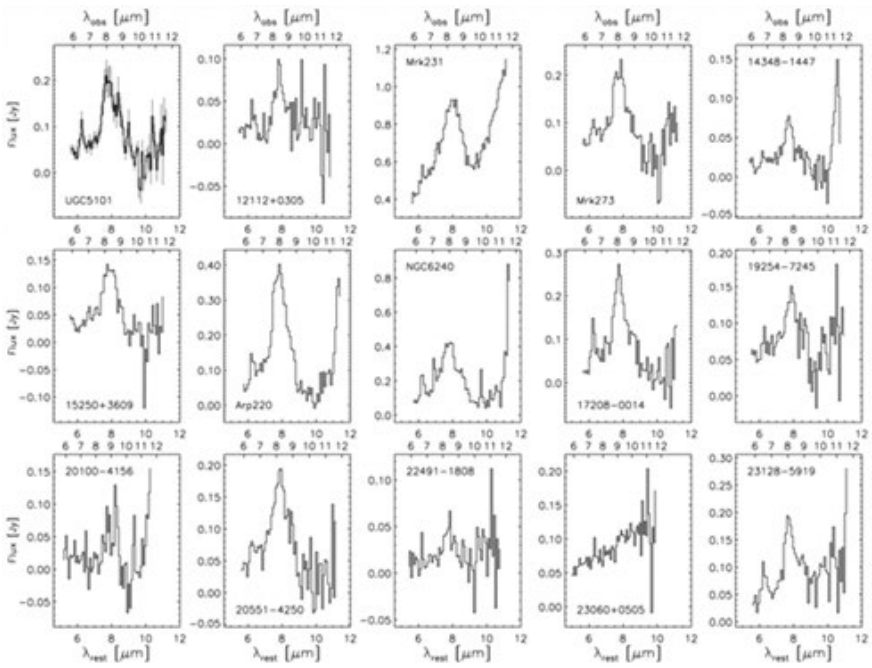

Figure 10.8: *ISOPHOT-S spectra of 15 ULIRGs. Observed wavelengths are shown at the top and rest wavelengths at the bottom of each spectrum (Genzel et al 1998).*

10.3 Gamma-ray bursters (GRBs)

GRBs are associated with mergers of compact stellar objects (neutron-stars or black-holes) or the death of the most massive stars (supernovae). GRB hosts were recently discovered because of the short-lasting optical emission of the afterglow, which is seen for less than a few weeks. GRB is a rare event in a galaxy (1 in 100000 years). GRBs are used probing theories of general relativity, black holes, cosmology, galaxy formation and evolution. GRB hosts are known in the local Universe as well as at very large distances, like GRB 090429B at $z = 9.4$ (Cucchiara et al. 2011). They are in any case linked with massive star formation, implicitly assuming the presence of large amount of interstellar medium to be present in the host galaxy. Surprisingly the metallicity of the host galaxies shows a large spread of more than two orders of magnitude, with no trend with redshift. We saw that the part of the UV and optical radiation of the star forming regions is reprocessed by the galactic dust, thus infrared radiation is a good measure of the star forming activity. We also note that already at $z > 1$ the UV part of the spectrum starts to be redshifted to the NIR. So we may have significant infrared radiation in the restframe spectrum as well in the redshifted spectrum for all redshifts. Most of the so called dark GRBs are optical faint because they are obscured by high dust extinction columns of the host galaxy. Figure 10.4 shows a GRB host at a moderate redshift of z=1.118.

Herschel FIR observations of GRBs were performed and the results are to be seen soon.

10.4 Dust at high redshifts

It may appear surprising that dust is so prominent in the high redshift Universe, where metallicity is expected to be much lower than it is at the local Universe. First of all we note that dust can be abundant also in low-metallicity star-forming dwarf galaxies (e.g., Madden et al. 2006). Recent theoretical developments support the assumption that significant amounts of dust can be created on short timescales by supernovae and by asymptotic giant branch stars (see eg. Valiante et al. 2009). It is still not yet clear how massive dusty starbursts occur and evolve, but it is expected that in very short timescales dust can be formed in an initially metal-free ISM as seen in a few luminous distant quasars. Finding dust at z=6 (Bertoldi et al. 2003) means it was present right after the re-ionization of the Universe.

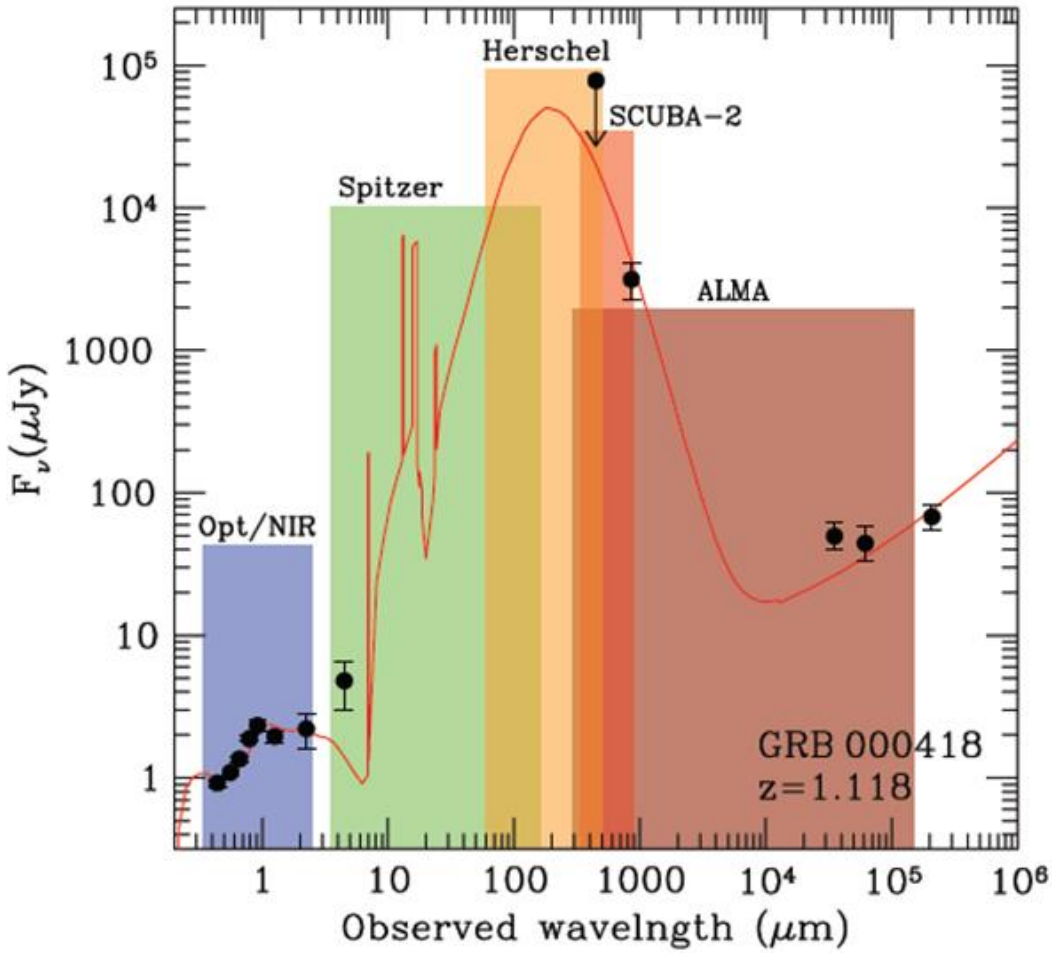

Figure 10.9: *Spectral energy distribution of a typical GRB host galaxy, the host of GRB 000418 at z = 1:118. Shaded areas show the coverage of present FIR, submm and radio telescopes. (Savaglio 2012)*

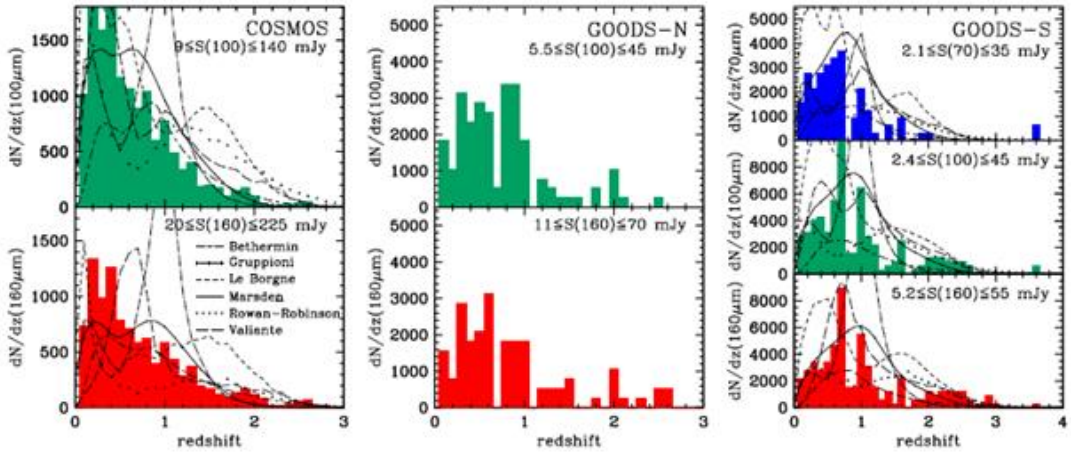

Figure 10.10: *Redshift derivative dN/dz for PACS-detected sources in COSMOS (left), GOODS-N (center) and GOODS-S (right), normalized to a 1 deg^2 area, and above the 80% photometric completeness limit. Black lines refer to models and are reported only at the GOODS-S and COSMOS depths for clarity sake. (Figrue 4. from Berta et al. 2011)*

10.5 The Cosmic Infrared Background

The extragalactic background light (EBL) is the relic emission of all processes of structure formation in the Universe. About half of this emission, called the Cosmic Infrared Background (CIB) is emitted in the 8–1000 μm range, and peaks around 150 μm. It is essentially due to the star formation (Puget et al. 1996; Fixsen et al. 1998; Hauser et al. 1998; Lagache et al. 1999; Gispert et al. 2000; Hauser & Dwek 2001; Kashlinsky 2005; Lagache et al. 2005).

The cosmic infrared background (CIB) is the second strongest component of the extragalactic background (the strongest being the cosmic microwave background). The extragalactic background is the accumulated light of distant, unresolved galaxies. The CIB is a relic radiation of the star and galaxy formation history of the Universe, therefore it is very important for cosmological and galaxy formation/evolution studies. Most of its light is a reprocessed starlight or other kind of radiation produced e.g. by active galactic nuclei: radiation emitted at optial, ultraviolet and X-ray wavelengths are absorbed by dust and re-emitted in the infrared due to its temperature. According to recent surveys, the CIB was mostly emitted by “main sequence” star forming galaxies (Nordon et al. 2012). The shape of the CIB is also affected by the fact, that most of its building sources are fairly redshifted. In the far-infrared the strongest contribtuion comes for sources at $1<z<2$, and this typical z-value is even higher in the submm. A summary of efforst to detect the CIB at various wavelengths is given in Hauser & Dwek (2001), including the results obtained e.g. from DIRBE, IRAS, ISO, HST, 2MASS data. Recent results either based on reprocess satellite observatory data (IRAS: Miville-Deschenes & Lagache 2005; and ISO: e.g. Kiss et al. 2001, Dole et al. 2003) or based on the measurements of the Spitzer Space Observatory (e.g. Dole et al. 2004 & 2006; Papovich et al. 2004).

The CIB spectral energy distribution (SED) is an important constraint for the infrared galaxies evolution models (e.g. Lagache et al. 2004; Franceschini et al. 2010; Le Borgne et al. 2009; Pearson & Khan 2009; Rowan-Robinson 2009; Valiante et al. 2009). It gives the budget of infrared emission since the first star. The distribution of the flux of sources responsible for this background is also a critical constraint.

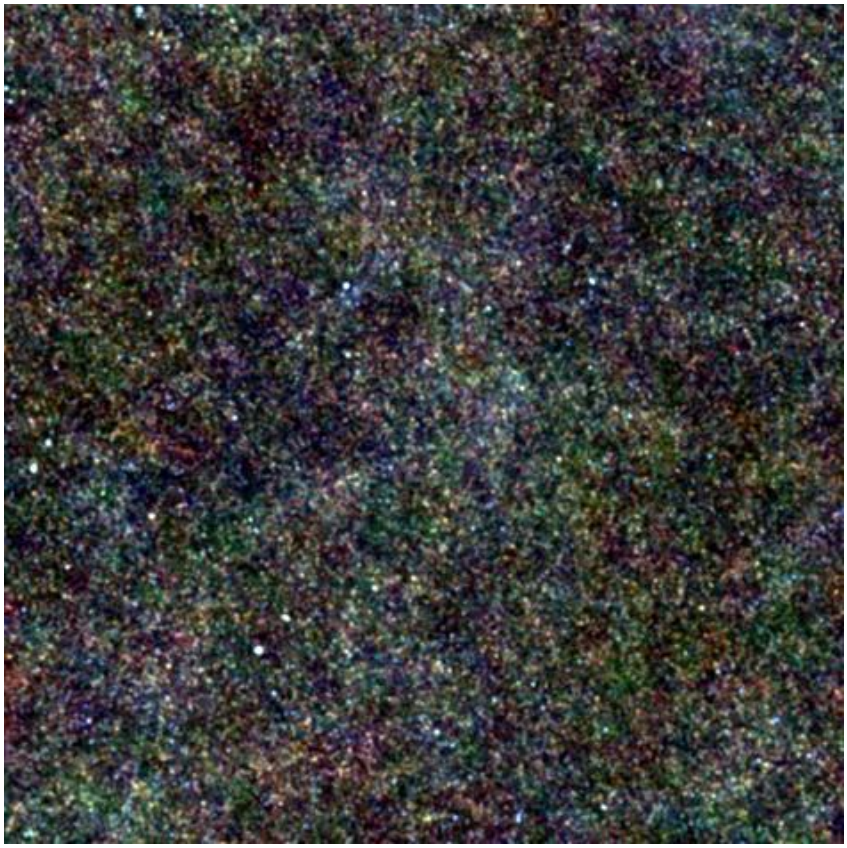

Figure 10.11: *The "Lockman Hole" region as seen by the Herschel Space Observatory. All of the little dots in this picture are distant galaxies. One of the typical ways to examine the CIB is to measure the collective light by galaxies identified in deep infrared images. Regions with very low Galactic surface brightness (such as the Lockman Hole North) are ideal for CIB studies. . Today source counts (statistical properties of all sources that could be*

identified) are far more important, especially with Herschel which could not be absolutely calibrated due to the warm mirror, but was able to perform surveys of sources very effectively. Image credit: ESA/Herschel/SPIRE/HerMES http://www.nasa.gov/mission_pages/herschel/herschel20110216i.html

Today source counts (statistical properties of all sources that could be identified) are far very important estimating the CIB. Herschel was not absolutely calibrated due to its warm mirror, but was able to perform surveys of point sources very effectively.

Berta et al. (2011) defined number counts combining Herschel PACS observations of the GOODS-S, GOODS-N, Lockman Hole and COSMOS areas. Their survey spans from 1 mJy to few hundreds mJy.

The $z_{50\%}$ *half-light redshift* is defined as the redshift up to which the sum of the flux from extragalactic sources with $z < z_{50\%}$ gives 50% of the total flux observed in the given wavelength or band. Apperently the half-light redshift varies with wavelength, $z_{50\%}$ =0.58, 0.67 and 0.73 at the three PACS wavelengths of 70μm 100μm and 160μm respectively. The distribution moves towards earlier epochs at longer wavelengths: while the 70 micron CIB is mainly produced by z<=1.0 objects, the contribution of z>1.0 sources reaches 50% at 160 micron. Most of the CIB resolved in the three PACS bands was emitted by galaxies with infrared luminosities 10^{11} L_{Sun} < L_{FIR} <10^{12} L_{Sun}.

The finding that more than half of the resolved CIB was emitted at redshift z≤1 may contradict with earlier assumptions on the star forming history of the Universe.

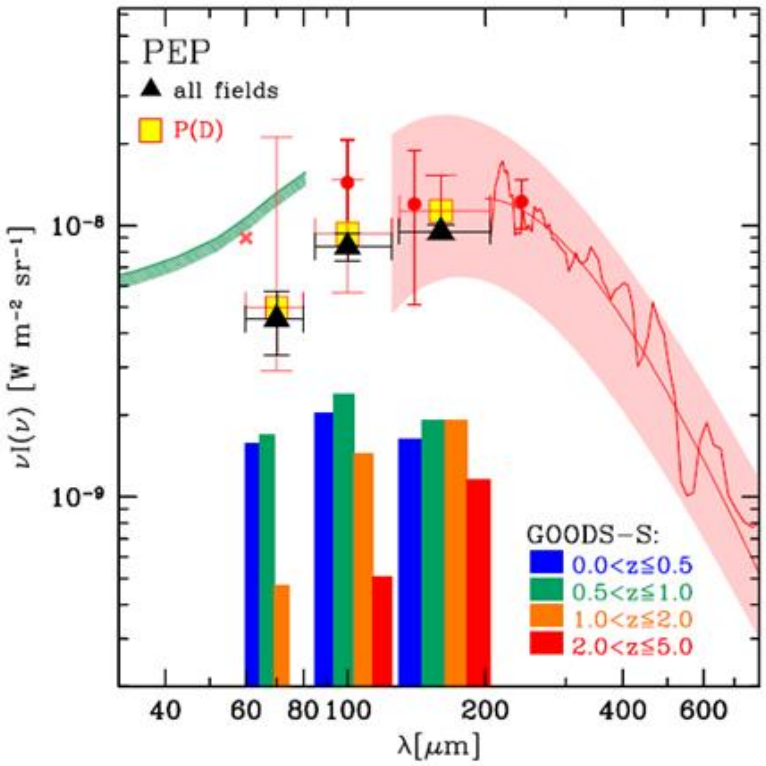

Figure 10.12: *The cosmic infrared background (Fig 13. from Berta et al. 2011). Black filled triangles represent the total CIB emitted above the PEP flux limits, based on resolved number counts in GOODS-S, GOODS-N, Lockman Hole and COSMOS. Yellow squares belong to the P(D) analysis in GOODS-S. Histograms denote the*

contribution of different redshift bins to the CIB, over the flux range covered by GOODS-S. Literature data include: DIRBE measurements (filled circles, 1σ errors), FIRAS spectrum (solid lines above 200μm), modified Black Body (shaded area), 60μm IRAS fluctuation analysis (cross), and γ-ray upper limits (green hatched line below 80μm)

References and further reading to the chapter:

Berta, S. et al. 2011: *"Building the cosmic infrared background brick by brick with Herschel/PEP"*, A&A, 532, 49

Bertoldi, F. et al. 2003: *"Dust emission from the most distant quasars",* A&A, 406, L55

Braine, J. 2012: *"HERM33ES The Herschel M33 Extended Survey*, http://herschel.esac.esa.int/FirstResultsSymposium/presentations/B11_BraineJ_HERM33ES.pdf

Brinchmann, J. et al. 2004: *"The physical properties of star-forming galaxies in the low-redshift Universe"*, MNRAS, 351, 1151

Cucchiara, A. et al. 2011: *"A Photometric Redshift of z ~ 9.4 for GRB 090429"*, ApJ, 736, 7

Dole, H., Lagache, G., Puget, J.-L. 2003: *"Predictions for Cosmological Infrared Surveys from Space with the Multiband Imaging Photometer for SIRTF"*, ApJ, 585, 617

Dole, H., Lagache, G., Puget, J.-L., et al. 2006: *"The cosmic infrared background resolved by Spitzer. Contributions of mid-infrared galaxies to the far-infrared background"*, A&A, 451, 417

Dole, H., Le Floc'h, E., Pérez-González, P. G. et al. 2004: *"Far-infrared Source Counts at 70 and 160 Microns in Spitzer Deep Surveys"*, ApJS, 154, 87

Fischer et al. 1999: *"An LWS spectroscopic survey of infrared bright galaxies"*, ESASP, 427, 817

Fixsen, D. J., Dwek, E., Mather, J. C., Bennett, C. L., & Shafer, R. A. 1998: *"The Spectrum of the Extragalactic Far-Infrared Background from the COBE FIRAS Observations"*, ApJ, 508, 123

Franceschini, A., Rodighiero, G., Vaccari, M., Berta, S., Marchetti, L., Mainetti, G. 2010: *"Galaxy evolution from deep multi-wavelength infrared surveys: a prelude to Herschel"*, A&A, 517, 74

Fritz, J., Franceschini, A. & Hatziminaoglou, E. 2006: „*Revisiting the infrared spectra of active galactic nuclei with a new torus emission model*", MNRAS, 366, 767

Galliano, F., Dwek, E. and Chanial, P. 2008: *"Stellar Evolutionary Effects on the Abundances of Polycyclic Aromatic Hydrocarbons and Supernova-Condensed Dust in Galaxies"*, ApJ, 672, 214

Genzel, R., Lutz, D., Sturm, E. et al. 1998: **„***What Powers Ultraluminous IRAS Galaxies?"*, ApJ 498, 579

Gispert, R., Lagache, G., & Puget, J. L. 2000: *"Implications of the cosmic infrared background for light production and the star formation history in the Univers"*, A&A, 360, 1

Hauser, M. G., Arendt, R. G., Kelsall, T., et al. 1998: *"The COBE Diffuse Infrared Background Experiment Search for the Cosmic Infrared Background. I. Limits and Detection"*, ApJ, 508, 25

Hauser, M.G., Dwek, E., 2001: *"The Cosmic Infrared Background: Measurements and Implications"*, ARA&A, 39, 249

Johnson, H. L. 1966: *"Infrared Photometry of Galaxies"*, ApJ, 143, 187

Kashlinsky, A. 2005: *"Cosmic infrared background and early galaxy evolution [review article]"*, Phys. Rep., 409, 361

Kennicutt, Jr. R. C. 1998: *"Star Formation in Galaxies Along the Hubble Sequence"*, ARA&A, 36, 189

Kiss, Cs., Abraham, P., Klaas, U., Lemke, D., Juvela, M., 2001: *"Sky confusion noise in the far-infrared: Cirrus, galaxies and the cosmic far-infrared background"*, A&A, 379, 1161

Klaas, U. et al. 2001: *„Infrared to millimetre photometry of ultra-luminous IR galaxies"*, A&A, 379, 823

Kramer, C. et al. 2010, *"PACS and SPIRE photometer maps of M 33: First results of the HERschel M 33 Extended Survey (HERM33ES)"*, A&A, 518, 67

Kwok, S. & Zhang, Y. 2011: *"Mixed aromatic-aliphatic organic nanoparticles as carriers of unidentified infrared emission features"*, Nature, 479, 80

Kwok, S. & Zhang, Y. 2013: *"Unidentified Infrared Emission Bands: PAHs or MAONs?"*, ApJ, 771, 5

Lagache, G., Abergel, A., Boulanger, F., D´esert, F. X., & Puget, J.-L. 1999: *"First detection of the warm ionised medium dust emission. Implication for the cosmic far-infrared background",* A&A, 344, 322

Lagache, G., Dole, H., Puget, J.-L., et al. 2004: *"Polycyclic Aromatic Hydrocarbon Contribution to the Infrared Output Energy of the Universe at z ~= 2"*, ApJS, 154, 112

Le Borgne, D., Elbaz, D., Ocvirk, P., & Pichon, C. 2009: *"Cosmic star-formation history from a non-parametric inversion of infrared galaxy counts"*, A&A, 504, 727

Madden, S. C. et al. 2006: *"ISM properties in low-metallicity environments"*, A&A, 446, 877

Mattila, K. 2006: privet communication

Mattila, K. 2006: *"The 1-μm discontinuity in the extragalactic background light spectrum: an artefact of foreground subtraction"*, MNRAS, 372, 1253

Mattila, K. et al. 1999: *"Detection of widely distributed UIR band emission in the disk of NGC 891"*, A&A, 342, 643

Meurer G. R. et al. 1997: *The Panchromatic Starburst Intensity Limit at Low and High Redshift*, AJ, 114, 54M

Miville-Deschenes, M.-A., Lagache, G., 2005: *"IRIS: A New Generation of IRAS Maps"*, ApJS, 157, 302

Murphy, T. W. Jr., Soifer, B.T., Matthews, K., & Armus, L. 2001a: *"Age Dating Ultraluminous Infrared Galaxies along the Merger Sequence"*, ApJ, 559, 201

Neugebauer, G., Becklin, E. and Hyland, A. R. 1971: *"Infrared Sources of Radiation"*, ARA&A, 9, 67

Nordon, R. et al. 2012: *"The Impact of Evolving Infrared Spectral Energy Distributions of Galaxies on Star Formation Rate Estimates"*, ApJ, 745, 182

Papovich, C., Dole, H., Egami, E., et al., 2004: *"The 24 Micron Source Counts in Deep Spitzer Space Telescope Surveys"*, ApJS, 154, 70

Pearson, C., & Khan, S. A. 2009: *"Submillimetre surveys: the prospects for Herschel"*, MNRAS, 399, L11

Pérez-Torres, M. A. 2013: *"Digging deep into the ULIRG phenomenon: When radio beats dust"*, Highlights of Spanish Astrophysics VII, Proceedings of the X Scientific Meeting of the Spanish Astronomical Society (SEA), held in Valencia, July 9 - 13, 2012, Eds.: J.C. Guirado, L.M. Lara, V. Quilis, and J. Gorgas., pp.35-46

Puget, J.-L., Abergel, A., Bernard, J.-P., et al. 1996: *"Tentative detection of a cosmic far-infrared background with COBE"*, A&A, 308, L5

Puget, J.-L., Lagache, G., Clements, D. et al. 1999: *"FIRBACK. I. A deep survey at 175 microns with ISO, preliminary results"*, A&A, 345, 29

Rowan-Robinson, M. 2009: *"A new model for infrared and submillimetre counts"*, MNRAS, 394, 117

Sanders, D. B.et al. 1988a: *"Ultraluminous infrared galaxies and the origin of quasars"*, ApJ, 325, 74

Savaglio, S. 2012: *"Gamma-ray burst host galaxies at low and high redshift"*, AN, 333, 480

Schmidt, M., & Green, R.F. 1983: *"Quasar evolution derived from the Palomar bright quasar survey and other complete quasar surveys",* ApJ, 269, 352

Valiante, R.et al. 2009: *"Stellar sources of dust in the high-redshift Universe"*, MNRAS, 397, 1661

Valiante, E., Lutz, D., Sturm, E., Genzel, R., & Chapin, E. 2009: *"A Backward Evolution Model for Infrared Surveys: The Role of AGN- and Color-L $_{TIR}$ Distributions"*, ApJ, 701, 1814

Veilleux, S., Sanders, D. B., & Kim, D.-C. 1999: *"New Results from a Near-Infrared Search for Hidden Broad-Line Regions in Ultraluminous Infrared Galaxies"*, ApJ, 522, 139

Wright, G. S., Joseph, R. D., & Meikle, W. P. 1984: *"The ultraluminous interacting galaxy NGC6240"*, Nature, 309, 430

http://herschel.cf.ac.uk/kingfish

http://www.ast.cam.ac.uk/research/kingfish

Chapter 11. The infrared confusion

11.1 Confusion noise

Imagine that we have an ideal telescope in space, outside Earth's atmosphere, that has zero instrument noise. Can we perform photometry of a point source with an infinite accuracy with this equipment? Certainly not, mostly because the sky around our target is not empty. If our target is faint, it may be outshined by other sources or sky structures in its vicinity; or it may be so close to another source that we cannot separate them. Independently of the capabilities of our instruments, the sky background sets a limit on the detectability of our targets – this phenomenon is usually referred to as *confusion noise*. By definition, confusion noise is the uncertainty in the determination of point source flux due to the uncertainty in the determination of the background flux, hence can be expressed in [Jy] in most cases. When we talk about confusion noise we usually consider the *astrophysical* components only. Other components of the background related to the instrument (e.g. straylight) or to the atmosphere (airglow or other telluric contamination) are not counted as confusion noise components. To contribute to the confusoin noise, the background has to be stohastic, i.e. it has to change from one place to the other in an unpredictable way (a random field). A background that is smooth or changes from place to place in a predictable way (e.g., a periodic one) does not produce any confusion. A background may be intrinsically diffuse (like the interstellar medium) or may be the accumulated light of unresolved sources (like the extragalactic background, see below).

The sky backgrounds are usually composed of several components. The first mathematical description of confusion noise was introduced in the 1970's in radio astronomy (Condon 1974), and described the common effect of an ensemble of discrete point sources for the measurement uncertainty of single sources. There are two important criteria to clearly detect a point (or compact) source: the source flux has to be well above the average fluctuation amplitude of the background (photometric criterium) and the source has to be far enough from sources of similar brightness so that they could be detected individually (source density criterium). These two criteria together set the confusion limit: above this level compact sources can be clearly detected (see e.g. Dole et al. 2003, for an introduction).

In typical optical measurements the confusion limit is not encountered. Exceptions are e.g. the dense star clusers, where the source density criterium is matched. In the infrared, confusion limits, especially the photometric criterium, often have a serious impact on the measurements. This is partly due to the characteristics of infrared detectors -- especially their poor resolving power compared to those working in the optical -- and partly due to the astrophysical properties of the infrared sky background.

It has to be noted, that the interpretation of confusion noise is different in an unbiased survey (when we want to detect all sources above a certain limit) and when observing an individual source, that is known to exist at a certain sky position (and is detected e.g. at shorter wavelengths). In the latter case it is possible in certain conditions to integrate below the confusion limit set by the whole ensemble of sources.

11.2 Confusion limit

To calculate the actual confusion limit, we have to evaluate both the photometry and the source density criterion – as mentioned above, the larger of the two is going to define the actual limit. When a background component is made of discrete sources, then the confusion noise is defined as:

$$\sigma_c^2 = \int f^2(\vartheta,\phi)\,d\vartheta\,d\phi \int_0^{S_{lim}} S^2 \frac{dN}{dS}\,dS \qquad (11.1)$$

, where f(θ,φ) is the two-dimensional beam profile, S is the source brightness and dN/dS is the differential source count function (number of sources per brightness interval, usually expressed in [Jy^{-1} sr^{-1}]). The integration runs for all sources below the confusion limit, S_{lim}. The photometric criterion is defined by choosing a signal-to-noise ratio q_{phot} for the faintest detectable source:

$$q_{phot} = \frac{S_{\lim}}{\sigma_c(S_{\lim})} \tag{11.2}$$

The actual confusion limit has to be calculated from this implicit equation: we calculate σ_c for decreasing (or increasing) S_{lim} values until the ratio of these two numbers equals to q_{phot}.

To set the source density criterion we define a minimum degree of completeness of the detection of sources above the limiting flux S_{lim} – some of the sources with fluxes above S_{lim} cannot be detected because they are too close to another source with a flux above S_{lim}. If the spatial distribution of sources is Poissonian, the probability of finding a nearest neighbour with $S \geq S_{lim}$ at a distance closer than the minimum angular separation θ_{min} , is given by:

$$P(< \theta_{min}) = 1 - \exp(-\pi N \theta^2_{min}) \tag{11.3}$$

A typical acceptable completeness limit is 90%, i.e. P(<min) is usually set to 0.1. The minimum angular separation is used to be expressed using the full width at half magnitude (FWHM) of the beam $\theta_{min} = k\theta_{FWHM}$, where k is a constant, typically between 0.8 and 1.

In a typical example, one can choose e.g. k=0.8, i.e. we require that the two sources should be separated by at least $0.8\theta_{FWHM,}$). P is usually set to 10%, so 90% of the sources should be detectable above the source density limit SSDC. In the same way as for the photometry criterion we define a corresponding qSDC with: $q_{SDC} = S_{SDC}/\sigma_{SDC.}$

As the typical area of a measuring aperture is $\Omega = 1.14\ \theta_{FWHM}^2$ in the example above $N_{SDC} = 0.0597 / \Omega$ [sources per beam]. This quantity is difficult to interpret therefore usually its reciprocal is used – the value above would correspond to 16.7 [beam per source], i.e. on average there would be one source above the flux limit in an area corresponding to 16.7 times the area of the measuring aperture (Ω), and the detection probability would be 90% due to nearby sources.

In the case of a diffuse background the structure is usually characterized by the structure function, which is:

$$S(\underline{\theta}) = \left\langle \left| F(\underline{x} - \underline{\theta}) - F(\underline{x}) \right|^2 \right\rangle \tag{11.4}$$

where F(x) is the flux at a specific sky position and θ is the separation of the two sky positions. The average runs over all positions (x) of a specific map. In the general one dimensional case S(θ) can be calculated by the following integral:

$$S(\theta) = \frac{1}{\tau} \int_{-\infty}^{+\infty} \Pi\left(\frac{x}{r}\right) \left| F(x-\theta) - F(x) \right|^2 dx \tag{11.5}$$

where $\frac{1}{\tau}\Pi\left(\frac{x}{r}\right)$ is the window function. In this interpretation the structure function is calculated in the spatial domain. However, it can also be calculated in the Fourier (spatial frequency) domain:

$$S(\theta) = \frac{1}{\tau} \int_{-\infty}^{+\infty} \sin\ c(s\tau) \left| \exp(-2\pi i \theta s) - 1 \right| \left| \overline{F}(s) \right|^2 ds \tag{11.6}$$

where F(s) is the Fourier transform of the observed sky brightness F(x). The reason for this transformation is that diffuse backgrounds are usually characterized by their Fourier power spectrum $P=|F(s)|^2$. In many cases the power spectrum follow a power law, and can be described as:

$$P = P_0 \left(\frac{f}{f_0} \right)^{\alpha} \tag{11.7}$$

where α is the spectral index, P is the Fourier power at the spatial frequency f, and P_0 is the power at the spatial frequency f_0. It can be shown that for such a power-law power spectrum the structure function will have the form:

$$S \propto \left(\frac{d}{d_0} \right)^{2-\alpha} P_0 \tag{11.8}$$

where d is the size of the measuring aperture and d_0 is a reference aperture size. On the other hand, S(θ) is just the expected value of the fluctuation amplitude (variation of sky brightness from one place to the other), and hence the corresponding mean scatter, or confusion noise is:

$$N(\theta) = \sqrt{S(\theta)\Omega} \tag{11.9}$$

(multiplied by the beam or measuring aperture area Ω for convenience). If we are now back to the spatial domain again, the confusion noise due to a diffuse, power-law background will be:

$$N(\theta) \propto \left(\frac{d}{d_0} \right)^{1-\alpha/2} P_0^{1/2} \tag{11.10}$$

11.3 Confusion noise in the observed flux densities

Confusion noise is the uncertainty in the determination of point source fluxes due to the stochastic background. The point source flux is as equation (11.11) shows the difference of the measured $F_{obs}(\lambda)$ source + background flux and the $F_{bg}(\lambda)$ background flux.

When the diffuse background sky brightness has a random variation from place to place and/or there are unresolved sources, then there is an unpredictable $F_{bg}(\lambda)$ flux in the beam and the source flux $F_s(\lambda)$ can not be derived with a better accuracy than $F_s(\lambda) \pm \delta F_{bg}(\lambda)$, where $\delta F(\lambda)$ the confusion, and $F'_{bg}(\lambda)$ is our estimation of the background flux in the beam.

$$F_{obs}(\lambda) = F_s(\lambda) + F_{bg}(\lambda) = F_s(\lambda) + F'_{bg}(\lambda) + \delta F_{bg}(\lambda) \tag{11.11}$$

The sky background is usually composed of several components (see chapter 4), and we must account for all those to have an estimate of $\delta F_{bg}(\lambda)$.

11.4 The infrared confusion noise

The infrared the sky background is strong compared to the brightness of typical sources, and as a consequence, the confusion noise caused by these background components is also relatively strong.

The infrared sky brightness have the following main components (see Figure 4.4):

1. Emitting particles in Earth's atmosphere (specific ions, molecules and airglow). For space-borne instruments these effect are do not play a role.

2. Faint stars in the Milky Way. This is an important component for near- to mid-infrared wavelengths, but has a negligible contribution for longer wavelengths ($\lambda > 70\mu m$)

3. Zodiacal Light and minor bodies in the solar system. This is the dominant component of the sky background at MIR wavelengths.

4. The Galactic cirrus emission -- quasi-thermal emission of dust in weak gas clouds in the Milky Way. This is the dominant component for wavelengths $\lambda > 70\mu m$.

5. The extragalactic background -- accumulated and unresolved light of distant galaxies.

6. The cosmic microwave background also have an important contribution in strength, but the fluctuation amplitudes are small, and well below the detection limits of PACS and SPIRE.

For space-borne FIR instruments the important confusion noise components are astrophysical. These are (1) dust and minor bodies in the solar system, (2) the Galactic cirrus emission, (3) and the extragalactic background (see Chapter 10).

If we consider a specific spatial resolution (a specific telescope/instrument and flux extraction method) the combined confusion noise can be calculated as:

$$\sigma_{tot}^2 = \sigma_{CIB}^2 + \sigma_{cirr}^2 + \sigma_{ZL}^2 + \ldots \qquad (11.12)$$

In this example σ_{tot} is the total confusion noise, and σ_{CIB}, σ_{cirr} and σ_{ZL} are the confusion noise components due to the cosmic infrared background, the Galactic cirrus, the Zodiacal emission, respectively, and there may be additional components not accounted here.

While the cosmic infrared background is an important contribution at all infrared wavelengths (from 1μm to 300μm, with a peak in brightness at ~100μm) to the total sky brightness and to the confusion noise, not all components have notable contributions at all wavelengths. At shorter wavelengths (<10μm) faint Galactic stars are still bright enough to give an important contribution. Galactic cirrus is important for wavelengths > 50μm. The Zodiacal emission and the main belt asteroids contribute mostly at mid-infrared (10-40μm) wavelengths. Even the cosmic microwave background has a notable contribution to the total sky brightness at ~300μm and at longer wavelengths. However, it has only very small fluctuations ($<10^{-4}$K of the 2.7K black body), therefore its contribution to the confusion noise is negligible. In the case of the other components the typical fluctuations amplitudes with respect to the brightness of that specific component are in the order of a few per cent.

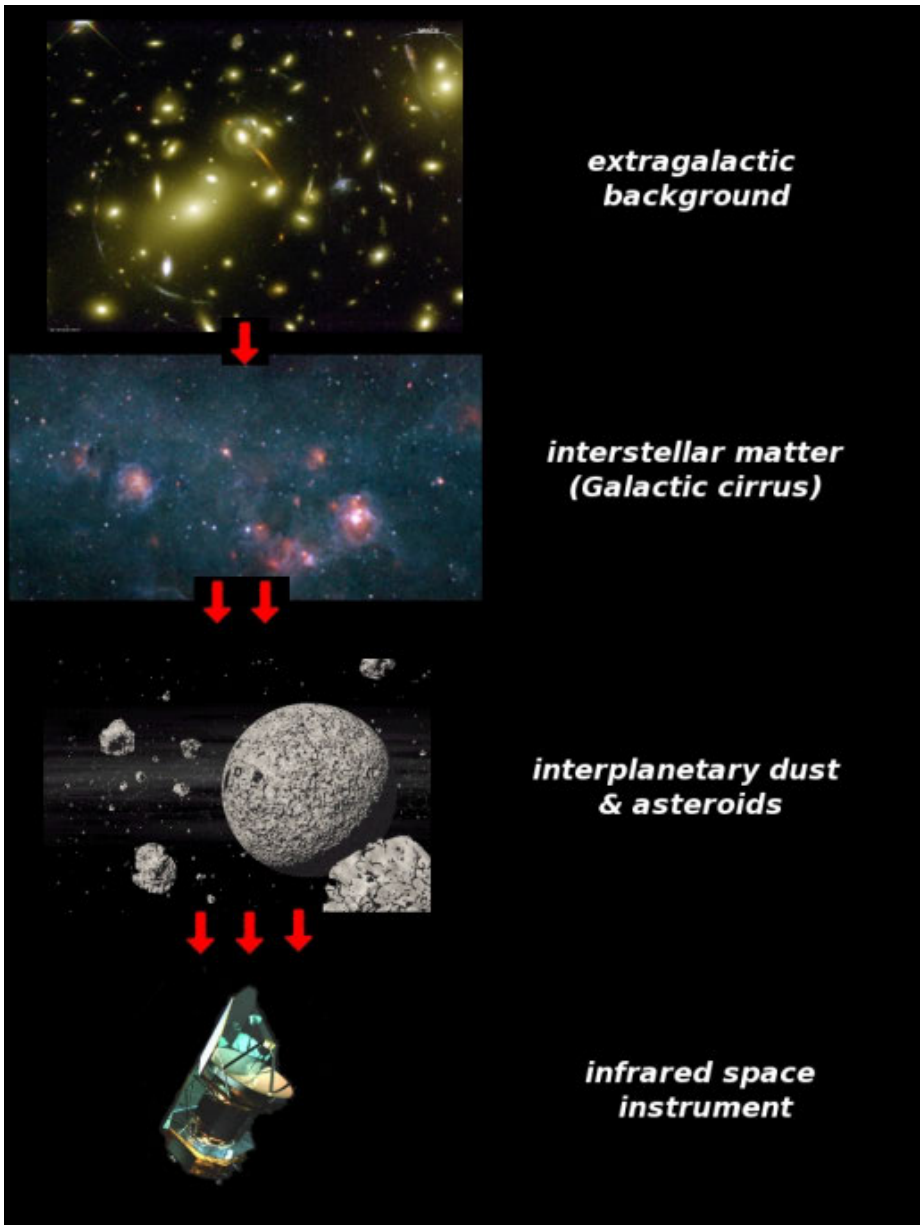

Figure 11.1: *Main components of the far-infrared confusion noise*

11.5 Estimating the components of the infrared confusion noise

11.5.1 Sources of FIR emission in the Solar System

There are two major sources of FIR and sub-mm emission in the Solar System that can contribute to the confusion noise. These are the thermal emission of dust particles of the Zodiacal Light nebula, with a typical temperature of ~280K, and the thermal emission of the asteroid populations.

The zodiacal light emission is a major contributor to the sky brighness throughout the infrared wavelength regime, with a superior contribution in the mid-infrared. The declining spectral energy distribution towards longer wavelengths make the ZL emission less important for the FIR and sub-mm wavelengths. Moreover, this emission is quite smooth, and small-scale fluctuations – which are necessary to produce confusion noise -- are not present in the ZL nebula, at least at or above the arcminute scale angular resolutions reached by ISOPHOT, as was shown by Ábrahám et al. (1997), see on Figure 11.2. However, due to the recent improvements in infrared detector sensitivity, the Zodiacal emission will be the main limiting factor for future space instruments working in this wavelength domain.

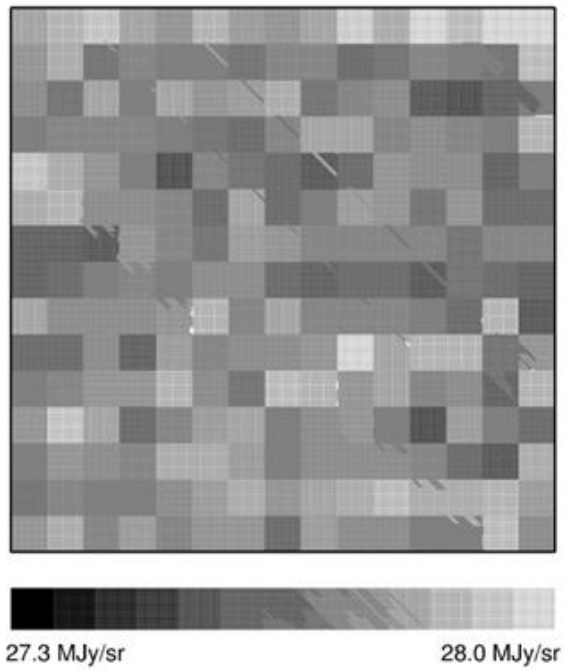

Figure 11.2: *ISOPHOT drift-corrected map obtained at the North Galactic Pole. Main components of the far-infrared confusion noise (Figure 1 from Ábrahám et al. 1997)*

Smaller scale fluctuations, in principle, are likely to exist, but the presence of such structures was not yet confirmed by recent observations of the Spizter Space Telescope (see e.g. the Spitzer GO program "The Production of Zodiacal Dust by Asteroids and Comets" by M. Sykes). Therefore, currently no contribution of ZL confusion noise is considered in the Herschel Confusion Noise Estimator. However, this is a field of active research, and new results may be implemented in the HCNE in later versions.

Small (~km sized) bodies in the main asteroid belt could contribute significantly to the confusion noise at mid-infrared wavelengths in some observing configurations, especially when observing them around opposition from Earth (this is usually not allowed for space instruments due to their visibility constraints). N and Q bands are the most affected by this phenomenon (Kiss et al. 2008). Since these bodies are essentially point sources, the actual strength of their confusion noise contribution can be calculated in a way similar to that of the cosmic infrared background (see above), if their differential source count function (dN/dS) is known.

It is an important question whether faint asteroids, which are individually below the detection limits, could contribute significantly to the confusion noise of space-borne FIR and sub-mm instruments, especially those of Herschel. In a recent work Kiss et al. (2006) investigated this issue. In order to take into account these asteroids, a reliable statistical model was needed, including minor bodies smaller than a few kilometers in diameter. Recently Tedesco et al. (2005) presented the "Statistical Asteroid Model" (hereafter SAM). This model is based on a population of $\sim 1.9 \times 10^6$ asteroids obtained from the complete known asteroid sample (as of 1999), plus extrapolation of the size-frequency distribution (SFD) of 15 asteroid dynamical families and three background populations, to a diameter

limit of 1km. The validity of the SAM was demonstrated by comparing SAM predictions with ISO measurements at 12μm (Tedesco and Desert, 2002) and Spitzer measurements at the 8μm and 24μm bands (Meadows et al., 2004). Asteroid counts from both surveys show good agreement with the SAM predictions.

Spatial and sky positions of all asteroids were calculated for a the time period from 2000 January 1 to 2012 December 31, with a time resolution of 5 days. This step size was sufficient to give a good coverage of solar elongations. For the brightness calculations the Standard Thermal Model (STM; Lebofsky et al. 1986) was applied. A grid of 0.5'x0.5' cells was defined in the sky (in ecliptic coordinates), and asteroid counts above specific flux limits were determined for each cell, as well as the confusion noise due to asteroids in that particular cell. The confusion noise was calculated from the 'observed' distribution of all asteroids in that specific cell for each wavelength. These confusion noise values are lower limits since there is an unknown contribution of small (fainter) asteroids, which were considered. However, bright asteroids are the dominant sources of confusion and asteroids smaller than ~1km in diameter would not contribute to the confusion noise significantly.

Using these model calculations all-sky confusion noise maps were constructed and expected number counts were calculated for the sensitivity limits of the instruments. The main trend shows a strong concentration of asteroids and a corresponding peak of confusion noise at the local anti-solar point and an extended "cloud" is present around the current maximum. Seasonal variations are also not negligible. For Herschel, asteroid confusion would not be negligible in anti-solar direction, however, solar aspect constraints for satellites usually do not allow to observe towards opposition targets (see Fig 11.3). Therefore no asteroid confusion noise component is included in the Herschel Confusion Noise Estimator.

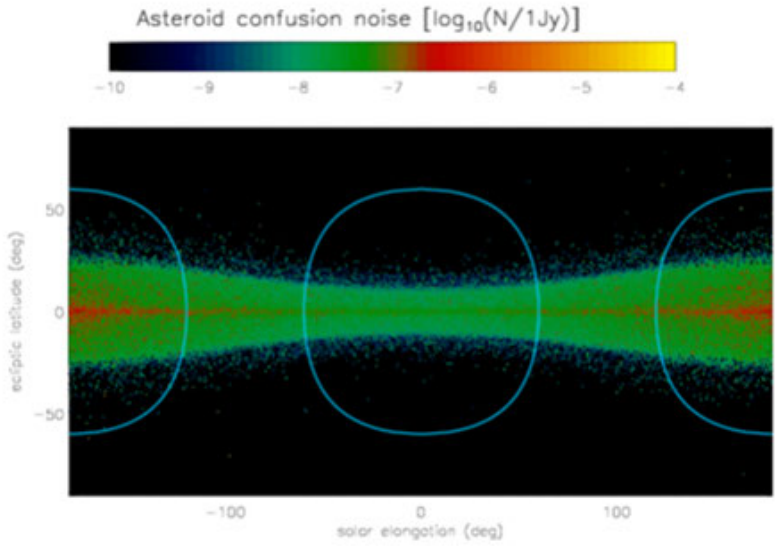

Figure 11.3: *Asteroid confusion noise for the PACS red photometric band. Asteroid confusion noise, calculated for the PACS photometer red band (λ ~175μm). Horizontal axis represent the solar elongation (λ- λ_0), while the vertical axis represent the ecliptic latitude. The Sun is in the middle of the figure at (0,0) and the anti-solar direction is at the horizontal edges of the image ((-180,0) and (180,0)). Colours represent the strength of the asteroid confusion noise, as indicated by the colour bar on the top. Although asteroid confusion may not be negligible around the anti-solar direction in some cases, Herschel will not be permitted to look in these directions due to the solar visibility constraints. These regions are indicated by blue circles in the figure.*

In Kiss et al. (2006) it was also investigated whether a colder population of asteroids (e.g. those in the Kuiper belt) can contribute more the FIR and sub-mm confusion noise than the Main Belt asteroids considered in the SAM model. The results show that although in a hypothetical population behind the Main Belt the peak of the SEDs of the asteroids are shifted to longer wavelengths, this cannot compensate for the very fast drop in brightness due to the increasing solar and terrestrial distance of these bodies (see Figure 11.4).

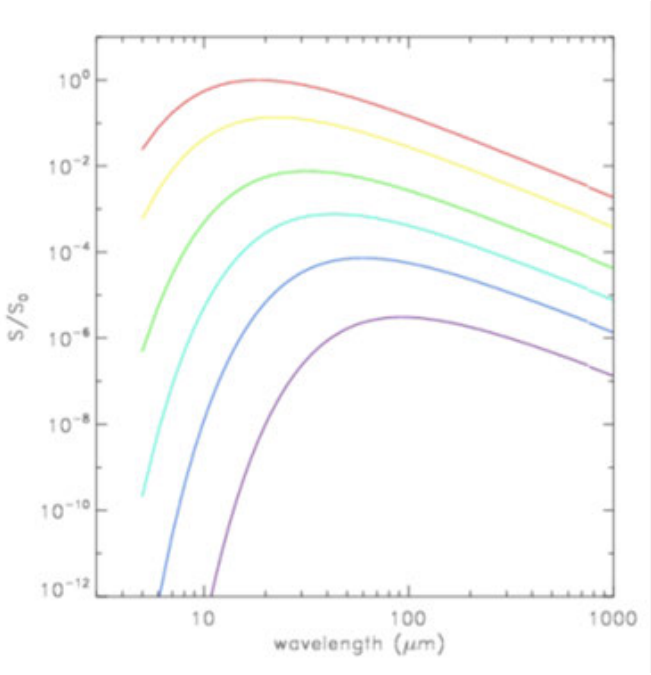

Figure 11.4: *Spectral energy distribtuion of far asteroids. Demonstration of the effect of the increasing Earth/Sun distance on the observed fluxes of the asteroids. S/S_0 is the ratio of measured S flux value at a specific wavelength and the reference flux value S_0 (the maximum value of the spectral energy distribution at Δ=1AU). The curves correspond to (Δ =1, 2, 5, 10, 20 and 50AU, from top to bottom, respectively and $r_0 = \Delta + 1AU$ in all cases. Δ and r_0 are the terrestrial and solar distances of the asteroids, respectively.*

11.5.2 Interstellar medium

The interstellar medium show a strong concentration around the Galactic plane and this feature is conspicuous at many wavelengths. However, there is another component of the interstellar medium, which is not sticked to low Galactic latitudes. The Galactic cirrus emission -- discovered by IRAS (Low et al. 1984) -- is the thermal emission of dust in weak and cool interstellar HI clouds (typically $n(H) \leq 10^2 cm^{-3}$ and $T \approx 20K$). It has a smooth modified blackbody SED with an emissivity index of $\beta \approx 2$, with some additional infrared cooling lines. This is a strong source of emission, and dominates the sky for wavelengths $\lambda > 70\mu m$, even at high Galactic latitudes. The cirrus emission is very structured, and show a typical filamentary structure.

The main characteristic of the cirrus emission -- or in general that of the interstellar medium -- is its spatial structure at a specific wavelength. This is usually described by the spectral index, α, of the power spectrum of the image, averaged over annuli (see Kiss et al., 2003, for a summary). With this parameter the power spectrum is,

$$P = P_0 \times (f / f_0)^{\alpha} \tag{11.13}$$

where $\boldsymbol{P}$ is the power at the spatial frequency $\boldsymbol{f}$ and $\boldsymbol{P_0}$ is the power at the spatial frequency $\boldsymbol{f_0}$. Due to this parameterization the structure of cirrus is equivalent to that of a fractal. The spatial structure is important in separating the cirrus from the other components of the sky background, since this is different from those of the CIB Poissonian distribution at low spatial frequencies) or of other components. Although the SED of the cirrus emission is quite well determined in the whole sky, its shape is not very different from that of the cosmic infrared background, therefore their separation in this way is not easy.

Molecular clouds with densities significantly higher than that of cirrus show a similar fractal structure (see. e.g. Falgarone et al. 2004), therefore the cirrus structure models can easily be extended to higher surface brightness regions.

There are essentially two kind of approaches to characterize the confusion noise or sky brightness fluctuations of the emission from the interstellar medium at a specific sky position; both methods have their own pros and cons. Below we describe the two methods in some detail.

In the work by Jeong et al. (2005 & 2006) the fluctuations are considered to show the same power spectrum along the whole spatial frequency range and are independent of wavelength. Jeong et al. (2005) used the SFD 100μm maps to characterize the local cirrus structure down to the resolution of IRAS. This power spectrum has been extrapolated to higher spatial frequencies, and high frequency noise is added to the original, low frequency maps. The confusion noise is calculated on these noise-coadded maps. Extrapolation to other wavelengths is done by applying a two-component dust model and the SFD 100μm emission maps. Temperatures are determined using the DIRBE 100 and 240μm measurements and fixed emissivity laws (β_1=1.67 and β_1=2.70, see Finkbeiner et al. 1999).

The greatest advantage of the method is, that the confusion noise determination is very local, and therefore can account for local deviations of the behavior of the cirrus emission. On the other hand it was shown in Kiss et al. (2003), that the spectral index # is different at various wavelengths, at least for regions of medium and high surface brightness. Since the Jeong et al. (2005) method use the SFD 100μm maps to generate power spectrum at all wavelengths, this effect is not taken into account, and can lead to unrealistic confusion noise values, especially at wavelengths significantly longer than 100μm. The main reason behind the different a at various wavelengths is the presence of a colder component (with a temperature of 15K or below) in the FIR emission. This component is hardly visible at 100μm due to its temperature and by not be accounted at all in longer wavelength maps generated from the 100μm information only.

A further shortcoming of this method -- using SFD 100μm maps to derive the power spectrum at low spatial frequencies -- is related to the behavior of detector responsivity of survey observations that scanned the sky with a fixed integration time (Miville-Deschenes & Lagache, 2005).

For small flux changes the detector stabilization times are longer than for larger ones, therefore the amplitude of the intensity fluctuations are underestimated at low flux and at small scales (see Coulais & Abergel, 2000, for a model of detector stabilization times). This means that the power spectrum of these maps are apparently steeper than they are in reality, especially for faint fields.

Power spectra taken this way underestimate the fluctuation power at the highest spatial frequencies. This is in agreement with the results by Kiss et al. (2003), where a shallower spectrum with a α -2.3 spectral index was found for the cirrus component in fields with weak cirrus contribution, in contrast to the generally accepted value of α=-3, deduced from IRAS scans.

From the technical point of view, the calculation required to generate the maps are relatively time are resource consuming. This is acceptable for specific regions, but it may be problematic to extend this method for the whole sky.

Kiss et al. (2001, 2003 & 2005) used a different approach to characterize the sky brightness fluctuations of the cirrus emission. The original idea was introduced and applied for IRAS scans by Helou & Beichman (1991) and by Gautier et al. (1992). In this approach the amplitude of the sky brightness fluctuations (i.e. the confusion noise) depends mainly on the resolving power of the instrument and the brightness of the local background. The confusion noise depends on a few parameters, and can be described by a simple equation. Once these parameters are known the strength of the confusion noise depends on the brightness of the local background only. Interpolation or extrapolation to other wavelengths can be done by using the wavelength scaling of the resolving power and the spectral energy distribution of the emission of the ISM (cirrus). The different structure at different wavelengths can also be taken into account.

An important parameter of this method is the spectral index a of the cirrus structure. The most extensive investigation of this parameter has been done by Kiss et al. (2003). Based on the analysis of ISO/ISOPHOT maps at multiple wavelength, the wavelength and brightness dependence of α was determined for the spatial scales and filter bands available with ISO/ISOPHOT. Extrapolations to smaller angular scales, however, have to rely on assumptions and extrapolation of the low spatial frequency results with this method as well. In general, the cirrus confusion noise is described by an equation similar to the one below:

$$N_{CIRR} = c_1 \times \left(\frac{\lambda}{D}\right)^{1-\alpha/2} \times B^{\eta} \tag{11.14}$$

Here N_{cirr} is the confusion noise due to the cirrus component, B is the surface brightness of the field, a is the spectral index of the logarithmic power spectrum, averaged in annuli (see Kiss et al. 2001, 2003 & 2005 for details), λ is the wavelength of the observation and D is the effective diameter of the telescope's primary mirror. The parameters c1 and h has to be determined from measurements. For IRAS 100μm scans Helou & Beichman (1990) found the following relation (they applied α=-3):

$$\frac{N_{H\&B}}{1mJy} = 0.3 \times \left(\frac{\lambda}{100\mu m}\right)^{2.5} \left(\frac{D_t}{1m}\right)^{-2.5} \left(\frac{B_\lambda}{1MJysr^{-1}}\right)^{1.5} \tag{11.15}$$

where $N_{H\&B}$ is the cirrus confusion noise, λ is the wavelength of the measurement, D is the diameter of the telescope's primary mirror, and B is the mean surface brightness of a specific field. The exponent of 2.5 of the measurement wavelength (or the -2.5 of the telescope diameter) indicate that the cirrus emission has a *measured* spectral index of –3. This finding has turned out to be roughly valid for other telescopes and instruments (e.g. ISO/ISOPHOT, Spitzer/MIPS and Herschel/PACS and SPIRE), although they were working at different wavelengths and angular resolutions. This equation shows that if cirrus confusion noise is our limiting factor, it can be overcome in two main ways: choosing a shorter wavelength or using larger mirror. Due to the large exponent of 2.5 the improvement is significant even in the case of a relatively small change. A very good example is the Herschel Space Observatory (primary mirror of 3.5m) versus the Infrared Space Observatory (ISO, primary mirror of 0.6m): while the ISO measurements were cirrus confusion dominated even in the best cosmic windows (that has the lowest cirrus contamination in the sky) at 100μm, Herschel/PACS measurements at the same wavelength are dominated by the confusion noise due to the cosmic far-infrared background, the accumulated light of distant galaxies. This latter component does not decrease for higher spatial resolution like the cirrus noise, and therefore cannot be overcome by a larger primary mirror (see e.g. Kiss et al., 2005, for a summary).

Kiss et al. (2003 & 2005) extended this analysis to a series of ISO/ISOPHOT bands, and obtained the parameters describing the confusion noise related to cirrus at different wavelengths.

These results have been scaled to the resolution of other infrared space instruments (e.g. Herschel/ PACS), assuming, that spectral index a remains unchanged for higher spatial frequencies. In these calculations the brightness-dependent spectral index (introduced by Kiss et al. 2003) was also taken into account. The most important limitation of this method is, that local deviations from the general brightness-dependence of the cirrus confusion noise are not taken into account.

Once the parameters (c_1, α, and η) are known, the calculation of the confusion noise strength is easy, and very straightforward.

11.5.3 The cosmic infrared background

The numerous sources of the CIB are randomly distributed in the sky and therefore forms a background which show spatial fluctuations, i.e. contribute to the confusion noise of the sky background. Since the detection of many sources in the CIB is an important goal for space infrared telescopes (for Herschel as well), it is important to emphasis again, that the actual confusion noise may be different for an 'unbiased survey' (detection of as many so far unknown sources as possible) or for the photometric accuracy of a single target. For deep surveys clearly detected sources do not contribute to the background any more. Since in realistic source counts fainter sources are more numerous only sources around or below a certain flux level contribute to the confusion noise.

11.6 An example: The Herschel Confusion Noise Estimator

11.6.1. Importance of a sky confusion noise estimator for the Herschel Space Telescope

As discussed in the chapters above, there are two main components, which has a notable conttribution to the confusion noise for Herschel/PACS and SPIRE photometric observations. These are the extragalactic background (specifically the cosmic infrared background) and the thermal emission of the interstellar medium in the Galaxy. This latter one consits of two main components: the dust related to the mostly molecular gas, concentraed around the Galactic midplane, and a more extended emission, related the dust in weak neutral hydrogen clouds, the Galactic cirrus emission. Confusion noise due to other components (zodiacal light, asteroids) has proved to be negligible for the Herschel mission (see above) therefore has not been considered hereafter.

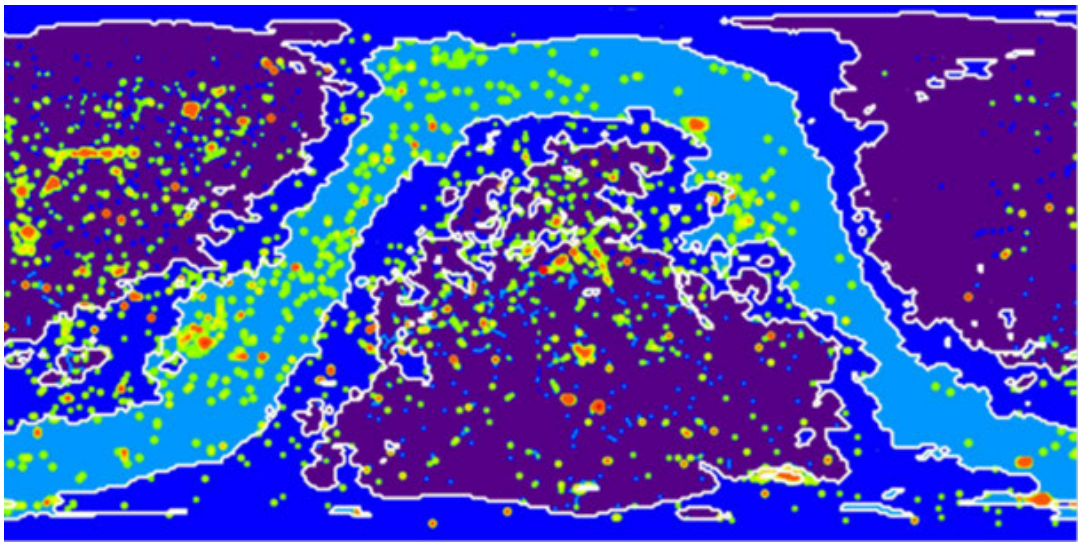

Figure 11.5: *Relative strength of the major confusion noise components for PACS. The relative strength of confusion noise component for the PACS red (175μm) photometric band in equatorial (FK5) coordinates. Three kind of regions are discriminated according to the dominant source of confusion noise: deep blue, CIB dominated; medium blue, cirrus and CIB are in the same order; light blue, cirrus (ISM) dominated. The light blue region closely follow the shape of the Galactic plane. Overlays represent the ISO pointing density of a specific 'cell' in the sky (0.5°x0.5°). Blue dots mark single pointing, while red spots are the most frequetly visited positions.*

We demonstrate the relative strength of the two main components in the sky for the PACS red band in Figure 11.5. The CIB is the dominant component for high Galactic latitudes. The expected contribution to confusion noise in the PACS blue bands is ~0.1mJy or below, while it is at in the 1mJy level for the PACS red filter (see e.g. Jeong et al. 2006). SPIRE will have to face about 6.7mJy, 9.6mJy and 7.7mJy CIB 1σ confusion noise values in the 250, 350 and 500μm bands, respectively.

In these regions the contribution of the cirrus emission is negligible. However, closer to the Galactic plane the cirrus component becomes dominant. For medium surface brightness regions the cirrus contribution can reach confusion noise values in the order of 1mJy in the PACS blue bands and ~10mJy in the PACS red band. For the SPIRE filters the cirrus confusion noise remains in the ~10mJy order for medium surface brightness regions, since the intensifying confusion noise by the increasing wavelength is compensated by the declining SED of the cirrus, compared to the FIR.

11.6.2 General comments

The Herschel Confusion Noise Estimator (HCNE) is described in detail in the document "Requirements for the integration of the Herschel Confusion Noise Estimator Prototype", version 1 (latest version: 2006 April 24). Below we summarize the science related issues of the HCNE only. As discussed above, there are only two components of the sky background that give notable contribution for the confusion noise at the photometric bands of Herschel/PACS and SPIRE. These are the thermal emission of the interstellar medium (Galactic cirrus) and the extragalactic background (namely the cosmic infrared background).

Due to their weakness, other sources, e.g. the Zodiacal Light and asteroid population in the Mail Belt, are not considered as contributors to the confusion noise. However, the HCNE code have been designed in a way, that any component which can be described by a the functional form of the multiplication of two functions ($L(\lambda)\times S(\alpha,\delta)$) can be easiliy included in the code at a later stage, since dummy functions of this kind are left in the code. Here $L(\lambda)$ is a purely wavelength dependent function and $S(\alpha,\delta)$ is a purely coordinate-depedent one.

Since the HCNE is used to give estimates for the detection of single stellar sources, it uses the 'single target' or 'full' interpretation of the confusion noise, i.e. the effect of detected sources are not taken into account separetely.

11.6.3 Cosmic infrared background:

In the current version of HCNE only the isotropic component of the cosmic infrared background is considered. This means, that using the functional form above $S(\alpha,\delta)_{CIB}$=const. for any α and δ, and the $L(\lambda)$ function is the 'spectral energy distribution of the confusion noise'. In the present version the cosmic infrared background and their fluctuations are calculated using the model of infrared galaxies at Institut d'Astrophysique Spatiale. The model is described in details in Lagache et al. (2003) and Lagache et al. (2004), and data products related to the model are publicly available at the URL: http://www.ias.u-psud.fr/irgalaxies/. The immediate output of the model at a specific wavelength is a fluctuation power (P, units of Jy^2sr^{-1}), which is then converted to confusion noise amplitude (N) using the effective solid angles (Ω) of the detector pixels: $N = (P\times\Omega)^{1/2}$

In later versions of HCNE the effect of galaxy clustering and its effect to the confusion noise may be considered. Recent results show that galaxy clustering increases the source confusion by ~10% for the Herschel mission (Negrello et al. 2004).

11.6.4 Galactic cirrus

Mainly due to its simplicity over the method used by Jeong et al. (2005), Kiss (2007) used the method described in Kiss et al. (2005) to account for the confusion noise due to Galactic cirrus -- or in general due to the thermal emission of the interstellar medium. To simplify the technical realization of this component in HCNE, Kiss (2007) used pre-calculated confusion noise values in a double parameter lookup table. The two independent variables are the wavelength λ and the surface brightness I_λ. The structure of the emitting medium is considered through the spectral index α (see Sect. 4) and is wired into the lookup tables through its λ and I_λ dependence, i.e. in the calculation of the cirrus confusion noise $N_{cirr}(\lambda,I\lambda)$ the specific $\alpha(\lambda,I\lambda)$ is applied.

11.6.5 Measurement configuration

Measurement configurations are important in calculating the confusion noise values, each measurement configuration has a different confusion noise level, even when using the same instrument/filter setup (see Kiss et al. 2005). In HCNE the confusion noise values of the different components (CIB and cirrus) are stored for a given 'reference' configuration only. Actual confusion noise values are calculated using the confusion noise values of this reference configuration, and coefficients relevant for the current configuration. These coefficients are calculated in advance, and stored in lookup tables in HCNE. The coefficients themselves depend on the basic parameters of the observing

configuration as set in the HSPOT observation designing tool. The relevant HSPOT parameters are listed in Kiss et al (2005).

References and further reading to the chapter:

Ábrahám, P., Leinert, Ch., Lemke, D., 1997: *"Search for brightness fluctuations in the zodiacal light at 25 MU M with ISO"*, A&A, 328, 702

Bond, J.R., Carr, B.J., Hogan, C.J., 1986: *"Spectrum and anisotropy of the cosmic infrared background"*, ApJ, 306, 428

Condon, J.J., 1974: *"Confusion and Flux-Density Error Distributions"*, ApJ, 188, 279

Coulais, A., Abergel, A., 2000: *"Transient correction of the LW-ISOCAM data for low contrasted illumination"*, A&AS, 141, 533

Dole, H., Lagache, G., Puget, J.-L. 2003: *"Predictions for Cosmological Infrared Surveys from Space with the Multiband Imaging Photometer for SIRTF"*, ApJ, 585, 617

Dole, H., Lagache, G., Puget, J.-L., et al. 2006: *"The cosmic infrared background resolved by Spitzer. Contributions of mid-infrared galaxies to the far-infrared background"*, A&A, 451, 417

Dole, H., Le Floc'h, E., Pérez-González, P. G. et al. 2004: *"Far-infrared Source Counts at 70 and 160 Microns in Spitzer Deep Surveys"*, ApJS, 154, 87

Falgarone, E., Hily-Blant, P., Leverier, F., 2004: *"Structure of Molecular Clouds"*, Ap&SS, 292, 89

Gautier III, T.N., Boulanger, F., Péault, M., Puget, J.-L., 1992: *"A calculation of confusion noise due to infrared cirrus"*, AJ, 103, 1313

Hauser, M.G., Dwek, E., 2001: *"The Cosmic Infrared Background: Measurements and Implications"*, ARA&A, 39, 249

Helou, G., Beichmann, C.A., 1990: *"The confusion limits to the sensitivity of submillimeter telescopes"*, in: From Ground Based to Space-Born Sub-mm Astronomy, Proc. of the 29th Liege Interational Astrophyiscal Coll. (ESA Publ.), p. 117

Jeong, W.-S., Lee, H.M., Pak, S., Nakagawa, T., Kwon, S.M., Pearson, C.P., White, G.J.,

2005: *"Far-infrared detection limits - I. Sky confusion due to Galactic cirrus"*, MNRAS, 357, 535

Jeong, W.-S., Pearson, C.P., Lee, H.M., Pak, S., Nakagawa, T., 2006: *"Far-infrared detection limits - II. Probing confusion including source confusion"*, MNRAS, 369, 281

Kiss, Cs. 2007: "The Herschel Confusion Noise Estimator", http://herschel.esac.esa.int/Docs/HCNE/pdf/HCNE_ScienceDoc.pdf

Kiss, Cs., Ábrahám, P., Klaas, U., Lemke, D., Juvela, M., 2001: *"Sky confusion noise in the far-infrared: Cirrus, galaxies and the cosmic far-infrared background"*, A&A, 379, 1161

Kiss, Cs., Ábrahám, P., Klaas, U., Lemke, D., Heraudeau, Ph., del Burgo, C., Herbstmeier, U., 2003: *"Small-scale structure of the galactic cirrus emission"*, A&A, 399, 177

Kiss, Cs., Klaas, U., Lemke, D., 2005: *"Determination of confusion noise for far-infrared measurements"*, A&A, 430, 343

Kiss, Cs., Pál, A., Müller, Th., Ábrahám, P., 2006, *"An asteroid model of the infrared sky"*, PADEU, 17, 135

Kiss, Cs., Pál, A., Müller, T. G., Ábrahám, P., 2008, *"The impact of main belt asteroids on infrared-submillimetre photometry and source counts"*, A&A, 478, 605

Lagache, G., Dole, H., Puget, J.-L., 2003: *"Modelling infrared galaxy evolution using a phenomenological approach"*, MNRAS, 338, 555

Lagache, G., Dole, H., Puget, J.-L., et al. 2004: *"Polycyclic Aromatic Hydrocarbon Contribution to the Infrared Output Energy of the Universe at z ~= 2"*, ApJS, 154, 112

Leinert, Ch., Bowyer, S., Haikala, L. K., 1998: *"The 1997 reference of diffuse night sky brightness"*, A&AS, 127, 1

Meadows, V.S., Bhattacharya, B., Reach, W.T., 2004: *"The Spitzer First Look Survey-Ecliptic Plane Component: Asteroids and Zodiacal Background"*, ApJS, 154, 469

Miville-Deschenes, M.-A., Lagache, G., 2005: *"IRIS: A New Generation of IRAS Maps"*, ApJS, 157, 302

Negrello, M., Magliocchetti, M., Moscardini, L., et al., 2004: *"Confusion noise at far-infrared to millimetre wavelengths"*, MNRAS, 352, 493

Papovich, C., Dole, H., Egami, E., et al., 2004: *"The 24 Micron Source Counts in Deep Spitzer Space Telescope Surveys"*, ApJS, 154, 70

Tedesco, E.F., Cellino, A., Zappalá, V., 2005: *"The Statistical Asteroid Model. I. The Main-Belt Population for Diameters Greater than 1 Kilometer"*, AJ, 129, 2869

Chapter 12. Appendix: Hungarian infrared studies

12.1 Properties of dust in galactic interstellar clouds

Changes of dust properties in dark clouds

By comparing maps of extinction and infrared emission, we found moderate increase of the far-infrared emissivity in dark clouds. This feature is usually interpreted as the growth of interstellar dust grains by coagulation or by ice-mantle formation. The growth of dust particles should also be observed in the optical wavelength range by the change of extinction properties at different wavelengths; these changes are usually described by one single parameter, the ratio of total over selective extinction, R_V. To test the relationship between the far-infrared emissivity and R_V, we observed six target fields with the Wide Field Camera mounted on the Isaac Newton Telescope (Observatorio del Roque de los Muchachos, La Palma) in B, V and R photometric bands, on May 29-30, 2006. The target fields were previously observed by the ISOPHOT instrument on board the ISO satellite in the far-infrared. We find that far-infrared emissivity has a clear dependence on temperature. The emissivity is enhanced by a factor of usually less than 2 in the low dust temperature regime of 12K≤Td≤14K. This result suggests larger grain sizes in those regions.

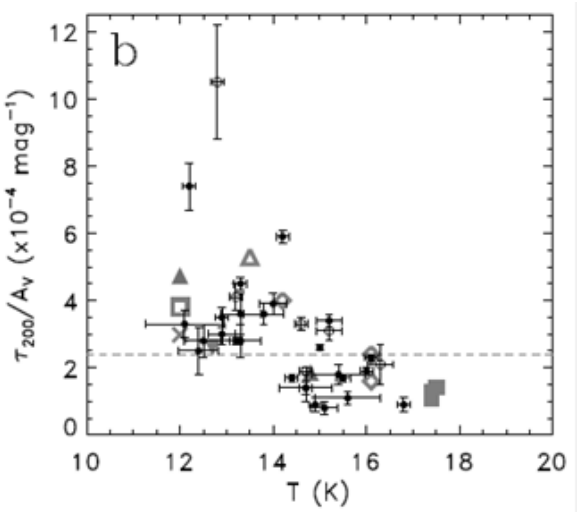

Figure 12.1: *Relationship between I_{200}/A_V and the dust temperature. Black dots with error bars mark the fields investigated in this study. Open circles with error bars mark the reprocessed del Burgo et al. (2003) target fields. We also present recent results published in other papers, marked by gray symbols. (Kiss et al. 2006)*

However, the emissivity increase of typically below 2 restricts the possible grain growth processes to ice-mantle formation and coagulation of silicate grains, and excludes the coagulation of carbonaceous particles on the scales of the regions we investigated. In the temperature range 14 K ≤ Td ≤ 16 K a systematic decrease of emissivity is observed with respect to the values of the diffuse interstellar matter. (Kiss et al. 2006)

12.2 Time variable dust emission in young stellar objects

Infrared variability as a new possibility to explore circumstellar disk structure

The infrared emission of young stellar objects is in almost always thermal radiation of dust grains. Careful analysis of ground-based and space-borne infrared observations revealed variability of a growing number of young stellar objects in the 1-100 umm wavelength range. We developed a new method, in which the lightcurves at different wavelengths can be interpreted via comparison with synthetic time-dependent spectral energy distributions. This technique may place strong constraints on basic assumptions of circumstellar disk models, and serve as an efficient diagnostic tool of the circumstellar structure. (Ábrahám et al. 2006a)

Long-term infrared variability of the UX Ori-type star SV Cep

We investigated the long-term optical-infrared variability of SV Cep and explained it in the context of an existing UX Ori (UXOR) dust disc model. A 25-month monitoring programme was completed with the Infrared Space Observatory in the 3.3-100 micron wavelength range. Following a careful data reduction, the infrared light curves were correlated with the variations of SV Cep in the V band. A remarkable correlation was found between the optical and the far-infrared light curves. In the mid-infrared regime, the amplitude of variations was smaller, with a hint for a weak anticorrelation with the optical changes. In order to interpret the observations, we modelled the spectral energy distribution of SV Cep assuming a self-shadowed disc with a puffed-up inner rim, using a two-dimensional radiative transfer code. We found that modifying the depth of the inner rim, the wavelength dependence of the long-term optical-infrared variations was well reproduced, except the mid-infrared domain. The origin of variation of the rim depth might be fluctuation in the accretion rate in the outer disc. The mid-infrared behaviour was tested by adding an optically thin envelope to the system, but this model failed to explain the far-infrared variability. Infrared variability was a powerful tool to discriminate between models of the circumstellar environment. The proposed mechanism of variable rim depth may not be restricted to UXOR stars, but might be a general characteristic of intermediate-mass young stars. (Juhász et al. 2007)

12.3 Infrared emission and dust properties in eruptive young stellar objects

The outburst of the eruptive young star OO Serpentis between 1995 and 2006

OO Serpentis is a deeply embedded pre-main sequence star in the Serpens NW star-forming region. The star went into outburst in 1995 and gradually faded afterwards. In many respects its eruption resembled the well-known FU Orionis-type (FUor) or EX Lupi-type (EXor) outbursts. Since very few such events have ever been documented at infrared wavelengths, our aim was to study the temporal evolution of OO Ser in the infrared. OO Ser was monitored with the Infrared Space Observatory in the 3.6-100 μm wavelength range, starting 4 months after peak brightness and covering a period of 20 months. Eight years later, in 2004-2006 we again observed OO Ser at 2.2 and 12 μm from the ground and complemented this dataset with archival Spitzer observations also from 2004. We analysed these data with special attention to source confusion and constructed light curves at 10 different wavelengths as well as spectral energy distributions. The outburst caused brightening in the whole infrared regime. According to the infrared light curves, OO Ser started a wavelength-independent fading after the peak brightness. Later the flux decay became slower but stayed practically wavelength-independent. The fading is still ongoing, and current fading rates indicate that OO Ser will not return to quiescent state before 2011. The outburst timescale of OO Ser seems to be shorter than that of FUors, but longer than that of EXors. The outburst timescale and the moderate luminosity suggest that OO Ser is different from both FUors and EXors, and shows some similarities to the recently erupted young star V1647 Ori. Based on its SED and bolometric temperature, OO Ser seems to be an early class I object, with an age of $<10^5$ yr. As proposed by outburst models, the object is probably surrounded by an accretion disc and a dense envelope. This picture is also supported by the wavelengthindependence of the fading. Due to the shorter outburst timescales, models developed for FUors can only work for OO Ser if the viscosity parameter in the circumstellar disc, α, is set to an order of magnitude higher value than usual for FUors. (Kóspál et al. 2007)

High-resolution polarimetry of Parsamian 21: the structure of an edge-on FU Ori disc

We analysed the first high spatial resolution near-infrared direct and polarimetric observations of Parsamian 21, obtained with the VLT/NACO instrument. We complemented these measurements with archival infrared observations, such as HST/WFPC2 imaging, HST/NICMOS polarimetry, Spitzer IRAC and MIPS photometry, Spitzer IRS spectroscopy as well as ISO photometry.

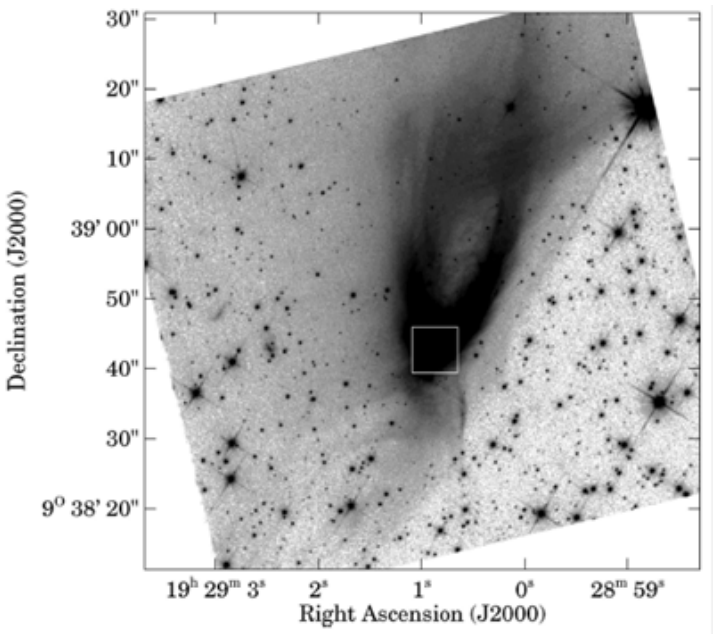

Figure 12.2 a: *HST/WFPC2 image of Parsamian 21 taken through the F814W filter. The intensity scale is square root and brightness increases from light to dark. (Kóspál et al. 2008)*

Our main conclusions are the following: (1) we argue that Parsamian 21 is probably an FU Orionis-type object; (2) Parsamian 21 is not associated with any rich cluster of young stars; (3) our measurements reveal a circumstellar envelope, a polar cavity and an edge-on disc; the disc seems to be geometrically flat and extends from approximately 48 to 360 AU from the star; (4) the SED can be reproduced with a simple model of a circumstellar disc and an envelope; (5) within the framework of an evolutionary sequence of FUors proposed by Green et al. (2006) and Quanz et al. (2007), Parsamian 21 can be classified as an intermediate-aged object.

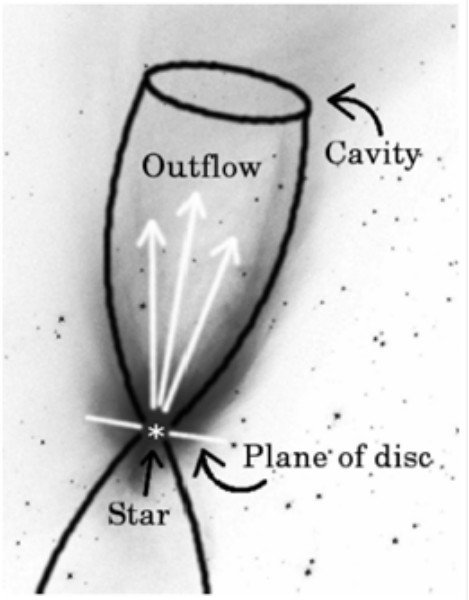

Figure 12.2 b: *Scematic model of Parsamian 21: The central star is surrounded by an edge-on disc. Perpendicular to the disc, the star drives a bipolar outflow (Kóspál et al. 2008).*

12.4 The outburst of V1647 Orionis

The 2004-2006 Outburst and Environment of V1647 Ori

We studied the brightness and spectral evolution of V1647 Ori during its recent outburst in the period 2004 February-2006 September. We performed a photometric follow-up in the bands V, RC, IC, J, H, and Ks, as well as visible and near-IR spectroscopy. The main results derived from combining our data with those published by other authors are as follows: the brightness of V1647 Ori stayed more than 4 mag above the preoutburst level until 2005 October, when it started a rapid fading. In the high state we found a periodic component in the optical light curves with a period of 56 days. The delay between variations of the star and variations in the brightness of clumps of nearby nebulosity corresponds to an angle of 61deg+/-14deg between the axis of the nebula and the line of sight. The overall appearance of the infrared and optical spectra did not change in the period 2004 March-2005 March, although a steady decrease of H I emission-line fluxes could be observed. In 2006 May, in the quiescent phase, the He I 1.083 μm line was observed in emission, contrary to its deep blueshifted absorption observed during the outburst. The J-H and H-Ks color maps of the infrared nebula reveal an envelope around the star whose largest extension is about 18" (0.03 pc). The color distribution of the infrared nebula suggests reddening of the scattered light inside a thick circumstellar disk. Comparison of the Ks and Hα images of McNeil's Nebula, the conical nebulosity illuminated by V1647 Ori, shows that HH 22A, the Spitzer infrared source, and the bright clump C of the nebula may be unrelated objects. We show that the observed properties of V1647 Ori could be interpreted in the framework of the thermal instability models of Bell and coworkers. V1647 Ori might belong to a new class of young eruptive stars, defined by relatively short timescales, recurrent outbursts, a modest increase in bolometric luminosity and accretion rate, and an evolutionary state earlier than that of typical EXors. (Acosta-Pulido et al. 2007.)

First AU-scale observations of V1647 Orionis with VLTI/MIDI

The young eruptive star V1647 Ori was observed with MIDI, the mid-infrared interferometric instrument at the Very Large Telescope Interferometer (VLTI), on March 2, 2005. We presented the first spectrally resolved interferometric visibility points for this object. Our results showed that (1) the mid-infrared emitting region was extended, having a size of approximately 7 AU at 10 micron; (2) no signatures of a close companion could be seen; (3) the 8-13 micron spectrum exhibited no obvious spectral features (see Figure 12.3).

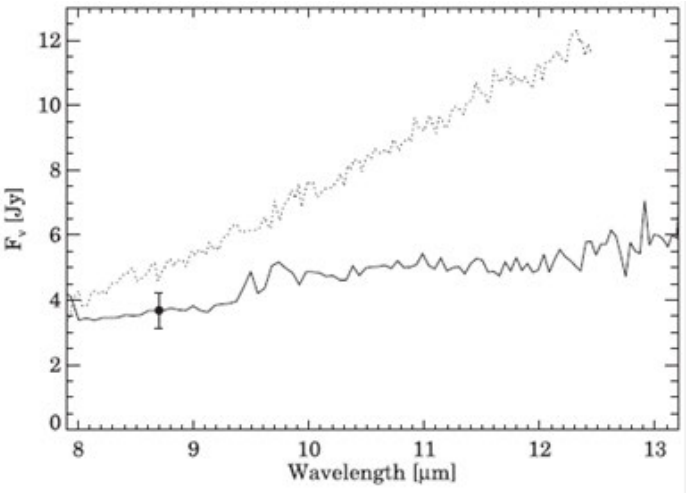

Figure 12.3: *N-band spectra of V1647 Ori at different epochs: solid line – VLTI/MIDI (March 2, 2005, this study); dotted line – UKIRT/Michelle (March 11, 2004)*

Comparison with similar observations of Herbig Ae stars suggested that V1647 Ori probably possessed a disk of moderate flaring. A simple disk model of T~r^(-0.53), surface density of D~r^(-1.5) and M_d=0.05 solar mass was able to fit both the spectral energy distribution and the observed visibility values simultaneously. (Ábrahám et al. 2006b)

Dynamics during outburst⋆ Multiepoch interferometric observations of V1647 Ori

It is hypothesised that all low-mass young stellar objects undergo eruptive phases during their early evolution. Such phases can last some months – several decades, and are characterised by 2-6 magnitude optical brightening. These eruptions are thought to be due to highly increased mass accretion from the disk. Understanding these

eruptive objects might be crucial for the understanding of the evolution of Sun-like stars and their planetary systems. Monitoring the variations of source properties of these outbursting objects is the way to constrain the eruption model. The outburst of V1647 Ori (2003-06) offered a rare opportunity to investigate such accretion event. V1647 Ori was targeted in a large number of observing programs during this recent outburst. By means of our interferometry observing campaign, we aimed at investigating/tracing the temporal evolution of the structure of the inner (few AU) circumstellar environment of V1647 Ori, which plays an important role in the outburst. We observed V1647 Ori with MIDI on the VLTI during this outburst. We used the radiative transfer code MC3D to fit the spectral energy distributions and interferometry data from different epochs. The comparison allows us to trace structural changes in the system on AU-scales. Here we present mid-infrared interferometry data obtained in the second successful observing run in September 2005 and the results of the modeling of four different stages of the outburst. The results show the disk and the envelope are similar to those of non-eruptive young star and the variation of the accretion rate during the outburst. Furthermore we found evidence of significant changes in the structure of the circumstellar matter. Most of our results fit in the canonical picture of young eruptive stars. Although this study could not reveal the trigger and mechanism of the outburst, but provided dynamical information from the regions of the innermost few AUs the system: a surprising episode accompanying the end of the outburst is indicated. (Mosoni et al. 2013)

12.5 The outburst of EX Lupi

EX Lupi in quiescence

EX Lupi is the prototype of EXors, a subclass of low-mass pre-main sequence stars whose episodic eruptions are attributed to temporarily increased accretion. In quiescence the optical and near-infrared properties of EX Lup cannot be distinguished from those of normal T Tau stars. Here we investigate whether it is the circumstellar disk structure that makes EX Lup an atypical Class II object. During outburst the disk might undergo structural changes. Our characterization of the quiescent disk is intended to serve as a reference for studying the physical changes related to one of EX Lupi's strongest known eruptions in 2008 Jan-Sep. We searched the literature for photometric and spectroscopic observations including ground-based, IRAS, ISO, and Spitzer data. After constructing the optical-infrared spectral energy distribution (SED), we compared it with the typical SEDs of other young stellar objects and modeled it using the Monte Carlo radiative transfer code RADMC. We determined the mineralogical composition of the 10 μm silicate emission feature and also gave a description of the optical and near-infrared spectra. The SED is similar to that of a typical T Tauri star in most aspects, though EX Lup emits higher flux above 7 μm. The quiescent phase data suggest low-level variability in the optical-mid-infrared domain. By integrating the optical and infrared fluxes, we derived a bolometric luminosity of 0.7 Lsun. The 10 μm silicate profile could be fitted by a mixture consisting of amorphous silicates, but no crystalline silicates were found. A modestly flaring disk model with a total mass of 0.025 Msun and an outer radius of 150 AU was able to reproduce the observed SED. The derived inner radius of 0.2 AU is larger than the sublimation radius, and this inner gap sets EX Lup apart from typical T Tauri stars. (Sipos et al. 2009)

Episodic formation of cometary material in the outburst

The Solar System originated in a cloud of interstellar gas and dust. The dust is in the form of amorphous silicate particles and carbonaceous dust. The composition of cometary material, however, shows that a significant fraction of the amorphous silicate dust was transformed into crystalline form during the early evolution of the protosolar nebula. How and when this transformation happened has been a question of debate, with the main options being heating by the young Sun and shock heating. Using observations taken with the Spitzer Space Telescope, we discovered mid-infrared features in the outburst spectrum of EX Lupi that were not present in quiescence. We attributed them to crystalline forsterite, and concluded that the crystals were produced through thermal annealing in the surface layer of the inner disk by heat from the outburst, a process that has hitherto not been considered. The observed lack of cold crystals excludes shock heating at larger radii. (Ábrahám et al. 2009)

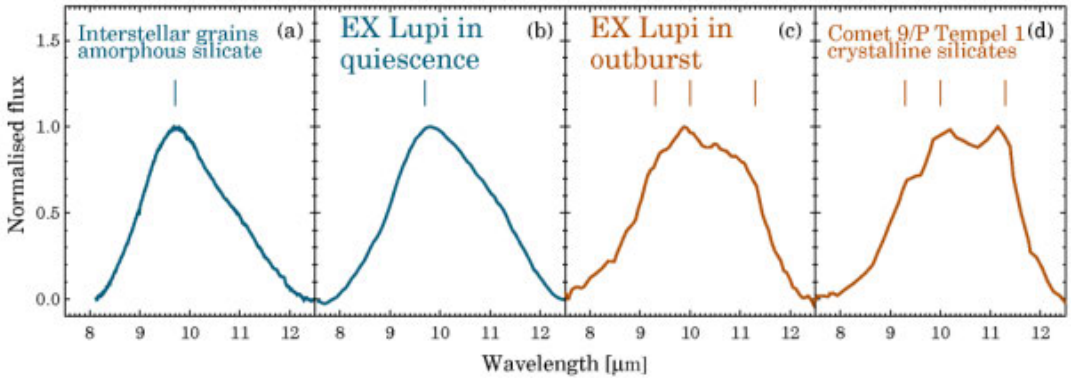

Figure 12.4: *Silicate emission in the 10 micrometer range. (a) amorphous grains in the interstellar medium; (b) Spitzer spectrum of EX Lup in 2005, in quiescent phase; (c) our Spitzer spectrum of EX Lup in the middle of the present outburst; (d) Spitzer IRS spectrum of the ejecta from comet 9/P Tempel 1 during the Deep Impact experiment. After a linear baseline removal, the spectra were normalized to their peak value. Panels (a) and (b) exhibit the triangular shape silicate profile attributed to amorphous silicate grains; vertical dash marks peak wavelength. In panels (c) and (d) peaks and shoulders due to crystalline silicates (mainly forsterite; red dashes) can be identified. The spectrum of EX Lup changed during its outburst, giving for the first time clear signs of on-going crystal formation.*

Fundamental Vibrational Transition of CO during Outburst of EX Lupi in 2008

We obtained monitoring observations of EX Lup in the CO fundamental band of 4.6–5.0 μm during its outburst in 2008. The observations were carried out at the VLT and the Subaru Telescope in 6 epochs from April to August 2008, covering the plateau of the outburst and the return to a quiescent state. The CO spectra consists of 3 components: outburst, quiescent emission lines, and possible disk wind absorption. The outburst spectrum is characterized by broad line emission (FWZI > 200 km s^{-1}) from highly excited vibrational levels (v6). The rotational temperature is Tx =4000–4500 K, while the vibrational temperature is significantly lower (Tv 2000 K). The broad emission lines are short lived, decaying on the same timescale as the optical outburst. The line profiles are double peaked, implying the emitting gas is orbiting around the star at 0.03–0.4 AU.

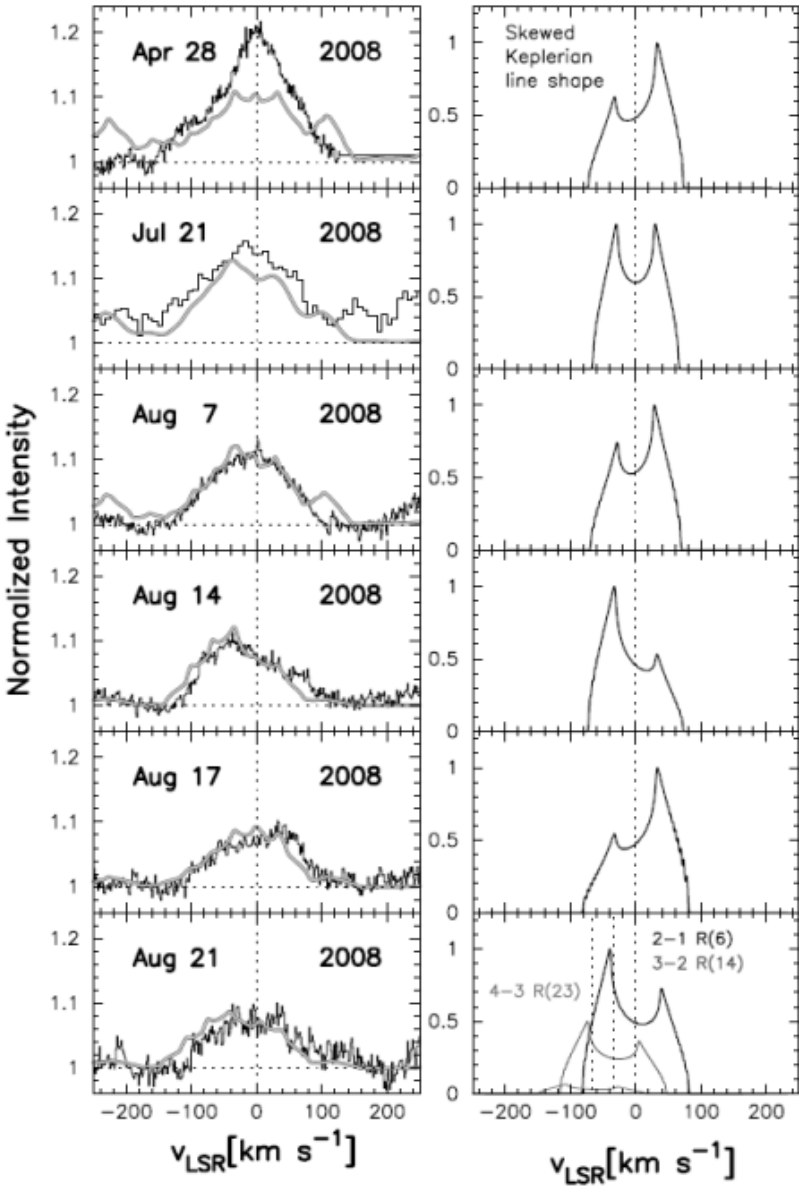

Figure 12.5: *Variation of the CO R(6) v=2-1 (λ=4.6675μm) line profiles: observed (left) and modelled (right) – see text (Goto et al. 2011).*

The quiescent component is characterized by narrow emission lines (50 km s^{-1} in FWHM) near the systemic velocity of EX Lup with a constant equivalent width (1.2–1.7)°—10−4 μm throughout the whole observing epochs. These emission lines appear exclusively in v=1-0 with rotational excitation temperatures 3100–3700 K. The velocity width translates to orbiting radius 0.4 AU, which is directly outside the outburst region. The disk wind appeared toward later epochs as absorption lines at −80 km s−1 on the blue shoulder of the quiescent emission lines. The temporal variation of the CO spectra indicates the presence of definite outer boundary around high accretion region. The outburst contained within small disk radius favors localized disk instability, rejecting the mechanisms that involves global disk instability unlikely, such as unidentified binary companion, or infall of protoplanetary cores. (Goto et al. 2011)

The 2008 outburst of EXLup - Silicate crystals in motion

EXLup is the prototype of the EXor class of eruptive young stars. These objects show optical outbursts which are thought to be related to runaway accretion onto the star. In our previous study we observed in-situ crystal formation in the disk of EXLup during its recent outburst in 2008, making the object an ideal laboratory to investigate circumstellar crystal formation and transport. This outburst was followed by a campaign of ground-based and Spitzer

Space Telescope observations. We modeled the spectral energy distribution of EXLup in the outburst from optical to millimeter wavelengths with a 2D radiative transfer code. Our results show that the shape of the SED at optical wavelengths is rather consistent with a single temperature blackbody than a temperature distribution. We also found that this single temperature component emitted 80–100% of the total accretion luminosity. We concluded that a thermal instability, the currently accepted model of EXor outbursts, was likely not the triggering mechanism of the 2008 outburst of EXLup. Our mid-infrared Spitzer spectra revealed that the strength of all crystalline bands between 8 and 30 μm increased right after the end of the outburst. Six months later, however, the crystallinity in the 10 micron complex decreased.

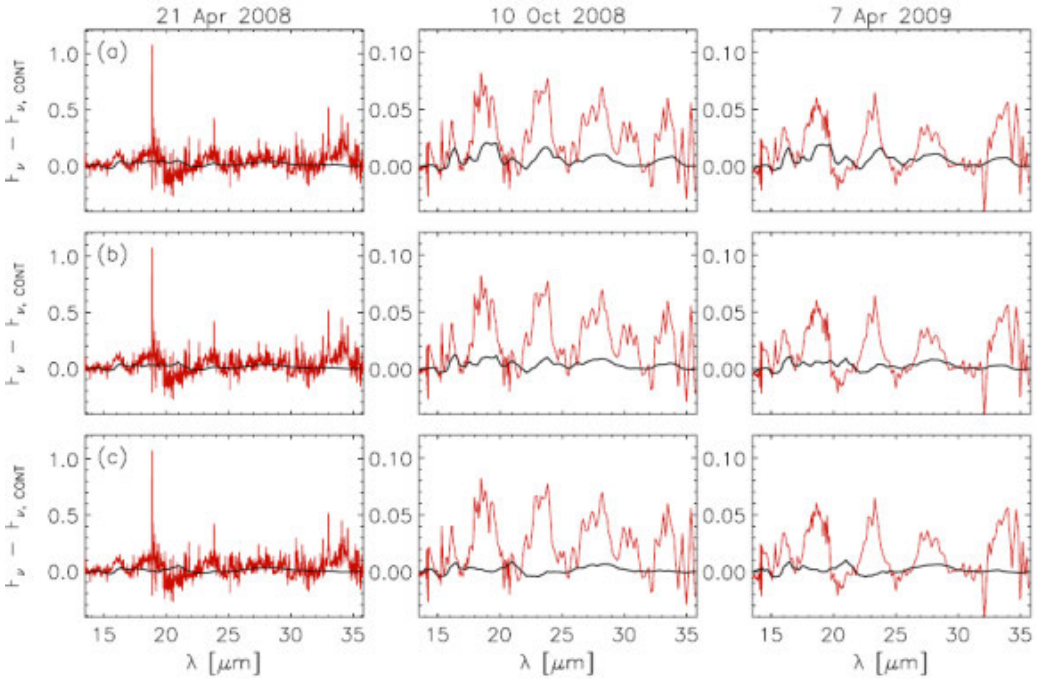

Figure 12.6: *Silicate bands of EXLupi increased right after burst then decreased (Juhász et al. 2012, see text).*

We modeled the midinfrared spectral evolution of EXLup with a 2D radiative transfer code and a 1+1D vertical mixing code. Our results show that, although vertical mixing should be stronger during the outburst than in the quiescent phase, fast radial transport of crystals (e.g., by stellar/disk wind) was required to reproduce the observed mid-infrared spectra. (Juhász et al. 2012)

Near-infrared spectroscopy of EX Lupi in outburst

We performed medium-resolution near-infrared spectroscopy of the young eruptive star EX Lup, taken during its extreme outburst in 2008. We detected several emission lines (H, He, metals, CO). By analysing these lines, we draw conclusions about the physical conditions in the emitting gas. (Kóspál et al. 2011)

12.6 Properties of debris dust

Investigation of the Vega-phenomenon among F-type stars

One of the major discoveries of the IRAS mission was that main-sequence stars can be accompanied by circumstellar dust disks (Vega phenomenon). We observed a sample of 78 Vega candidate stars with the IRS and MIPS instruments on-board the Spitzer Space Telescope. All stars were in the spectral range of F0-F9, resulting in a rather homogeneous sample in terms of stellar mass and luminosity. Our investigation focused on the following issues: (i) the temporal evolution of debris disks, concentrating on the evolution of the geometrical structure of the disk; (ii) individual systems with very high fractional luminosity; (iii) old stars with warm debris disks; and (iv) debris disks in young moving groups. Our results can be used to verify model predictions for F stars, and they can

also be compared with the outcome of similar programs dedicated to A- and G-type stars. (Moór et al. 2006; Moór et al. 2011)

The Discovery of New Warm Debris Disks Around F-type Stars

We discovered four rare debris disks with warm excesses around F stars, significantly increasing the number of such systems known in the solar neighborhood. Three of the disks are consistent with the predictions of steady-state planetesimal disk evolution models. The oldest source, HD 169666, displays a dust fractional luminosity too high to be in a steady state and we suggest that this system recently underwent a transient event of dust production. In addition, two spectra of this star separated by approximately three years show silicate emission features, indicative of submicron- to micron-sized grains. We argue that such small grains would be rapidly depleted and their presence in both spectra suggests that the production of small dust is continuous over a timescale of at least a few years. We predict that systems showing variable mid-infrared spectra, if they exist, will provide valuable help in distinguishing the possible scenarios proposed for dust replenishment.

12.7 Properties of cosmic dust in high-z galaxies

A Far Infrared Study of SN Ia host galaxies

We observed 50 high-z ($0.1 < z < 1$) SN Ia host galaxies with the MIPS camera on board the Spitzer Space Telescope at the three photometric bands (24, 70 and 160 microns). The galaxies were selected to be detectable up to $z \sim 1$. Their 24, 70 and 160 micron Hubble-diagrams (i.e. redshift vs. brightness) provide information about the dust content of the galaxies, and show whether the visible-light observations should be corrected for an unexpected dust content. Out of the 50 high-z ($0.1 < z < 1$) SN Ia host galaxies 8 were detected at 24 and only 1 at 70 micron.

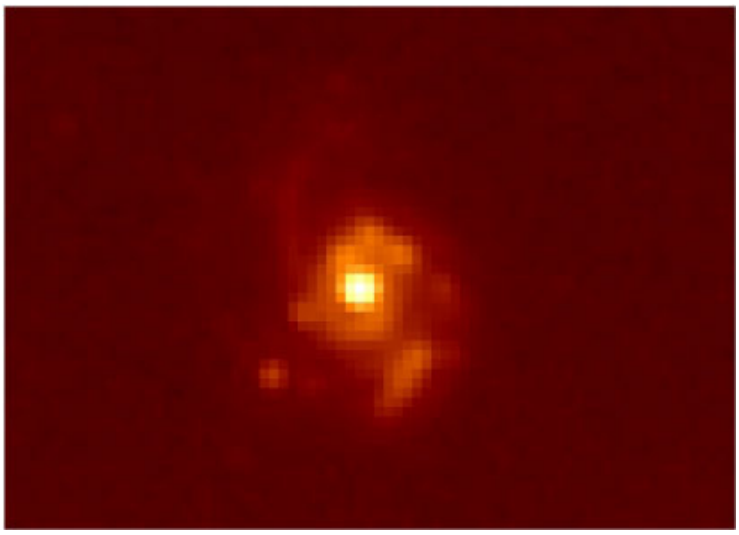

Figure 12.7: *Spitzer MIPS 24 micron image of a SN Ia host galaxy (Balázs 2006).*

This galaxy is the brightest among those detected in 24 micron. The observed brightness of the detected hosts can be compared with the IRAS galaxies assuming an appropriate SED after K correction. The low percentage of detected hosts in the whole sample may indicate that most of the hosts do not contain anomalous amount of dust. We are just at the beginning of the detailed analysis of the data and more comprehensive results are expected in the future. (Balázs et al. 2006)

References and further reading to the chapter:

Ábrahám, P. et al. 2006a: **"***Infrared Variability as a New Possibility to Explore Circumstellar Disk Structure"*, Proc. of Visions for infrared astronomy, Paris

Ábrahám, P. et al. 2006b: *"First AU-scale observations of V1647 Orionis with VLTI/MIDI"*, A&A, 449, L13

Ábrahám, P. et al. 2009: *"Episodic formation of cometary material in the outburst of a young Sun-like star"*, Nature, 459, 224

Acosta-Pulido, J. A. et al. 2007: *"The 2004-2006 Outburst and Environment of V1647 Ori"*, AJ, 133, 2020

Balázs, L. et al. 2006: *"Far Infrared Study of SN Ia Host Galaxies"*, Proc. of Visions for Infrared Astronomy, Paris

Goto, M. et al. 2011: *"Fundamental Vibrational Transition of CO During the Outburst of EX Lupi in 2008"*, ApJ, 728, 5

Juhász, A. et al. 2007: *"Long-term infrared variability of the UX Ori-type star SV Cep",* MNRAS, 374, 1242

Juhász, A. et al. 2012, *"The 2008 Outburst of EX Lup—Silicate Crystals in Motion",* ApJ, 744, 118

Kiss, Cs., et al 2006: *"Constraints on the nature of dust particles by infrared observations"*, MNRAS, 373, 1213

Kóspál et al. 2007: *"The outburst of the eruptive young star OO Serpentis between 1995 and 2006",* A&A, 470, 211

Kóspál, Á. et al. 2008: *"The Extreme Outburst of EX Lup in 2008: Optical Spectra and Light Curve"*, IBVS, 5819, 1

Kóspál, Á. et al. 2011: *"Near-infrared Spectroscopy of EX Lupi in Outburst"*, ApJ, 736, 72

Moór, A. et al. 2006: *"Nearby Debris Disk Systems with High Fractional Luminosity Reconsidered"*, Apj, 644, 525

Moór, A. et al. 2011: *"Structure and Evolution of Debris Disks Around F-type Stars. I. Observations, Database, and Basic Evolutionary Aspects",* 193. 4

Mosoni, L. et al. 2013: *"Dynamics during outburst. VLTI observations of the young eruptive star V1647 Orionis during its 2003-2006 outburst",* A&A, 552, 62

Sipos, N. et al. 2009: *"EX Lupi in quiescence"*, A&A, 507, 881

Chapter 13. Animated images

13.1 Blackbody radiation - interactive

- see Chapter 1.2, Figure 1.5
- file: 1_Planck_function.swf

13.2 Orion Nebula multiwavelength

- see Chapter 2.2, Figure 2.2
- file: 2_Orion_multiwavelength.gif

13.3 M51 galaxy observed with different telescopes

- see Chapter 2.6, Figure 2.9
- file: 3_M51_different_telescopes.gif

13.4 M51 galaxy multiwavelength

- see Chapter 3, Figure 3.4
- file: 4_M51_multiwavelength.gif

13.5 Anharmonic oscillator

- see Chapter 3, Figure 3.8
- file: 5_Anharmonic_oscillator.gif

13.6 Anthracene – interactive

- see Chapter 3, Figure 3.14
- file: 6_Anthracene_vibration.jar

13.7 Chopping-nodding observation

- see Chapter 4, Figure 4.7
- file: 7_Chop_nod_observation.gif

13.8 Galactic centre multiwavelength

- see Chapter 6, Figure 6.3

- file: 8_Gal_center_multiwavelength.gif

13.9 Infrared dark cloud multiwavelength

- see Chapter 6, Figure 6.4
- file: 9_IRDC_multiwavelength.gif

13.10 Separation of AKARI point source types

- see Chapter 6, Figure 6.8
- file: 10_AKARI_point_source_types.mp4

13.11 Planck Space Observatory's multi-wavelength view of the sky – interactive

- see Chapter 6, Figure 6.10
- file: 11_Planck

13.12 CMB by COBE, WMAP, and Planck – interactive

- see Chapter 6, Figure 6.11
- file: 12_CMB

13.13 Barnard 68 dark cloud multiwavelength

- see Chapter 8, Figure 8.4
- file: 13_B68_multiwavelength.gif

13.14 ISM density and temperature from Herschel measurements

- see Chapter 8, Figure 8.10
- file: 14_Herschel_ISM_column_density.gif

13.15 Young stellar object classes

- see Chapter 9, Figure 9.5
- file: 15_YSO_classes.gif

13.16 Planet formation

- see Chapter 9, Figure 9.10

- file: 16_Planet_formation.mpg

13.17 Young stellar object properties – interactive

- see Chapter 9, Figure 9.11
- file: 17_YSO_SED_interactive.jar